Tesis Doctoral

Programa de Doctorado en Bioingeniería

Estrategias funcionales para favorecer la osteogénesis y angiogénesis en andamios vitrocerámicos multicapa dopados iónicamente

---

Paula M. Riosalido de Lucas

Director de la tesis
Dr. D. Ángel Murciano Cases

Codirectora de la tesis
Dra. Dña. Piedad N. De Aza Moya

Instituto de Bioingeniería

Universidad Miguel Hernández de Elche

Elche, 2025

INDICIOS DE CALIDAD

La presente Tesis Doctoral, titulada **"Estrategias funcionales para favorecer la osteogénesis y angiogénesis en andamios vitrocerámicos multicapa dopados iónicamente**", realizada por Dña. PAULA M. RIOSALIDO DE LUCAS, se presenta bajo la modalidad de tesis por compendio de las siguientes publicaciones:

L. Jeevithan, **P. M. Riosalido,** Á. Murciano, P. Velásquez, P. N. De Aza, J. Elango, W. Wu, J. E. Mate Sanchez de Val,
In Vitro Biocompatibility and stem cell regenerative assessment of hollow hydroxyapatite spheres deposited Wollastonite/$Ca_2P_6O_{17}$/TCP/Doped-Wollastonite Scaffolds
Ceram. Inter 50, 37779-89 (2024)
DOI: 10.1016/j.ceramint.2024.07.141
Factor de Impacto (2023): 5.1
Puesto que ocupa / Nº de revistas en su área (2023): materials science: ceramic: 3/31(Q1-D1)

P. M. Riosalido, P. Velásquez, Á. Murciano, P. N. De Aza.
Surface Morphology Modulation in Multilayer Scaffolds via Ion Doping for Bone Tissueb Engineering
J. Am. Ceram. Soc. Vol 108 (3) pp 1-15 (2025) e20269
DOI: 10.1111/jace.20269
Factor de Impacto (2023): 3.5
Puesto que ocupa / Nº de revistas en su área (2023): materials science: ceramic: 4/31(Q1)

P. M. Riosalido, P. Velásquez, Á. Murciano, P. N. De Aza.
Multilayer Scaffolds Designed with Bioinspired Topography for Bone Regeneration
Ceram. Inter 51 (10) pp 13363-13373 (2025).
DOI: 10.1016/j.ceramint.2025.01.180
Factor de Impacto (2023): 5.1
Puesto que ocupa / Nº de revistas en su área (2023): materials science: ceramic: 3/31(Q1-D1)

P. M. Riosalido, M. Arango-Ospina, P. Velásquez, Á. Murciano, A. R. Boccaccini, P. N. De Aza

Bioactive Scaffolds Harnessing Ionic Modifications to Promote Osteogenesis and Angiogenesis in Bone Regeneration

Boletín de la Sociedad Española de Cerámica y Vidrio (2025).
DOI: 10.1016/j.bsecv.2025.100447
Factor de Impacto (2023): 2.7
Puesto que ocupa / Nº de revistas en su área (2023): materials science: ceramic: 7/31(Q1)

El Dr. D. *Ángel Murciano Cases*, director, y la Dra. Dña. *Piedad N. De Aza Moya*, codirectora de la tesis doctoral titulada **"Estrategias funcionales para favorecer la osteogénesis y angiogénesis en andamios vitrocerámicos multicapa dopados".**

INFORMAN:

Que Dña. *Paula M. Riosalido de Lucas* ha realizado bajo nuestra supervisión el trabajo titulado **"Estrategias funcionales para favorecer la osteogénesis y angiogénesis en andamios vitrocerámicos multicapa dopados iónicamente"** conforme a los términos y condiciones definidos en su Plan de Investigación y de acuerdo con el Código de Buenas Prácticas de la Universidad Miguel Hernández de Elche, cumpliendo los objetivos previstos de forma satisfactoria para su defensa pública como tesis doctoral.

Lo que firmamos para los efectos oportunos, en Elche a 03 de junio de 2025.

Director de la tesis	Codirectora de la tesis
Dr. D. *Angel Muricano Cases*	Dra. Dña. *Piedad N. De Aza Moya*

La Dra. Dña. *Piedad N. De Aza Moya*, Coordinadora del Programa de Doctorado en Bioingeniería

INFORMA:

Que Dña. *Paula M. Riosalido de Lucas* ha realizado bajo la supervisión de nuestro Programa de Doctorado el trabajo titulado **"Estrategias funcionales para favorecer la osteogénesis y angiogénesis en andamios vitrocerámicos multicapa dopados iónicamente"** conforme a los términos y condiciones definidos en su Plan de Investigación y de acuerdo al Código de Buenas Prácticas de la Universidad Miguel Hernández de Elche, cumpliendo los objetivos previstos de forma satisfactoria para su defensa pública como tesis doctoral.

Lo que firmo para los efectos oportunos, en Elche a 03 de junio de 2025.

Profa. Dra. Dña. *Piedad N. De Aza Moya*

Coordinadora del Programa de Doctorado en Bioingeniería

La presente Tesis Doctoral ha sido posible gracias a la financiación otorgada por la Conselleria de Innovación, Universidades y Sociedad Digital de la Generalitat Valenciana, en el marco del programa para grupos de investigación consolidados (CIACO/2021/157).

Asimismo, se enmarca en el proyecto PID2020-116693RB-C21, concedido por la Agencia Estatal de Investigación y el Ministerio de Ciencia e Innovación (MCIN/AEI/10.13039/501100011033).

ÍNDICE GENERAL

ACRÓNIMOS

3T3	Línea celular de fibroblastos murinos
AK	Akermanita – $Ca_2MgSi_2O_7$
ALP	Fosfatasa Alcalina
ARS	Tinción con Alizarina Roja
BLCs	Células de revestimiento óseo
BMPs	Proteínas morfogenéticas óseas
C2S	Silicato Dicálcico - Ca_2SiO_4
CB	Cristobalita - SiO_2
cCCM	Medio de Cultivo Acondicionado Acumulativo
cCCM-XD	Medio de Cultivo Acondicionado Acumulativo durante X días
CCK-8	Cell Counting Kit-8
CCM	Medio de Cultivo Acondicionado
COD	Crystalographic Open Database
CP	Pirofosfato de calcio – $Ca_2P_2O_7$
CS	Silicato Cálcico - $CaSiO_3$
CSX	Andamio completo con contenido variable de $MgCO_3$ (0-0.75 g)
DAPI	4',6-diamidino-2-fenilindol
EDX	Espectroscopía de dispersión de energía de rayos X
FDIS	Final Draft International Standard
FESEM	Microscopía Electrónica de Barrido por Emisión de Campo
FTIR	Espectroscopía por transformada de Fourier
HA	Hidroxiapatito - $Ca_{10}(PO_4)_6(OH)_2$
HFF-1	Human Foreskin Fibroblast-1
HFF-1	Línea celular de fibroblastos humanos
HSCs	Célula madre hematopoyética
ICP	Plasma Acoplado Inductivamente
ISO	Organización Internacional de Normalización
ITO	Ingeniería de tejido óseo
M(OR)n	Alcóxido metálico

MC3T3-E1	Línea celular de preosteoblastos murinos
M-CSF	Factor estimulante de colonias de macrófragos
MEC	Matriz extracelular
MSC	Células Madre Mesenquimales
MSCs	Células madre mesenquimales
MTT	Tetrazolio de 3-(4,5-dimetiltiazol-2-il)-2,5-difeniltetrazolio.
ncCCM	Medio de Cultivo Acondicionado No Acumulativo
Núcleo	CS-P6-TRIS
OES	Espectrometría de Emisión Óptica
OPG	Osteoprotegerina
P6	Ultrafosfato Cálcico - $Ca_2P_6O_{17}$
PBS	Solución Salina Tampón Fosfato
PLGA	Ácido poli(láctico-co-glicólico)
PTH	Hormona paratiroidea
PW	Pseudowollastonita - $CaSiO_3$
RANKL	RANK ligando
SBF	Suero Fisiológico Artificial
SEM	Microscopía Electrónica de Barrido
TCP	Fosfato Tricálcico - $Ca_3(PO_4)_2$
TD	Tridimita - SiO_2
TEOS	Ortosilicato de tetraetilo - $Si(OC_2H_5)_4$
TEP	Trietil fosfato - $C_6H_{15}O_4P$
TGF-β	Factor de crecimiento transformante
TRIS	Solución de ataque químico
VEGF	Factor de Crecimiento del Endotelio Vascular
WH	Whitlockita - $Ca_{10.115}Mg_{0.385}(PO_4)_7$
Wnt	Wingless-INT
WST-8	Sal de Tetrazolio Soluble en Agua-8
XRD	Difracción de Rayos X

RESUMEN

El tejido óseo posee una notable capacidad de autorregeneración, lo que le permite reparar lesiones y adaptarse a las demandas mecánicas. Sin embargo, dicha capacidad puede verse comprometida por factores como el envejecimiento o la presencia de enfermedades concomitantes. El tratamiento habitual de estas lesiones se basa en la aplicación de injertos óseos, siendo especialmente relevantes los de naturaleza cerámica debido a su baja inmunogenicidad, alta disponibilidad y similitud con la fase mineral del hueso. No obstante, aún no se ha logrado desarrollar un injerto que combine, de forma simultánea, las propiedades químicas, mineralógicas, físicas y biológicas necesarias para garantizar la eficacia del implante a largo plazo.

En este contexto, la presente Tesis Doctoral plantea el diseño y desarrollo de andamios multicapa, concebidos para combinar fases con propiedades complementarias que permitan satisfacer dichos requisitos. Para ello, se formularon andamios que integran en una única estructura las fases $CaSiO_3$, $Ca_2P_6O_{17}$ y $Ca_3(PO_4)_2$. Las técnicas empleadas para la obtención de dichos andamios fueron el proceso sol-gel y la técnica de réplica de esponja polimérica.

Los andamios desarrollados presentaron una estructura policristalina, con un núcleo compuesto por SiO_2 y cristales de $Ca_2P_2O_7$ embebidos en una matriz vítrea. Por otro lado, los recubrimientos externos proporcionaron fases bioactivas y reabsorbibles, como CS, β-TCP, whitlockita y akermanita. Respecto a las propiedades físicas, los andamios mostraron una resistencia mecánica en el rango de 1.8–2 MPa y una porosidad total cercana al 85%, valores alineados con las propiedades del hueso trabecular.

Además, considerando el potencial del dopaje iónico para modular las propiedades de los materiales, y el papel de los iones en la regulación de procesos celulares clave, se incorporó Li en la fase P6, y se dopó el recubrimiento externo de CS con Na, K, y cantidades variables de Mg (0-0,75 g $MgCO_3$).

La cantidad de Mg introducida como dopante no afectó significativamente a la porosidad o resistencia mecánica, sin embargo, moduló el comportamiento bioactivo y la microestructura de los andamios CSX. Durante los ensayos de bioactividad, se determinó que cantidades de $MgCO_3$ entre 0,4 g (CS04) y 0,5 g (CS05) optimizaron la formación de apatito, promoviendo un precipitado temprano y sostenido a lo largo de los 21 días de estudio. En particular, el andamio CS04 presentó una microestructura lamelar, que fue recubierta progresivamente por precipitado de apatito hasta quedar completamente cubierta en el día 14. Por su parte, el andamio CS05 exhibió una superficie heterogénea, caracterizada por la presencia de estructuras granulares y abastonadas. Sobre esta

superficie, se desarrolló un precipitado que experimentó una evolución desde estructuras entrelazadas (día 1) hacia una morfología poliédrica (día 3) y, posteriormente, microesferas huecas de apatita (día 7) que se mantuvieron hasta el día 14. La formación de estas microesferas se atribuye al mecanismo de maduración de Ostwald, favorecido por la elevada densidad de carga superficial inducida por el dopaje con Mg. Desde una perspectiva funcional, la topografía lamelar destaca por su biomimetismo estructural, mientras que las microesferas representan una plataforma prometedora para la liberación controlada de fármacos o agentes bioactivos.

Una vez realizados los ensayos de bioactividad, se procedió a evaluar la biocompatibilidad de los andamios CS0 (control), CS04 y CS05, en líneas celulares murinas (fibroblastos 3T3 y preosteoblastos MC3T3-E1) y humanas (fibroblastos HFF1 y células madre mesenquimales). Concretamente se evaluó la citocompatibilidad, el potencial osteogénico indirecto de los andamios mediante la exposición de MSCs a los productos de disolución, así como el potencial osteogénico directo en MC3T3-E1. Asimismo, se valoró el potencial angiogénico mediante la cuantificación de VEGF en sobrenadantes celulares de MC3T3-E1. Adicionalmente, se comparó la proliferación de fibroblastos 3T3 sembrados sobre las diferentes topografías exhibidas por CS04 y CS05 antes y después de los ensayos de bioactividad.

Todos los andamios mostraron una citocompatibilidad adecuada, reflejada en una proliferación celular sostenida tanto en el enfoque directo como en el indirecto, una morfología fenotípicamente conservada y una interacción célula-andamio robusta. El análisis de los productos de disolución reveló una liberación predominante de silicio y litio, elementos implicados en la activación de rutas osteogénicas y angiogénicas, especialmente la vía Wnt. Asimismo, se determinó que las modificaciones topográficas inducidas por el Mg, tanto el patrón lamelar de CS04, en particular su variante recubierta por apatito, como las microesferas huecas observadas en CS05, favorecieron una mayor proliferación celular respecto al resto de morfologías.

En cuanto al potencial osteogénico, los ensayos en MSCs demostraron que los productos de disolución liberados por los andamios promovieron una mayor diferenciación osteoblástica tras 21 días, como se refleja en el aumento de la expresión de ALP y en una mayor mineralización respecto al control. De forma similar, en los ensayos directos, los preosteoblastos MC3T3-E1 cultivados sobre los andamios presentaron una actividad osteogénica superior, con una mayor deposición de calcio y una actividad específica de ALP incrementada respecto al control tras 21 días. Estos efectos fueron ligeramente más acentuados en el andamio CS04, lo que se atribuye a su topografía lamelar biomimética. En cuanto al potencial angiogénico, se registró un aumento del 170 % en la liberación de VEGF en los sobrenadantes celulares de MC3T3-E1, lo cual, junto con la elevada

porosidad de los andamios, refuerza su idoneidad como soporte estructural para la vascularización tisular.

En conclusión, en la presente Tesis Doctoral se han desarrollado andamios bioactivos de tercera generación, con diseño multicapa y degradación controlada, capaces de liberar iones osteo- y angiogénicos de forma sostenida. Su elevada porosidad, topografías biomiméticas y dopaje iónico les confieren un comportamiento bioactivo avanzado, presentándose como candidatos prometedores en ITO.

ABSTRACT

Bone tissue possesses a remarkable capacity for self-regeneration, allowing it to repair injuries and adapt to mechanical demands. However, this capacity can be compromised by factors such as ageing or the presence of concomitant diseases. The usual treatment for such lesions is based on the application of bone grafts, with those of a ceramic nature being particularly relevant due to their low immunogenicity, high availability and similarity to the mineral phase of bone. However, the development of a graft that combines the chemical, mineralogical, physical and biological properties necessary to guarantee the long-term efficacy of the implant has not yet been achieved.

In this context, this Doctoral Thesis proposes the design and development of multilayer scaffolds, conceived to combine phases with complementary properties to meet these requirements. In order to achieve this objective, scaffolds integrating $CaSiO_3$, $Ca_2P_6O_{17}$ and $Ca_3(PO_4)_2$ phases into a single structure were formulated. The techniques used to obtain these scaffolds were the sol-gel process and the polymer sponge replication technique.

The developed scaffolds exhibited a polycrystalline structure, with a core composed of SiO_2 and $Ca_2P_2O_7$ crystals embedded in a glassy matrix. Conversely, external coatings provided bioactive and resorbable phases, such as CS, β-TCP, whitlockite and akermanite. Regarding physical properties, the scaffolds demonstrated a mechanical strength within the range of 1.8-2 MPa, and a total porosity close to 85%, values aligned with the properties of trabecular bone.

Furthermore, considering the potential of ion doping to modulate material properties, and the role of ions in regulating key cellular processes, Li was incorporated into the P6 phase, and the outer CS coating was doped with Na, K, and varying amounts of Mg (0-0.75 g $MgCO_3$).

The amount of Mg introduced as a dopant did not significantly affect the porosity or mechanical strength, however, it was found to modulate the bioactive behaviour and microstructure of the CSX scaffolds. During the bioactivity tests, it was determined that amounts of $MgCO_3$ between 0.4 g (CS04) and 0.5 g (CS05) optimised apatite formation, promoting early and sustained precipitation throughout the 21-day study. In particular, the CS04 scaffold exhibited a lamellar microstructure, which was progressively covered by apatite precipitate until it was completely covered by day 14. Conversely, scaffold CS05 exhibited a heterogeneous surface, characterised by the presence of granular and abased structures. On this surface, a precipitate developed and evolved from interlocking structures (day 1) to a polyhedral morphology (day 3) and, subsequently, hollow apatite

microspheres (day 7) that were maintained until day 14. The formation of these microspheres is attributed to the Ostwald maturation mechanism, which is favoured by the high surface charge density induced by Mg doping. From a functional perspective, the lamellar topography stands out for its structural biomimicry, while the microspheres represent a promising platform for the controlled release of drugs or bioactive agents.

Once the bioactivity assays were performed, the biocompatibility of the CS0 (control), CS04 and CS05 scaffolds was evaluated in murine (3T3 fibroblasts and MC3T3-E1 pre-osteoblasts) and human (HFF1 fibroblasts and mesenchymal stem cells) cell lines. Specifically, the cytocompatibility, the indirect osteogenic potential, assessed by exposing MSCs to the dissolution products, as well as the direct osteogenic potential in MC3T3-E1 were assesed. Furthermore, angiogenic potential was evaluated by quantification of VEGF release in MC3T3-E1 cell supernatants. Additionally, the proliferation of 3T3 fibroblasts seeded on the different topographies exhibited by CS04 and CS05 before and after bioactivity assays was compared.

All scaffolds demonstrated adequate cytocompatibility, reflected in sustained cell proliferation in both direct and indirect approaches, phenotypically conserved morphology and robust cell-scaffold interaction. The analysis of the dissolution products revealed a predominant release of silicon and lithium, elements involved in the activation of osteogenic and angiogenic pathways, especially the Wnt pathway. It was also determined that the topographical modifications induced by Mg, both the lamellar pattern of CS04, in particular its apatite-coated variant, and the hollow microspheres observed in CS05, favoured a higher cell proliferation than the other morphologies.

In terms of osteogenic potential, assays on MSCs demonstrated that the dissolution products released by the scaffolds promoted increased osteoblast differentiation after 21 days, as reflected by increased ALP expression and increased mineralisation compared to the control. Similarly, in direct assays, MC3T3-E1 preosteoblasts cultured on the scaffolds exhibited superior osteogenic activity, with increased calcium deposition and increased ALP-specific activity relative to the control after 21 days. These effects were slightly more pronounced in the CS04 scaffold, which is attributed to its biomimetic lamellar topography. Regarding the angiogenic potential, there was a 170% increase in VEGF release in MC3T3-E1 cell supernatants, which, together with the high porosity of the scaffolds, reinforces their suitability as a structural support for tissue vascularisation.

In conclusion, this Doctoral Thesis has developed third generation bioactive scaffolds, with multilayer design and controlled degradation, capable of releasing osteo- and angiogenic ions in a sustained manner. Their high porosity, biomimetic topographies and ionic doping confer them an advanced bioactive behaviour, presenting them as promising candidates in ITO.

1. INTRODUCCIÓN

1.1 Envejecimiento poblacional y salud ósea

El avance en el sistema sanitario en las últimas décadas ha sido tan significativo que logros que anteriormente se consideraban inimaginables, hoy son una realidad que ha transformado de manera radical la medicina y la salud pública [1, 2]. Mejoras en la higiene, la introducción de vacunas, el desarrollo de la genómica, la promoción de un estilo de vida saludable y el uso generalizado de agentes farmacológicos son solo algunos de los hitos alcanzados [2]. Si bien este progreso ha venido acompañado de un aumento en la esperanza y calidad de vida, también ha causado grandes cambios en el perfil demográfico mundial. Según la Organización Mundial de la Salud, se prevé que para 2050, la población de personas mayores de 60 años se duplique y alcance los 2.100 millones [3]. Todo esto plantea nuevos retos en salud pública derivados del envejecimiento poblacional, en concreto los aspectos relacionados con las fracturas óseas [4-6].

En consonancia con otros sistemas orgánicos, el esqueleto experimenta una serie de procesos degenerativos asociados al envejecimiento que progresivamente comprometen su funcionalidad [5, 6]. Este declive se manifiesta a través de una disminución de la masa ósea, denominada clínicamente como osteopenia u osteoporosis, un aumento en la fragilidad estructural, y una disminución en la capacidad de remodelación y regeneración tisular [5, 6]. Como consecuencia, se eleva de forma significativa el riesgo de fracturas y se favorece el desarrollo de morbilidad asociada y pérdida de autonomía funcional, fenómenos especialmente relevantes en el contexto de una población global que experimenta un envejecimiento demográfico sostenido.

Estudios recientes estiman que, anualmente se producen 178 millones de fracturas nuevas, dentro de un total de 455 millones de casos prevalentes [4,5]. Además de la carga económica que estas cifras suponen para el sistema sanitario y la productividad laboral, las limitaciones de los tratamientos actuales conllevan, en muchos casos, consecuencias en la calidad de vida del paciente incluyendo pérdida de movilidad permanente o períodos prolongados de inmovilidad. Estos datos destacan la necesidad de seguir investigando tratamientos eficaces que aborden diferentes aspectos relacionados con la salud ósea.

1.2 Fisiología ósea

El hueso, componente principal del esqueleto, constituye una estructura multifuncional que proporciona soporte mecánico al cuerpo y permite el movimiento como componente esencial del aparato locomotor [7-12]. Además de proporcionar soporte estructural y

protección a los órganos vitales, el sistema óseo alberga la médula ósea, responsable de la formación de las células sanguíneas [5, 7-11]. Asimismo, se constituye como el principal depósito de calcio y fósforo del organismo, desempeñando un papel clave en el mantenimiento de la homeostasis mineral sistémica [5, 7-11].

El esqueleto humano está formado por una amplia variedad de huesos con distintas morfologías, clasificados clásicamente en cuatro tipos: largos, cortos, planos e irregulares [6, 8, 10, 11]. Esta diversidad estructural responde a las funciones específicas que cumple cada tipo óseo dentro del aparato locomotor. Independientemente de sus diferencias morfológicas, todos los huesos comparten una organización interna jerárquica compuesta por dos tipos de tejido óseo: el hueso cortical y el hueso trabecular (Figura 1), cuya proporción relativa varía según la localización esquelética [6-8, 10].

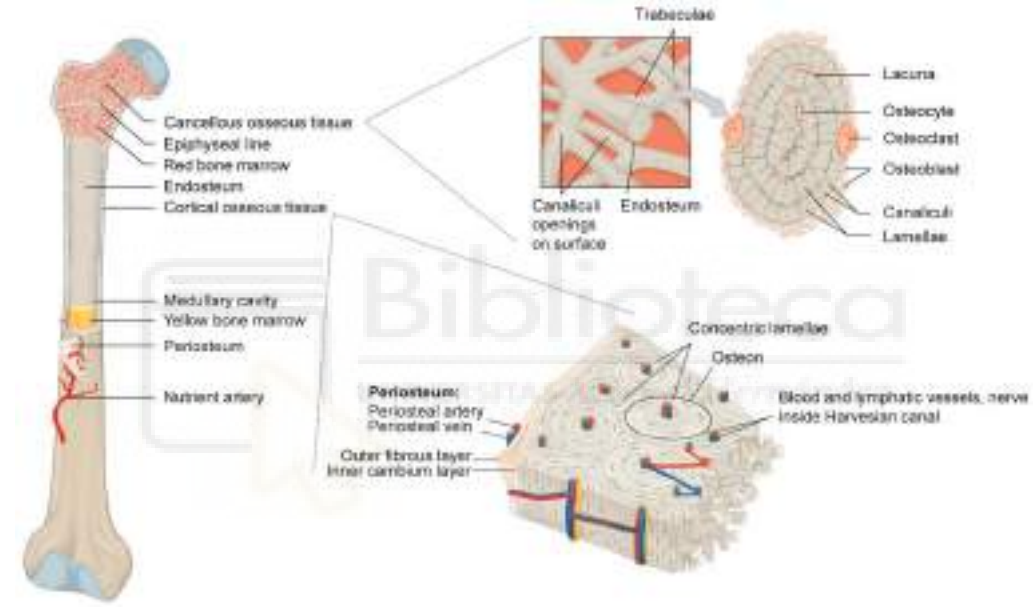

Figura 1 | Anatomía ósea. Estructura hueso cortical y trabecular [7].

1.2.1 Tipos de hueso y su función

El hueso cortical, también denominado compacto, constituye aproximadamente el 80% de la masa ósea total y se localiza en la periferia de los huesos [10, 11]. Se caracteriza por su alta densidad y baja porosidad (5-10%), lo que le confiere una elevada resistencia a la compresión (100-230 MPa) [10, 11]. Su estructura está altamente organizada en sistemas de lamelas concéntricas alrededor de canales vasculares denominados canales de Havers, a través de los cuales discurren vasos sanguíneos y fibras nerviosas (Figura 1) [7, 10, 11, 13].

En contraste, el hueso trabecular, o esponjoso, representa el 20% restante y tradicionalmente se encuentra en el interior de los huesos [11]. Está constituido por una

red tridimensional de trabéculas interconectadas que delimitan espacios ocupados por la médula ósea hematopoyética. Su porosidad es notablemente más alta (entre el 50 y el 90%, dependiendo de la localización), lo que se traduce en una resistencia mecánica es muy inferior que la del hueso cortical (1.5-9 MPa) [7, 10, 11, 13]. No obstante, su función no es simplemente estructural, también participa en la distribución interna de cargas y el amortiguamiento de impactos [10].

1.2.2 Matriz Extracelular

La matriz extracelular (MEC) ósea constituye una estructura altamente compleja y organizada, que no solo proporciona soporte mecánico al tejido, sino que también desempeña un papel esencial en la homeostasis del hueso [11]. Desde el punto de vista composicional, se trata de un material compuesto, o composite, formado por una fase orgánica, una fase inorgánica, agua y lípidos [11]. La fase orgánica representa aproximadamente entre el 20 y el 40% de la masa ósea (en peso húmedo) y está compuesta en su mayoría por colágeno tipo I (alrededor del 90% de la fracción orgánica), junto con pequeñas cantidades de colágeno tipos III y V, y proteínas no colágenas como glicoproteínas y proteoglicanos, que contribuyen a conferir elasticidad y flexibilidad al tejido [9-12, 14].

La fase inorgánica del hueso representa entre el 50% y el 70% de su peso y, aunque se acepta ampliamente que está compuesta principalmente por hidroxiapatito ($Ca_{10}(PO_4)_6(OH)_2$), un mineral que actúa como reservorio de calcio y fósforo, en realidad, los apatitos biológicos no son estequiométricos [6, 8-10, 12, 14]. Estos presentan una composición variable, caracterizada por una carbonatación parcial, deficiencia en calcio y sustituciones iónicas que modifican su estructura cristalina, solubilidad y resistencia mecánica, lo que a su vez influye en las propiedades funcionales del hueso [12, 15, 16]. Algunos de los iones sustituyentes más habituales son Na^+, K^+o Mg^{2+} (sustituyendo al Ca^{2+}), SiO_4^{4-} (sustituyendo al PO_4^{3-}), o Cl^-, F^- y CO_3^{2-} (sustituyendo al OH^-) [6, 8, 9, 12, 15].

Desde una perspectiva funcional, esta dualidad estructural es fundamental: mientras que la matriz orgánica aporta tenacidad y capacidad de absorción de energía, evitando la fractura ante impactos súbitos, la fase mineral confiere rigidez y capacidad de soportar cargas [6, 8]. No obstante, esta relación no es estática. Durante el envejecimiento, se observa un aumento progresivo del contenido mineral del tejido óseo, lo cual incrementa la rigidez y la resistencia a la deformación plástica, a expensas de una reducción de la tenacidad, es decir, una mayor fragilidad estructural [6].

1.2.3 Fracción celular ósea

La fracción celular del tejido óseo está compuesta por células responsables de su formación y remodelación: osteoblastos, osteocitos, BLCs y osteoclastos.

Los osteoblastos, derivados de MSCs, se diferencian mediante la activación de rutas de señalización específicas como BMP y Wnt, y la expresión secuencial de factores clave como Runx2 [6, 8-12, 14, 17, 20, 19]. Estas células se especializan en la síntesis de proteínas del osteoide, incluyendo colágeno tipo I, osteocalcina, osteopontina o TGF-β, entre otras [9-11, 14, 18, 19, 20]. Tras completar la formación de la matriz ósea orgánica, los osteoblastos pueden sufrir apoptosis, quedar en estado quiescente como BLCs o diferenciarse en osteocitos [20] (Figura 2).

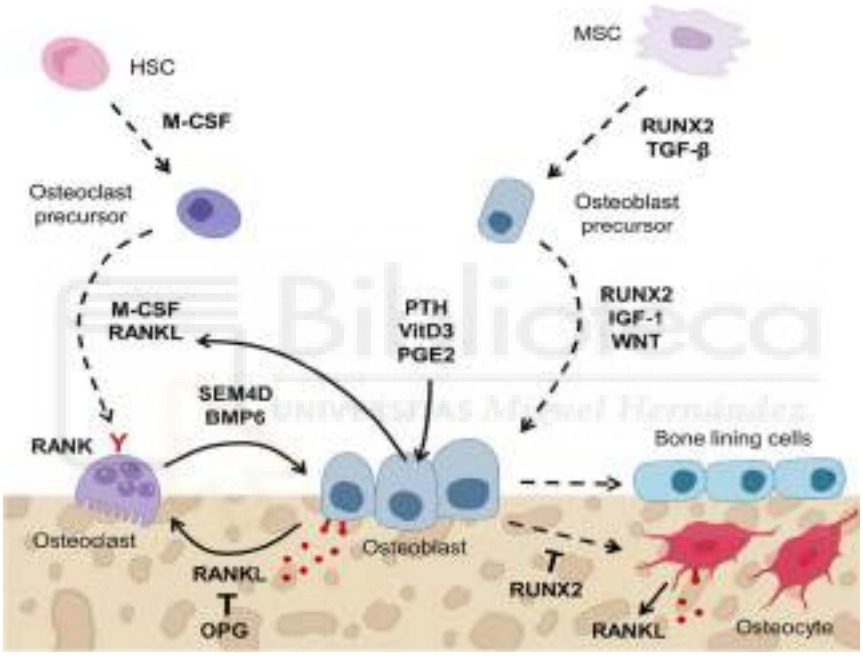

Figura 2 | Representación esquemática de la regulación de la osteoblastogénesis y osteoclastogénesis [19]

Los osteocitos, alojados en la matriz mineralizada dentro de lagunas óseas, presentan una morfología dendrítica con prolongaciones citoplasmáticas que recorren los canalículos, conductos que atraviesan la matriz mineral y permiten la comunicación celular [6, 8-10, 17, 21]. Estas prolongaciones crean una red altamente interconectada permite a los osteocitos actuar como mecanosensores detectando cargas mecánicas y regulando la actividad de osteoblastos y osteoclastos, lo que posiciona a los osteocitos como coordinadores clave en el remodelado óseo [8, 9, 17, 21].

Los osteoblastos que se transforman en BLCs, que permanecen de forma quiescente, se encuentran recubriendo las superficies óseas en reposo [8, 9]. Además, participan en la preparación de la matriz desmineralizada para la formación ósea y pueden reactivarse como osteoblastos, especialmente en respuesta a estímulos anabólicos.

Por otro lado, los osteoclastos son células multinucleadas, terminalmente diferenciadas, derivadas de progenitores hematopoyéticos del linaje monocito/macrófago (Figura 2) [6, 8-10, 12, 20]. Su diferenciación es regulada por las vías de señalización M-CSF, ITAL-RANKL y RANK-RANKL, en el que osteoblastos, osteocitos y células mesenquimales osteoprogenitoras secretan M-CSF o RANKL para promover la osteoclastogénesis, o osteoprotegerina que actúa como el inhibidor competitivo de RANKL impidiendo la osteoclastogenesis [8, 9, 18-20]. Una vez diferenciados, los osteoclastos están especializados en la reabsorción del hueso. Por un lado, degrada la parte mineral mediante la acidificación del microambiente a través de bombas de protones y canales de cloro [8-10, 12, 18]. Por otro lado, la liberación de enzimas como catepsina K, digieren la fase orgánica del hueso, originando, en última instancia, las lagunas de Howship [8-10, 18]. La degradación del componente mineral del hueso, constituido principalmente por cristales de HA, conlleva la liberación de calcio y fosfato al medio extracelular. Este mecanismo sitúa al hueso como un reservorio mineral dinámico y le confiere un papel clave en el mantenimiento de la homeostasis mineral, particularmente en la regulación de los niveles séricos de calcio.

1.2.4 Metabolismo óseo

A pesar de su apariencia inerte, el tejido óseo constituye un sistema altamente dinámico sometido a un proceso continuo de remodelación, esencial para la reparación de fracturas, la adaptación mecánica del esqueleto y el mantenimiento de la homeostasis mineral. Este proceso es llevado a cabo por la acción coordinada de osteoclastos, osteoblastos, osteocitos y células de revestimiento, cuya actividad está regulada por señales locales y sistémicas.

El ciclo de remodelación ósea comprende tres fases principales: (1) activación de la osteoclastogénesis en respuesta a estímulos locales como RANKL y M-CSF, o sistémicos como la liberación sostenida de PTH, que conducen a la resorción del hueso; (2) una fase de transición, durante la cual la degradación de la matriz ósea libera factores almacenados en el osteoide, como las BMPs o TGF-β, que inducen la diferenciación de osteoblastos a partir de MSCs; y (3) formación de nuevo tejido óseo mediante la síntesis del osteoide y su posterior mineralización por parte de los osteoblastos (Figura 3) [9, 18-20]. Este proceso está finamente regulado por una red de señales intercelulares que permite a las células óseas modular recíprocamente sus funciones en respuesta a las demandas fisiológicas [18, 19]. Así, los osteoblastos pueden secretar mediadores que regulan la diferenciación y actividad de los osteoclastos, mientras que estos últimos liberan factores durante la resorción que influyen en la maduración de los osteoblastos [10, 19]. Esta comunicación bidireccional, que incluye mecanismos previamente descritos como el sistema RANKL/RANK/OPG, garantiza el equilibrio entre formación y resorción ósea.

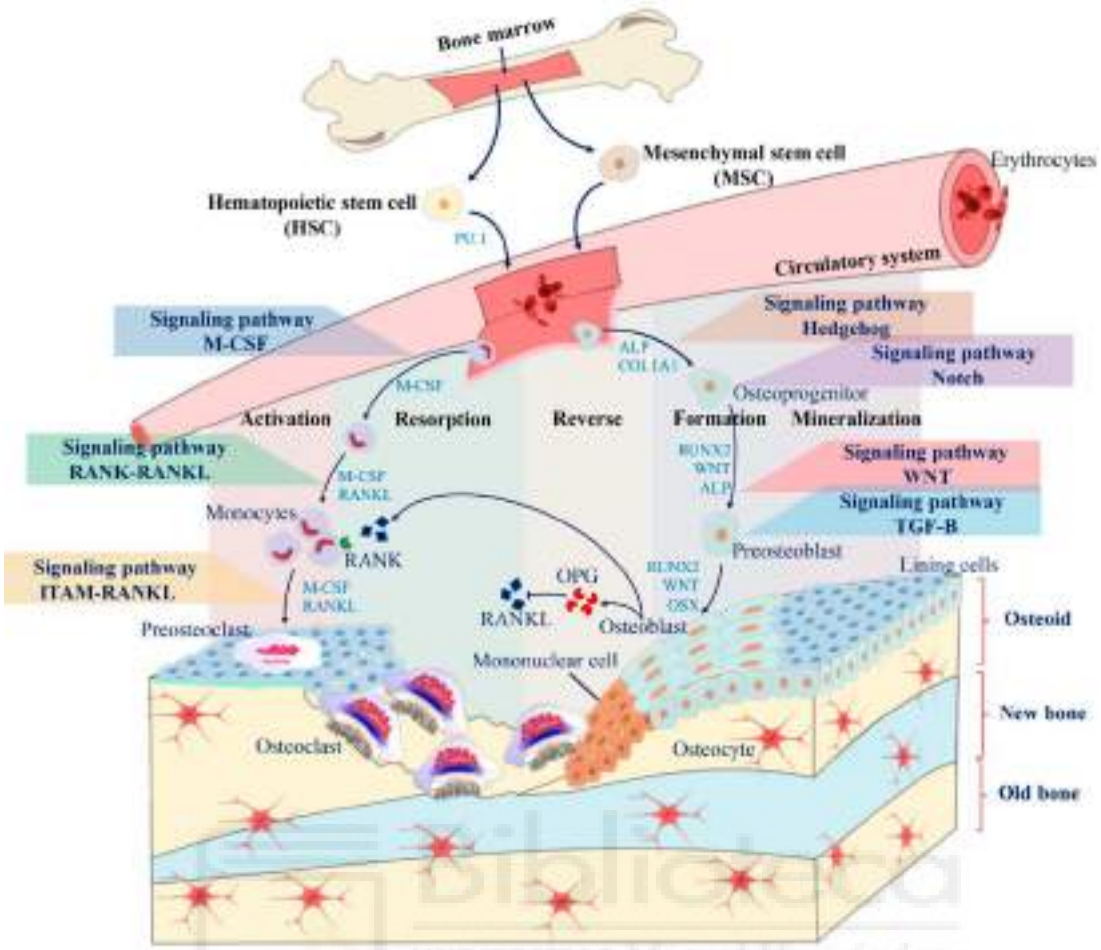

Figura 3 | Fases del ciclo de remodelación ósea y mecanismos de regulación implicados en el mantenimiento de la homeostasis ósea [20].

Sin embargo, con el envejecimiento este equilibrio tiende a desacoplarse, inclinándose a favor de la resorción ósea, lo que da lugar a una pérdida progresiva de masa ósea. Este fenómeno afecta de forma más temprana al hueso trabecular, debido a su mayor superficie específica y tasa de recambio, provocando el adelgazamiento y la pérdida de conectividad de las trabéculas [6, 10]. Paralelamente, el hueso cortical experimenta un incremento de la porosidad y un adelgazamiento de su grosor [6, 10]. En conjunto, estos cambios comprometen la arquitectura ósea y disminuyen la calidad y resistencia del esqueleto.

1.2.5 Biomecánica ósea

El tejido óseo es una estructura compleja con una notable capacidad de adaptación a las demandas mecánicas. Esta propiedad se debe a la combinación de una MEC, que actúa como un material compuesto dotado de rigidez, resistencia y cierta flexibilidad, y de un componente celular encargado de regular la remodelación ósea. Gracias a esta integración, el hueso es capaz de soportar las cargas del movimiento y modificar su estructura en función de ellas.

La mecanosensibilidad del tejido óseo está mediada principalmente por los osteocitos, localizados en el sistema lacuno-canalicular [9, 10, 17, 21]. Ante estímulos mecánicos, incluso dentro de rangos fisiológicos, se generan microdeformaciones en la matriz que provocan el desplazamiento del fluido intersticial [8, 6, 17, 21]. Este flujo activa mecanorreceptores en la membrana de los osteocitos, desencadenando una cascada de señales que modulan la actividad de osteoblastos y osteoclastos según la magnitud, frecuencia y duración del estímulo [6, 8, 11, 17, 21, 22]. Este proceso se enmarca en la Ley de Wolff, formulada por Julius Wolff en el siglo XIX, que establece que el hueso se organiza y remodela estructuralmente en función de las cargas que soporta [11, 17, 22].

En condiciones fisiológicas, se mantiene un equilibrio dinámico que preserva la masa y la arquitectura ósea [17, 22]. Sin embargo, la reducción del estímulo mecánico, como ocurre durante la inmovilización, la exposición prolongada a microgravedad o en situaciones de stress shielding inducidas por ciertos implantes metálicos que absorben la carga, favorecen la resorción ósea [21-23]. Por el contrario, cargas elevadas o repetitivas desencadenan una respuesta adaptativa con incremento localizado de la densidad ósea, como se observa en el radio distal de los tenistas, donde el tejido óseo se refuerza frente a la tensión mecánica repetida generada por el golpeo de la raqueta [24].

1.3 Sustitutos óseos

Aunque el tejido óseo posee una notable capacidad de autorregeneración, esta habilidad está condicionada por diversos factores. La edad avanzada, el tamaño y la complejidad de la lesión, así como la presencia de patologías concomitantes, pueden comprometer significativamente la eficacia del proceso reparativo [5, 6, 14, 16]. En estos casos, la intervención médica se vuelve necesaria para restaurar la integridad estructural y funcional del hueso.

Actualmente, existen múltiples estrategias terapéuticas basadas en el uso de injertos óseos, que pueden clasificarse según su origen en dos grandes grupos: injertos naturales e injertos sintéticos.

1.3.1 Injertos naturales

Existen tres tipos de injertos naturales:

(1) El autoinjerto óseo, que consiste en la transferencia de tejido óseo del propio paciente desde un sitio donante a la zona lesionada y constituye el tratamiento de referencia o gold standard cuando la capacidad regenerativa del hueso está comprometida [14, 16, 25-27]. Este tipo de injerto reúne las propiedades biológicas y mecánicas, sin riesgo de rechazo inmunológico ni transmisión de enfermedades [14, 16, 28, 27]. No obstante, su disponibilidad es limitada y su

principal desventaja radica en la morbilidad asociada al sitio donante, con complicaciones como dolor crónico o infección [14, 16, 25-28].

(2) Como alternativa, pueden emplearse aloinjertos, derivados del tejido óseo humano esterilizado, y en ocasiones descelularizado, proveniente de donantes [25, 27, 28]. Si bien evitan la necesidad de una segunda intervención quirúrgica, presentan un mayor coste, así como riesgo de transmisión de enfermedades, rechazo inmunológico y menor integración ósea, lo que incrementa el riesgo de fractura [16, 25-30].

(3) Los xenoinjertos, procedentes de otras especies, principalmente vaca, oveja o cerdo, comparten estas limitaciones y presentan, además, barreras culturales y éticas que pueden dificultar su aceptación clínica [26, 27, 29, 30].

Ante estas limitaciones, los sustitutos óseos sintéticos han adquirido una creciente relevancia en las últimas décadas como alternativa prometedora para la regeneración y reparación ósea.

1.3.2 Injertos sintéticos

Los injertos óseos sintéticos, o biomateriales, son materiales de origen artificial, diseñados para interactuar de forma controlada y segura con tejidos vivos. En este contexto, el prefijo bio- no implica que el material sea de origen biológico, sino que alude a su biocompatibilidad, entendida como la capacidad del material para desempeñar su función terapéutica sin inducir efectos adversos locales o sistémicos, como toxicidad o respuesta inmune inapropiada [23].

En comparación con los injertos de origen biológico, los biomateriales sintéticos ofrecen ventajas notables, como su disponibilidad ilimitada, la reproducibilidad de sus propiedades fisicoquímicas gracias a procesos de fabricación estandarizados, y su facilidad de esterilización [16, 25]. Estas características los convierten en una opción cada vez más empleada en el ámbito clínico [16, 28, 31].

Para ilustrar esta tendencia, en Alemania, según datos de la Oficina Federal de Estadística, en 2008 el 74,1 % de las intervenciones quirúrgicas que requerían sustitución ósea utilizaron autoinjertos, el 14,1 % emplearon aloinjertos y el 11,8 % recurrieron a injertos sintéticos [31]. Sin embargo, en 2018, los autoinjertos representaron el 54,9 %, los aloinjertos el 21,3 % y los injertos sintéticos el 23,9 %, lo que supone un incremento del 134,4 % en el uso de biomateriales como alternativa para la sustitución ósea [31].

1.3.2.1 Generaciones de biomateriales

El uso de materiales con fines terapéuticos se remonta a la antigüedad [32, 33]. Sin embargo, el concepto moderno de biomaterial no comenzó a consolidarse hasta el periodo posterior a la Segunda Guerra Mundial, cuando se produjo un notable impulso tanto en la investigación científica como en su aplicación clínica [32, 34]. Desde entonces, el campo de los biomateriales ha experimentado una evolución significativa, clasificándose en tres

generaciones en función de su comportamiento biológico y del grado de interacción con el tejido huésped.

- **Biomateriales de primera generación**

Introducidos a partir de la década de 1960, estos biomateriales fueron concebidos como soluciones sustitutivas con fines estrictamente estructurales [29, 32, 35, 36]. Su diseño se centra en reproducir las propiedades físicas y mecánicas del tejido dañado, son biocompatibles y bioinertes, es decir, no interactúan activamente con los tejidos circundantes. Su presencia en el organismo genera una reacción que conduce a la formación de una cápsula fibrosa alrededor del implante, aislándolo del entorno biológico [26, 29, 35, 36]. Entre los materiales más representativos de esta generación se encuentran los metales, cerámicas como la alúmina y la zirconia, y polímeros sintéticos como el polimetilmetacrilato, entre otros [23, 26, 29].

- **Biomateriales de segunda generación**

Desarrollados a partir de la década de 1970, los biomateriales de segunda generación supusieron un cambio de paradigma, ya que fueron diseñados no solo para sustituir tejido, sino también para interactuar funcionalmente con él [26, 35, 36]. Dentro de esta categoría se distinguen los biomateriales bioactivos y los biodegradables.

Por un lado, los biomateriales bioactivos se caracterizan por su capacidad para inducir una respuesta biológica específica que favorece una unión directa entre el material y el tejido huésped [29, 35]. Por otro lado, los biomateriales biodegradables, se degradan progresivamente en el entorno fisiológico, permitiendo su sustitución por tejido regenerado sin necesidad de intervención quirúrgica adicional [29, 35, 36]. Algunos ejemplos representativos de biomateriales bioactivos de segunda generación incluyen cerámicas como el HA y el CS, así como materiales biodegradables, entre los que destacan polímeros naturales como el colágeno y poliésteres alifáticos sintéticos [15, 26, 29, 36].

- **Biomateriales de tercera generación**

A partir de la década de 1990 surgieron los biomateriales de tercera generación cuya función principal es la regeneración tisular [26, 35, 36]. Para ello se combinan simultáneamente biomateriales de segunda generación con propiedades bioactivas y biodegradables, estructurados en forma de andamios tridimensionales temporales [35, 37]. Estos materiales no solo proporcionan resistencia mecánica, sino que también están diseñados para inducir procesos de regeneración mediante la activación de respuestas celulares específicas [26, 35, 37]. Esta activación puede lograrse mediante estrategias como la modificación superficial del material o la liberación controlada de factores de

crecimiento, citocinas o iones [16, 26]. Dentro de los biomateriales de tercera generación destacan los biopolímeros, los hidrogeles funcionalizados y las biocerámicas [32, 38].

1.3.2.2 Biocerámicas

Los materiales cerámicos constituyen una fuente esencial de biomateriales en el ámbito de la ingeniería biomédica. Según su comportamiento en el entorno biológico, se clasifican en tres grandes grupos: bioinertes, bioactivas y reabsorbibles [29, 37]. Desde el punto de vista estructural, pueden diferenciarse por su grado de cristalinidad en cerámicas cristalinas, vidrios amorfos y vitrocerámicas [37]. Finalmente, atendiendo a su composición química, se agrupan principalmente en fosfatos y silicatos cálcicos [37].

A continuación, se describen las principales biocerámicas empleadas en regeneración ósea, con especial atención a aquellas que son objeto de estudio en esta Tesis Doctoral.

- **Fosfatos cálcicos**

Las biocerámicas bioactivas y biodegradables más empleadas en regeneración ósea están basadas en fosfatos cálcicos, debido a su estrecha similitud con la fase mineral del tejido óseo [15, 16, 26]. Estas están compuestas por iones calcio (Ca2+) combinados con ortofosfatos (PO_4^{3-}), meta- (PO^{3-}), piro- ($P_2O_7^{4-}$) o ultrafosfatos, un término menos definido que engloba estructuras altamente polimerizadas de fosfato [16, 28, 29]. En base a su estabilidad energética, se degradan de menor a mayor estabilidad desde ultrafosfato a ortofosfato pasando por pirofosfato. Este proceso facilita la mineralización ósea [16, 39, 40].

En este sentido, el ultrafosfato cálcico ($Ca_2P_6O_{17}$) y el pirofosfato cálcico ($Ca_2P_2O_7$), ofrecen propiedades prometedoras. El primero, con una estructura densa y parcialmente desordenada, ha demostrado su capacidad de densificación cuando se emplea como recubrimiento, rellenando fisuras preexistentes y mejorando la resistencia mecánica del material [41, 42]. El segundo, considerado un intermediario en la mineralización del osteoide, muestra buena biocompatibilidad y resistencia a la compresión [30].

Entre los compuestos más utilizados se encuentran el α y β-TCP, ($Ca_3(PO_4)_2$) y el HA ($Ca_{10}(PO_4)_6(OH)_2$), ampliamente valorados por su biocompatibilidad y capacidad de unión al tejido óseo [16, 28, 29, 40, 43]. Mientras que el α y β-TCP es reabsorbible, el HA sintético es altamente estable, lo que dificulta su reemplazo por tejido nuevo [16, 28, 40]. Por otro lado, ambos presentan limitaciones mecánicas, lo que restringe su aplicación en entornos sometidos a carga [16, 40].

- **Silicatos cálcicos**

Los silicatos cálcicos constituyen otra clase relevante de biocerámicas utilizadas en la regeneración de tejido óseo, principalmente por su elevada bioactividad [15, 26, 29]. Sin

embargo, a diferencia de otros materiales bioactivos, los silicatos cálcicos liberan iones de silicio durante su degradación, los cuales están implicados en el metabolismo óseo, particularmente en la activación de osteoblastos [15, 26, 28, 29]. En esta línea, los fosfatos cálcicos dopados con silicio han demostrado una mayor bioactividad y mejores propiedades mecánicas en comparación con sus homólogos no modificados [15, 26, 29].

Entre los silicatos cálcicos más investigados se encuentra el CS ($CaSiO_3$); el silicato dicálcico (Ca_2SiO_4); y la akermanita ($Ca_2MgSi_2O_7$) [26, 29]. De ellos, el CS ha suscitado especial interés por su elevada bioactividad *in vitro*, correlacionada con una excelente osteointegración y biocompatibilidad en estudios *in vivo* [15, 26]. No obstante, su elevada fragilidad continúa siendo un obstáculo para su aplicación en contextos sometidos a esfuerzos mecánicos significativos [15, 26].

Las limitaciones inherentes de los biomateriales desarrollados hasta la fecha han impulsado la búsqueda de alternativas y la evolución de estrategias innovadoras, siendo este el fin de la ingeniería de tejido óseo.

1.4 Ingeniería de tejido óseo

El campo de la ingeniería de tejido óseo (ITO) se consolidó hace aproximadamente tres décadas, apoyado en un conocimiento profundo de la estructura, biomecánica y metabolismo del tejido óseo. Su objetivo principal es desarrollar injertos funcionales que estimulen la regeneración, superando las limitaciones de los injertos autólogos, alogénicos y xenogénicos tradicionales.

La ITO constituye una estrategia terapéutica prometedora para el tratamiento de lesiones óseas y trastornos esqueléticos. Su eficacia se basa en la integración sinérgica de cuatro componentes fundamentales:

- **Andamios bioactivos y biocompatibles**, diseñados para imitar con precisión las propiedades y funciones de la MEC del tejido óseo [14, 42, 44- 46].
- **Células osteogénicas**, responsables de la síntesis y mineralización de la matriz [38, 40, 42].
- **Vascularización** adecuada, esencial para aportar nutrientes, eliminar productos de desecho y favorecer la integración del en el entorno biológico [25, 27, 43, 44].
- **Señales que dirigen el proceso regenerativo**, como factores osteogénicos y/o angiogénicos, capaces de promover el reclutamiento celular, la diferenciación fenotípica deseada y la formación de nuevo tejido [40, 43-45].

En conjunto, la ITO se enmarca dentro del campo de los biomateriales de tercera generación, caracterizados por inducir procesos de autorregeneración mediante la activación específica de rutas celulares.

A pesar de los avances logrados, persiste la necesidad de conseguir una integración funcional entre los andamios óseos y el sistema vascular, de modo que se garantice una coordinación entre los procesos de osteogénesis y angiogénesis, condición indispensable para el éxito del implante y la regeneración tisular sostenida a largo plazo [25, 27, 43, 44].

1.4.1 Andamios para la regeneración ósea

Los andamios son estructuras tridimensionales que actúan como soportes temporales para células y tejidos durante el proceso de regeneración, de modo que, a medida que el tejido se regenera, el andamio se degrada de forma controlada y es reemplazado por tejido neoformado [25, 33, 46, 44]. Su diseño debe considerar las particularidades del tejido diana, con el objetivo de emular en la mayor medida posible sus propiedades estructurales y funcionales.

El diseño de andamios para ITO exige una evaluación rigurosa de sus propiedades químicas y mineralógicas, físicas y biológicas, con el fin de reproducir fielmente la estructura, función y comportamiento del tejido óseo nativo, y predecir con mayor fiabilidad su comportamiento *in vivo*.

1.4.2 Diseño de andamios

1.4.2.1 Propiedades químicas y mineralógicas

Las propiedades químicas y mineralógicas de un biomaterial son factores clave que determinan su funcionalidad, biocompatibilidad y desempeño en sistemas biológicos. Estas propiedades están estrechamente vinculadas a su estructura atómica y molecular, que define los tipos de enlaces químicos presentes, así como la organización estructural y la cristalinidad, que influyen en la estabilidad y reactividad del material [39, 47, 48].

Es esencial distinguir entre las propiedades químicas superficiales y las de volumen, ya que estas tienen implicaciones diferentes en el comportamiento del biomaterial [47]. Dado que la superficie constituye el límite de la estructura tridimensional del material, los átomos de esta zona no están rodeados del máximo número de átomos o iones, lo que aumenta su reactividad en comparación con los átomos en el interior [47]. Mientras que las **propiedades superficiales** afectan las respuestas celulares a través de aspectos como la **humectabilidad**, la adsorción de proteínas, la adhesión celular y, en consecuencia, la biocompatibilidad, las **propiedades internas** regulan aspectos fundamentales como la **reactividad**, la biodegradabilidad, y el carácter ácido o básico del biomaterial, todos ellos determinantes en su desempeño en un entorno biológico [39, 46-48]. La **biodegradabilidad** de un biomaterial resulta particularmente relevante, dado que durante el proceso de descomposición se liberan subproductos tales como iones, fragmentos poliméricos o partículas metálicas [26, 29, 39, 46, 48]. Estos subproductos pueden inducir

diversos efectos biológicos, que abarcan desde respuestas citotóxicas no deseadas, hasta efectos beneficiosos [29]. Un ejemplo representativo lo constituyen los fosfatos cálcicos, cuya disolución da lugar a la liberación de iones de calcio y fosfato que, a su vez, son capaces de favorecer la diferenciación osteoblástica y estimular la formación de nueva fase mineral ósea.

1.4.2.2 Propiedades físicas

Las **propiedades mecánicas** de un biomaterial son determinantes para su desempeño en aplicaciones sometidas a carga, como es el caso de los implantes óseos. Estas propiedades reflejan la capacidad del material para soportar esfuerzos sin experimentar fallos estructurales ni deformaciones plásticas. En este contexto, resulta fundamental que los andamios emulen el comportamiento mecánico del tejido óseo, especialmente en términos de resistencia a la compresión, tracción, flexión y fatiga, a fin de evitar la fractura del implante o el "stress shielding", que se caracteriza por la resorción del hueso nativo [23, 27, 40, 43, 49].

Por otra parte, la **porosidad** del material, a pesar de comprometer su resistencia mecánica y aumentar la complejidad de fabricación, resulta fundamental para su integración biológica [26, 28, 40, 41]. Una arquitectura porosa adecuada permite la difusión de nutrientes y oxígeno, así como la migración celular y la formación de vasos sanguíneos, favoreciendo la colonización del andamio [33, 39, 40, 43, 48- 51]. En particular, una porosidad interconectada y jerarquizada es clave para facilitar procesos como la angiogénesis y la osteoconducción, contribuyendo a una fijación estable y a una integración efectiva con el tejido óseo circundante [29, 33, 40, 43, 49- 51].

Otro aspecto físico fundamental en el diseño de andamios para aplicaciones óseas es la **topografía superficial**, al constituir la interfaz directa entre el biomaterial y el tejido receptor [40, 43, 49]. Las propiedades topográficas, que comprenden tanto la rugosidad como patrones definidos a micro y nanoescala, desempeñan un papel crucial en la regulación de la respuesta celular [33, 43, 50]. Diversas configuraciones, como superficies rugosas, con surcos, lamelares, con cavidades, pilares, crestas o morfologías esféricas, han sido ampliamente estudiadas por su capacidad para modular la adhesión celular mediante la influencia en la adsorción de proteínas sobre la superficie del andamio [33, 40, 43, 50-52]. Este mecanismo resulta esencial para la interacción con células eucariotas, a diferencia de lo que ocurre con las bacterias, que pueden adherirse directamente al material [40, 50].

En comparación con superficies lisas o pulidas, estas modificaciones topográficas incrementan significativamente el área superficial, ampliando la extensión disponible para el anclaje celular [40, 43]. Además, las células perciben estas características mediante receptores de adhesión como las integrinas, lo que activa cascadas de

señalización intracelular [40, 51, 52]. Por ejemplo, se ha demostrado que las superficies rugosas favorecen, respecto a las pulidas, la adsorción proteica, la adhesión y proliferación celular, así como la capacidad osteoinductiva del andamio y, específicamente, las microestructuras alineadas, como las lamelares, inducen la expresión de genes osteogénicos [40, 43, 50- 52].

1.4.2.3 Propiedades biológicas

En el contexto de la ITO, los andamios deben cumplir una serie de requisitos biológicos fundamentales. La **biocompatibilidad** es indispensable para asegurar una interacción adecuada con el entorno biológico, sin inducir efectos secundarios adversos [27, 29, 40]. Por otro lado, en aplicaciones orientadas a la regeneración tisular, la **bioactividad** adquiere un papel central. Este término hace referencia a la capacidad de un material para inducir una respuesta biológica específica que favorezca la formación de una unión funcional entre el tejido y el biomaterial [56].

En el caso particular del tejido óseo, la bioactividad suele asociarse con la capacidad del material para inducir la precipitación de HA sobre su superficie al estar en contacto con fluidos biológicos, dado que el HA constituye el principal componente mineral de la MEC ósea [28, 29, 34, 49, 55].

En el diseño de andamios para ITO, se consideran tres conceptos clave: osteoconducción, osteoinducción y osteointegración [16, 25, 27, 49, 56]. Mientras que la **osteoconducción** se refiere a la capacidad del material para guiar el crecimiento del tejido óseo a lo largo de su superficie, la **osteoinducción** alude a la inducción de la osteogénesis [29, 37, 49, 56]. En este sentido, los biomateriales osteoinductores son aquellos capaces de reclutar e inducir la diferenciación de MSCs hacia la línea osteoblástica, promoviendo así la formación de tejido óseo [37]. Por último, la **osteointegración**, estrechamente relacionada con la bioactividad, describe la formación de una unión estable y funcional entre el andamio y el tejido óseo del huésped, lo cual resulta determinante para el éxito del implante a largo plazo [37].

1.4.3 Métodos de obtención

Existen numerosas técnicas para obtener biomateriales en diferentes tipos de andamios, que pueden agruparse en dos categorías principales: técnicas convencionales y técnicas de fabricación aditiva [50, 56]. Las primeras incluyen métodos como el electrospinning, el secado por congelación (freeze drying) o el proceso sol-gel, mientras que la estereolitografía y la bioimpresión son ejemplos representativos de la fabricación aditiva [41, 46, 50, 56]. Cada una de estas metodologías afecta de forma distinta la arquitectura interna del andamio, modificando propiedades como el tamaño, la morfología y la interconectividad de los poros, así como sus características mecánicas [41, 50, 56, 57].

En esta Tesis Doctoral se emplea el método sol-gel combinado con la técnica de réplica de esponja polimérica. A continuación, se describen ambas metodologías y su aplicación en la obtención de estructuras porosas tridimensionales para andamios en ITO.

1.4.3.1 Proceso Sol-gel

El proceso de síntesis sol-gel para la obtención de materiales cerámicos fue descubierto en el siglo XIX, aunque su relevancia científica y tecnológica no se consolidó hasta el siglo XX [35, 54]. En la actualidad, esta técnica es ampliamente utilizada en la fabricación de biomateriales avanzados, debido a su versatilidad y a su capacidad para modificar superficies inorgánicas mediante recubrimientos que mejoran propiedades como la biocompatibilidad o la bioactividad [26, 35, 56-58].

El método sol-gel permite la obtención de materiales vítreos, cerámicos y vitrocerámicos de alta pureza y homogeneidad, a temperaturas considerablemente más bajas que las requeridas en los métodos tradicionales en estado sólido [29, 35, 58]. Este proceso se basa en la polimerización controlada de precursores dispersos en una solución coloidal (sol), compuesta habitualmente por dichos precursores, agua, un catalizador y, en determinados casos, un co-disolvente [35, 57, 58]. Estos componentes experimentan una transición hacia un estado gelificado (gel) mediante reacciones de hidrólisis y condensación. Los precursores más utilizados son los alcoxidos metálicos ($M(OR)_n$), donde M representa un elemento metálico y R un grupo alquilo de alta reactividad con el agua, que facilita la formación de monómeros reactivos que, tras condensarse, dan lugar a una red tridimensional continua [35, 44, 56, 58].

$$M(OR)_n + xH_2O \rightarrow (OH)_x - M(OR)_{n-x} + xROH$$

$$(OR)_{n-x}M - (OH)_X + (OH)_X - M(OR)_{n-x} \rightarrow (OR)_{n-x}M - O - M(OR)_{n-x} + H_2O$$

La formación de dicha red marca el inicio de la gelificación, produciendo la transición del sistema desde la fase sol a gel, caracterizada por un incremento progresivo en la viscosidad [35, 58]. El gel obtenido es una estructura porosa en la que se encuentra atrapada una fase líquida, la cual debe eliminarse mediante un proceso de secado para consolidar el material [35, 57, 58].

Posteriormente, se aplica un tratamiento térmico de sinterizado que permite densificar la estructura y obtener el material final con las propiedades deseadas. En los casos en que se pretende generar un recubrimiento, se requiere una etapa intermedia en la que el sol se deposita sobre la superficie del sustrato antes del secado. Entre las técnicas más empleadas para este fin se destacan el dip-coating (inmersión), el spin-coating (centrifugación) y el spray-coating (pulverización), todas ellas ampliamente documentadas en la literatura científica [35, 59].

1.4.3.2 Técnica de réplica de esponjas poliméricas

La técnica de réplica de esponjas poliméricas constituye un ejemplo representativo de dip-coating compatible con el método sol-gel, desarrollada en la década de 1960 para la fabricación de materiales cerámicos porosos [59]. Esta metodología se basa en el uso de una plantilla polimérica y porosa desechable, cuya estructura se reproduce mediante la deposición por inmersión en una suspensión cerámica (barbotina) o en una solución sol-gel. Posteriormente, se sinterizan sobre la esponja, eliminando la plantilla.

Las propiedades del producto final, como la porosidad o el espesor del recubrimiento, pueden ajustarse en función del tipo de plantilla empleada y del número de inmersiones realizadas, lo que confiere a esta técnica una notable versatilidad.

Una vez aplicada la suspensión, se procede al sinterizado a temperaturas generalmente superiores a 600 °C [47, 59]. Durante este tratamiento térmico, la esponja, de naturaleza orgánica, se descompone y elimina, lo que permite obtener una estructura cerámica porosa consolidada en un único paso.

Actualmente, la técnica de réplica de esponjas polimérica es reconocida por su simplicidad, bajo coste y eficacia en la obtención de andamios tridimensionales con elevada porosidad e interconectividad capaces de reproducir la arquitectura del hueso trabecular [47, 59].

1.4.4 Estrategias biomiméticas

Los enfoques biomiméticos en el diseño de biomateriales buscan alcanzar una compatibilidad funcional, estructural y biológica con el tejido a reemplazar, con el fin de favorecer la regeneración de tejidos complejos. Actualmente, se han desarrollado múltiples estrategias dirigidas a reproducir las características del tejido diana, bajo la premisa, ampliamente aceptada, de que una mayor similitud con el entorno nativo incrementa las probabilidades de éxito del implante a largo plazo. Estas estrategias incluyen tanto aproximaciones estructurales y mecánicas como la incorporación de señales bioquímicas que modulan el comportamiento celular.

1.4.4.1 Andamios multicapa

A pesar de los avances significativos en el desarrollo de biomateriales para aplicaciones en ITO, aún no se ha logrado identificar un material que reúna, de forma simultánea, todas las propiedades necesarias para una regeneración ósea eficaz. En este contexto, los andamios multicapa se perfilan como una alternativa prometedora, al permitir la combinación de distintas fases con propiedades complementarias en una única estructura [42, 53-55]. Esta estrategia se basa en la aplicación de recubrimientos funcionales capaces de modificar la topografía, la bioactividad y otras propiedades clave del andamio, con el

fin de optimizar su rendimiento global. Por ejemplo, una fase con elevada resistencia mecánica, pero limitada bioactividad, puede recubrirse con otra que favorezca la osteointegración incorporando diferentes iones. De este modo se logra un equilibrio entre robustez estructural y capacidad de interacción biológica. Este enfoque permite superar las limitaciones asociadas a los materiales monofásicos y obtener materiales compuestos.

1.4.4.2 Dopaje iónico

Los iones metálicos desempeñan un papel esencial en los sistemas biológicos, actuando como macro o microelementos que cumplen funciones estructurales y fisiológicas fundamentales, además de participar en múltiples reacciones bioquímicas [61, 62]. Su importancia como agentes terapéuticos ha sido ampliamente reconocida, ya que actúan como cofactores enzimáticos y modulan rutas de señalización clave en la regeneración de tejidos [61-63]. Debido a su potencial toxicidad a concentraciones elevadas, los iones suelen incorporarse como dopantes en cantidades reducidas [27, 39, 42, 61, 62]. En este contexto, el dopaje iónico se presenta como una estrategia atractiva, por su bajo coste, estabilidad química y su compatibilidad con los procesos de fabricación de andamios bioactivos, que comúnmente implican el uso de disolventes orgánicos o temperaturas elevadas, condiciones que limitan la incorporación de agentes terapéuticos orgánicos [26, 62].

Además de sus efectos biológicos, el dopaje iónico tiene la capacidad de modificar las propiedades estructurales y superficiales de los materiales [39, 61]. En materiales cristalinos, la inclusión de dopantes genera defectos que dificultan la propagación de grietas. También altera la morfología de los cristales, modificando la topografía superficial, un factor crucial en la interacción entre las células y el material [61]. Así, el dopaje iónico se posiciona como una estrategia eficaz para introducir nuevas funcionalidades en los biomateriales.

Por otra parte, esta técnica puede considerarse una estrategia biomimética, dado que los apatitos biológicos no son estequiométricos, sino que presentan deficiencias de calcio y contienen diversos iones sustituyentes como Na^+, K^+ o Mg^{2+}. Así, cuando el andamio se degrada y libera estos iones al entorno fisiológico, éstos pueden ser incorporados en el HA, favoreciendo la formación de una fase mineral más semejante a la del hueso nativo.

1.4.4.3 Liberación controlada de moléculas bioactivas

Además de la liberación controlada de iones metálicos mencionada previamente, los andamios bioactivos pueden servir como vehículos para la administración localizada de otros agentes terapéuticos, como fármacos o factores de crecimiento [25, 26, 45, 64]. Se han desarrollado diversas estrategias de encapsulación y liberación, tales como la incorporación de estructuras degradables en la superficie del andamio, como

nanopartículas o microesferas, y el uso de polímeros biodegradables que facilitan la formación de sistemas de liberación [16, 32, 33, 45, 46, 64]. En estos casos, los agentes terapéuticos se pueden almacenar en cavidades internas, como dominios lamelares o poros, dentro de la matriz del material.

En el contexto de la ITO, los andamios bioactivos pueden incorporar diversos agentes terapéuticos que favorecen la regeneración del tejido óseo. Entre ellos se incluyen factores de crecimiento, como M-CSF y BMPs, que estimulan la proliferación y diferenciación osteoblástica, así como fármacos con actividad antiresortiva, agentes antineoplásicos y antibióticos que contribuyen a la prevención de infecciones postquirúrgicas asociadas al implante [16, 25, 33, 45, 46]. Además, estos sistemas pueden ser diseñados para permitir la liberación localizada de células, como las MSCs, lo que amplía significativamente las posibilidades terapéuticas al combinar la señalización bioquímica y celular en un mismo dispositivo [45, 64].

2.OBJETIVOS

A pesar de los avances en la ingeniería de tejido óseo, todavía no se ha logrado desarrollar un material que cumpla con todos los requisitos para una regeneración ósea efectiva. Además, persisten desafíos clínicos clave, como la integración y la vascularización de los injertos óseos, factores esenciales para asegurar la funcionalidad del implante a largo plazo.

Con el fin de obtener andamios que cumplan con los requisitos previamente descritos, la presente Tesis Doctoral tiene como **objetivo principal** el desarrollo de andamios multicapa que integren en una única estructura las fases $CaSiO_3$, $Ca_2P_6O_{17}$ y $Ca_3(PO_4)_2$. Además, teniendo en cuenta el potencial del dopaje iónico para modular las propiedades de los materiales y la capacidad de los iones para regular procesos celulares clave, los andamios serán dopados con Li_2O, Na_2O, K_2O y MgO.

Para el desarrollo del objetivo principal, se establecen los siguientes objetivos específicos:

1. **Síntesis de los andamios**: Desarrollar andamios mediante la combinación del método sol-gel y la técnica de réplica de esponja polimérica, basados en el sistema SiO_2-CaO-P_2O_5, e incorporando Li_2O, Na_2O, K_2O y MgO como dopantes y modificadores de la red.
2. **Optimización del proceso de síntesis**: Mejorar el proceso de obtención para lograr andamios bioactivos, centrándose en la estabilidad de las fases formadas y garantizando su efectividad en los ensayos posteriores.
3. **Caracterización fisicoquímica y mineralógica**: Realizar un análisis exhaustivo de las propiedades fisicoquímicas y mineralógicas de los andamios, evaluando las variaciones que ocurren durante la deposición de los distintos recubrimientos.
4. **Modificación de la topografía superficial**: Modular la morfología superficial de los andamios mediante dopaje iónico con concentraciones variables de MgO.
5. **Evaluación de la bioactividad *in vitro***: Determinar el comportamiento bioactivo *in vitro* de los andamios mediante inmersión en SBF, siguiendo la normativa ISO/FDIS 23317:2017.
6. **Modificación de la morfología de los precipitados de apatito**: Analizar el efecto de las distintas concentraciones de MgO en la morfología y la composición elemental de los precipitados de apatito formados durante los ensayos de bioactividad.
7. **Estudio de la citotoxicidad**: Evaluar la citocompatibilidad de los andamios y sus productos de disolución en cultivos celulares de diferentes tipos (humanos y

murinos), para determinar su impacto en la morfología celular, la viabilidad y la proliferación.

8. **Estudio de la influencia de la topografía en la proliferación celular:** Analizar el impacto de las distintas morfologías desarrolladas en los objetivos 4 y 6 sobre la proliferación celular en diversos tipos celulares de origen humano y murino.
9. **Estudio del potencial osteogénico**: Analizar el potencial osteogénico de los andamios y sus productos de disolución, evaluando la capacidad de inducción de la diferenciación ósea en preosteoblastos MC3T3-E1 y MSCs (osteoinducción), así como para favorecer la osteoconducción.
10. **Evaluación del potencial angiogénico**: Investigar la capacidad de los andamios para estimular la liberación de VEGF, un factor clave en la formación de nuevos vasos sanguíneos.

3. MATERIALES Y MÉTODOS

En esta Tesis Doctoral se desarrollaron andamios biocerámicos multicapa para la regeneración ósea, combinando fases bioactivos y reabsorbibles con dopantes iónicos. En este capítulo se describe el diseño y la metodología de síntesis de los andamios, mediante la combinación del método sol-gel y la técnica de réplica de esponja polimérica. Además, se presentan las técnicas empleadas para la caracterización físicoquímica, mineralógica y estructural, así como la evaluación de la bioactividad y biocompatibilidad *in vitro* mediante ensayos con líneas celulares de origen humano y murino.

3.1 Diseño de andamios multicapa

El diseño de los andamios multicapa, busca mejorar las propiedades para la regeneración ósea mediante la combinación de materiales cerámicos dispuestos en capas, las cuales poseen distintas características. Estos andamios presentan una estructura que incluye un núcleo vitrocerámico (CS-P6), diseñado para proporcionar propiedades mecánicas, recubierto por capas de materiales reabsorbibles (TCP) y bioactivos (CS) que favorecen la regeneración ósea (Figura 1). El primer recubrimiento, formado por silicato cálcico, fue seleccionado para actuar como estructura molde 3D porosa y reservorio de calcio, permitiendo la posterior deposición de la capa vítrea P6 sin comprometer la integridad estructural, ya que los moldes orgánicos empleados en la técnica de réplica de esponja polimérica se calcinan a altas temperaturas.

La fase vítrea P6 se aplica como segunda capa para contrarrestar la fragilidad del silicato cálcico, formando el núcleo vitrocerámico. Su capacidad para fundir lo convierte en un material cementante que une los cristales y rellena grietas preexistentes, aumentando la densificación del sistema y, con ello, la resistencia a la compresión. Además, esta fase se dopó con iones de Li, lo que permite reducir la temperatura de fusión y mejorar aún más la resistencia mecánica.

Como tercer recubrimiento, se empleó TCP, una fase reabsorbible que actúa como reservorio de iones calcio y fosfato, favoreciendo la deposición de matriz mineral ósea. Gracias a su similitud química con el HA ($Ca_{10}(PO_4)_6(OH)_2$, el TCP ($Ca_3(PO_4)_2$) también favorece la osteointegración. Finalmente, como recubrimiento externo e interfaz célula-andamio, se utilizó nuevamente silicato cálcico debido a su conocida bioactividad y capacidad para estimular la regeneración ósea. Este recubrimiento se dopó con iones de sodio, potasio y magnesio, ajustando la concentración de magnesio para modificar las propiedades fisicoquímicas y biológicas del material.

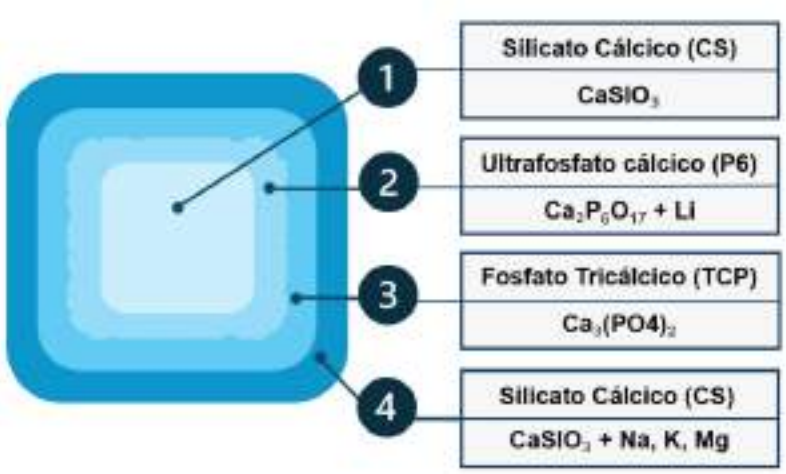

Figura 4 | Esquema de las capas del andamio multicapa, indicando las fórmulas químicas de cada material y los dopantes empleados.

3.2 Preparación

A continuación, se expone el procedimiento para la obtención de los andamios multicapa, así como los materiales utilizados en su obtención.

I: Preparación de la disolución sol-gel

Las disoluciones empleadas para la obtención de las distintas capas del andamio fueron preparadas mediante el proceso sol-gel. Para ello, se llevó a cabo la hidrólisis de los precursores TEOS y TEP en medio ácido, ajustando el pH final de las disoluciones en un rango de 2 a 3. En la Tabla 1 se presentan las cantidades de cada reactivo empleado para la síntesis de cada una de las capas.

Tabla 1 | Composición química detallada de los andamios multicapa, desglosada por capas

		Reactivos									
Capa	**Composición**	**TEOS**	**TEP**	**H_2O**	**Etanol**	**HCl**	**$CaCO_3$**	**Li_2CO_3**	**Na_2CO_3**	**K_2CO_3**	**$MgCO_3$**
		(mL)					(g)				
1	**CS**	19.28	-	20	5	1	8.62	-	-	-	-
2	**P6**	-	18.46	20	5	2	3.72	1	-	-	-
3	**TCP**	-	10.96	20	5	2	9.68	-	-	-	-
4	**CS0**	19.28	-	20	5	1	8.62	-	0.5	0.5	-
4	**CS04**	19.28	-	20	5	1	8.62	-	0.5	0.5	0.4
4	**CS05**	19.28	-	20	5	1	8.62	-	0.5	0.5	0.5
4	**CS06**	19.28	-	20	5	1	8.62	-	0.5	0.5	0.6
4	**CS075**	19.28	-	20	5	1	8.62	-	0.5	0.5	0.75

II: Recubrimiento y secado

Capa 1: Esponjas de poliuretano de 20 ppi, utilizadas como molde polimérico, se sumergieron en la disolución sol-gel. A continuación, se retiró el exceso y se secaron brevemente a una temperatura de, aproximadamente, 185ºC, repitiendo el proceso hasta cubrir completamente la esponja, necesitando aproximadamente 0.1 g de material. Una vez obtenidas, se procedió a la sinterización.

Capas 2-4: A continuación, el andamio de CS obtenido en el paso anterior fue recubierto con P6. Tras la inmersión en la disolución correspondiente, se eliminó el exceso y se procedió al secado del recubrimiento, seguido de su sinterización. Este procedimiento se repitió para las capas de TCP y CS.

Para asegurar la funcionalidad de cada capa se depositaron los siguientes recubrimientos y cantidades de material:

- En la capa 2 se aplicaron un total de 20 recubrimientos (aproximadamente 0.3 g de material).
- En la capa 3 se aplicó un único recubrimiento (aproximadamente 0.1 g) debido a la alta viscosidad de la disolución.
- En la capa 4, se aplicaron una media de 5 recubrimientos de alguna de las formulaciones químicas detallas en la Tabla 1, con un peso aproximado de 0.1 g.

III: Sinterización

El proceso de sinterización de la primera capa (CS) consistió en un tratamiento térmico que incluyó una rampa de calentamiento de 55 horas hasta alcanzar los 1050°C, seguida de 8 horas de mantenimiento y 12 horas de enfriamiento hasta alcanzar la temperatura ambiente.

Para el resto de las capas (2-4), se empleó un proceso de sinterización más rápido que consistió en una rampa de calentamiento de 9 horas hasta los 1050°C, que se mantuvo durante 8 horas, para concluir con una rampa de enfriamiento de 12 horas.

IV: Ataque químico

Debido a la alta reactividad de la fase vítrea P6, cuya disolución excesiva puede modificar el pH local e interferir en los ensayos de bioactividad o en los ensayos celulares, se eliminó el exceso de P6 mediante un ataque químico. Para ello, se utilizó una solución TRIS, compuesta por HCl, tris(hidroximetil)aminometano y $CaCl_2$, con un pH de 7.3. Este tratamiento se aplicó durante 24 horas a 50°C tras la deposición de la segunda capa (P6), formando así el núcleo vitrocerámico de CS-P6-TRIS.

Para una descripción más detallada de las condiciones de preparación de las disoluciones sol-gel y el proceso de fabricación de los andamios biocerámicos, se remite a las secciones: “2.1. Design and fabrication of multilayer scaffolds” del Artículo 1 y “2.1. Multilayer scaffolds assembly” del Artículo 2, “2.1. Fabrication of multilayer scaffolds” del Artículo 3 y “2.1 Materials preparation” del Artículo 4.

3.3 Caracterización fisicoquímica y mineralógica

Los andamios fueron caracterizados desde el punto de vista mineralógico mediante XRD, con el objetivo de analizar la evolución de la composición cristalina a medida que se depositaban las distintas capas. Los difractogramas experimentales obtenidos se compararon con los patrones de referencia de la base de datos COD, empleando el software de análisis de fases Match! 3.

Adicionalmente, se identificaron los grupos funcionales presentes en las distintas capas mediante FTIR, lo que permitió obtener una caracterización más detallada de la composición química de los andamios.

Para caracterizar las propiedades físicas, se realizó un estudio de la estructura macroscópica de los andamios mediante microscopía óptica, mientras que el análisis de la microestructura se llevó a cabo utilizando la técnica FESEM-EDX.

Adicionalmente, dentro de la caracterización de las propiedades físicas, se determinó la porosidad de los andamios a través de diferentes métodos según el tamaño de poro. Los macroporos fueron caracterizados mediante picnometría según el principio de Arquímedes, mientras que la distribución de microporos (<300 micras) se estudió mediante porosimetría de mercurio. Además, se evaluó la resistencia mecánica de los andamios mediante una prueba de compresión simple. Dentro de este contexto, se investigó la biodegradabilidad de los andamios en una solución de PBS, registrando la pérdida de peso a lo largo del tiempo del estudio.

Las condiciones de ensayo para cada una de las técnicas mencionadas se detallan en la sección "2.2. Material physicochemical characterization" del Artículo 1, y en la sección "*2*.2. Physico-chemical characterization" y “2.4.1. Weight loss” del Artículo 2 y en la sección "2.2.1. Mineralogical characterization”, “2.2.2. Macro and microstructure characterization" y “2.2.3. Physical characterization” del Artículo 3.

3.4 Bioactividad *in vitro*

Los ensayos de bioactividad *in vitro* evalúan la capacidad de los materiales para inducir la precipitación de apatito cuando se exponen a fluido biológico artificial (SBF), cuya composición iónica simula la del plasma sanguíneo. La precipitación de apatito se utiliza

como indicador de la osteointegración o capacidad de los materiales para unirse químicamente al tejido óseo *in vivo* [35].

Para realizar los ensayos de bioactividad *in vitro*, los andamios fueron introducidos en SBF en un baño en agitación a 37ºC, replicando las condiciones fisiológicas, tal como indican las directrices de la norma ISO/FDIS 23317:2017. Transcurridos intervalos de tiempo, previamente establecidos, los andamios fueron extraídos y analizados mediante FESEM-EDX. Además, se recolectaron alícuotas del SBF remanente para estudiar la interacción iónica entre las biocerámicas y el SBF mediante ICP-OES.

Los detalles completos de los ensayos se encuentran en la sección "2.3 *In vitro* bioactivity evaluation" del Artículo 1 y en la sección "*2.3 In vitro bioactivity test*" del Artículo 2.

3.5 Biocompatibilidad *in vitro*

La caracterización biológica de los andamios se realizó evaluando su comportamiento en presencia de diversos tipos celulares de origen humano y murino. El objetivo fue determinar su citocompatibilidad, osteoinducción, osteoconducción, inmunomodulación y propiedades proangiogénicas.

Los ensayos se llevaron a cabo utilizando los siguientes modelos celulares:

- **Fibroblastos murinos 3T3**

  Para evaluar la citocompatibilidad de los andamios y sus productos de disolución sobre fibroblastos murinos 3T3, se emplearon los ensayos MTT y AlamarBlue, los cuales proporcionan información sobre la viabilidad celular y la función metabólica de las células en respuesta al material. Adicionalmente, se caracterizó la composición iónica de los productos de disolución mediante ICP-OES.

  Los detalles de estos ensayos se pueden encontrar en la sección "2.4 *In vitro* biological evaluation" del Artículo 1 y sección "*2.4.2. Ionic characterisation of CCM", "2.4.3. Indirect cell viability evaluation" y "2.5.3D direct cell culture"* del Artículo 2.

- **Células madre mesenquimales de médula ósea humana**

  Esta línea celular se empleó para evaluar la citotoxicidad, osteoinducción y respuesta inflamatoria de los andamios y/o sus productos de disolución. Este doble enfoque permite estudiar el efecto directo del andamio sobre las células cultivadas en su superficie y el efecto indirecto inducido por los productos de disolución de los andamios, simulando el efecto *in vivo* en células vecinas.

  La citotoxicidad se evaluó de forma directa e indirecta mediante el ensayo CCK-8, que mide la viabilidad celular. Además, se empleó SEM para analizar la

morfología celular de las MSCs cultivadas sobre los andamios y detectar posibles alteraciones estructurales derivadas del contacto con el material.

La diferenciación osteogénica, se evaluó mediante la actividad de la fosfatasa alcalina (ALP), un conocido marcador de diferenciación osteogénica, mediante tinción específica. Asimismo, los depósitos de calcio, indicadores de la mineralización de la matriz extracelular, se detectaron mediante tinción con alizarina roja (ARS) y Von Kossa. Estas técnicas permitieron evaluar la formación de matriz mineralizada tras la exposición de las células a los productos de disolución del andamio.

Los detalles de estos ensayos se pueden encontrar en la sección "2.6 Biocompatibility", "*2.7. Effect of the scaffolds in inflammatory response",* "2.8 *Effect of the scaffolds on cell morphology" y "2.9 Osteogenic differentiation"* del Artículo 3.

- **Fibroblastos humanos HFF-1**

  Los fibroblastos, a pesar de no ser células óseas, desempeñan un papel crucial en la regeneración ósea mediante la formación de tejido de granulación, la modulación inflamatoria y la promoción de la diferenciación de MSCs en osteoblastos. Por ello, se estudió la citotoxicidad y la respuesta inflamatoria en estas células.

  La citotoxicidad, tanto de manera directa como indirecta, se evaluó mediante el ensayo CCK-8, complementado por el análisis de la morfología de los fibroblastos fijados sobre los andamios mediante SEM.

  Los detalles de estos ensayos se pueden encontrar en la sección "2.6 Biocompatibility", "*2.7. Effect of the scaffolds in inflammatory response",* y "2.8 *Effect of the scaffolds on cell morphology"* del Artículo 3.

- **Preosteoblastos murinos MC3T3-E1**

  Los preosteoblastos murinos se utilizaron para estudiar el efecto celular de la exposición al andamio en células óseas en una etapa temprana de diferenciación, permitiendo investigar tanto los procesos de diferenciación osteogénica como otros aspectos clave de la regeneración ósea. En este contexto, se evaluó la citocompatibilidad de los andamios y sus productos de disolución, cuya composición fue determinada mediante ICP-OES, utilizando el ensayo CCK-8. Además, se analizó la morfología celular tras la exposición directa e indirecta a los andamios mediante SEM y microscopía de fluorescencia con tinción DAPI-calceína. La diferenciación osteogénica de los preosteoblastos expuestos

directamente al andamio se evaluó mediante la cuantificación de la ALP y la tinción con rojo de alizarina, que tiñe específicamente los depósitos de calcio. Finalmente, se evaluó la capacidad proangiogénica de los andamios mediante la cuantificación de VEGF en los sobrenadantes celulares.

Los detalles de estos ensayos se pueden encontrar en la sección "*2.3 In vitro biocompatibility assessment", ""2.4 Osteogenic assessment" y "2.5 Angiogenic assessment"* del Artículo 4.

4. RESULTADOS Y DISCUSIÓN

Esta Tesis Doctoral se organiza en cuatro artículos que abordan diferentes aspectos del desarrollo y de la evaluación de andamios multicapa de tercera generación. Los dos primeros artículos se centran en la caracterización mineralógica, fisicoquímica y bioactiva de los andamios, junto con una evaluación preliminar de la citotoxicidad para descartar posibles efectos tóxicos del material o de sus productos de disolución. Los dos artículos restantes se enfocan en el análisis de las propiedades biológicas necesarias para la regeneración ósea, como la osteoinducción, osteoconducción, inmunomodulación y propiedades angiogénicas.

4.1 Obtención y caracterización fisicoquímica de las capas de los andamios multicapa

Para evaluar el comportamiento de los andamios, se estudió la evolución de sus propiedades fisicoquímicas, mineralógicas y estructurales tras la deposición y sinterización de cada capa (Figura 4). Como resultado, se obtuvieron andamios de geometría cilíndrica con un diámetro de 0.9 ± 0.1 cm y una altura de 0.8 ± 0.1 cm, con una arquitectura altamente porosa e interconectada (Figura 5).

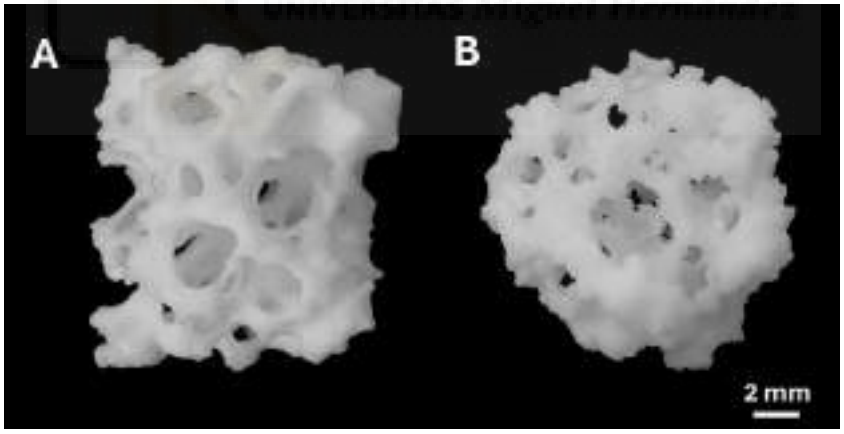

Figura 5 | Imágenes representativas de los andamios multicapa, obtenidas mediante microscopía óptica, desde las perspectivas lateral (A) y superior (B).

4.1.1 Composición cristalina

En ITO, la composición mineralógica de los andamios desempeña un papel crucial, ya que condiciona su bioactividad, biodegradabilidad, biocompatibilidad y resistencia mecánica [47, 48]. El empleo de andamios multicapa, compuestos por capas de materiales cerámicos sol-gel con propiedades distintas, permite obtener estructuras multifásicas y multifuncionales. Esto facilita el cumplimiento de los requisitos esenciales para una

regeneración ósea efectiva, consiguiendo combinaciones de propiedades que serían difíciles de alcanzar con un solo material.

La composición mineralógica de los andamios, a medida que se depositaron las capas de material, se muestra en la Figura 6. La Figura 6A muestra las fases cristalinas de las primeras capas hasta obtener el núcleo vitrocerámico (CS-P6-TRIS). La primera capa de CS está formada por pseudowollastontia. Sin embargo, tras la aplicación de la capa P6, no se detectó CS, en su lugar aparecieron nuevas fases cristalinas. La composición mineralógica de esta capa consistió en sílice, pirofosfato de calcio y una menor proporción de β-TCP. Estas fases se formaron debido a la migración iónica entre las capas durante el tratamiento de sinterización. Este fenómeno se atribuyó a la presencia de P6, un ultrafosfato de calcio con una estructura de alta energía. En presencia de calcio, la estructura de este ultrafosfato se desestabiliza, facilitando la conversión de $Ca_2P_6O_{17}$ a $Ca_2P_2O_7$ y, en menor medida, a $Ca_3(PO_4)_2$, lo que provoca la transformación del $CaSiO_3$ en SiO_2, una fase libre de calcio, dado que el CS actúa como fuente de Ca^{2+}.

Debido a que la transformación del P6 en las fases anteriormente indicadas es incompleta, y la reactividad del mismo en SBF es alta, se procedió a realizar un ataque químico utilizando TRIS para eliminar el exceso de ultrafosfato. Tras comparar las fases antes y después del ataque químico (Figura 6A), no se observaron variaciones significativas, aunque sí se registró una disminución en la señal de fondo en la región amorfa del material ($0< 2\theta<10$). Además, los iones liberados tras el ataque químico fueron caracterizados mediante ICP-OES (ventana Figura 6A) lo que permitió detectar la liberación de P^{3-} y Li^{+} a la solución de ataque, produciendo la hidrólisis del P6 y, por lo tanto, la eliminación del exceso del mismo.

La Figura 6B-C muestra las fases cristalinas tras la adición de la capa biodegradable (β-TCP) y de la capa bioactiva dopada (CSX). Tras la adición del β-TCP, la composición cristalina fue similar a la del núcleo vitrocerámico, con un aumento notable en la señal de β-TCP (Figura 6B). Finalmente, en los andamios completos CSX, se identificaron SiO_2, $Ca_2P_2O_7$ y $Ca_3(PO_4)_2$ como los componentes predominantes, además de $CaSiO_3$ en menor proporción (Figura 6C). Asimismo, en las muestras CS04, CS05, CS06 y CS075, se identificaron fases ricas en Mg, formadas debido al dopaje iónico, como akermantita y whitlockita, una variante no estequiométrica de β-TCP rica en Mg. La intensidad de los picos correspondientes a estas fases fue directamente proporcional a la cantidad de Mg utilizado como dopante. Asimismo, se observó una disminución en la intensidad del pico principal de SiO_2 ($2\theta = 21.9°$).

Cada una de las fases obtenidas en las distintas capas del andamio, cumplen con una función fundamental en la regeneración ósea. A continuación, se describe brevemente su función:

En los andamios, la sílice, aporta estabilidad estructural y, al ser biocompatible, estimula la proliferación celular y, por ende, promueve la regeneración ósea [66, 67].

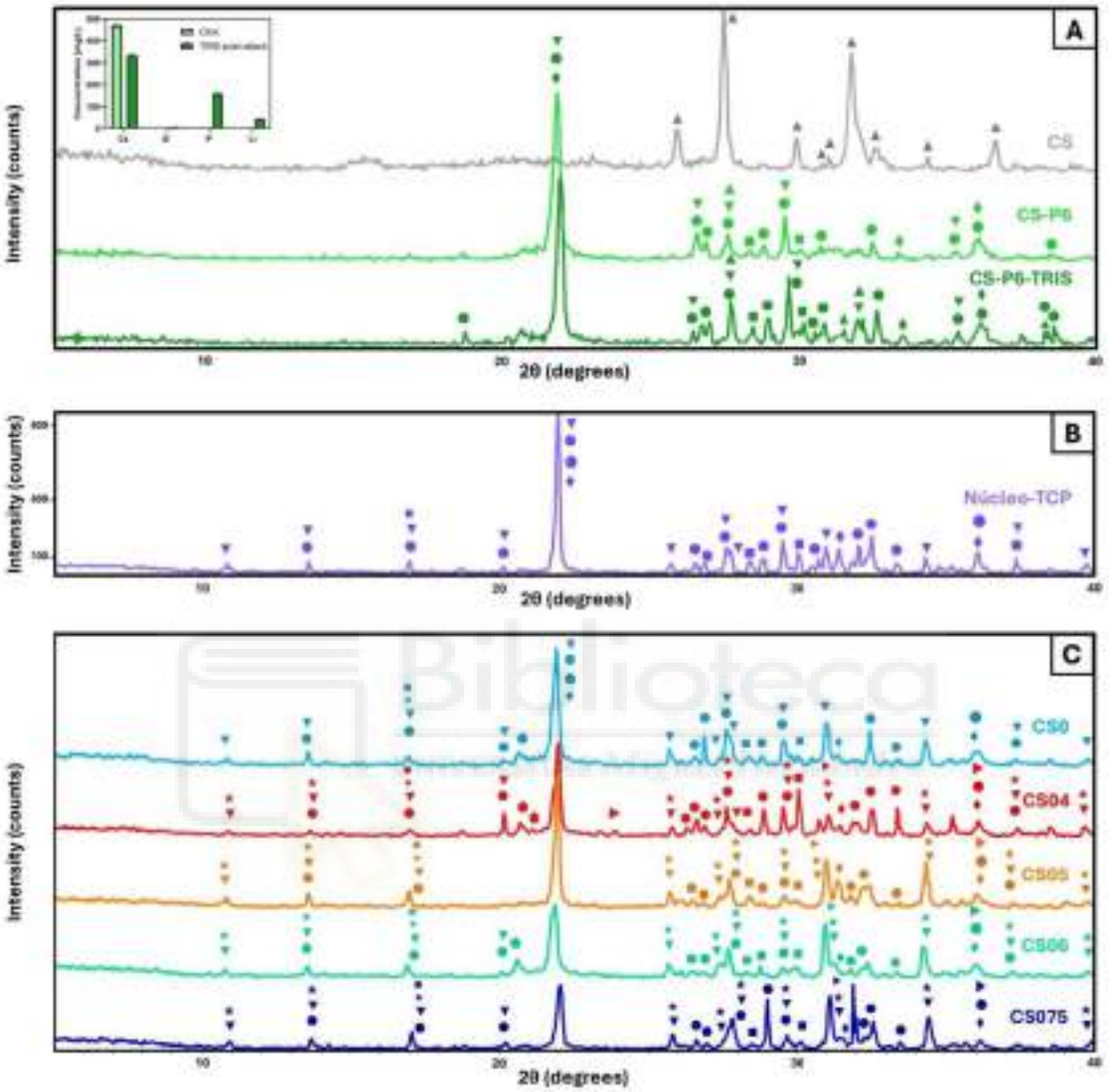

Figura 6 | Difractogramas de XRD de las distintas capas que conforman los andamios multicapa. Leyenda: ▲- PW: $CaSiO_3$; ♦- CB: SiO_2; ●- CP: $Ca_2P_2O_7$; ▼- TCP: $Ca_3(PO_4)_2$; ■- CS: $CaSiO_3$; ⬟-TD: SiO_2; ★-WH: $Ca_{10.115}Mg_{0.385}(PO_4)_7$); ▶-AK: $Ca_2MgSi_2O_7$

El pirofosfato de calcio, presente en el núcleo del andamio, juega un papel fundamental en la remodelación ósea [30], aunque ha sido menos investigado que otros fosfatos de calcio. A pesar de que el pirofosfato ha sido tradicionalmente considerado un inhibidor de la calcificación, su interacción con la ALP revela un comportamiento más complejo [68-71]. Esta enzima, que se expresa en osteoblastos durante la fase de maduración de la matriz ósea, hidroliza el pirofosfato inorgánico, liberando fosfato y calcio, elementos esenciales para la formación de apatito, el principal componente mineral del hueso [68-70, 72]. De este modo, la presencia de $Ca_2P_2O_7$ en el andamio puede facilitar la

mineralización ósea. Además, estudios *in vivo* realizados en bovinos y en humanos han demostrado que los implantes que contienen este material presentan una tasa de degradación óptima, junto con una mayor integración y mineralización del tejido óseo [70, 73, 74].

A diferencia del pirofosfato de calcio, el β-TCP es un material ampliamente utilizado, y reconocido por su capacidad osteoconductora y osteoinductora [16, 40]. Su naturaleza bioresorbible permite conseguir una degradación progresiva, facilitando así que los andamios sean reemplazos por tejido óseo neoformado [16, 28, 40]. En los andamios, esta fase coexiste con su variante parcialmente sustituida por magnesio, la whitlockita, un mineral que se encuentra muy presente en el hueso humano, lo que mejora el biomimetismo de la estructura [40]. Además, es rico en magnesio, un elemento esencial en la diferenciación osteogénica [40, 64]. De manera similar, la akermanita, también presente en el andamio, actúa como una fuente de magnesio, además de proporcionar bioactividad, biocompatibilidad y osteoconductividad [29, 64].

Finalmente, el CS, presente en la superficie del andamio, combina bioactividad y biocompatibilidad [15, 26, 29]. Al estar en contacto con el medio biológico, su capacidad para inducir la precipitación de apatito desde las primeras etapas del proceso regenerativo es crucial para lograr una osteointegración óptima. Además, el CS promueve la adhesión celular y la proliferación de osteoblastos, favoreciendo la regeneración de la zona dañada [26, 29, 75, 76].

4.1.2 Composición química

La Figura 7 muestra los espectros FTIR de los andamios CS04 y CS05 en representación de todos los andamios CSX. Esta técnica proporcionó información complementaria a la obtenida por XRD (Figura 6). Mientras que XRD identifica las fases cristalinas, FTIR permite detectar los grupos funcionales presentes, ofreciendo una caracterización complementaria.

En ambos andamios, se identificaron los grupos funcionales Si-O-Si, PO_4^{3-}, $P_2O_7^{2-}$ y HPO_4^{2-} mediante espectroscopía FTIR. Las bandas asociadas a los fosfatos (PO_4^{3-}) corresponden a distintos modos vibracionales: (i) estiramiento asimétrico a 1000 y 1030 cm^{-1}, (ii) estiramiento simétrico a 940 y 975 cm^{-1} y (iii) flexión a 600, 588 y 550 cm^{-1}. Asimismo, el grupo HPO_4^{2-} se identificó a 920 cm^{-1}. El grupo fosfato es característico del β-TCP y la whitlockita, ambos identificados en XRD. Sin embargo, la similitud de los patrones de difracción entre el β-TCP y la whitlockita dificulta una identificación concluyente de esta variante sustituida. En este contexto, la espectroscopía FTIR permite la detección del grupo HPO_4^{2-}, un marcador estructural exclusivo de la whitlockita, confirmando la identificación de esta fase en la muestra [77, 78].

Para el grupo Si-O-Si, se observaron bandas en dos regiones principales: (i) estiramiento asimétrico o flexión en el rango de 1216-1000 cm^{-1} y (ii) estiramiento simétrico con señales a 975 y 795 cm^{-1}. También se detectó una banda de oscilación de Si-O-Si a 458 cm^{-1} y otra a 920 cm^{-1} correspondiente al enlace Si-O-NBO. Estos resultados FTIR, junto con los datos de XRD, permiten confirmar la presencia de wollastonita, akermanita y cristobalita en la muestra.

Por último, la presencia del grupo $P_2O_7^{2-}$ se confirmó en ambos andamios mediante señales a 725, 920 y 1216 cm^{-1}. Estos datos son consistentes con el pirofosfato de calcio, previamente detectado mediante XRD.

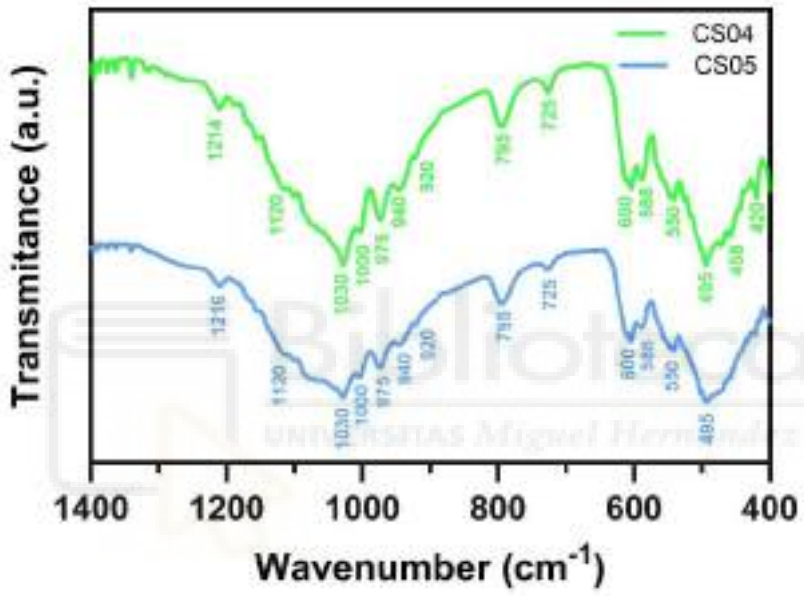

Figura 7 | Espectros FTIR de los andamios CS04 y CS05

La comparación de los espectros de CS04 y CS05 revela un patrón general similar, con la mayoría de las bandas coincidiendo. Sin embargo, en CS05, las bandas correspondientes a los fosfatos son significativamente más anchas. Este efecto se atribuye a la mayor concentración de $MgCO_3$ utilizado como dopante en CS05 [79]. La introducción de dopantes genera defectos cristalinos y variabilidad en los enlaces, lo que provoca desplazamientos en las frecuencias de vibración. Esta variabilidad altera la forma en que los enlaces interactúan con la radiación infrarroja, lo que resulta en un ensanchamiento de las bandas de los espectros FTIR.

4.1.3 Propiedades físicas: Resistencia mecánica y porosidad

En esta sección, correspondiente a la caracterización física, las Figuras 8 y 9 muestran los valores obtenidos de macroporosidad, resistencia a la compresión, así como la porosidad acumulativa y diferencial de los distintos andamios desarrollados.

La Figura 8 presenta los resultados de picnometría y resistencia mecánica. Tras la deposición de la primera capa de CS, se obtuvo una estructura con una macroporosidad del 95%, determinada por el molde polimérico, y una resistencia mecánica insuficiente para su manipulación y caracterización. La incorporación de la fase vítrea P6 incrementó significativamente la resistencia a la compresión, alcanzando 2.4 MPa, y redujo la macroporosidad al 89%. Este efecto se atribuye a la función cementante y cohesiva de P6, que favorece la compactación de las partículas y la formación de una estructura más densa. Además, el dopaje con litio, respaldado por estudios previos en fosfatos cálcicos, potencia las propiedades mecánicas del material [61, 80].

Tras el ataque con TRIS y la consiguiente hidrólisis del P6, la resistencia a la compresión disminuyó a 1.9 MPa, acompañada de un ligero aumento en la macroporosidad, que ascendió al 90%. La aplicación de las dos capas exteriores adicionales, TCP y CSX, no produjo cambios significativos en las propiedades mecánicas ni en la macroposidad total tal y como se puede observar en la Figura 8.

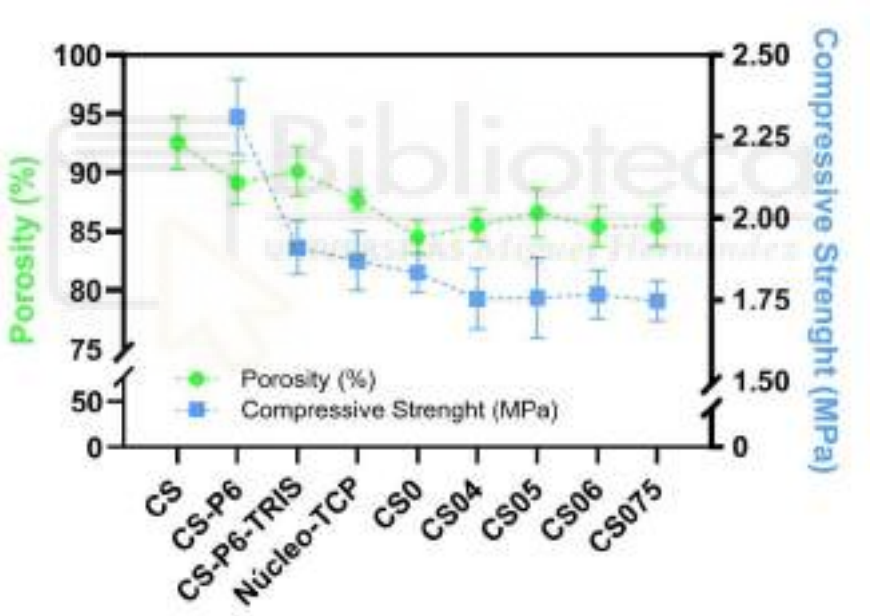

Figura 8 | Evolución de la macroporosidad y la resistencia a la compresión tras la deposición sucesiva de cada capa.

La Figura 9 y la Tabla 2 muestran la evolución de la distribución de la microporosidad, determinada por porosimetría de Hg, conforme se aplican las distintas capas del andamio. Para la primera capa CS, se observó un mayor volumen de mercurio intruido, lo que refleja una mayor microporosidad (45%), con un predominio de la porosidad interpartícula (>1 μm), que representa el 27 %. En cuanto al tamaño de los poros, se identificaron tres regiones principales: (200-61 μm), (25-4 μm) y, finalmente, los poros en la región intrapartícula (0.1–0.01 μm), que representan el 18 % restante.

Tabla 2 | Distribución de la microporosidad

Muestra	Microporosidad interpartícula (>1 µm) (%)	Microporosidad intrapartícula (<1 µm) (%)	Microporosidad total (< 300 µm) (%)
CS	27	18	45
CS-P6	16	17	33
Núcleo-TCP	25	11	35
CS0	23	13	36
CS04	22	12	34
CS06	26	11	37

Tras el segundo recubrimiento de P6, se observó una disminución significativa de la microporosidad total hasta el 33%, reflejado por una caída en el volumen intruido de Hg. Asimismo, se identificó una reducción de la porosidad interpartícula hasta el 16%, reflejada por un desplazamiento hacia la derecha de la curva. La porosidad intrapartícula se mantuvo prácticamente invariable, representando el 17% restante. En cuanto a los tamaños de poro, se observan dos principales regiones: de 200-4 µm y de 4.6 a 0.05 µm. Este efecto se atribuye a la densificación inducida por la fase P6, cuya alta viscosidad favorece la obstrucción de los poros.

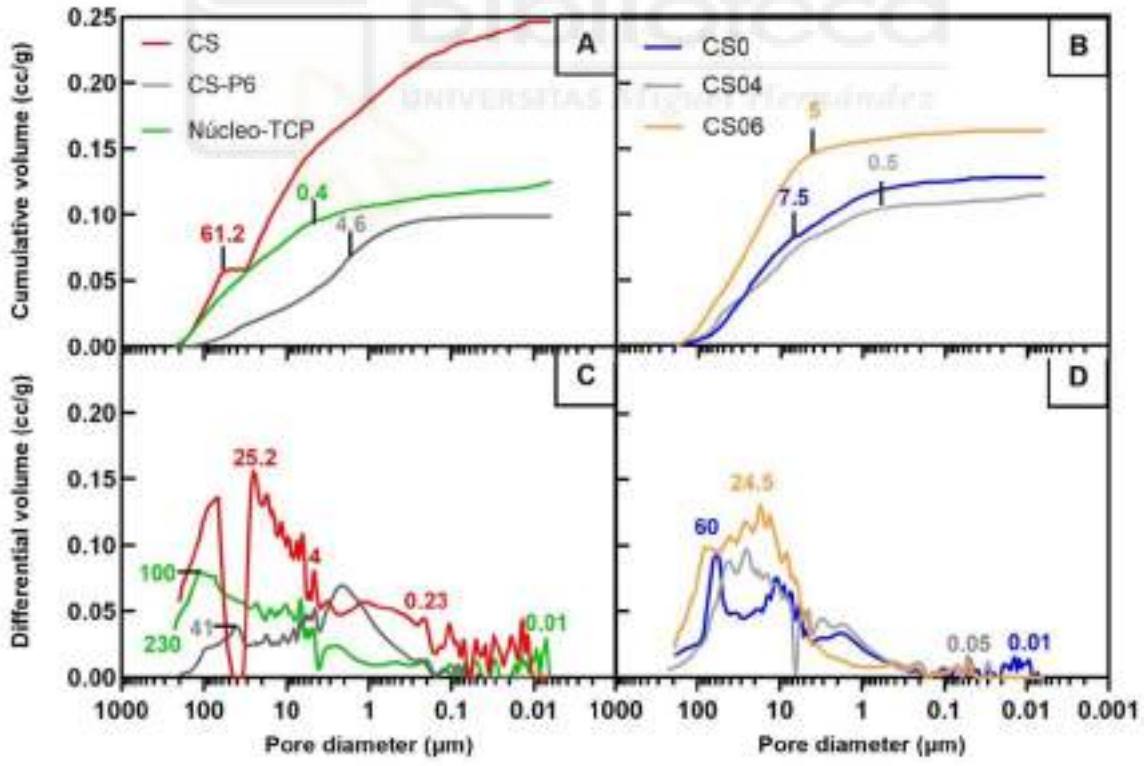

Figura 9 | Curvas obtenidas mediante la técnica de porosimetría por intrusión de mercurio: (A) porosidad acumulativa (B) porosidad diferencial de los andamios más representativos.

El ataque químico con TRIS provocó la hidrólisis parcial del P6, favoreciendo en cierta medida la apertura de los poros. Esto permitió que, tras la aplicación del recubrimiento de TCP, se recuperase el predominio de la porosidad interpartícula (25 %) y, en parte, la microporosidad total, que aumentó al 35 %. Respecto al tamaño de los poros, se identificaron dos regiones principales comprendidas entre 230 y 0.4 μm, y entre 0.2 y 0.01 μm. Aunque estos rangos son comparables a los de CS-P6, su presencia fue mayor, como indica el incremento en el volumen intruido de mercurio.

Finalmente, para evaluar la microporosidad de los andamios multicapa CSX, se seleccionaron CS0, CS04 y CS06 como andamios representativos, ya que no se observaron diferencias significativas atribuibles a la variación en el dopaje con Mg (Figura 8). Los andamios CSX no mostraron cambios notables en la distribución de tamaños de poro, observándose principalmente dos regiones: una primera entre 200 y 5 μm, y una segunda entre 0.2 y 0.01 μm. En cuanto a la microporosidad, se mantuvo relativamente constantes: porosidad interpartícula (22-26 %), intrapartícula (11-13 %) y microporosidad total (34-37 %).

Para evaluar la idoneidad de estos implantes, es fundamental comprobar su compatibilidad física y mecánica con el hueso, con el fin de evitar riesgos como la resorción ósea o la fractura del implante. Aunque los valores pueden variar según la localización, o factores como la edad o el sexo, se estima que la porosidad del hueso trabecular oscila entre el 50% y el 90%, y su resistencia mecánica entre 1.7 y 7.5 MPa [7, 10, 13]. Al comparar estos valores con los obtenidos de los andamios, se observa que están comprendidos dentro de este rango (Figura 8). Este rango no solo favorece una integración efectiva, sino que también permite aplicar carga controlada durante el proceso regenerativo. Este factor es crucial, ya que, según la Ley de Wolff, la estimulación mecánica favorece la remodelación y mineralización ósea, mejorando la calidad del tejido regenerado [11, 17, 22]. Como resultado, se acelera tanto la regeneración ósea como la recuperación del paciente.

La porosidad jerarquizada es fundamental para la regeneración tisular, ya que influye en procesos biológicos que ocurren a distintas escalas. Los andamios estudiados presentan una estructura porosa que varía desde macroporos, que permiten la formación de vasos sanguíneos, hasta microporos (50-150 μm) que promueven la migración celular, y poros en la región intrapartícula (< 1 μm) que permiten el intercambio de nutrientes y desechos. Esta organización jerárquica es esencial para lograr una regeneración ósea eficiente [24, 26].

4.1.4 Modulación de la microestructura mediante dopaje iónico

El análisis microestructural realizado mediante FESEM-EDX, permitió observar la evolución de la morfología superficial, a medida que se depositaron y sinterizaron las distintas capas del andamio (Figura 10).

El andamio inicial, compuesto exclusivamente por CS, presentó una topografía homogénea caracterizada por estructuras globulares con una relación Ca/Si de ≈ 1, lo que permitió confirmar la presencia de $CaSiO_3$, previamente detectado mediante XRD (Figura 6A). Tras recubrir la estructura con P6, se observó una superficie con estructuras poligonales con una relación Ca/P ≈ 1 en la periferia, típica del pirofosfato, y una relación Ca/P ≈ 1.4 en la región central, próxima al valor del TCP. En esta región central, además, se distinguió un grano redondeado, rico en silicio y deficiente en calcio. Estos resultados respaldan la hipótesis planteada en el apartado 4.1.1 sobre la migración iónica entre capas, sugiriendo que el grano central corresponde a SiO_2, derivado de la transformación de $CaSiO_3$ tras la cesión de calcio al P6. Como resultado de esta transformación, las regiones cercanas al grano reciben una mayor cantidad de calcio, favoreciendo la formación de TCP. Por el contrario, en las zonas distales, el ultrafosfato se transforma en una fase estable con una relación Ca/P más baja, como el pirofosfato de calcio. Estos cristales se encuentran rodeados por una fase vítrea deficiente en calcio (Ca/P + Si ≈ 0.017), correspondiente al remanente amorfo de las transformaciones.

Tras el ataque químico con TRIS, los límites de grano quedaron más expuestos, debido a la hidrólisis parcial del P6. Posteriormente, al aplicar el tercer recubrimiento, compuesto por TCP, se observó una superficie laminar cuya composición coincidió con la del TCP Ca/P ≈ 1.5, consistente con los resultados de XRD (Figura 6B).

A continuación, se analizó la microestructura de los andamios dopados con distintas cantidades de Mg. En el caso de CS0, tras la aplicación de la última capa, se identificó una superficie con estructuras redondeadas similares a gotas, con una relación Ca/Si ≈ 0.5, acompañadas de granos poligonales de mayor tamaño con un Ca/P ≈ 1.5, correspondientes a TCP.

La topografía del andamio CS04 presentó un patrón lamelar, con estructuras de 4 ± 0.2 μm de ancho y un espaciado de 7.0 ± 0.1 μm, formadas por granos de silicofosfatos cálcicos con una relación Ca + Mg/P + Si ≈ 0.9. Esto sugiere la posible presencia de $CaSiO_3$ parcialmente sustituido con Mg^{2+} en lugar de Ca^{2+}, y PO_4^{3-} reemplazando a SiO_4^4. Esta microestructura es de particular relevancia para la regeneración esquelética, dado que el hueso se organiza en láminas distribuidas de manera irregular. Este biomimetismo no solo proporciona una ventaja biológica significativa, sino también biomecánica, al permitir una distribución adecuada de las cargas.

La superficie del andamio CS05 resultó ser heterogénea, con estructuras en forma de bastones con un Ca/Si ≈ 2, sugiriendo la presencia de silicato dicálcico (Ca_2SiO_4), y granos poligonales de silicofosfatos cálcicos con un Ca/P +Si ≈ 1.5.

La microestructura del andamio CS06 fue similar a la de CS0, pero con una mayor cantidad de cristales de TCP. Finalmente, CS075 presentó una estructura angulosa, constituida exclusivamente por granos poligonales de TCP y pirofosfato de calcio.

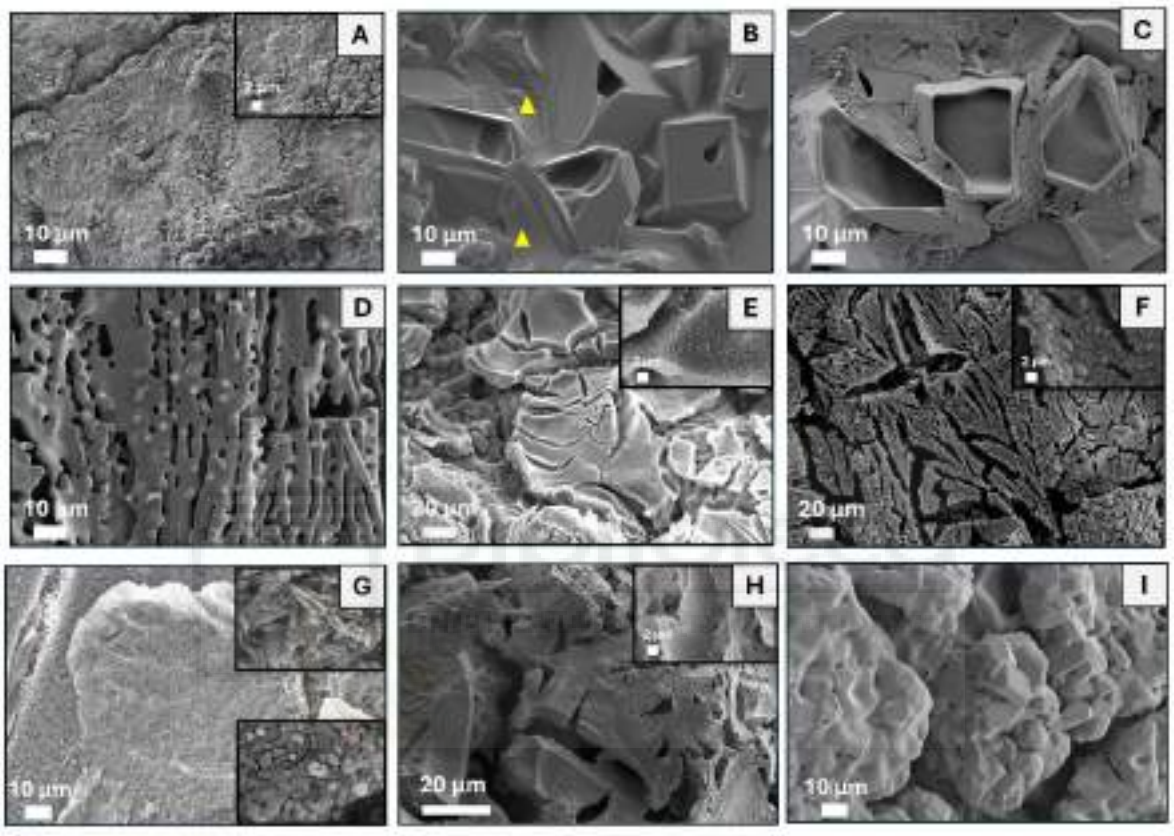

Figura 10 | Topografía de los andamios tras la deposición sucesiva de cada capa. Micrografías obtenidas mediante FESEM-EDX de CS (A), CS-P6 (B), CS-P6-TRIS (C), Núcleo-TCP (D), CS0 (E), CS04 (F), CS05 (G), CS06 (H) y CS075 (I).

Los datos sugieren que pequeñas variaciones en la cantidad de $MgCO_3$ afectan la microestructura y composición superficial de los andamios. A través del dopaje iónico, se ha logrado modular la morfología superficial, observándose una transición desde estructuras redondeadas hasta la formación de bastones o láminas. Además, la presencia de fosfatos cálcicos está directamente relacionada con la cantidad de Mg dopante, lo que sugiere que el Mg^{2+} compensa el déficit iónico causado por la migración de calcio entre capas. Este mecanismo podría explicar la formación de whitlockita, observada en los difractogramas XRD (Figura 6C), y confirmada mediante FTIR (Figura 7), así como la disminución en la intensidad del pico principal de la cristobalita a medida que se incrementa la cantidad de MgCO3 utilizado como dopante (Figura 6C).

4.1.5 Biodegradación

La biodegradación es un aspecto fundamental de los andamios de tercera generación cuya finalidad es la regeneración y no el reemplazo del tejido dañado. En la Figura 11 se muestran los perfiles de biodegradación de los andamios completos CSX a lo largo de 21 días en PBS (pH 7.4; 37 °C). Durante los primeros 7 días, la tasa de degradación muestra una clara relación con la cantidad de dopante, siendo considerablemente superior en los andamios dopados en comparación a CS0. A partir de la segunda semana, las tasas tienden a estabilizarse, alcanzando un valor cercano al 15% al cabo de 21 días.

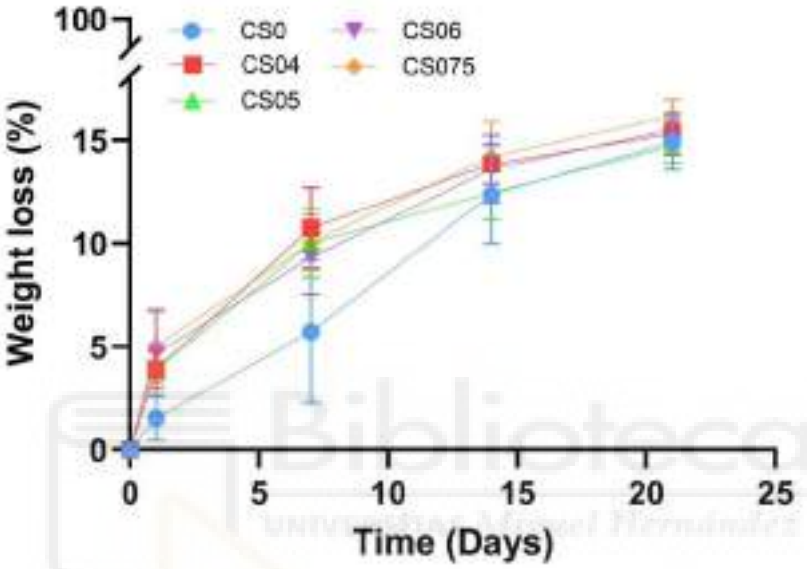

Figura 11 | Biodegradación *in vitro* de los andamios CSX durante 21 dias en PBS.

Para comprender esta variabilidad inicial, es necesario considerar la composición de la superficie expuesta al PBS. Como se describe en el apartado anterior 4.1.4, el Mg^{2+} podría compensar el déficit iónico y favorecer la formación de TCP en la capa externa, que, dada su naturaleza reabsorbible, podría favorecer la disolución. Además, en los andamios dopados, se encuentra presente junto con su variante rica en Mg, la whitlockita. Esta sustitución iónica genera distorsiones en la estructura que disminuyen la cristalinidad y estabilidad, facilitando la disolución. Estos resultados resaltan el efecto del dopaje con Mg en la biodegradación, lo que sugiere que esta modificación podría ser utilizada para regular la tasa de degradación inicial de los andamios. Este aspecto es fundamental, ya que si el andamio se disuelve demasiado rápido, pierde su función estructural y compromete la regeneración ósea. Por otro lado, una disolución excesivamente lenta puede reducir el espacio disponible para el crecimiento del nuevo tejido.

4.2 Bioactividad *in vitro*

El éxito de un implante óseo radica, entre otras cosas, en conseguir una buena osteointegración. Esta capacidad de unirse al hueso *in vivo* es fundamental para la

funcionalidad a largo plazo y evitar el desajuste del implante. En este sentido, se estudió la bioactividad *in vitro* de los andamios completos CSX (Figura 9).

Inicialmente, el andamio CS0 presentó una superficie compuesta por estructuras de silicatos cálcicos con diferente contenido en fosforo. En el día 1 se identificaron estructuras fibrilares entrelazadas, con una relación Ca/P+Si ≈ 0.5, hasta bastones más definidos tras 3 días, caracterizados por una mayor contribución de P, resultando en un Ca/P+Si ≈ 1. Este comportamiento se mantuvo hasta el séptimo día, lo que favoreció la formación de un precipitado con morfología similar al apatito y un ratio Ca/P ≈ 1.6, muy próximo al del hidroxiapatito estequiométrico. Además, se identificó un contenido residual de Mg (0.5 at. %), proveniente del SBF, que se mantuvo sin grandes modificaciones a lo largo del estudio. A partir de este momento, el contenido en silicio del precipitado comenzó a aumentar, con la consecuente reducción de fósforo, lo que resultó en un Ca/P ≈ 2.3 en el día 14 del estudio. Dado que altas relaciones Ca/P favorecen la disolución de los apatitos, se identificaron áreas donde el precipitado había comenzado a disolverse. Finalmente, tras 21 días, el precipitado se disolvió por completo, revelando cristales con una distribución de Ca/P a lo largo de su estructura similar a la observada en el núcleo, siendo próxima a 1 en la periferia y próxima a 1.5 en la región central, así como estructuras redondeadas con un Ca/Si ≈ 0.5.

La superficie lamelar de CS04 presentó un patrón morfológico distinto respecto a su análogo no tratado con SBF (Figura 7). Tras un día de inmersión, las lamelas se volvieron notablemente más delgadas, revelando nanolamelas de 700 ± 100 nm y microlamelas de 1.5 ± 0.9 μm, con un espaciado promedio de 2.8 ± 0.4 μm y una longitud de 9.4 ± 2.2 μm. A partir del tercer día, se observó la formación de un delgado precipitado en la superficie que cubría parcialmente la estructura lamelar. Este precipitado presentó una relación Ca/P ≈ 1.7 con una presencia de Mg de ≈ 0.9 at. %. Al cabo de una semana, el precipitado mantuvo una relación Ca/P constante (≈ 1.7) y una ligera disminución en el contenido de Mg (≈ 0.8 at. %). A pesar de la acumulación de precipitado, la estructura lamelar todavía claramente reconocible mostrando canales de aproximadamente 343 ± 52 nm (▲) en su superficie. A las dos semanas, el precipitado acumulado cubrió completamente la estructura lamelar subyacente, adoptando una morfología uniforme que permaneció estable hasta el final del estudio, con una composición constante. Los canales previamente identificados aumentaron su densidad con el tiempo, lo que indica un proceso continuo de modificación en la superficie. El Ca/P se mantuvo en ≈ 1.6, y el contenido de Mg en ≈ 0.7 at. %. La microestructura biomimética laminar del andamio, mantenida hasta el día 7, permite orientar el crecimiento celular, pudiendo contribuir a una regeneración eficiente y organizada [43, 81].

El andamio CS05 exhibió la formación temprana de un precipitado de tipo apatito, observable desde el primer día de inmersión en SBF. Inicialmente, dicho precipitado se presentó en forma de fibras o bastones entrelazados dispersos sobre una matriz de granos poligonales. Tras tres días, el precipitado cubrió homogéneamente la superficie, adoptando una morfología cuadrangular poco definida. No obstante, al cabo de una semana, evolucionó hacia una estructura más ordenada, caracterizada por cristales aciculares típicos del hidroxiapatito, dispuestos en microesferas de aproximadamente 2-3 μm de diámetro, con un orificio central profundo que sugiere una estructura hueca. Estas microesferas persistieron hasta el día 14 para finalmente fusionarse y desaparecer a 21 días, resultando en la formación de un recubrimiento continuo.

Los cambios morfológicos observados fueron consecuencia de modificaciones en la composición química y en la cristalinidad del precipitado. El análisis EDX mostró una evolución en la relación Ca/P, con valores de aproximadamente 1.3 en el día 1, 1.7 en el día 3, acompañado de un elevado contenido de Si (Ca/Si ≈ 2.2), 1.6 en los días 7 y 14, y 1.5 en el día 21. Este proceso estuvo acompañado por una reducción progresiva en el contenido de Mg que pasó de 1.2 at. % en el día 1 a 0.9 at. % en el día 7, manteniéndose en ese valor hasta el final del estudio.

La morfología cuadrangular observada al tercer día fue la menos definida y, la de menor cristalinidad, lo que puede atribuirse a la incorporación de iones silicato (SiO_4^{4-}) en la red del apatito mediante la sustitución parcial de los grupos fosfato (PO_4^{3-}) [15, 82-85]. Este fenómeno genera distorsiones estructurales que restringen el crecimiento cristalino, reduciendo el tamaño de los cristales y alterando su morfología.

Por otro lado, la formación de microesferas huecas está influenciada por la presencia de Mg^{2+}, con mayor densidad de carga que el Ca^{2+}. Su incorporación en la estructura del apatito induce tensiones internas que favorecen procesos de disolución-reprecipitación. Este mecanismo, asociado al fenómeno de maduración de Ostwald, promueve una redistribución progresiva del Mg^{2+} en la solución, generando un precipitado inicial con alto contenido de este elemento y elevado estrés cristalino [79, 86, 87]. Conforme el precipitado madura, su estructura se reconfigura, favoreciendo la formación de microesferas huecas, como las observadas en CS05-7D y CS07-14D. Esta hipótesis también podría explicar la aparición de los canales identificados en CS04.

Las microesferas huecas presentan un alto potencial como sistemas de liberación controlada de moléculas bioactivas, dado su carácter biodegradable y su composición bioactiva basada en apatitos. Además, su composición confiere un doble efecto terapéutico, derivado tanto de la liberación del agente terapéutico como de los iones liberados durante la degradación de las microesferas, tales como Ca^{2+}, PO_4^{3-}, Mg^{2+} y SiO_4^{4-}, estrechamente ligados a la fisiología ósea [61, 64]. Asimismo, aunque el tamaño

de estas microesferas (2–3 μm) es mayor que el de otros sistemas habitualmente empleados para la liberación de moléculas bioactivas, como nanopartículas poliméricas, liposomas o nanopartículas mesoporosas de sílice, su escala permite que actúen como vehículos capaces de inmovilizar o encapsular dichas nanopartículas [88, 89].

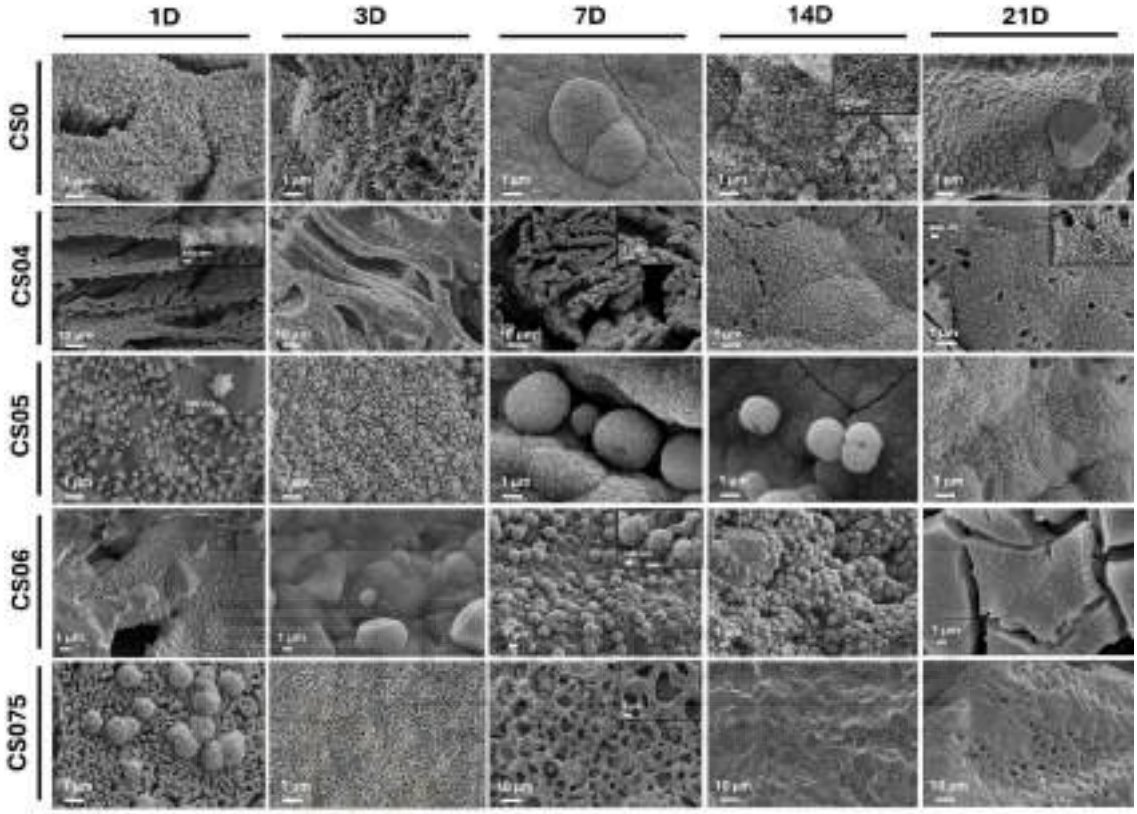

Figura 12 | Comportamiento bioactivo de los andamios CSX a lo largo de 21 días

Continuando con los resultados de bioactividad, el primer día de estudio del andamio CS06, presentó una superficie similar a la observada en CS0, caracterizada por estructuras redondeadas con una relación Ca/Si ≈ 0.5, junto con cristales poligonales de mayor tamaño con Ca/P ≈ 1.5. Tras tres días de inmersión en SBF, se formó un precipitado formando esferas irregulares, con una relación Ca/P ≈ 1.4 y un 1.2 at. % de Mg, depositadas sobre un fondo de cristales con Ca/P ≈ 1.5. Sin embargo, a diferencia de las esferas observadas en CS05-7D, estas estructuras eran compactas. La superficie permaneció prácticamente inalterada hasta el séptimo día, mostrando un precipitado con una relación Ca/P ≈ 1.6 y un contenido en Mg invariable. A los 14 días, se identificó una mayor acumulación del precipitado, aunque sin llegar a cubrir completamente la superficie. Respecto a la composición elemental, se registró una ligera disminución en la relación Ca/P hasta ≈ 1.4 y un aumento en la concentración de Mg hasta un 2.2 at. %, acompañado de una morfología aplanada y menos definida. Finalmente, al cabo de 21 días, el precipitado desapareció, dejando expuesta una microestructura muy similar a la observada en el control no expuesto a SBF (Figura 10) y en CS06-1D.

El andamio CS075 presentó una rápida formación de precipitado. Tras un día de inmersión en SBF, se identificaron aglomerados esféricos similares a los observados en CS06, formados por estructuras que recuerdan la morfología cuadrada de CS05-3D. Su composición elemental reveló una relación Ca/P ≈ 1.5, con un alto contenido en silicio, resultando en un Ca/Si ≈ 1.5 y un contenido de Mg de un 1.4 at. %. Después de tres días, la superficie quedó completamente cubierta por un precipitado acicular, con una relación Ca/P ≈ 1.5 y un menor contenido de Si, reflejado en un Ca/Si ≈ 3.5 y mayor de Mg hasta un 1.9 at. %. No obstante, tras siete días, se observó una microestructura en forma de anillos cuya composición elemental mostró Ca/P ≈ 1.5. A los 14 días, la superficie adquirió un aspecto diferente, caracterizado por la presencia de estructuras poligonales con un Ca/P ≈ 1.3 en la zona central y Ca/P ≈ 1 en la periferia. Finalmente, al cabo de 21 días, se observaron cristales con una relación Ca/P ≈ 1.8. Estos hallazgos sugieren un proceso de disolución progresiva del andamio. Inicialmente, el material mostró bioactividad (D1-D3), seguida por la aparición de una estructura anillada con una composición Ca/P ≈ 1.5, correspondiente a la del fosfato tricálcico (D7). La disolución continuó hasta alcanzar una estructura consistente con el núcleo del material (D21).

Uno de los objetivos de esta tesis es inducir modificaciones morfológicas en el apatito precipitado mediante el dopaje iónico del recubrimiento externo CSX. Durante el proceso de disolución, iones como Na^{+}, K^{+}, Mg^{2+}, Ca^{2+} y Si^{4+}, se liberan al medio y, posteriormente, se incorporan a los cristales de apatito, mejorando el biomimetismo del sistema. Las sustituciones iónicas en la estructura cristalina de los apatitos han sido ampliamente estudiadas, y es bien conocido que la composición del apatito biológico difiere de la fórmula estequiométrica ($Ca_{10}(PO_4)_6(OH)_2$) [83-85]. Habitualmente, estos apatitos son deficientes en calcio y presentan iones sustituyentes como Mg^{2+}, Cl^{-}, Na^{+}, CO_3^{2-} o SiO_4^{4-}, los cuales inducen distorsiones en la red cristalina y reducen su cristalinidad, como se observa en CS05-3D y CS075-1D.

Entre las sustituciones iónicas identificadas en los ensayos de bioactividad, los apatitos enriquecidos en silicio han demostrado promover la osteogénesis *in vivo* y favorecer una remodelación ósea aproximadamente el doble de rápida que los deficientes en Si [82, 84]. Por su parte, los apatitos dopados con magnesio favorecen la regeneración ósea al estimular procesos clave como la diferenciación osteogénica y la mineralización de la matriz ósea, además de exhibir actividad antimicrobiana [82, 90, 91].

Los resultados de bioactividad no solo actúan como indicadores cualitativos de osteointegración, sino que también reflejan la velocidad y eficiencia de este proceso. Kokubo et al. describieron la correlación entre la rapidez de precipitación de apatitos y el grado de crecimiento tisular, mostrando que los materiales capaces de formar apatito en menor tiempo logran una unión ósea más rápida *in vivo*, favoreciendo la regeneración

[92]. En este sentido, CS04 y, especialmente CS05, podrían favorecer una unión al hueso acelerada.

Para estudiar la liberación de iones de los andamios y su incorporación en el precipitado de apatito, se evaluó la composición iónica del SBF a lo largo del estudio (Figura 13). Los resultados obtenidos evidencian una tendencia común en todos los andamios bioactivos, caracterizada por una relación inversa entre el Si^{4+} y el P^{3-}. A medida que el andamio se disuelve, se observa un incremento en la concentración de Si^{4+} en el SBF, mientras que la concentración de P^{3-} disminuye, como consecuencia de su incorporación a los precipitados de apatito. Este proceso se prolonga hasta alcanzar un estado de saturación, que resulta en la precipitación de compuestos ricos en silicio, como se observa en CS0-21D y CS06-21D (Figura 12). Estos compuestos desempeñan dos funciones: por un lado, inducen la disolución del apatito existente y, por otro, actúan como núcleos para la formación de nuevo apatito. Este mecanismo de bioactividad intermitente ha sido previamente descrito en otros materiales por otros autores [93].

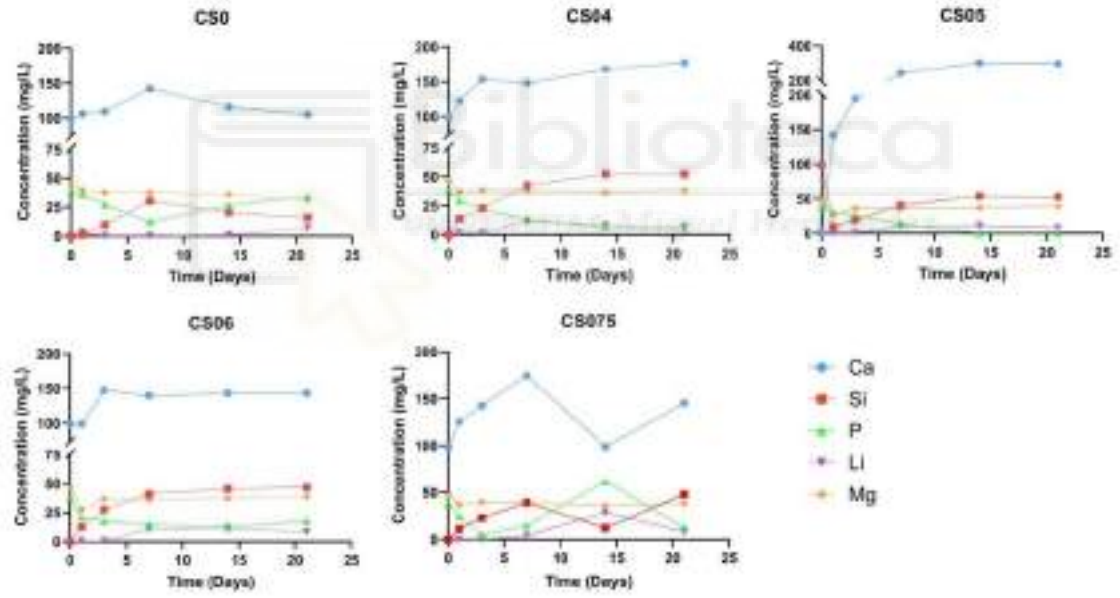

Figura 13 | Variación de las concentraciones iónicas en el SBF a lo largo del estudio de bioactividad

En el caso del andamio CS0, la disminución de la concentración de P^{3-} es constante hasta el día 7, mientras que en los andamios CS04 y CS05 se mantiene a lo largo de todo el estudio hasta alcanzar valores cercanos a 0. El andamio CS06 muestra una disminución de P^{3-} durante los primeros 7 días, seguida de una meseta hasta el día 14 y un ligero aumento en el día 21, coincidiendo con la precipitación y disolución del apatito. Finalmente, en el andamio CS075, la concentración de P^{3-} cae inicialmente hasta el día 3, coincidiendo con la formación de los primeros precipitados, aumentando posteriormente debido a su disolución (Figura 12). A partir del día 14, vuelve a descender, mostrando el

comportamiento intermitente descrito. Este comportamiento dinámico es análogo al del hueso, que experimenta un proceso continuo de formación y resorción (ver Apartado 1.2.4).

A pesar de la relación esperada entre la variación de P^{3-} y la de Ca^{2+}, esencial para la precipitación de apatito, los niveles de Ca^{2+} permanecen elevados (>100 mg/L) y no muestran una correlación directa con P^{3-}. Esto sugiere que la concentración de Ca en los andamios es lo suficientemente alta como para equilibrar la cantidad precipitada con la disuelta.

En cuanto a los iones dopantes minoritarios, como Li^{+} y Mg^{2+}, se observaron ligeras variaciones. Dado que el Li se encuentra en el núcleo como dopante de P6, su liberación puede servir como un indicador de la degradación del andamio. Los andamios con menor contenido de Mg (CS0, CS04, CS05 y CS06) muestran una liberación más sostenida y menos pronunciada de Li^{+} en comparación con CS075, donde la liberación aumenta significativamente tras 14 días. Esto coincide con los resultados de biodegradación (Figura 7), que indican una mayor tasa de degradación para el andamio CS075, debido a su composición superficial más rica en Mg (Apartados 4.1.4 y 4.1.5). El comportamiento del Mg^{2+} es similar en todas las muestras: tras un día de inmersión en SBF, su concentración disminuye y se estabiliza en torno a 30-40 mg/L. Como se ha observado mediante FESEM-EDX, los precipitados de apatito incorporan Mg en su estructura, lo que está estrechamente relacionado con la formación de microesferas huecas y la aparición de canales. Según el mecanismo de maduración de Ostwald [86, 87], sería este precipitado inicial rico en Mg, el responsable de introducir tensiones estructurales que favorecen su disolución y posterior reorganización, dando lugar a microesferas huecas en CS05 o a canales en CS04, dependiendo de la cantidad de Mg dopante empleada. En el caso de CS0, aunque también se observa la precipitación inicial de Mg, este proviene exclusivamente del SBF, lo que limita su disponibilidad y, por ende, su efecto en la reorganización estructural del precipitado.

4.3 Biocompatibilidad

La selección de los andamios para la caracterización biológica *in vitro* se basó en los resultados obtenidos de la caracterización fisicoquímica y bioactiva. Aunque todos los andamios CSX presentaron una composición, propiedades físicas y un perfil de biodegradación adecuados, los andamios CS04 y CS05 destacaron por su mayor idoneidad para aplicaciones en ingeniería de tejido óseo. En particular, ambos mostraron bioactividad temprana, en el tercer día para CS04 y en el primer día para CS05, y sostenida a lo largo del estudio, acompañada de modificaciones morfológicas significativas. Las láminas de CS04 podrían inducir el direccionamiento del crecimiento

celular, mientras que las esferas huecas de CS05 resultarían idóneas para la encapsulación y liberación controlada de moléculas bioactivas.

En los artículos 1 y 2, la caracterización biológica se limitó al análisis de citotoxicidad con el objetivo de descartar efectos adversos sobre la viabilidad celular. Una vez confirmada la citocompatibilidad de los andamios, en los artículos 3 y 4 se realizó una caracterización biológica más detallada, centrada en evaluar propiedades específicas para la regeneración del tejido óseo. Además, en el artículo 3, el andamio CS0 se incluyó como control experimental debido a su ausencia de magnesio, con el objetivo de evaluar si la incorporación de este ion en el andamio CS05 podría inducir efectos biológicos beneficiosos adicionales a su implicación en la formación de microesferas huecas en SBF.

4.3.1 Citotoxicidad

Se realizó un estudio *in vitro* de la compatibilidad celular de los andamios CS0, CS04 y CS05, así como de sus productos de disolución, utilizando tres ensayos colorimétricos distintos: MTT, alamarBlue y CCK8, empleados para evaluar la viabilidad celular y la actividad metabólica.

Asimismo, estos ensayos permitieron investigar cómo la microestructura superficial influye en el comportamiento celular. Con este objetivo, se compararon las diferentes topografías obtenidas en un mismo andamio a lo largo del estudio de bioactividad (Figura 12), en relación con el andamio no expuesto a SBF (Figura 7). En el artículo 1, se comparó la viabilidad celular del andamio CS05-0D, antes de la inmersión en SBF, con la morfología cuadrada de CS05-3D, las microesferas huecas de CS05-7D y la superficie lisa de CS05-21D. Por otro lado, en el artículo 2, se comparó la proliferación celular tras la exposición a las distintas topografías del andamio CS04, incluyendo las láminas gruesas de CS04-0D, las láminas delgadas de CS04-1D, las láminas con precipitado de apatito de CS04-7D y la superficie lisa de CS04-14D.

4.3.1.1 Efecto directo

La citotoxicidad directa, ensayada sobre el propio andamio, se evaluó en distintos tipos celulares mediante los ensayos MTT, alamarBlue y CCK-8 (Figura 14).

El ensayo MTT sobre fibroblastos murinos 3T3, reveló una proliferación celular mayor en los andamios recubiertos con apatito (CS05-3D, CS05-7D y CS05-21D) en comparación con CS05-0D (Figura 14A). Aunque las diferencias eran sutiles tras el primer día de cultivo, se hicieron más evidentes a las 48 horas y alcanzaron su punto máximo al tercer día. Entre los distintos grupos, CS05-7D mostró la respuesta biológica más favorable, lo que sugiere que su morfología de microesferas, al igual que las láminas en CS04, aumenta el área superficial efectiva del andamio, lo que facilita la adhesión

celular. Asimismo, se observó un crecimiento constante de la población celular para todos los grupos de estudio, confirmando la citocompatibilidad de CS05.

De manera similar, el ensayo alamarBlue reveló diferencias significativas en la viabilidad celular en función de la microestructura del andamio CS04 (Figura 14B). Desde el primer día, los andamios con precipitados de apatito (CS04-7D y CS04-14D) presentaron una mayor viabilidad celular en comparación con los grupos sin precipitados, destacándose CS04-7D como el más favorable. A partir del tercer día y hasta el final del estudio, CS04-7D mantuvo una proliferación celular significativamente superior, en particular frente a CS04-1D, cuya microestructura es análoga, salvo por la ausencia del recubrimiento de apatito. Esto sugiere que la presencia de apatito promueve el crecimiento de fibroblastos 3T3. Este hallazgo se encuentra en concordancia con estudios previos que indican que el hidroxiapatito no solo es biocompatible, sino que también puede estimular la proliferación celular en fibroblastos [94, 95]. Asimismo, la comparación entre los andamios recubiertos con apatito mostró una CS04-7D mayor población celular, lo que indica que su microestructura laminar ofrece un entorno más propicio para la adhesión y proliferación celular. Este efecto podría atribuirse al aumento del área superficial generado por la disposición laminar, lo que incrementa la disponibilidad de sitios para el anclaje celular y potencia la interacción célula-material.

Para ampliar el estudio a células humanas, se realizó un análisis de citotoxicidad en fibroblastos primarios humanos HFF-1. En este caso, se evaluó la proliferación celular a los 3 y 7 días de cultivo en los andamios CS0-0D y CS05-7D mediante el ensayo CCK-8 (Figura 14C). Los resultados mostraron un aumento en la población celular con el tiempo, lo que indica la citocompatibilidad de ambos andamios. Además, al igual que en los resultados obtenidos en fibroblastos murinos (Figura 14A-B), que mostraron una mayor proliferación celular en los andamios recubiertos con apatito, CS05-7D favoreció una mayor proliferación celular en comparación con CS0-0D, que no contiene apatito.

Asimismo, se evaluó la viabilidad y la capacidad proliferativa de las MCSc humanas sembradas sobre los andamios CS0-0D y CS05-7D mediante el ensayo CCK-8 (Figura 14D). Los resultados tras 3 y 7 días de cultivo mostraron un incremento significativo en la población celular con el tiempo, siendo este aumento particularmente pronunciado en las MSCs cultivadas sobre CS05-7D. Este hallazgo resulta particularmente relevante, ya que una adecuada respuesta celular por parte de las MSCs es crucial para el éxito de los tratamientos de regeneración ósea, debido a su capacidad para diferenciarse en osteoblastos y participar activamente en la formación de nuevo tejido óseo.

Por último, se llevó a cabo el ensayo CCK-8 en preosteoblastos murinos MC3T3-E1 sembrados sobre los andamios CS04 y CS05 (Figura 14E). A diferencia de las MSCs, que son células indiferenciadas con potencial osteogénico, la línea celular MC3T3-E1

presenta un grado de diferenciación más avanzado dentro del linaje óseo, lo que permite evaluar el desempeño de los andamios en células comprometidas con la formación ósea. Se observó un aumento progresivo en la población celular para ambos andamios, lo que confirma su citocompatibilidad. Aunque las diferencias no alcanzaron significación estadística, CS05 mostró una tendencia a favorecer una mayor viabilidad celular en comparación con CS04.

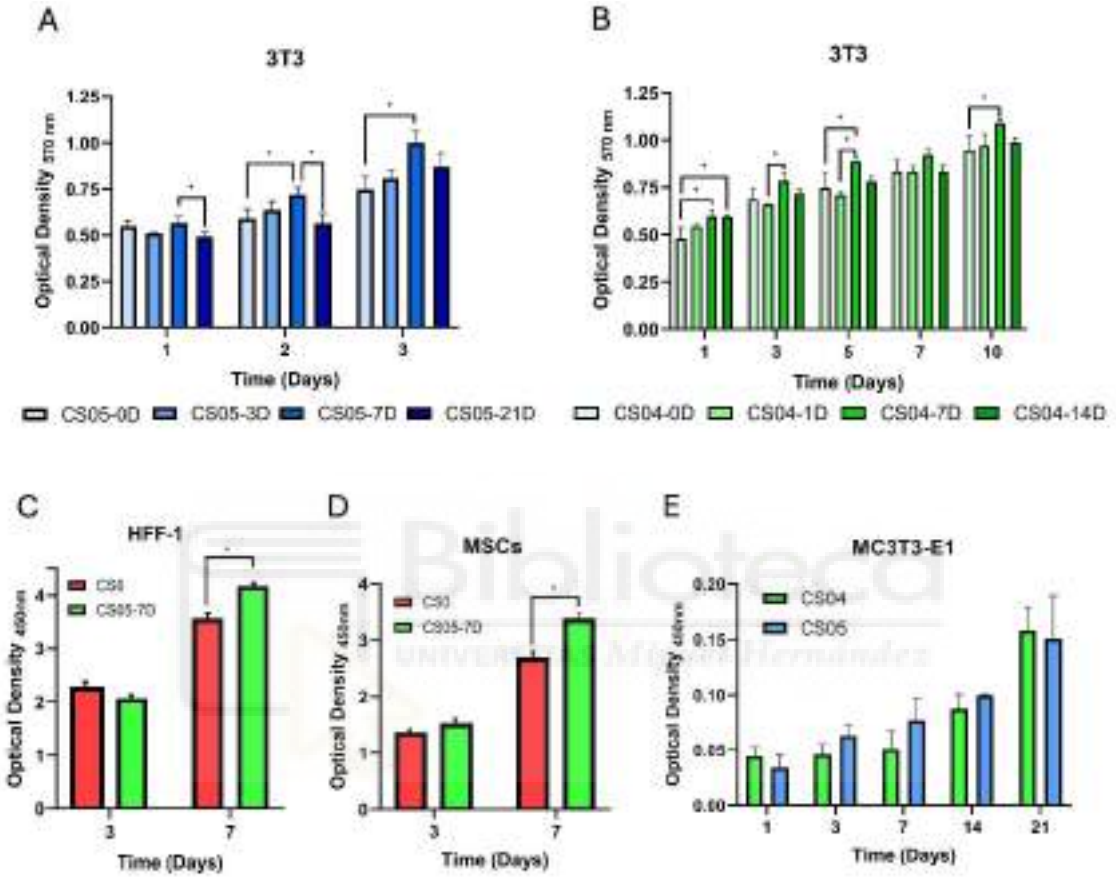

Figura 14 | Evaluación de la citotoxicidad de los andamios en distintas líneas celulares. Resultados de la viabilidad celular determinados mediante los ensayos MTT (A) y alamarBlue (B) en fibroblastos murinos 3T3, y mediante CCK-8 en fibroblastos humanos HFF-1 (C), MSCs humanas de médula ósea (D) y preosteoblastos murinos MC3T3-E1 (E).

Otro indicador esencial de la salud y funcionalidad celular en ingeniería de tejido óseo es la morfología celular. Una morfología fenotípica extendida sugiere una interacción favorable entre la célula y el material, favoreciendo la adhesión, proliferación y diferenciación celular. Por el contrario, en superficies no biocompatibles, las células tienden a adoptar una forma contraída, minimizando el área de contacto con el material. Estos cambios morfológicos suelen estar asociados con estrés celular y pueden comprometer la adhesión, llegando incluso a inducir apoptosis o necrosis.

En este sentido, complementando los ensayos de viabilidad celular, se analizó mediante SEM la morfología de las células HFF-1, MSCs y MC3T3-E1 fijadas sobre los andamios (Figura 15).

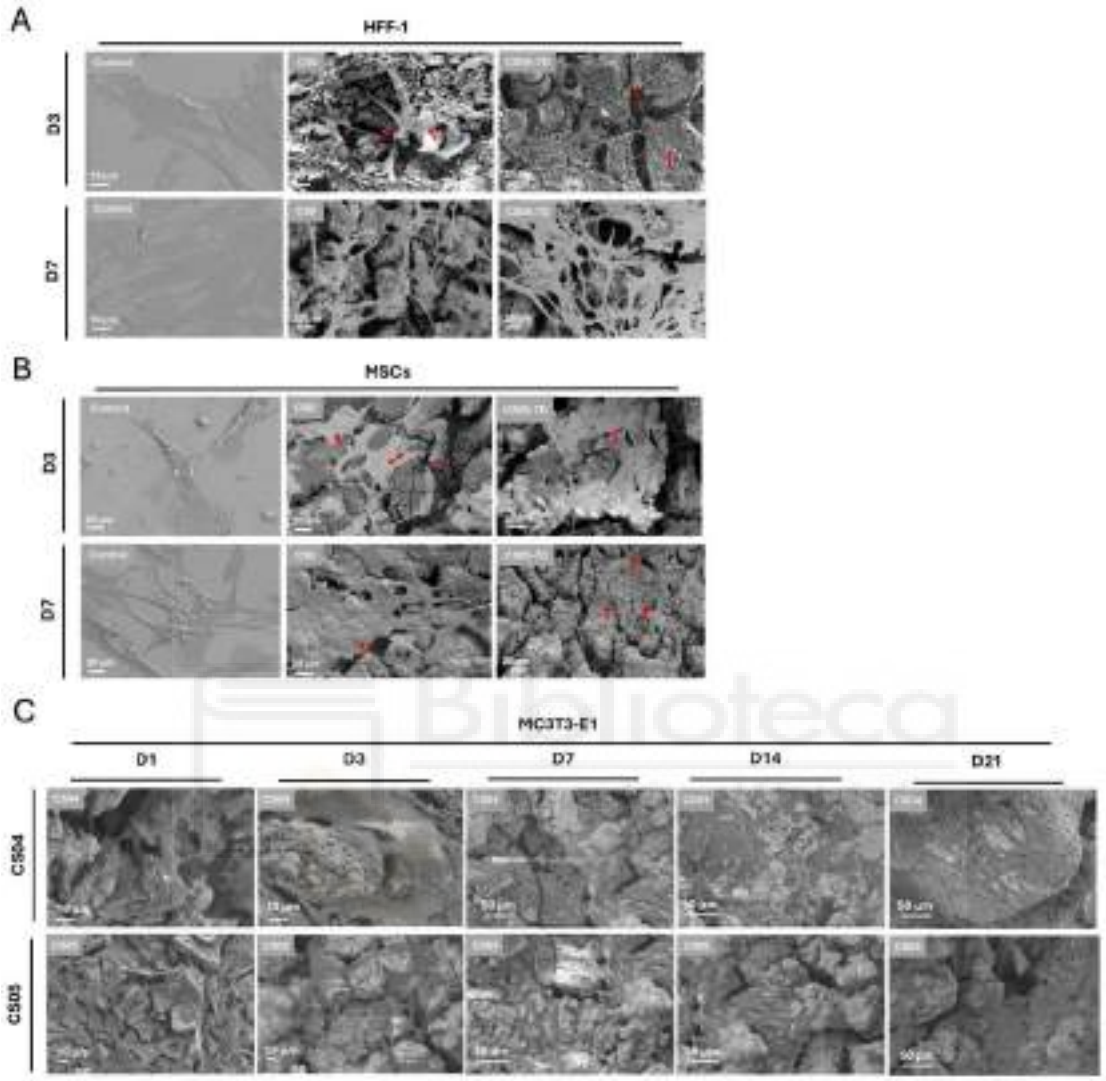

Figura 15 | Morfología celular tras cultivar distintos tipos celulares sobre los andamios CS0 y CS05-7D (A-B) y CS04 y CS05 (C).

Las células HFF-1 fijadas sobre CS0-0D y CS05-7D tras 3 y 7 días de cultivo (Figura 15A ⬆), mostraron una morfología, alargada y fusiforme extendiéndose a lo largo del andamio, con un aspecto similar al del control en plástico (Figura 15A). Además, se observó una acumulación progresiva de células en la superficie de los andamios, lo que sugiere una interacción celular favorable.

De manera similar, las MSCs fijadas sobre CS0-0D y CS05-7D tras 3 y 7 días de cultivo (⬆), presentaron una morfología alargada característica del tipo celular, lo que confirma la biocompatibilidad del material (Figura 15B).

Finalmente, las células MC3T3-E1 fijadas sobre los andamios CS04 y CS05 mostraron una morfología extendida, con presencia de filopodios y lamelipodios, lo que indica una adhesión y migración celular adecuadas (Figura 15C). Asimismo, se observó una colonización progresiva de la superficie del andamio a lo largo de los 21 días de estudio, aunque no se alcanzó una cobertura completa.

4.3.1.2 Efecto indirecto

Los andamios, en el entorno fisiológico, experimentan un proceso de disolución debido a la interacción con los fluidos biológicos. Evaluar el efecto indirecto de los andamios, a través de sus productos de disolución, permite analizar su impacto en las células vecinas, las cuales, aunque no estén en contacto directo con el material, pueden influir en el proceso de regeneración ósea mediante la síntesis y mineralización de la matriz ósea.

Este efecto indirecto se estudió en todos los tipos celulares ya mencionados mediante dos enfoques. El primero es un abordaje acumulativo, donde el andamio intacto se sumerge en medio de cultivo celular durante 24, 48 o 72 horas, permitiendo su disolución progresiva y la acumulación de los productos liberados. El segundo consiste en preparar disoluciones de concentración definida (10 y 100 mg/mL) de andamios triturados. A diferencia del anterior, en este caso, la disolución ocurre de forma simultánea para todas las capas. Además, esta solución se mantiene en paralelo con el estudio celular, renovando el medio de cultivo de forma periódica, lo que imita el aclaramiento fisiológico.

En primer lugar, se evaluó la viabilidad celular de los fibroblastos murinos 3T3 tras 1, 2 y 3 días de exposición a los productos de disolución de CS04 y CS05, utilizando el enfoque acumulativo a concentraciones de 15 y 30 mg/mL.

Los resultados del ensayo MTT, que evalúa la respuesta celular al cCCM de CS05, mostraron un crecimiento celular constante que incluso superó al del control tratado con medio de cultivo sin productos de disolución, permitiendo descartar efectos citotóxicos (Figura 16A). Además, se observó que, para ambas concentraciones, aunque de forma más pronunciada para 15 mg/mL, el efecto pro-proliferativo era directamente proporcional al tiempo de disolución de los andamios (cCCM-7D > cCCM-3D > cCCM-1D), lo que sugiere que la acumulación de los productos de disolución resulta beneficiosa.

De forma similar, el ensayo alamarBlue permitió evaluar la citotoxicidad del cCCM de CS04 en fibroblastos 3T3 (Figura 16B). En este caso, se prepararon tres disoluciones: cCCM-1D, cCCM-2D y cCCM-3D, nuevamente a concentraciones de 15 y 30 mg/mL. Como en los resultados obtenidos con el ensayo MTT, se observó un crecimiento celular que superó al del control. Esta inducción de la división celular fue, en general, mayor para la concentración de 30 mg/mL. Entre todas las disoluciones, cCCM-2D, a ambas concentraciones, fue la que mostró la mayor capacidad de inducir proliferación celular.

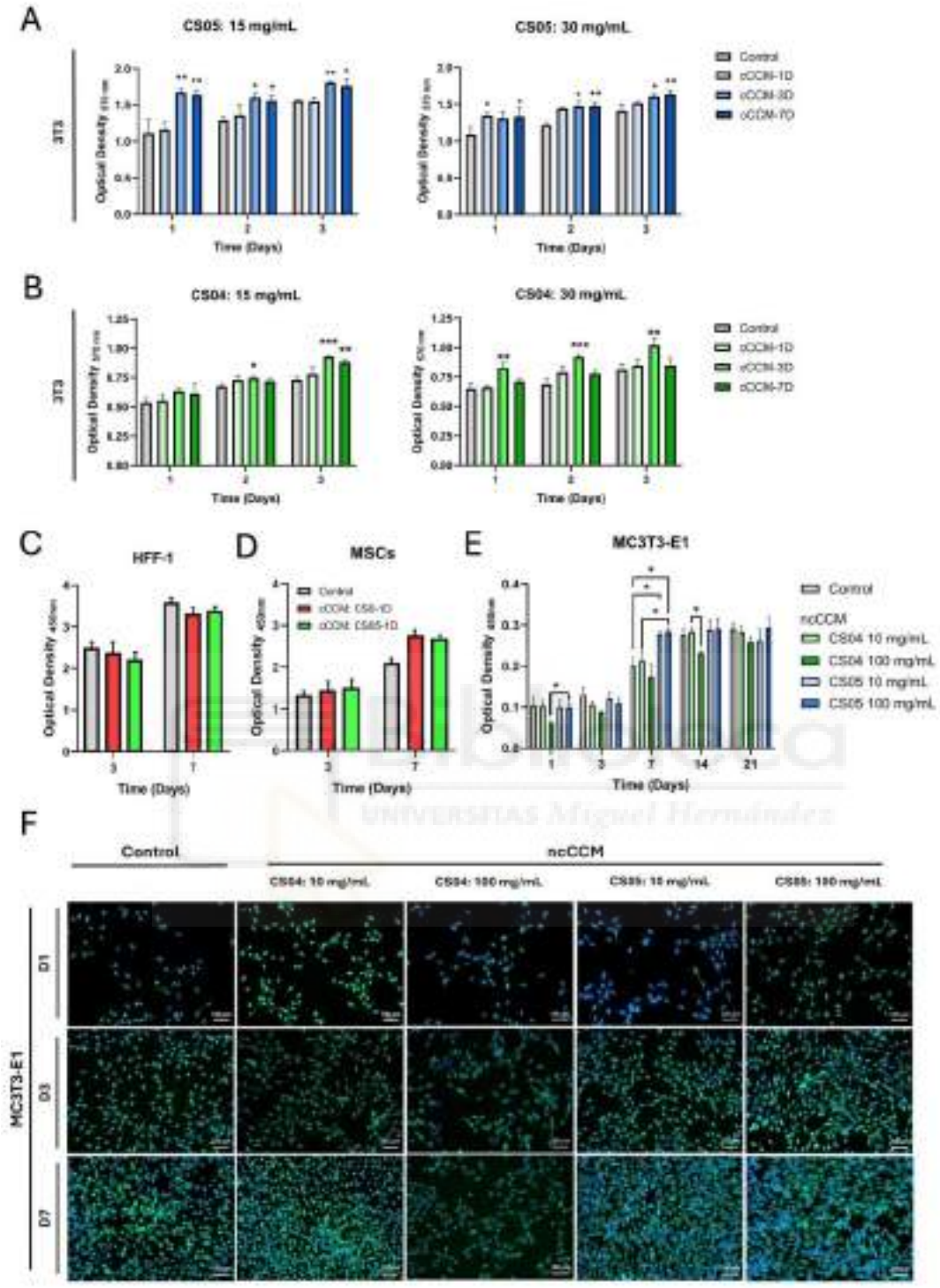

Figura 16 | Evaluación de la citocompatibilidad de los productos de disolución de los andamios mediante enfoques acumulativo (A-D) y no acumulativo (E-F). Análisis de viabilidad celular en fibroblastos murinos 3T3 tras la exposición al cCCM de CS05 mediante MTT (A) y al cCCM de CS04 mediante alamarBlue (B). Evaluación de la proliferación mediante CCK-8 en HFF-1 (C) y MSCs de médula ósea (D) tras la exposición al cCCM de CS0-1D y CS05-1D. En el enfoque no acumulativo, se evaluó la viabilidad (E) y morfología celular (F) de MC3T3-E1 tras la exposición al ncCCM de CS04 y CS05.

También se evaluó, mediante el ensayo CCK-8, el efecto del cCCM-1D de CS0 y CS05-7D sobre la viabilidad celular de fibroblastos humanos HFF-1 tras 3 y 7 días de cultivo (Figura 16C). Los resultados mostraron un comportamiento similar al observado en fibroblastos murinos 3T3, con proliferación continua y ligeramente superior al control. Sin embargo, este efecto fue menos pronunciado que en el caso anterior, probablemente debido a que, tras 1 día de disolución, se acumulan menos productos de disolución, lo que resulta en un impacto más moderado sobre la viabilidad celular. Los resultados indicaron una buena citocompatibilidad de los productos de disolución, sin diferencias estadísticamente significativas entre los cCCM-1D de CS0 y CS05-7D.

El efecto de los cCCM-1D de CS0 y CS05-7D también se evaluó en MSCs mediante el ensayo CCK-8, tras 3 y 7 días de cultivo, observándose el mismo comportamiento que en los fibroblastos HFF-1 (Figura 16D).

Para continuar con este estudio, se procedió a analizar los efectos de los productos de disolución mediante un enfoque no acumulativo, un enfoque replicando el proceso de aclaramiento corporal. En este caso los medios de cultivo acondicionados se denominarán no acumulativos, o ncCCM. Se estudiará el ncCCM de CS04 y CS05 a lo largo de 21 días en preosteoblastos MC3T3-E1.

La Figura 16E muestra un incremento progresivo en la población celular a lo largo del tiempo en cada grupo de tratamiento, lo que sugiere que los productos de disolución del andamio son citocompatibles. Aunque la viabilidad celular es ligeramente inferior a la del control al inicio, a partir del séptimo día se observa un aumento significativo en todos los grupos tratados. En particular, CS05, a ambas concentraciones, mostró valores significativamente más altos que el control y CS04 a la misma concentración. A partir del día 14, la proliferación celular parece alcanzar un punto de saturación, dado que el cultivo 2D ha ocupado toda el área disponible, limitando el crecimiento posterior. Sin embargo, en el caso de CS04 a 100 mg/mL, debido a la menor población celular inicial, se observó un ligero aumento en la viabilidad, probablemente porque aún quedaba superficie disponible para la proliferación.

Finalmente, se evaluó la morfología celular de MC3T3-E1 a lo largo de 7 días tras la exposición al ncCCM de CS04 y CS05 a 10 y 100 mg/mL (Figura 16F). Tras 1 día de cultivo, se observaron células adheridas a la placa de cultivo, mostrando su morfología característica fusiforme, cuya densidad aumentó a lo largo del estudio. Aunque el ensayo CCK-8 se realizó hasta el día 21, solo se incluyeron imágenes hasta el día 7, ya que, como se muestra en la Figura 16E, a partir de este día la proliferación celular alcanzó una meseta, probablemente debido a la saturación de la placa, que impidió obtener información adicional.

Para obtener una visión más clara del mecanismo o los iones involucrados en esta respuesta celular, se caracterizó iónicamente el cCCM-XD y el ncCCM mediante ICP-OES (Figura 17). Los iones pueden clasificarse en tres categorías según su comportamiento: iones liberados, iones capturados e iones fluctuantes.

Respecto a los iones liberados, en el cCCM-XD de CS04 y CS05, se observó la liberación de Si^{4+}, Li^{+} y P^{3-}. Sin embargo, en el ncCCM de CS04 y CS05, se observó la liberación de Ca^{2+}, Si^{4+} y Li^{+}. La liberación de Si^{4+} es particularmente relevante en aplicaciones ortopédicas debido a su conocido papel en la osteogénesis, estando bien documentado su impacto en la mejora de la diferenciación osteogénica y la mineralización ósea [27, 64, 82]. Al comparar el grado de liberación entre ambos enfoques, se observó que en el cCCM-XD, tan solo en 3 días se alcanza una concentración de Si^{4+} muy similar a la liberada por el ncCCM a la mayor concentración, lo que sugiere que su acumulación durante períodos más prolongados podría resultar citotóxica.

Respecto al litio, aunque es un metal alcalino tóxico, se ha demostrado que tiene propiedades angiogénicas y osteogénicas cuando se incorpora como dopante en materiales cerámicos, tanto en condiciones *in vitro* como *in vivo* [61, 64, 96]. Wang et al. demostraron que el litio tiene un efecto pro-proliferativo sobre las células madre mesenquimatosas óseas [96], además de actuar como un activador de la vía Wnt, implicada en la formación de vasos sanguíneos y osteogénesis [30, 61]. Al comparar las cantidades liberadas en los enfoques acumulativo y no acumulativo, se observa una mayor liberación en el primero, como era de esperar, aunque sin alcanzar niveles tóxicos.

Por otro lado, la liberación de Ca^{2+} ocurre en el enfoque no acumulativo, pero no en el acumulativo. Esto podría explicarse porque, en el enfoque acumulativo, el andamio se disuelve capa por capa. Según la teoría de la migración iónica del calcio entre capas (apartado 4.1.1), el calcio tiende a difundir hacia el núcleo del andamio, lo que hace que no esté tan presente en la superficie. Sin embargo, en el enfoque no acumulativo, se exponen a la disolución todas las fases del material, incluyendo las del núcleo, debido a que el andamio ha sido triturado. Dado el alto contenido de CaO en las muestras, no es sorprendente que el calcio se libere en este caso.

En cuanto a los iones capturados por el andamio en cCCM-XD de CS04 y CS05, se destacan principalmente el Ca^{2+} y el Mg^{2+}, mientras que en el caso del ncCCM, los iones predominantes son el P^{3-} y el Mg^{2+}. Dado que las diferencias esperadas en los productos de disolución de los andamios dependen principalmente de la cantidad de $MgCO_3$ utilizado como dopante, y dado que no se observó liberación de Mg^{2+} en los andamios que contienen este ion, se decidió no caracterizar el cCCM de CS0, ya que este no incluye Mg en su composición. No obstante, sería interesante realizar estudios adicionales en

presencia de osteoclastos, capaces de resorber minerales, lo que podría promover la liberación de estos iones al medio.

Finalmente, en ambos casos se observó que los iones Na^+ y K^+, que están presentes en altas concentraciones en el medio de cultivo (control), mostraban un comportamiento oscilante, siendo capturados y liberados de manera cíclica por los andamios a lo largo del estudio.

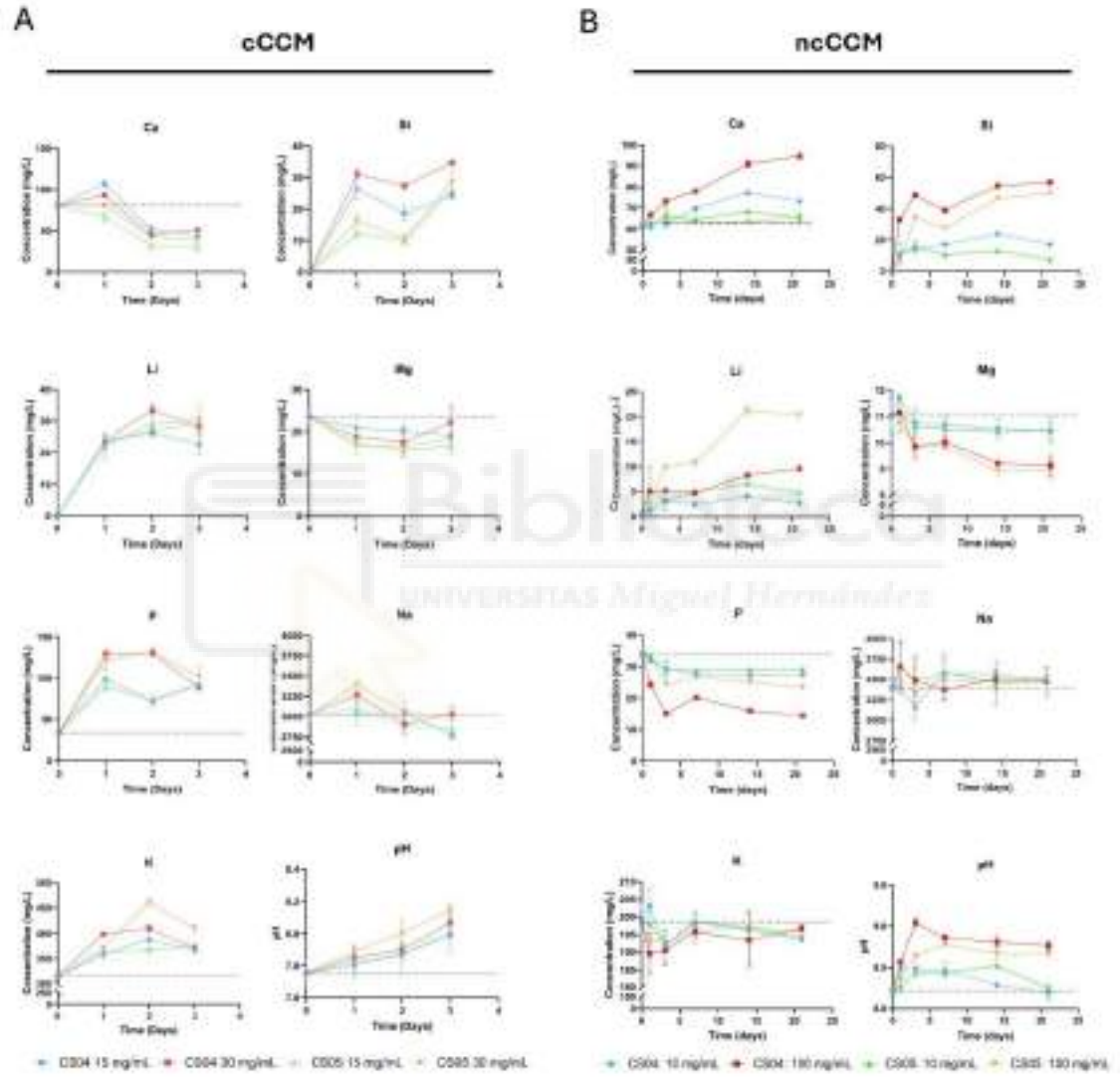

Figura 17 | Variación de la concentración iónica de los productos de disolución de CS04 y CS05 mediante un enfoque acumulativo (A) y no acumulativo (B).

4.3.2 Diferenciación osteogénica

Los andamios formados por materiales de tercera generación desempeñan un papel fundamental en la regeneración ósea, ya que no solo proporcionan soporte estructural, sino que también estimulan activamente la diferenciación osteogénica.

Para evaluar la capacidad de osteoinducción de los andamios multicapa, se analizó su capacidad para inducir la diferenciación osteoblástica mediante dos enfoques complementarios (Figura 15). En primer lugar, se llevó a cabo mediante un enfoque indirecto, en el que se estudió la diferenciación de las MSCs cultivadas en presencia de cCCM-1D de CS0 y CS05-7D durante 21 días (Figura 15A). Posteriormente, en un enfoque directo, se evaluó la diferenciación de preosteoblastos MC3T3-E1 cultivados sobre los andamios CS04 y CS05 (Figura 15B). Para ello, se emplearon tres técnicas de tinción ampliamente utilizadas en el estudio de la osteogénesis: ARS, von Kossa y ALP. Mientras que las tinciones de ARS y von Kossa permiten identificar la deposición de calcio en la matriz extracelular, la tinción de ALP proporciona información sobre la actividad enzimática de la fosfatasa alcalina, un marcador ampliamente reconocido de diferenciación osteogénica [67, 98].

Respecto al método indirecto, todas las muestras analizadas presentaron una adecuada proliferación celular, manteniendo una morfología fenotípica característica (Figura 15A). Sin embargo, se observaron diferencias en la intensidad de las tinciones, siendo significativamente mayor en las células tratadas con cCCM en comparación con el control. Este resultado concuerda con los datos obtenidos mediante ICP-OES, que revelaron una mayor concentración de Si^{4+}, Li^{+} y P^{3-} en el cCCM. Si bien el papel del Si y el Li en la osteogénesis ha sido previamente discutido (ver apartado 4.3.1.2), el P también desempeña una función clave. Estudios previos han demostrado que los iones de P^{3-} pueden modular múltiples procesos osteogénicos, incluida la activación de la expresión de osteopontina, una proteína esencial en la formación ósea [98, 99].

En el enfoque directo, se evaluó la actividad osteogénica de los andamios CS04 y CS05 mediante ARS y la cuantificación de la actividad de la ALP en cultivos de MC3T3-E1 durante 21 días (Figura 18B-D). Dado que la tinción ARS detecta depósitos de calcio y los andamios CS04 y CS05 presentan un alto contenido de CaO, se sometió a estos andamios al mismo protocolo de tinción para establecer un control (0D) que permitiera discriminar la señal de fondo atribuible al material. Desde el día 0, la tinción ARS en los andamios mostró un tono rosado, que progresivamente adquirió una tonalidad morada al día 7, y un rojo intenso a los días 14 y 21, lo que reflejó una mineralización gradual de la matriz extracelular (Figura 18B). La cuantificación de ARS, presentada en la Figura 18C, mostró una evolución colorimétrica similar entre el control y los andamios.

Durante los primeros 14 días, la señal de ARS fue mayor en el control, lo que coincidió con la aparición de los primeros nódulos de mineralización. No obstante, tras 21 días, se observó una mayor mineralización en las células cultivadas sobre CS04 y CS05, especialmente en CS04, que presentó diferencias estadísticamente significativas respecto al control. Estos resultados son consistentes con estudios previos que indican que el

subclon MC3T3-E1 comienza a depositar matriz ósea aproximadamente a los 10 días de cultivo.

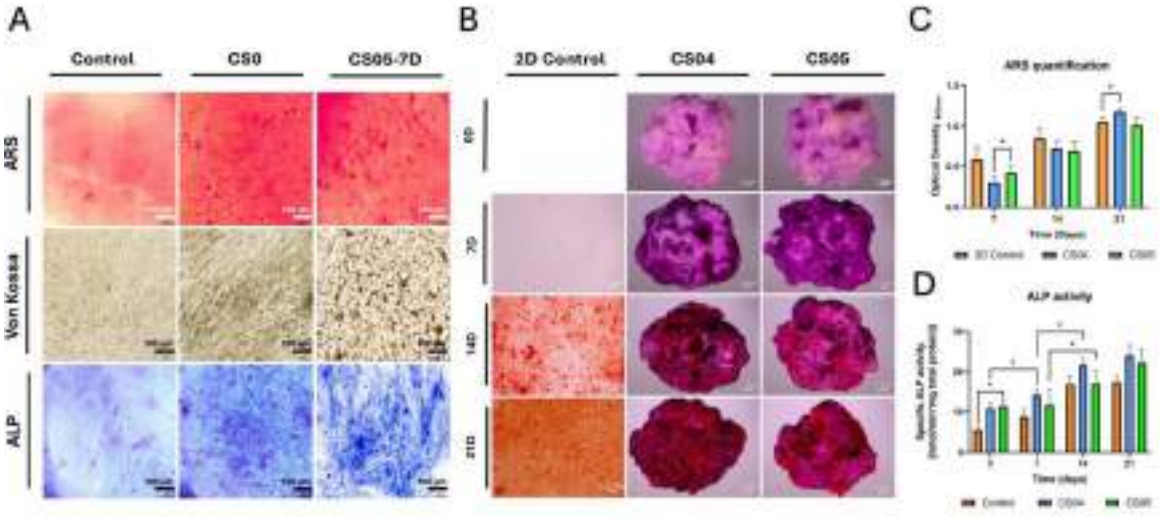

Figura 18 | Evaluación de la capacidad de osteoinducción de los andamios mediante un enfoque indirecto (A) y directo (B-D). Evaluación de la mineralización celular en MSCs mediante diferentes tinciones (A), y en MC3T3-E1 mediante ARS (A, B) y cuantificación de la actividad de la ALP (D).

La diferencia observada entre la deposición de calcio en CS04 y CS05 puede atribuirse a la microestructura de CS04, que forma estructuras lamelares similares a las del tejido óseo. El papel de la microestructura en la diferenciación de osteoblastos ha sido ampliamente documentado en la literatura científica. [33, 40, 43, 49, 50, 52, 100, 101]. Además, Abagnale et al. destacaron que las superficies con ranuras, como los surcos y crestas o las láminas, son especialmente beneficiosas para la diferenciación ósea [101].

Como complemento a este estudio, se cuantificó la actividad específica de la ALP en los preosteoblastos cultivados sobre los andamios CS04 y CS05 (Figura 18D). Se observó una mayor actividad en las células cultivadas sobre los andamios en comparación con el control 2D, manteniéndose esta diferencia a lo largo del estudio. Este incremento puede atribuirse al alto contenido de fosfatos de calcio en los andamios, principalmente pirofosfato de calcio y β-TCP, así como a su variante parcialmente sustituida, whitlockita, que actúan como sustrato para la enzima. Además, la alcalinización del medio inducida por la liberación de SiO_4^- genera un entorno bioquímico óptimo para la actividad de ALP, cuya función es más eficiente en condiciones alcalinas.

4.3.3 Propiedades angiogénicas

Para lograr una regeneración ósea efectiva, es fundamental la combinación de osteogénesis y angiogénesis. Entre las diversas vías angiogénicas, la señalización mediada por VEGF es la más ampliamente estudiada. En este contexto, se evaluó el

potencial angiogénico de los andamios CS04 y CS05 mediante la cuantificación de la liberación de VEGF en los sobrenadantes celulares, tomando como referencia el 100% de la liberación observada en el grupo control (Figura 19).

Durante la primera semana del estudio, no se observaron diferencias estadísticamente significativas entre las células del control y aquellas cultivadas sobre los andamios. Sin embargo, a los 14 días, estas diferencias se hicieron evidentes, con niveles de liberación de VEGF del 160% para CS05 y del 170% para CS04. A los 21 días, estas diferencias no solo se mantuvieron, sino que también mostraron un incremento en su significancia estadística. En conjunto con los resultados de porosidad (Figura 8), estos hallazgos sugieren que los andamios podrían favorecer la formación de una red vascular que infiltre su estructura, proporcionando el soporte nutricional necesario para las células en su interior.

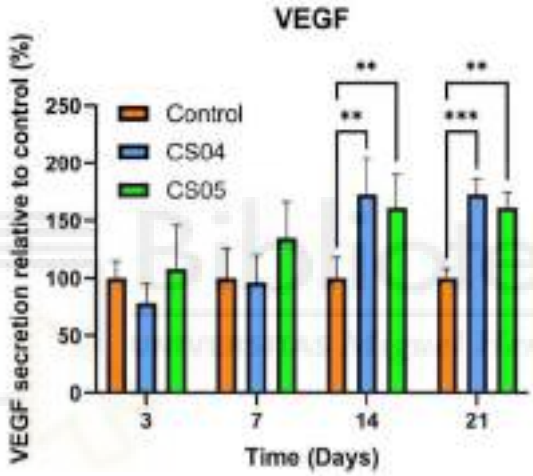

Figura 19 | Liberación de VEGF en sobrenadantes celulares de MC3T3-E1.

5. CONCLUSIONES Y PROYECCIONES FUTURAS

En este capítulo se recogen los principales resultados obtenidos a lo largo de la presente Tesis Doctoral, de acuerdo con los objetivos planteados en la misma. Además, se expone el impacto potencial de dichos resultados en el ámbito de los biomateriales y la ingeniería de tejido óseo, así como las posibles líneas de investigación futuras encaminadas a avanzar hacia su optimización y validación clínica.

5.1 Conclusiones

En el presente estudio, se han desarrollado andamios vitrocerámicos de tercera generación dentro del sistema SiO_2-CaO-P_2O_5, mediante la técnica de replicación de esponjas poliméricas, que permitió crear estructuras tridimensionales con una macroporosidad interconectada del 85%. A través del método sol-gel, se realizaron recubrimientos múltiples de los andamios por inmersión en la solución precursora de cada capa. Como resultado de la combinación de fases del enfoque multicapa, se obtuvieron andamios multifuncionales, compatibles física y mecánicamente con el hueso trabecular, biodegradables, bioactivos y biocompatibles.

La disposición secuencial de los recubrimientos, desde las capas internas hacia las externas, contribuyó de distinta forma a las propiedades finales del andamio:

- El recubrimiento de CS sirvió como molde y fuente de Ca^{2+}.
- El recubrimiento de P6 modificado con óxido de litio (Li_2O), mejoró las propiedades mecánicas, resultando una resistencia final a la compresión de 1.8 MPa.
- El recubrimiento de TCP actuó como reservorio iónico para la deposición de apatito.
- El recubrimiento de CS fue modificado con la incorporación de óxidos de sodio (Na_2O), potasio (K_2O) y distintas concentraciones de óxido de magnesio (MgO), aportando bioactividad y modificaciones en la topografía superficial.

Desde el punto de vista funcional, el Mg^{2+}, debido a la elevada densidad de carga, generó los resultados más significativos:

- Se identificó un rango óptimo de $MgCO_3$ entre 0,4 y 0,5 g (correspondiente a los andamios CS04 y CS05), que presentó los mejores resultados desde el punto de vista bioactivo y topográfico.

- El andamio CS04 presentó una microestructura laminar biomimética, que se mantuvo hasta el séptimo día del ensayo de bioactividad, momento en el que quedó oculta bajo un denso precipitado de apatito.
- El andamio CS05-7D presentó la formación de microesferas huecas de apatito, asociadas al fenómeno de maduración de Ostwald, con potencial aplicación para el almacenamiento y la liberación controlada de fármacos o biomoléculas.

Además, la diversidad mineralógica inducida por la combinación de la estrategia multicapa y el dopaje iónico, produjo la liberación de iones que, junto con las características topográficas de los andamios, desempeñaron un papel fundamental en el comportamiento biológico *in vitro*, arrojando los siguientes resultados:

- Los andamios CS0, CS04 y CS05 demostraron ser citocompatibles y evidenciaron una adecuada interacción célula-andamio en todos los tipos celulares evaluados.
- Los productos de disolución resultaron citocompatibles tanto en el enfoque acumulativo (cCCM) como en el no acumulativo (ncCCM), y propiciaron una proliferación celular mayor en todos los tipos celulares evaluados en comparación con el control.
- Se identificó la liberación de Si^{4+} y Li^{+}, dos iones con actividad osteogénica y angiogénica, en ambos enfoques. Adicionalmente, se detectó la liberación de P^{3-} en el cCCM y de Ca^{2+} en el ncCCM.
- Los estudios de osteoinducción mediante el método indirecto en MSCs humanas revelaron que el cCCM de los andamios CS0 y CS05 fue capaz de inducir una mayor expresión de la ALP y un incremento en la mineralización.
- En el método directo, los andamios CS04 y CS05 demostraron su capacidad osteogénica al estimular una mayor actividad específica de la ALP en preosteoblastos MC3T3-E1, así como una mayor formación de depósitos de calcio respecto al control.
- Los andamios CS04 y CS05 estimularon significativamente la liberación de VEGF en preosteoblastos MC3T3-E1, con incrementos de hasta un 170 % en comparación con el control, lo que demuestra su capacidad angiogénica.

5.2 Proyecciones Futuras

De cara a futuras líneas de investigación, resulta de especial interés evaluar el potencial efecto antimicrobiano de los andamios, asociado a la presencia y liberación de iones de silicio, dada su implicación en la inhibición del crecimiento bacteriano [27]. La confirmación de esta propiedad contribuiría a la prevención de infecciones postoperatorias, una de las principales complicaciones asociadas a la implantación de dispositivos médicos.

En segundo lugar, se plantea un análisis de la capacidad de carga y liberación controlada de agentes terapéuticos, aprovechando tanto los espacios interlamelares como las microesferas huecas generadas por la acción del magnesio. Estas estructuras presentan un elevado potencial como reservorios, permitiendo la liberación local de moléculas bioactivas personalizadas según el perfil clínico del paciente. Por ejemplo, la encapsulación de bisfosfonatos en pacientes con osteoporosis, agentes antineoplásicos en casos de osteosarcoma, o factores de crecimiento en situaciones que requieran una regeneración tisular acelerada.

Una vez caracterizadas estas funciones adicionales, el siguiente paso consistiría en el desarrollo de estudios preclínicos en modelos animales. Estos ensayos permitirán evaluar no solo la capacidad osteoinductora y osteoconductora de los andamios en condiciones fisiológicas reales, sino también aspectos clave como la calidad del tejido óseo neoformado, la vascularización inducida, la integración con el hueso huésped y la respuesta inmunológica asociada.

6. CONCLUSIONS

In this study, third-generation vitroceramic scaffolds were developed within the SiO_2-CaO-P_2O_5 system using the polymer sponge replication technique, which allowed the creation of three-dimensional structures with an interconnected macroporosity of 85%. Using the sol-gel method, multiple coatings were applied to the scaffolds by immersion in the precursor solution of each layer. As a result of the combination of phases in the multilayer approach, multifunctional scaffolds were obtained that are physically and mechanically compatible with trabecular bone, biodegradable, bioactive, and biocompatible.

The sequential arrangement of the coatings, from the inner to the outer layers, contributed in different ways to the final properties of the scaffold:

- The CS coating served as a template and source of Ca^{2+}.
- The P6 coating modified with lithium oxide (Li_2O) improved the mechanical properties, resulting in a final compressive strength of 1.8 MPa.
- The TCP coating acted as an ionic reservoir for apatite deposition.
- • The CS coating was modified by adding sodium oxide (Na_2O), potassium oxide (K_2O) and different concentrations of magnesium oxide (MgO), providing bioactivity and modifications to the surface topography.

From a functional point of view, Mg^{2+}, due to its high charge density, generated the most significant results.

- An optimal range of $MgCO_3$ between 0.4 and 0.5 g (corresponding to scaffolds CS04 and CS05) was identified, which exhibited the best results from a bioactive and topographical point of view.
- The CS04 scaffold presented a biomimetic laminar microstructure, which remained intact until the seventh day of the bioactivity test, at which point it was concealed beneath a dense apatite precipitate.
- • The CS05-7D scaffold showed the formation of hollow apatite microspheres, associated with the Ostwald ripening phenomenon, with potential application for the storage and controlled release of drugs or biomolecules.

Furthermore, the mineralogical diversity induced by the combination of the multilayer strategy and ionic doping led to the release of ions which, together with the topographical characteristics of the scaffolds, played a fundamental role in in vitro biological behaviour, yielding the following results:

- The CS0, CS04, and CS05 scaffolds proved to be cytocompatible and showed adequate cell-scaffold interaction in all cell types evaluated..
- • The dissolution products were found to be cytocompatible in both the cumulative (cCCM) and non-cumulative (ncCCM) approaches, and promoted higher cell proliferation in all cell types evaluated compared to the control.
- The release of Si^{4+} and Li^{+}, two ions with osteogenic and angiogenic activity, was identified in both approaches. Additionally, the release of P^{3-} was detected in the cCCM and Ca^{2+} in the ncCCM.
- • Osteoinduction studies using the indirect method in human MSCs revealed that the cCCM of scaffolds CS0 and CS05 was capable of inducing greater ALP expression and increased mineralisation.
- In the direct method, CS04 and CS05 scaffolds demonstrated their osteogenic capacity by stimulating greater specific ALP activity in MC3T3-E1 preosteoblasts, as well as greater calcium deposit formation compared to the control.
- The CS04 and CS05 scaffolds significantly stimulated VEGF release in MC3T3-E1 preosteoblasts, with increases of up to 170% compared to the control, demonstrating their angiogenic capacity.

BIBLIOGRAFÍA

[1] Jane Osareme, Ogugua, Muridzo Muonde, Chinedu Paschal Maduka, Tolulope O Olorunsogo, & Olufunke Omotayo. (2024). Demographic shifts and healthcare: A review of aging populations and systemic challenges. *International Journal of Science and Research Archive*, *11*(1). https://doi.org/10.30574/ijsra.2024.11.1.0067

[2] Boudoulas, K. D., Triposkiadis, F., Stefanadis, C., & Boudoulas, H. (2017). The endlessness evolution of medicine, continuous increase in life expectancy and constant role of the physician. In *Hellenic Journal of Cardiology* (Vol. 58, Issue 5). https://doi.org/10.1016/j.hjc.2017.05.001

[3] World Health Organization. (2024, October 1). *Ageing and health*. https://www.who.int/news-room/fact-sheets/detail/ageing-and-health

[4] Boudoulas, K. D., Triposkiadis, F., Stefanadis, C., & Boudoulas, H. (2017). The endlessness evolution of medicine, continuous increase in life expectancy and constant role of the physician. In *Hellenic Journal of Cardiology* (Vol. 58, Issue 5). https://doi.org/10.1016/j.hjc.2017.05.001

[5] Mancinelli, L., & Intini, G. (2023). Age-associated declining of the regeneration potential of skeletal stem/progenitor cells. In *Frontiers in Physiology* (Vol. 14). https://doi.org/10.3389/fphys.2023.1087254

[6] Boskey, A. L., & Coleman, R. (2010). Aging and bone. *Journal of dental research*, *89*(12), 1333–1348. https://doi.org/10.1177/0022034510377791

[7] Le, B. Q., Nurcombe, V., Cool, S. M. K., van Blitterswijk, C. A., de Boer, J., & LaPointe, V. L. S. (2017). The Components of bone and what they can teach us about regeneration. In *Materials* (Vol. 11, Issue 1). https://doi.org/10.3390/ma11010014

[8] Clarke, B. (2008). Normal bone anatomy and physiology. In *Clinical journal of the American Society of Nephrology : CJASN: Vol. 3 Suppl 3*. https://doi.org/10.2215/CJN.04151206

[9] Florencio-Silva, R., Sasso, G. R. D. S., Sasso-Cerri, E., Simões, M. J., & Cerri, P. S. (2015). Biology of Bone Tissue: Structure, Function, and Factors That Influence Bone Cells. In *BioMed Research International* (Vol. 2015). https://doi.org/10.1155/2015/421746

[10] Weatherholt, A. M., Fuchs, R. K., & Warden, S. J. (2012). Specialized connective tissue: Bone, the structural framework of the upper extremity. *Journal of Hand Therapy*, *25*(2). https://doi.org/10.1016/j.jht.2011.08.003

[11] Buck, D. W., & Dumanian, G. A. (2012). Bone biology and physiology: Part I. the fundamentals. In *Plastic and Reconstructive Surgery* (Vol. 129, Issue 6). https://doi.org/10.1097/PRS.0b013e31824eca94

[12] Feng, X. (2009). Chemical and Biochemical Basis of Cell-Bone Matrix Interaction in Health and Disease. *Current Chemical Biology*, *3*(2). https://doi.org/10.2174/187231309788166398

[13] Kaur, G., Kumar, V., Baino, F., Mauro, J. C., Pickrell, G., Evans, I., & Bretcanu, O. (2019). Mechanical properties of bioactive glasses, ceramics, glass-ceramics and composites: State-of-the-art review and future challenges. In *Materials Science and Engineering C* (Vol. 104). https://doi.org/10.1016/j.msec.2019.109895

[14] Lin, X., Patil, S., Gao, Y. G., & Qian, A. (2020). The Bone Extracellular Matrix in Bone Formation and Regeneration. In *Frontiers in Pharmacology* (Vol. 11). https://doi.org/10.3389/fphar.2020.00757

[15] Zhou, X., Zhang, N., Mankoci, S., & Sahai, N. (2017). Silicates in orthopedics and bone tissue engineering materials. In *Journal of Biomedical Materials Research - Part A* (Vol. 105, Issue 7). https://doi.org/10.1002/jbm.a.36061

[16] Hou, X., Zhang, L., Zhou, Z., Luo, X., Wang, T., Zhao, X., Lu, B., Chen, F., & Zheng, L. (2022). Calcium Phosphate-Based Biomaterials for Bone Repair. In *Journal of Functional Biomaterials* (Vol. 13, Issue 4). https://doi.org/10.3390/jfb13040187

[17] Chen, J. H., Liu, C., You, L., & Simmons, C. A. (2010). Boning up on Wolff's Law: Mechanical regulation of the cells that make and maintain bone. *Journal of Biomechanics*, *43*(1). https://doi.org/10.1016/j.jbiomech.2009.09.016

[18] Kim, J. M., Lin, C., Stavre, Z., Greenblatt, M. B., & Shim, J. H. (2020). Osteoblast-Osteoclast Communication and Bone Homeostasis. In *Cells* (Vol. 9, Issue 9). https://doi.org/10.3390/cells9092073

[19] Rodrigues, J., Sarmento, B., & Pereira, C. L. (2022). Osteosarcoma tumor microenvironment: the key for the successful development of biologically relevant 3D *in vitro* models. *In Vitro Models*, *1*(1). https://doi.org/10.1007/s44164-022-00008-x

[20] Jiménez-Ortega, R. F., Ortega-Meléndez, A. I., Patiño, N., Rivera-Paredez, B., Hidalgo-Bravo, A., & Velázquez-Cruz, R. (2024). The Involvement of microRNAs in Bone Remodeling Signaling Pathways and Their Role in the Development of Osteoporosis. *Biology*, *13*(7), 505. https://doi.org/10.3390/biology13070505

[21] Chen, J. H., Liu, C., You, L., & Simmons, C. A. (2010). Boning up on Wolff's Law: Mechanical regulation of the cells that make and maintain bone. *Journal of Biomechanics*, *43*(1). https://doi.org/10.1016/j.jbiomech.2009.09.016

[22] Woo, S. L. Y., Kuei, S. C., Amiel, D., Gomez, M. A., Hayes, W. C., White, F. C., & Akeson, W. H. (1981). The effect of prolonged physical training on the properties of long bone: A study of Wolff's law. *Journal of Bone and Joint Surgery - Series A*, *63*(5). https://doi.org/10.2106/00004623-198163050-00013

[23] Chen, Q., & Thouas, G. A. (2015). Metallic implant biomaterials. In *Materials Science and Engineering R: Reports* (Vol. 87). https://doi.org/10.1016/j.mser.2014.10.001

[24] Ducher, G., Courteix, D., Même, S., Magni, C., Viala, J. F., & Benhamou, C. L. (2005). Bone geometry in response to long-term tennis playing and its relationship with muscle volume: A quantitative magnetic resonance imaging study in tennis players. *Bone*, *37*(4). https://doi.org/10.1016/j.bone.2005.05.014

[25] Valtanen, R. S., Yang, Y. P., Gurtner, G. C., Maloney, W. J., & Lowenberg, D. W. (2021). Synthetic and Bone tissue engineering graft substitutes: What is the future? *Injury*, *52*. https://doi.org/10.1016/j.injury.2020.07.040

[26] Liu, Z., He, X., Chen, S., & Yu, H. (2023). Advances in the use of calcium silicate-based materials in bone tissue engineering. *Ceramics International*, *49*(11). https://doi.org/10.1016/j.ceramint.2023.03.063

[27] Fernandez de Grado, G., Keller, L., Idoux-Gillet, Y., Wagner, Q., Musset, A. M., Benkirane-Jessel, N., Bornert, F., & Offner, D. (2018). Bone substitutes: a review of their characteristics, clinical use, and perspectives for large bone defects management. In *Journal of Tissue Engineering* (Vol. 9). https://doi.org/10.1177/2041731418776819

[28] Wang, W., & Yeung, K. W. K. (2017). Bone grafts and biomaterials substitutes for bone defect repair: A review. In *Bioactive Materials* (Vol. 2, Issue 4). https://doi.org/10.1016/j.bioactmat.2017.05.007

[29] Venkatraman, S. K., & Swamiappan, S. (2020). Review on calcium- and magnesium-based silicates for bone tissue engineering applications. In *Journal of Biomedical Materials Research - Part A* (Vol. 108, Issue 7). https://doi.org/10.1002/jbm.a.36925

[30] Lin, F. H., Lin, C. C., Lu, C. M., Liu, H. C., Sun, J. S., & Wang, C. Y. (1995). Mechanical properties and histological evaluation of sintered β-Ca2P2O7 with Na4P2O7 · 10H2O addition. *Biomaterials*, *16*(10). https://doi.org/10.1016/0142-9612(95)99642-Y

[31] Rupp, M., Klute, L., Baertl, S., Walter, N., Mannala, G. K., Frank, L., Pfeifer, C., Alt, V., & Kerschbaum, M. (2022). The clinical use of bone graft substitutes in orthopedic surgery in Germany—A 10-years survey from 2008 to 2018 of 1,090,167 surgical interventions. *Journal of Biomedical Materials Research - Part B Applied Biomaterials*, *110*(2). https://doi.org/10.1002/jbm.b.34911

[32] Bhat, S., & Kumar, A. (2013). Biomaterials and bioengineering tomorrow's healthcare. In *Biomatter* (Vol. 3, Issue 3). https://doi.org/10.4161/biom.24717

[33] Fernandez-Yague, M. A., Abbah, S. A., McNamara, L., Zeugolis, D. I., Pandit, A., & Biggs, M. J. (2015). Biomimetic approaches in bone tissue engineering: Integrating biological and physicomechanical strategies. In *Advanced Drug Delivery Reviews* (Vol. 84). https://doi.org/10.1016/j.addr.2014.09.005

[34] Vallet-Regí, M. (2022). Evolution of Biomaterials. *Frontiers in Materials*, *9*. https://doi.org/10.3389/fmats.2022.864016

[35] Fernández-Hernán, J. P., Torres, B., López, A. J., & Rams, J. (2022). The Role of the Sol-Gel Synthesis Process in the Biomedical Field and Its Use to Enhance the Performance of Bioabsorbable Magnesium Implants. In *Gels* (Vol. 8, Issue 7). https://doi.org/10.3390/gels8070426

[36] Hench, L. L., & Thompson, I. (2010). Twenty-first century challenges for biomaterials. In *Journal of the Royal Society Interface* (Vol. 7, Issue SUPPL. 4). https://doi.org/10.1098/rsif.2010.0151.focus

[37] Vallet-Regí, M., & Salinas, A. J. (2018). Ceramics as bone repair materials. In *Bone Repair Biomaterials: Regeneration and Clinical Applications, Second Edition*. https://doi.org/10.1016/B978-0-08-102451-5.00006-8

[38] Mercado-Pagán, Á. E., Stahl, A. M., Shanjani, Y., & Yang, Y. (2015). Vascularization in Bone Tissue Engineering Constructs. *Annals of Biomedical Engineering*, *43*(3). https://doi.org/10.1007/s10439-015-1253-3

[39] Tajvar, S., Hadjizadeh, A., & Samandari, S. S. (2023). Scaffold degradation in bone tissue engineering: An overview. In *International Biodeterioration and Biodegradation* (Vol. 180). https://doi.org/10.1016/j.ibiod.2023.105599

[40] Lee, S. S., Du, X., Kim, I., & Ferguson, S. J. (2022). Scaffolds for bone-tissue engineering. *Matter*, 5(9), 2722–2759. https://doi.org/10.1016/j.matt.2022.06.003

[41] Stachel, D., Paulus, H., Svoboda, I., & Fuess, H. (1992). Crystal structure of calcium ultraphosphate, Ca2P6O17. *Zeitschrift Fur Kristallographie - New Crystal Structures*, *202*(1–2). https://doi.org/10.1524/zkri.1992.202.1-2.117

[42] Salazar, K., Murciano, Á., Velásquez, P., & De Aza, P. N. (2025). Obtaining characterization and in vitro behavior of 3D multilayer ceramic scaffolds Ca2SiO4/Ca2P6O17/Ca2SiO4-XSr. *Boletin de La Sociedad Espanola de Ceramica y Vidrio*, *64*(1), 57–68. https://doi.org/10.1016/j.bsecv.2024.12.001

[43] Amini, A. R., Laurencin, C. T., & Nukavarapu, S. P. (2012). Bone tissue engineering: Recent advances and challenges. *Critical Reviews in Biomedical Engineering*, *40*(5). https://doi.org/10.1615/CritRevBiomedEng.v40.i5.10

[44] Sarigol-Calamak, E., & Hascicek, C. (2018). Tissue Scaffolds As a Local Drug Delivery System for Bone Regeneration. In *Advances in Experimental Medicine and Biology* (Vol. 1078). https://doi.org/10.1007/978-981-13-0950-2_25

[45] Latif, S., Ameen, U., Ijaz, I., Imran, M., & Khan, M. N. (2024). Biomaterials and chemistry. *ACS Symposium Series* (pp. 1–25). American Chemical Society.

[46] Fu, Q., Saiz, E., Rahaman, M. N., & Tomsia, A. P. (2011). Bioactive glass scaffolds for bone tissue engineering: State of the art and future perspectives. In *Materials Science and Engineering C* (Vol. 31, Issue 7). https://doi.org/10.1016/j.msec.2011.04.022

[47] Schnabelrauch, M. (2017). Chemical bulk properties of biomaterials. In *Biomaterials in Clinical Practice: Advances in Clinical Research and Medical Devices*. https://doi.org/10.1007/978-3-319-68025-5_15

[48] Denry, I., & Kuhn, L. T. (2016). Design and characterization of calcium phosphate ceramic scaffolds for bone tissue engineering. *Dental Materials*, *32*(1). https://doi.org/10.1016/j.dental.2015.09.008

[49] Perić Kačarević, Ž., Rider, P., Alkildani, S., Retnasingh, S., Pejakić, M., Schnettler, R., Gosau, M., Smeets, R., Jung, O., & Barbeck, M. (2020). An introduction to bone tissue engineering. *International Journal of Artificial Organs* (Vol. 43, Issue 2). https://doi.org/10.1177/0391398819876286

[50] Wähnert, D., Greiner, J., Brianza, S., Kaltschmidt, C., Vordemvenne, T., & Kaltschmidt, B. (2021). Strategies to improve bone healing: Innovative surgical implants meet nano-/micro-topography of bone scaffolds. In *Biomedicines* (Vol. 9, Issue 7). https://doi.org/10.3390/biomedicines9070746

[51] Chi, J., Wang, M., Chen, J., Hu, L., Chen, Z., Backman, L. J., & Zhang, W. (2022). Topographic Orientation of Scaffolds for Tissue Regeneration: Recent Advances in Biomaterial Design and Applications. In *Biomimetics* (Vol. 7, Issue 3). https://doi.org/10.3390/biomimetics7030131

[52] Miyoshi, H., & Adachi, T. (2014). Topography design concept of a tissue engineering scaffold for controlling cell function and fate through actin cytoskeletal modulation. In *Tissue Engineering - Part B: Reviews* (Vol. 20, Issue 6). https://doi.org/10.1089/ten.teb.2013.0728

[53] Ros-Tárraga, P., Mata, N. A., Murciano, Á., Velasquez, P., & de Aza, P. N. (2019). Multilayer ceramic materials: A method to link bioactivity and durability. *Ceramics International*, *45*(17). https://doi.org/10.1016/j.ceramint.2019.08.072

[54] Mata, N. A., Ros-Tárraga, P., Velasquez, P., Murciano, A., & de Aza, P. N. (2020). New iron-doped multilayer ceramic scaffold with noncontinuous bioactive behavior. *Ceramics International*, *46*(10). https://doi.org/10.1016/j.ceramint.2020.03.198

[55] Gao, C., Deng, Y., Feng, P., Mao, Z., Li, P., Yang, B., Deng, J., Cao, Y., Shuai, C., & Peng, S. (2014). Current progress in bioactive ceramic scaffolds for bone repair and regeneration. In *International Journal of Molecular Sciences* (Vol. 15, Issue 3). https://doi.org/10.3390/ijms15034714

[56] Blokhuis, T. J., & Arts, J. J. C. (2011). Bioactive and osteoinductive bone graft substitutes: Definitions, facts and myths. *Injury*, *42*(SUPPL. 2). https://doi.org/10.1016/j.injury.2011.06.010

[57] Suamte, L., Tirkey, A., Barman, J., & Jayasekhar Babu, P. (2023). Various manufacturing methods and ideal properties of scaffolds for tissue engineering applications. In *Smart Materials in Manufacturing* (Vol. 1). https://doi.org/10.1016/j.smmf.2022.100011

[58] Navas, D., Fuentes, S., Castro-Alvarez, A., & Chavez-Angel, E. (2021). Review on Sol-Gel Synthesis of Perovskite and Oxide Nanomaterials. In *Gels* (Vol. 7, Issue 4). https://doi.org/10.3390/gels7040275

[59] Fiume, E., Ciavattini, S., Verné, E., & Baino, F. (2021). Foam replica method in the manufacturing of bioactive glass scaffolds: Out-of-date technology or still underexploited potential? In *Materials* (Vol. 14, Issue 11). https://doi.org/10.3390/ma14112795

[60] Gao, C., Deng, Y., Feng, P., Mao, Z., Li, P., Yang, B., Deng, J., Cao, Y., Shuai, C., & Peng, S. (2014). Current progress in bioactive ceramic scaffolds for bone repair and regeneration. In *International Journal of Molecular Sciences* (Vol. 15, Issue 3). https://doi.org/10.3390/ijms15034714

[61] Schatkoski, V. M., Larissa do Amaral Montanheiro, T., Canuto de Menezes, B. R., Pereira, R. M., Rodrigues, K. F., Ribas, R. G., Morais da Silva, D., & Thim, G. P. (2021). Current advances concerning the most cited metal ions doped bioceramics and silicate-based bioactive glasses for bone tissue engineering. In *Ceramics International* (Vol. 47, Issue 3). https://doi.org/10.1016/j.ceramint.2020.09.213

[62] Mouriño, V., Cattalini, J. P., & Boccaccini, A. R. (2012). Metallic ions as therapeutic agents in tissue engineering scaffolds: An overview of their biological applications and strategies for new developments. In *Journal of the Royal Society Interface* (Vol. 9, Issue 68). https://doi.org/10.1098/rsif.2011.0611

[63] Wang, X., Huang, S., & Peng, Q. (2023). Metal Ion-Doped Hydroxyapatite-Based Materials for Bone Defect Restoration. In *Bioengineering* (Vol. 10, Issue 12). https://doi.org/10.3390/bioengineering10121367

[64] O'Neill, E., Awale, G., Daneshmandi, L., Umerah, O., & Lo, K. W. H. (2018). The roles of ions on bone regeneration. In *Drug Discovery Today* (Vol. 23, Issue 4). https://doi.org/10.1016/j.drudis.2018.01.049

[65] Ferracini, R., Martínez Herreros, I., Russo, A., Casalini, T., Rossi, F., & Perale, G. (2018). Scaffolds as structural tools for bone-targeted drug delivery. In *Pharmaceutics* (Vol. 10, Issue 3). https://doi.org/10.3390/pharmaceutics10030122

[66] Pattanashetti, N. A., Biscaia, S., Moura, C., Mitchell, G. R., & Kariduraganavar, M. Y. (2019). Development of novel 3D scaffolds using BioExtruder by the incorporation of silica into polycaprolactone matrix for bone tissue engineering. *Materials Today Communications*, *21*. https://doi.org/10.1016/j.mtcomm.2019.100651

[67] Novotna, L., Chlup, Z., Jaros, J., Castkova, K., Drdlik, D., Pospisil, J., Hampl, A., Koutna, I., & Cihlar, J. (2022). Macroporous bioceramic scaffolds based on tricalcium phosphates reinforced with silica: microstructural, mechanical, and biological evaluation. *Journal of Asian Ceramic Societies*, *10*(2). https://doi.org/10.1080/21870764.2022.2053278

[68] Vimalraj, S. (2020). Alkaline phosphatase: Structure, expression and its function in bone mineralization. In *Gene* (Vol. 754). https://doi.org/10.1016/j.gene.2020.144855

[69] O'Neill, W. C. (2006). Pyrophosphate, alkaline phosphatase, and vascular calcification. In *Circulation Research* (Vol. 99, Issue 2). https://doi.org/10.1161/01.RES.0000234909.24367.a9

[70] Pujari-Palmer, M., Pujari-Palmer, S., Lu, X., Lind, T., Melhus, H., Engstrand, T., Karlsson-Ott, M., & Engqvist, H. (2016). Pyrophosphate stimulates differentiation, matrix gene expression and alkaline phosphatase activity in osteoblasts. *PLoS ONE*, *11*(10). https://doi.org/10.1371/journal.pone.0163530

[71] Song, L. (2017). Calcium and Bone Metabolism Indices. In *Advances in Clinical Chemistry* (Vol. 82). https://doi.org/10.1016/bs.acc.2017.06.005

[72] Engstrand, T., Kihlström, L., Lundgren, K., Trobos, M., Engqvist, H., & Thomsen, P. (2015). Bioceramic implant induces bone healing of cranial defects. *Plastic and Reconstructive Surgery - Global Open*, *3*(8). https://doi.org/10.1097/GOX.0000000000000467

[73] Engstrand, T., Kihlström, L., Lundgren, K., Trobos, M., Engqvist, H., & Thomsen, P. (2015). Bioceramic implant induces bone healing of cranial defects. *Plastic and Reconstructive Surgery - Global Open*, *3*(8). https://doi.org/10.1097/GOX.0000000000000467

[74] Engstrand, T., Kihlström, L., Neovius, E., Skogh, A. C. D., Lundgren, T. K., Jacobsson, H., Bohlin, J., Åberg, J., & Engqvist, H. (2014). Development of a bioactive implant for repair and potential healing of cranial defects: Technical note. *Journal of Neurosurgery*, *120*(1). https://doi.org/10.3171/2013.6.jns1360

[75] Ni, S., Chang, J., & Chou, L. (2006). A novel bioactive porous CaSiO3 scaffold for bone tissue engineering. *Journal of Biomedical Materials Research - Part A*, *76*(1). https://doi.org/10.1002/jbm.a.30525

[76] Ni, S., Lin, K., Chang, J., & Chou, L. (2008). β-CaSiO3/β-Ca3(PO4)2 composite materials for hard tissue repair: In vitro studies. *Journal of Biomedical Materials Research - Part A*, *85*(1). https://doi.org/10.1002/jbm.a.31390

[77] Kizalaite, A., Klimavicius, V., Balevicius, V., Niaura, G., Salak, A. N., Yang, J. C., Cho, S. H., Goto, T., Sekino, T., & Zarkov, A. (2023). Dissolution-precipitation synthesis and thermal stability of magnesium whitlockite. *CrystEngComm*, *25*(30). https://doi.org/10.1039/d3ce00602f

[78] Gopal, R., Calvo, C., Ito, J., & Sabine, W. K. (1974). Crystal Structure of Synthetic Mg-Whitlockite, Ca 18 Mg 2 H 2 (PO 4) 14 . *Canadian Journal of Chemistry*, *52*(7). https://doi.org/10.1139/v74-181

[79] Bauer, L., Antunović, M., Rogina, A., Ivanković, M., & Ivanković, H. (2021). Bone-mimetic porous hydroxyapatite/whitlockite scaffolds: preparation, characterization and interactions with human mesenchymal stem cells. *Journal of Materials Science*, *56*(5). https://doi.org/10.1007/s10853-020-05489-3

[80] Zhao, C. Q., Xu, X. C., Lu, Y. J., Wu, S. Q., Xu, Z. Y., Huang, T. T., & Lin, J. X. (2020). Doping lithium element to enhance compressive strength of β-TCP scaffolds manufactured by 3D printing for bone tissue engineering. *Journal of Alloys and Compounds*, *814*. https://doi.org/10.1016/j.jallcom.2019.152327

[81] Vernon, R. B., Gooden, M. D., Lara, S. L., & Wight, T. N. (2005). Microgrooved fibrillar collagen membranes as scaffolds for cell support and alignment. *Biomaterials*, *26*(16). https://doi.org/10.1016/j.biomaterials.2004.08.011

[82] Szurkowska, K., & Kolmas, J. (2017). Hydroxyapatites enriched in silicon – Bioceramic materials for biomedical and pharmaceutical applications. In *Progress in Natural Science: Materials International* (Vol. 27, Issue 4). https://doi.org/10.1016/j.pnsc.2017.08.009

[83] Pupilli, F., Ruffini, A., Dapporto, M., Tavoni, M., Tampieri, A., & Sprio, S. (2022). Design Strategies and Biomimetic Approaches for Calcium Phosphate Scaffolds in Bone Tissue Regeneration. In *Biomimetics* (Vol. 7, Issue 3). https://doi.org/10.3390/biomimetics7030112

[84] Ressler, A., Žužić, A., Ivanišević, I., Kamboj, N., & Ivanković, H. (2021). Ionic substituted hydroxyapatite for bone regeneration applications: A review. *Open Ceramics*, *6*. https://doi.org/10.1016/j.oceram.2021.100122

[85] Radulescu, D. E., Vasile, O. R., Andronescu, E., & Ficai, A. (2023). Latest Research of Doped Hydroxyapatite for Bone Tissue Engineering. In *International Journal of Molecular Sciences* (Vol. 24, Issue 17). https://doi.org/10.3390/ijms241713157

[86] Myszka, B., Schüßler, M., Hurle, K., Demmert, B., Detsch, R., Boccaccini, A. R., & Wolf, S. E. (2019). Phase-specific bioactivity and altered Ostwald ripening pathways of calcium carbonate polymorphs in simulated body fluid. *RSC Advances*, *9*(32). https://doi.org/10.1039/c9ra01473j

[87] Wen-shou, W., Cheng-Yan, X., Li, Y., & Wen-Zhu, S. (2008). Controlled synthesis of calcium tungstate hollow microspheres via ostwald ripening and their photoluminescence property. *Journal of Physical Chemistry C*, *112*(49). https://doi.org/10.1021/jp8074783

[88] Lin, Z., Wu, J., Qiao, W., Zhao, Y., Wong, K. H. M., Chu, P. K., Bian, L., Wu, S., Zheng, Y., Cheung, K. M. C., Leung, F., & Yeung, K. W. K. (2018). Precisely controlled delivery of magnesium ions thru sponge-like monodisperse PLGA/nano-MgO-alginate core-shell microsphere device to enable in-situ bone regeneration. *Biomaterials*, *174*. https://doi.org/10.1016/j.biomaterials.2018.05.011

[89] Wei, P., Yuan, Z., Cai, Q., Mao, J., & Yang, X. (2018). Bioresorbable Microspheres with Surface-Loaded Nanosilver and Apatite as Dual-Functional Injectable Cell Carriers for Bone Regeneration. *Macromolecular Rapid Communications*, *39*(20). https://doi.org/10.1002/marc.201800062

[90] Chen, S., Shi, Y., Zhang, X., & Ma, J. (2019). Biomimetic synthesis of Mg-substituted hydroxyapatite nanocomposites and three-dimensional printing of composite scaffolds for bone regeneration. *Journal of Biomedical Materials Research - Part A*, *107*(11). https://doi.org/10.1002/jbm.a.36757

[91] Alanis-Gómez, R. P., Hernández-Rosas, F., Olivares-Hernández, J. D., Rivera-Muñoz, E. M., Zapatero-Gutiérrez, A., Méndez-Lozano, N., Alanis-Gómez, J. R., & Velázquez-Castillo, R. (2024). Magnesium-doped hydroxyapatite nanofibers for medicine applications: Characterization, antimicrobial activity, and cytotoxicity study. *International Journal of Molecular Sciences*, *25*(22). https://doi.org/10.3390/ijms252212418

[92] Kokubo, T., & Takadama, H. (2006). How useful is SBF in predicting in vivo bone bioactivity? *Biomaterials*, *27*(15). https://doi.org/10.1016/j.biomaterials.2006.01.017

[93] Mata, N. A., Velasquez, P., Murciano, A., & de Aza, P. N. (2021). Multilayer Mg-pyrophosphate glass ceramic with discontinuous bioactivity. Physicochemical characterization. *Ceramics International*, *47*(10). https://doi.org/10.1016/j.ceramint.2021.02.044

[94] Cruel, P. T. E., dos Santos, C. P. C., Cueto, T. M., Avila, L. P. V., Buchaim, D. V., & Buchaim, R. L. (2024). Calcium hydroxyapatite in its different forms in skin tissue repair: A literature review. *Surgeries*, *5*(3), 640–659. https://doi.org/10.3390/surgeries5030051

[95] Derakhshi, M., Naseri, M., Vafaeipour, Z., Malaekeh-Nikouei, B., Jafarian, A. H., & Ansari, L. (2023). Enhanced wound-healing efficacy of electrospun mesoporous hydroxyapatite nanoparticle-loaded chitosan nanofiber developed using pluronic F127. *International Journal of Biological Macromolecules*, *240*. https://doi.org/10.1016/j.ijbiomac.2023.124427

[96] Wang, W., Wei, J., Lei, D., Wang, S., Zhang, B., Shang, S., Bai, B., Zhao, C., Zhang, W., Zhou, C., Zhou, H., & Feng, S. (2023). 3D printing of lithium osteogenic bioactive composite scaffold for enhanced bone regeneration. *Composites Part B: Engineering*, *256*. https://doi.org/10.1016/j.compositesb.2023.110641

[97] Darjanki, C. M., Prahasanti, C., Fitria A, E., Kusumawardani, B., Wijaksana, I. K. E., & Aljunaid, M. (2023). RUNX2 and ALP expression in osteoblast cells exposed by PMMA-HAp combination: An in vitro study. *Journal of Oral Biology and Craniofacial Research*, *13*(2). https://doi.org/10.1016/j.jobcr.2023.02.007

[98] Chatterjee, K., Sun, L., Chow, L. C., Young, M. F., & Simon, C. G. (2011). Combinatorial screening of osteoblast response to 3D calcium phosphate/poly(ε-caprolactone) scaffolds using gradients and arrays. *Biomaterials*, *32*(5). https://doi.org/10.1016/j.biomaterials.2010.10.043

[99] Beck, G. R., Zerler, B., & Moran, E. (2000). Phosphate is a specific signal for induction of osteopontin gene expression. *Proceedings of the National Academy of Sciences of the United States of America*, *97*(15). https://doi.org/10.1073/pnas.140021997

[100] Sebastián, E., Murciano, A., Madrigal, R., de Aza, P. N., & Velasquez, P. (2021). 3D CaP porous scaffolds with grooved surface topography obtained by the sol-gel method. *Ceramics International*, *47*(15). https://doi.org/10.1016/j.ceramint.2021.04.158

[101] Abagnale, G., Steger, M., Nguyen, V. H., Hersch, N., Sechi, A., Joussen, S., Denecke, B., Merkel, R., Hoffmann, B., Dreser, A., Schnakenberg, U., Gillner, A., & Wagner, W. (2015). Surface topography enhances differentiation of mesenchymal stem cells towards osteogenic and adipogenic lineages. *Biomaterials*, *61*. https://doi.org/10.1016/j.biomaterials.2015.05.030

ANEXOS

Artículo 1

Journal of the American Ceramic Society

Editor's Choice

THE EDITOR-IN-CHIEF RECOMMENDS THIS OUTSTANDING ARTICLE

Surface morphology modulation in multilayer scaffolds via ion doping for bone tissue engineering

Paula M. Rincalido, Pablo Velásquez, Ángel Murciano, Piedad N. De Aza

John Mauro

Editor-in-Chief

Journal of the American Ceramic Society

Received: 16 April 2024 | Revised: 10 October 2024 | Accepted: 3 November 2024

DOI: 10.1111/jace.20269

Journal of the American Ceramic Society

RESEARCH ARTICLE

Surface morphology modulation in multilayer scaffolds via ion doping for bone tissue engineering

Paula M. Riosalido[1] | **Pablo Velásquez**[1] | **Ángel Murciano**[2] | **Piedad N. De Aza**[1]

[1]Institute of Bioengineering, Miguel Hernandez University, Elche, Spain

[2]Department of Materials, Optical and Electronic Technology, Miguel Hernandez University, Elche, Spain

Correspondence
Pablo Velásquez, Institute of Bioengineering, Miguel Hernandez University, Avda. Universidad s/n 03202, Elche, Spain.
Email: pavelasquez@umh.es

Editor's Choice
The Editor-in-Chief recommends this outstanding article.

Funding information
MCIN/AEI/10.13039/501100011033 Spain, Grant/Award Number: PID2020-116693RB-C21; Ministerio de Ciencia e Innovación

Abstract

This work proposes the use of multilayer scaffolds as a strategy for developing biomimetic structures for bone tissue regeneration. The scaffolds consist of a glass–ceramic core composed of $CaSiO_3/Ca_2P_6O_{17}$, which provides mechanical properties of 2.3 MPa and a total porosity of ~74%. To modify the surface morphology a double bioactive coating consisting of $Ca_3(PO_4)_2/CaSiO_3$ doped with Na^+ and K^+, along with varying amounts of Mg^{2+} (0–0.75 g $MgCO_3$) was carried out giving a total porosity of 89.8%. The resulting scaffolds were assessed for in vitro bioactivity according to ISO 23317. After immersion in SBF, the W-05 scaffolds displayed diverse surface morphologies: square HA structure (W-05-3D), hollow HA spheres (W-05-7D) and smooth HA layer (W-05-21D). Cell viability of 3T3 fibroblasts exposed to W-05 scaffolds in direct and indirect assays at concentrations of 15 and 30 mg/mL was assessed according to ISO 10993–5. Initially, cell proliferation decreased compared to controls, but differences became non-statistically significant after 72 h. Hollow spheres (W-05-7D) enhanced cell viability compared to other morphologies and plastic controls. Additionally, degradation products of W-05 stimulated cell division, underscoring scaffold biocompatibility.

KEYWORDS
bone tissue engineering, hydroxyapatite, multilayer scaffolds, sol-gel

1 | INTRODUCTION

The field of bone tissue engineering (BTE) has significant potential for treating bone injuries and skeletal disorders. Its goal is to achieve effective bone regeneration by combining bioactive scaffolds, osteoprogenitor cells, and growth factors.[1–4]

However, to successfully integrate and support bone regeneration, scaffolds must exhibit characteristics similar to the native bone structure.[5–7] These properties include surface roughness, interporosity with adequate pore size, biodegradability, suitable mechanical properties and biocompatibility.[4–9] Despite significant progress in this field, critical challenges still remain.

In this sense, ceramic materials are a well-established source of biomaterials for bioengineering applications, particularly in BTE.[3,10–12] They are a promising choice for the design of bone scaffolds due to their biocompatibility, similarity to bone tissue, osteoconductive properties and biodegradability.[9,10] Calcium phosphates (CaP) are

of particular interest as they closely resemble the inorganic component of the bone matrix, both structurally and chemically.[12–14] Within this group, there are two main phases: hydroxyapatite (HA) and β-tricalcium phosphate (β-TCP). These phases are known for their high biocompatibility and in vitro bioactivity.[4,15]

Another family of ceramic materials that has attracted the attention of researchers is calcium silicate minerals.[16,17,19,20] They exhibit excellent bioactivity due to apatite formation and cell proliferation stimulation, in addition to a suitable degradability rate for enabling hard tissue formation.[20–22] Among these materials, wollastonite ($CaSiO_3$) stands as an interesting biomaterial due to its biocompatibility, biodegradability, and in vitro bioactivity.[18,20,21] However, the practical application of $CaSiO_3$ is limited by its inherent brittleness, low mechanical strength, and high ionic dissolution.[18,20]

Another common approach to achieve hard tissue regeneration is the employment of bioactive glasses (BG). These materials typically consist of silicate-, phosphate- or borate- based compositions, often incorporating elements such as sodium and calcium.[23,24] BGs exhibit an excellent bone-bonding ability derived from their well-known bioactivity.[25,26] Furthermore, their biodegradability facilitates material dissolution, yielding products that promote biological regenerative mechanisms including both angiogenesis and osteogenesis.[26,27]

On the basis of the above, the objective of this research is to create scaffolds that imitate the complex function and structure of bone. In this sense, the development of multilayer scaffolds stands as an interesting approach. These scaffolds incorporate several layers of different composition, which remain integrated into a single structure.[28–30] In this manner, each coating can be tailored to offer specific functions and features, such as mechanical support, improved cell adhesion and differentiation, or controlled release of bioactive molecules such as drugs or growth factors. This versatility provides an intriguing opportunity to exploit and combine the properties of different phases typically used in BTE.

The layered structures were specifically designed to fulfil different functions. Wollastonite was chosen as the internal material and template for subsequent layers. A coating of the glassy P6 phase ($Ca_2P_6O_{17}$) was then applied to increase mechanical strength due to its cohesive activity and ability to fill preexisting cracks.[31] The amorphous phase was doped with lithium (Li^+) to improve its mechanical properties.[32] Together, wollastonite and P6 form the ceramic-glass core.

The third layer of the structure contained β-TCP, which functioned as a reservoir for two ions closely linked to bone metabolism: phosphorus (PO_4^{3-}) and calcium (Ca^{2+}).

Wollastonite was chosen as a surface coating to provide silanol groups.[21] To enhance the bioactivity of the system and modify the morphology of the precipitated HA, it was doped with varying amounts of ions related to bone physiology, including sodium (Na^+),[33] potassium (K^+),[34] and magnesium (Mg^{2+}).[35]

2 | MATERIALS AND METHODS

2.1 | Design and fabrication of multilayer scaffolds

The multilayer scaffolds were obtained by preparing distinct layers using the sol–gel technique. Table 1 summarizes the chemical composition for manufacturing each coating. The initial number indicates the layer sequence, with 1 representing the innermost and 4 the outermost layer, followed by the name of the respective phase. In the case of the fourth layer, the numerical values after W indicate the quantity of magnesium carbonate in grams used to dope the outer layer of wollastonite, being 05 and 075, 0.5 g and 0.75 g of magnesium carbonate respectively.

Sol–gel solutions were formulated using appropriate reactants. Tetraethyl orthosilicate (TEOS, Aldrich 98%); triethyl phosphate (TEP, Aldrich ≥ 99.8%); calcium carbonate ($CaCO_3$, Sigma ≥ 99%); lithium carbonate (Li_2CO_3, Sigma-Aldrich ≥ 99%); sodium carbonate (Na_2CO_3, Sigma ≥ 99%); potassium carbonate (K_2CO_3, Sigma ≥ 99%); magnesium carbonate ($MgCO_3$, Sigma Aldrich ≥ 99%); Ethanol (C_2H_5OH, Carlo Erba ≥ 96%) as solvent and finally hydrochloric acid (HCl 37%, Ensure) as a catalyst.

In all cases, the corresponding compounds were reacted, and the solution's final pH was adjusted to a value between 2 and 3. In order to obtain the first layer, polyurethane sponges with a porosity of 20 ppi (quality materials) were submerged in the sol–gel solution with the 1-W composition, shown in Table 1. After immersion, the samples were dried for 10 min at a temperature of 185°C. The treatment is repeated ten times in order to ensure a uniform coating of the polyurethane sponge. Subsequently, a heat treatment was conducted, comprising a heating ramp of 55 h to reach 1050°C, followed by an 8 h maintenance period before allowing the system to cool to room temperature. Once the initial layer (1-W) has been formed, the second layer (2-P6-Li) of composition shown in Table 1, is obtained using the same methodology described earlier. Lithium is incorporated in a small amount in the formulation to facilitate the melting of the glassy phase. This assembly of the two innermost layers (1-W/2-P6-Li) is referred to as the core scaffold.

The excess of both, lithium and glassy phase of core scaffolds, is eliminated by immersion in 50 mL of the solution

TABLE 1 Chemical composition of multilayer scaffold coatings.

Layer	Reactives									
	TEOS (mL)	TEP	H_2O	Ethanol	HCl	$CaCO_3$ (g)	Li_2CO_3	Na_2CO_3	K_2CO_3	$MgCO_3$
1-W	19.28	–	20	5	1	8.62	–	–	–	–
2-P6-Li	–	18.46	20	5	2	3.72	1	–	–	–
3-TCP	–	10.96	20	5	2	9.68	–	–	–	–
4-W-0	19.28	–	20	5	1	8.62	–	0.5	0.5	–
4-W-05	19.28	–	20	5	1	8.62	–	0.5	0.5	0.5
4-W-075	19.28	–	20	5	1	8.62	–	0.5	0.5	0.75

Abbreviations: TEOS, tetraethyl orthosilicate; TEP, triethyl phosphate.

called TRIS, prepared by diluting tris(hydroxymethyl)-aminomethane and $CaCl_2$ in a ratio of 6.5:1 in distilled water to a final volume of 900 mL. The pH was adjusted to between 7.3 and 7.4 using HCl.

The core scaffold, after undergoing chemical etching with TRIS, was coated in accordance with the aforementioned methodology, using the 3-TCP and 4-W (0–0.75) compositions delineated in Table 1. The outermost layers were obtained through a heating ramp of 9 h to reach 1050°C, followed by 8 hours of maintenance before returning to room temperature.

2.2 | Materials physicochemical characterization

The cylindrical multilayer scaffolds underwent physicochemical characterization. They measured approximately 11.5 mm in diameter and 9.2 mm in height and weighed 0.45 ± 0.09 g.

2.2.1 | Mineralogical characterization: X-ray diffraction

X-ray diffraction patterns were acquired using an automated Bruker-AXS D8 Advance diffractometer employing CuKα radiation (1.54059 Å) to establish the mineralogical composition of the multilayer scaffold. Data collection was carried out following the vertical geometrical Bragg–Brentano ($\theta/2\theta$) configuration in plane reflection mode between 5° and 55° (2θ). The measurement steps were carried out in increments of 0.05°, with a duration of 5 s, while the X-ray tube was operated at 40 kV and 30 mA. The resulting diffractograms were compared to those in the Crystallography Open Database (COD) using Power Diffraction Match! version 3.16 Build 288 software.

2.2.2 | Physical evaluation

FESEM-EDX microstructure analysis

The microstructure's morphology and composition were analyzed using a field emission scanning electron microscope (FESEM, ZEISS SIGMA 300 VP) coupled with energy dispersive X-ray spectroscopy (EDX, ZEISS Smart-EDX). All samples were palladium coated prior to analysis.

Mechanical compressive strength test

To test the scaffold's compressive strength, scaffolds were subjected to a compression test using a simple manual test stand (SVL-1000 N, IMADA).

Porosity study

An exhaustive analysis of pore distribution and porosity (< 300 μm) was undertaken through the mercury porosimetry technique. A Poromaster 60 GT device manufactured by Quantachrome Instruments was used for this purpose, operating within a pressure range of 0.927–35248.6 psi. Porosity associated with pore sizes exceeding 300 μm was determined using a pycnometer filled with water, followed by the application of Archimedes' principle.

2.3 | In vitro bioactivity evaluation

In vitro bioactivity assays were conducted according to ISO/FDIS 23317 standard guidelines.[36] The scaffolds were immersed in 50 mL of simulated body fluid (SBF) and kept at 37 ± 0.5°C in a water bath with agitation for 1, 3, 7, 14, and 21 days. After drying the samples, FESEM-EDX was used to search and identify precipitates on the scaffold surfaces.

The SBF was analyzed using inductively coupled plasma optical emission spectrometry (ICP-OES, Perkin-Elmer Optima 2000™) to monitor changes in elemental concentrations.

2.4 | In vitro biological evaluation

The response of the W-05 scaffold to cells in vitro was evaluated according to ISO 10993–5 standards.[37] The study examined the direct effect of the W-05 scaffold on 3T3 murine embryonic fibroblasts before and after SBF exposure, as well as the indirect impact on cells mediated by its dissolution products (DP).

The 3T3 fibroblast cells were cultured in Petri dishes Dulbecco's modified Eagle medium (DMEM—Gibco) supplemented with 10% fetal bovine serum (FBS—Corning) and 1% penicillin/streptomycin (PS—Gibco) and incubated at 37°C in a humidified atmosphere with 5% CO_2. The cell culture medium was refreshed every 48 hours and subcultured when 80% confluence was reached.

2.4.1 | Direct cell culture

The study analyzed the cytotoxicity of the W-05 scaffold and the impact of its surface morphology on cells. Cell proliferation was compared across different scaffold topographies, including the scaffold without SBF (W-05-0D), the square morphology after 3 days of SBF exposure (W-05-3D), the hollow spheres on day 7 (W-05-7D), and the regular surface on day 21 (W-05-21D). The control group consisted of cells seeded on plastic. Before starting the assays, the scaffolds were sterilized by exposing each side of the structure to UV light for 4 h.

Then, the scaffolds underwent a pretreatment procedure to achieve surface wetting, allowing for protein adsorption and subsequent cell adhesion. The procedure involved completely covering the scaffold surface with culture medium supplemented with 10% FBS and incubating for 30 min at 37°C under a 5% CO_2 atmosphere. 24-well plates were used in this case due to the dimensions of the scaffold. After the incubation period, the culture medium was removed, and the cell seeding process began. Exactly 50,000 cells were seeded onto each scaffold in a 25 μm droplet, positioned at the central region of the scaffold surface to minimize cell adhesion to the plastic substrate of the well plate. The cells adhered for 30 min at 37°C with 5% CO_2. Culture medium was added to each well, ensuring complete coverage of the scaffold. The samples were incubated with cells for 24, 48, and 72 h.

Cell viability was assessed using the colorimetric viability 3-[4,5-dimethyl-2-thiazolyl]-2,5 diphenyltetrazolium bromide or MTT assay from Sigma-Aldrich.

The Microplate Reader RT-2100C (Neuvar Inc.) was used to obtain absorbance readings at 570 nm, following the manufacturer's instructions.

After each assay interval, the culture medium was removed. The scaffolds were then transferred to a new 24-well plate to exclude cells attached to the bottom of the well and not to the scaffold. As the scaffolds could not fit in the plate reader, 200 μL from each well were transferred to a 96-well plate, and the absorbance was measured at 570 nm.

2.4.2 | Indirect cell culture

To investigate the impact of ions released by the W-05 scaffold on cells, samples were incubated in DMEM supplemented with 10% FBS and 1% PS. After sterilization, the scaffolds were weighed, and two dilutions were made, always ensuring complete coverage of the sample. For the first dilution, 1 mL of culture medium was added for every 15 g of scaffold, while for the second dilution, 1 mL was added for every 30 g. Samples were incubated for 1, 3, and 7 days.

To study the effect of DP on cells, 96-well plates were seeded with a density of 15,000 cells/cm^2, 24 hours before the experiment to allow cell adherence. The culture medium was then replaced with conditioned medium, except for the control wells where fresh, unconditioned culture medium was added. The cells were incubated for 24, 48, and 72 h and MTT assay was performed.

2.5 | Statistical analysis

At each designated time point of the study, between-group comparisons were conducted using one-way analysis of variance (one-way ANOVA), followed by multiple comparisons using Tukey's test. Differences among groups were assessed for statistical significance using a predetermined alpha threshold of 0.05 and a 95% confidence level. Data are presented as mean ± SD. All statistical analyses were performed using GraphPad 8.0 software.

3 | RESULTS

3.1 | Physicochemical characterization of the core

The scaffolds were obtained through the creation of a glass-ceramic core, followed by the application of a double bioactive coating.

The experimental diffractograms of the W-P6-Li core before and after TRIS chemical etching are displayed in Figure 1A. The core scaffolds (W-P6-Li) were composed of cristobalite-SiO_2 (COD 96-900-8225) and calcium diphosphate-$Ca_2P_2O_7$ (COD 96-100-1557) as major

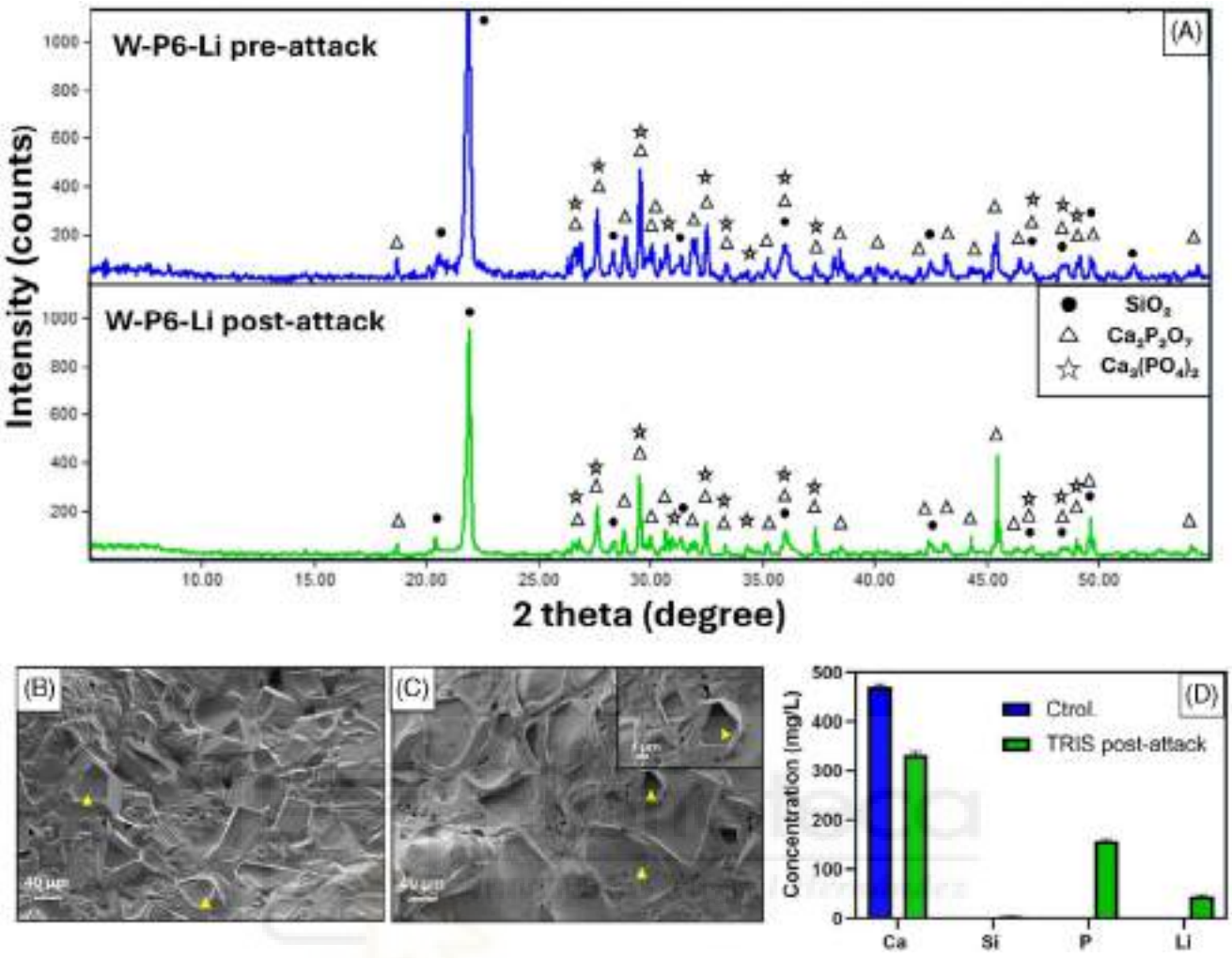

FIGURE 1 The effect of TRIS etching on the W-P6-Li core was characterized by X-ray diffraction (XRD) (A), field emission scanning electron microscope (FESEM)–energy dispersive X-ray spectroscopy (EDX) before (B), and after (C) treatment and inductively coupled plasma optical emission spectrometry (ICP-OES) (D).

crystalline phases, as well as a residual amount of β-TCP-$Ca_3(PO_4)_2$ (COD 96-151-7239) before TRIS exposure. These phases were also found in W-P6-Li attacked scaffolds. However, TRIS-etching resulted in a slight decrease in background at low 2θ angles.

To confirm the presence of the glassy phase visually, the sample underwent FESEM-EDX scanning (Figure 1B,C). Upon comparing the core's microstructure before and after the attack, it is evident that the core initially displayed large crystals that were covered by an amorphous phase (Figure 1B). However, after the TRIS treatment, the surface glassy phase decreased significantly (Figure 1C). Elemental analysis showed that this vitreous phase consisted mainly of Si and P with a low Ca content (Table S1 and Figure S1). Although the proportion of P and Si varied considerably, the Ca/P + Si ratio remained within the range of 0.015–0.018. However, large crystals were deficient in Si and showed a decreasing Ca/P ratio from the center (1.43–1.55) to the crystal boundary (0.93–1.14). On closer examination of the crystals, a small central grain (▲) composed of Si and poor in Ca can be seen. Additionally, precipitation of Ca-rich grains was observed following chemical etching.

The chemical treatment resulted in an increase in the concentration of P, Li, and Si in the TRIS solution, presumably from the core scaffolds. However, a decrease in Ca concentration was observed (Figure 1D).

3.2 | Physicochemical characterization of the scaffolds

As for the mineralogical characterization, the experimental XRD spectra (Figure 2) confirmed the presence of some of the formulated phases: wollastonite (◇) (COD 96-900-5779) and β-TCP (☆) (COD 96-151-7239). However, the new

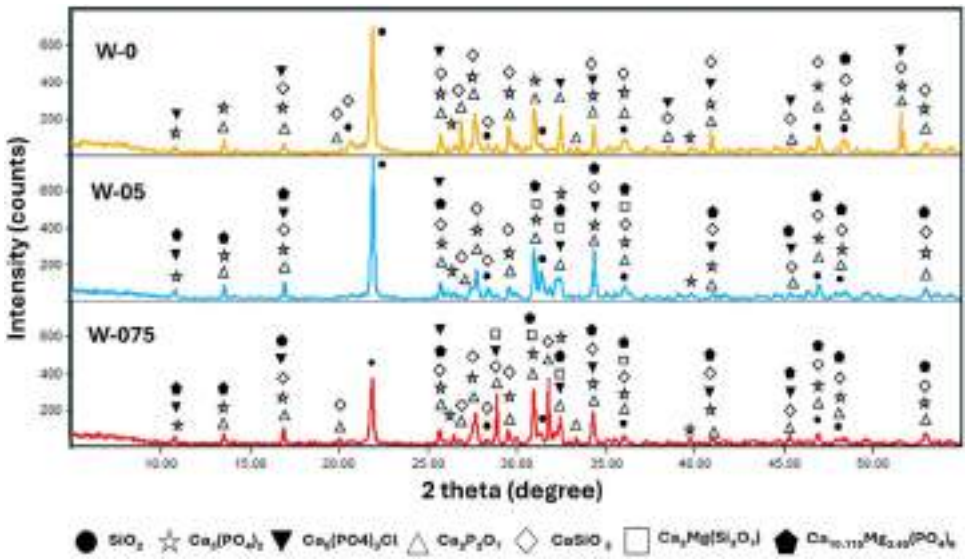

FIGURE 2 X-ray diffraction (XRD) spectra of overall scaffolds W-0, W-05, and W-075.

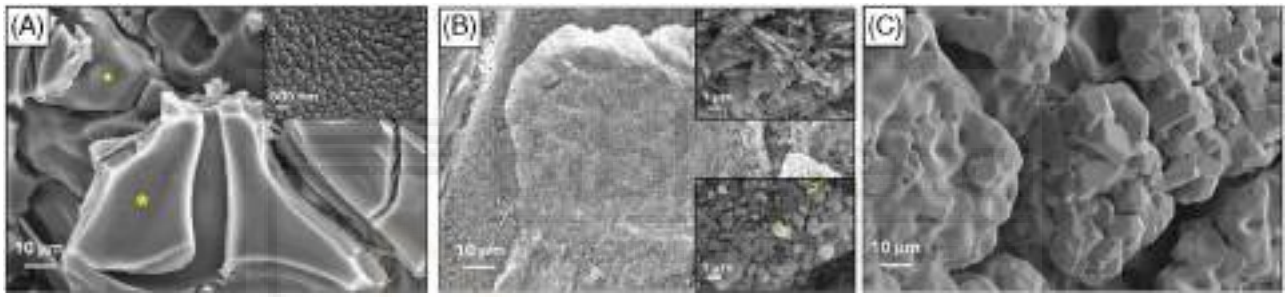

FIGURE 3 Field emission scanning electron microscope (FESEM) micrographs of the microstructure of scaffolds W-0 (A), W-05 (B), and W-075 (C).

crystalline phases were detected in the three scaffolds, including chlorapatites-$Ca_5(PO_4)_3Cl$ (▼) (COD 96-210-5266), as well as cristobalite (●) (COD 96-900-8225) and calcium diphosphate (△) (COD 96-100-1557), which were previously found in the core (Figure 1A). In addition, Mg-rich compounds were identified in W-05 and W-075 scaffolds. These phases were whitlockite-$Ca_{10.115}Mg_{3.85}(PO_4)_6$ (⬟) (COD 96-901-2137), a non-stoichiometric, Mg-rich phase derived from β-TCP, and akermanite-$Ca_2MgSi_2O_7$ (□), (COD 96-900-6942).

Figure 3 displays the microstructure analysis of the scaffolds W-0, W-05 and W-075 using FESEM-EDX. Sample W-0 (Figure 3A) outlines the deposition of two distinguishable layers: 3-TCP (•) and 4-W-0 (*). Although the surface of 4-W-0 appears smooth, enlarged images reveal rounded structures composed mainly of Ca and Si in a ratio of 0.55 to 0.75, as indicated by the EDX spectra (Table S2 and Figure S2). However, the surface of the W-05 scaffold exhibited various regular structures (Figure 3B). The elemental composition analysis revealed that grains XI and XII (see figure), were rich in calcium, silicon, and phosphorus. The Ca/P ratios were 2.63 and 4.48, the Ca/Si ratios were 3.47 and 2.36, and the Ca/P + Si ratios were 1.49 and 1.54, respectively. However, the elongated structures contained only Ca and Si in a ratio of 2.06–2.13. Regarding W-075 scaffold, the surface was homogeneously covered by polygonal CaP crystals. The Ca/P ratio ranged from 1.44 to 1.47 in the central zone and 1.35–1.37 at the edge.

With regard to the analysis of porosity, Figure 4A illustrates a representative scaffold of all the samples employed for the mercury porosimetry tests, which exhibits interconnected open porosity. The analysis of the W-P6-Li, W-0 and W-05 samples revealed similar pores characteristics, with two distinct regions (Figure 4B). The W-0 scaffolds mainly exhibited interparticle porosity, with an approximate pore diameter of 230–1.3 μm, and to a lesser extent intra-particle pores between 0.45 and 0.01 μm. Similarly, the porosity of the W-05 samples was mainly interparticle, with pore

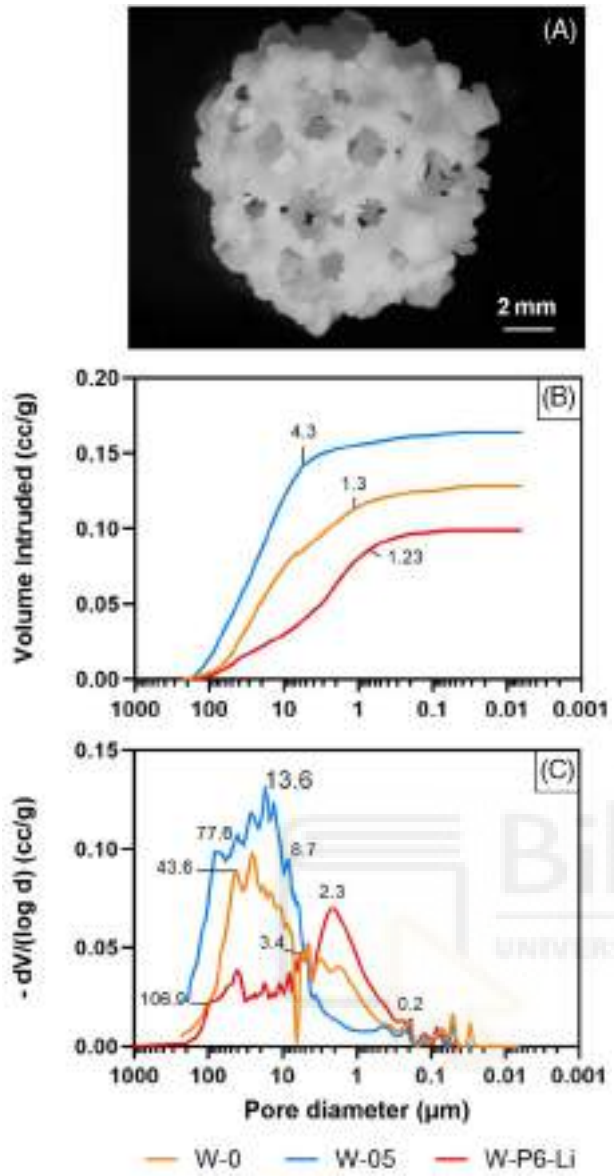

FIGURE 4 Representative optical image of the scaffolds (A) and curves derived from the mercury porosimetry technique: (B) cumulative, and (C) differential intrusion volume versus pore diameter.

diameters ranging from 190 to 4.3 μm. Intraparticle pores varied between 0.79 and 0.05 μm. Although the interparticle pore sizes of the core, W-P6-Li, were similar to those of samples W-0 and W-05 (199–1.23 μm), the abundance was notably lower. This is reflected by a decrease in the volume of intruded mercury. Figure 4B shows that the W-0 and W-05 scaffolds have the majority of pores in the range of 150 to 7 μm. However, the core exhibits a wider and more homogeneous range, with the main peak at 2.3 μm, shifted to the right compared to that of the W-0 and W-05 scaffolds. Additionally, all three samples exhibit pores below 100 nm.

Table 2 summarizes the physical properties of the scaffolds, including the compression test results which provided additional insights into the porosity results due to their inverse relationship.

Scaffold W-075 exhibited physical properties similar to those of scaffold W-05, indicating that the additional 0.25 g $MgCO_3$ did not have a significant impact.

3.3 | In vitro bioactivity evaluation

Regarding the bioactivity assays, the FESEM–EDX scanning revealed significant changes in surface morphology of the samples (Figure 5). Scaffold W-0, initially showed a Ca-Si precipitate resembling tangles with a ratio of 0.56–0.61 (Table S3 and Figure S3). A residual amount of P was also present, resulting in a Ca/P + Si ratio of about 0.5. After 3 days, the precipitate adopted an elongated morphology with a higher P content than the previous precipitate, resulting in a Ca/P ratio of 4.65–4.74, Ca/Si of 1.24–1.5 and Ca/P + Si of 0.98. However, after 1 week, the precipitate assumed a morphology very similar to that of HA and was composed mainly of Ca and P, with a Ca/P of 1.64–1.68, Ca/Si of 1.31–1.53 and Ca/P + Si of 24.08–25.7. After 2 weeks, the surface still showed apatite-type precipitates, although in some areas they had begun to dissolve. Elemental analysis showed that the precipitate was rich in silicon, calcium and phosphorus. The Ca/P ratios were 2.35–2.47, Ca/Si 8.17–9.4 and Ca/P + Si 1.76–1.81. On Day 21, polygonal grains of calcium and phosphorus were identified with a Ca/P ratio of 1.43–1.57 in the central region and 1.03–1.21 at the edge. There was also a rounded calcium–silicon phase with a Ca/Si ratio of 0.47–0.7.

Scaffold W-05 displayed a precipitate from the first day of immersion in SBF, which gradually accumulated as the immersion time increased. The precipitate underwent significant morphological changes, initially forming tangles, adopting a square shape after 3 days, and evolving into spheres on the seventh day. These spheres, consisting of thin needles, persisted until day 14 before coalescing and disappearing on day 21. EDX analyses showed Ca/P ratios of 1.32–1.35 on Day 1, 1.6–1.75 on Day 3, 1.54–1.6 on Day 7, 1.6–1.69 and 1.53–1.6 on Day 21. It should be noted that although the precipitates did not contain significant amounts of Si on Days 1, 7, 14 and 21, a high Si content was detected on Day 3. This resulted in a Ca/Si ratio of 2–2.5 and a Ca/P + Si ratio of 0.88–1.03.

With regards to W-075 scaffold, small spherical precipitates appeared after one day of immersion in SBF. The elemental analysis revealed high levels of Ca, Si, and P, with the following ratios: Ca/Si of 1.22–1.73, Ca/P of 1.46–1.53, and a Ca/P + Si ratio of 0.53–0.81. After 3 days, the spherical precipitates were evenly distributed across the surface, with an almost unchanged Ca/P ratio of 1.51–1.53, as well as a Ca/Si of 3.19–3.81 and Ca/P + Si of 1.03–1.1.

TABLE 2 Porosity and compressive strength of the core (W-P6-Li) and the overall W-0 and W-05 scaffolds.

Sample	Intraparticle Porosity* (%)	Interparticle Porosity*	Porosity (< 300 μm)*	Porosity (> 300 μm)**	Compressive Strength*** (MPa)
W-P6-Li	11.38	9.38	20.8 ± 0.1	74.5 ± 0.1	2.3 ± 0.5
W-0	7.47	18.11	25.6 ± 0.1	87.6 ± 0.1	1.9 ± 0.3
W-05	3.24	27.13	30.4 ± 0.1	89.8 ± 0.1	1.8 ± 0.6

*Hg Porosimetry Technique.
**Picnometry.
***Simple Manual Test Stand.

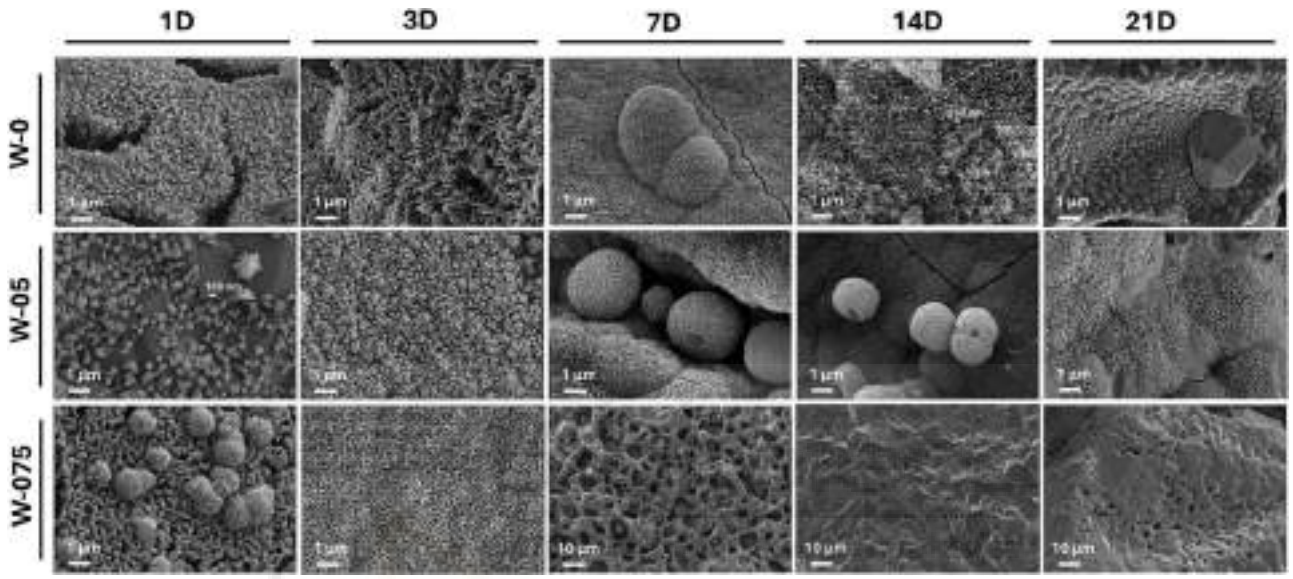

FIGURE 5 Scanning electron microscope (SEM) micrographs of W-0, W-05 and W-075 scaffolds after 1, 3, 7, 14 and 21 days of immersion in simulated body fluid (SBF).

However, the precipitate disappeared completely after 7 days, revealing a ring-shaped microstructure based on calcium and phosphorus in a ratio of 1.43–1.5. After 14 days in SBF, no precipitates were observed, only calcium phosphate crystals, with a Ca/P ratio of 1.29–1.33 in the central part and of 1.01–1.19 in the peripheral part. Finally, after 21 days of immersion, calcium phosphate crystals were again identified, but in this case with a higher calcium content, resulting in a Ca/P ratio of 1.62–1.86.

The variation of Si, Ca, P, Li and Mg was monitored by ICP-OES throughout the 21-day test to complement the bioactivity studies. Figure 6 displays the curves obtained for each scaffold. The results indicate that when the sample is bioactive and has a CaP precipitate, there is a decrease in the concentration of P in the SBF. Conversely, when the sample loses bioactivity, the P concentration in the SBF increases.

While samples W-0 and W-05 show almost no changes in lithium concentration, a noticeable oscillating behaviour of Li is observed in the W-075 scaffold. Specifically, the concentration in SBF increases from Days 7 to 14 before falling again on Day 21.

3.4 | In vitro biological evaluation

The W-05 scaffold was chosen for in vitro cellular assays as the primary aim of this research is to modulate the surface morphology of scaffolds to enhance their biological properties. According to the in vitro bioactivity results, this scaffold displayed hollow HA-like spheres, making it a potential controlled release agent.

The study investigated the impact of W-05 scaffold surface morphology on cell proliferation before (Figure 3B) and after SBF exposure (Figure 5-3D, 7D, 21D), in addition to assessing cytotoxicity.

Regarding the direct assay (Figure 7A), a decrease in cell viability was observed in all scaffold types after 24 h of treatment when compared to the control group. This difference was particularly noticeable in W-05-3D

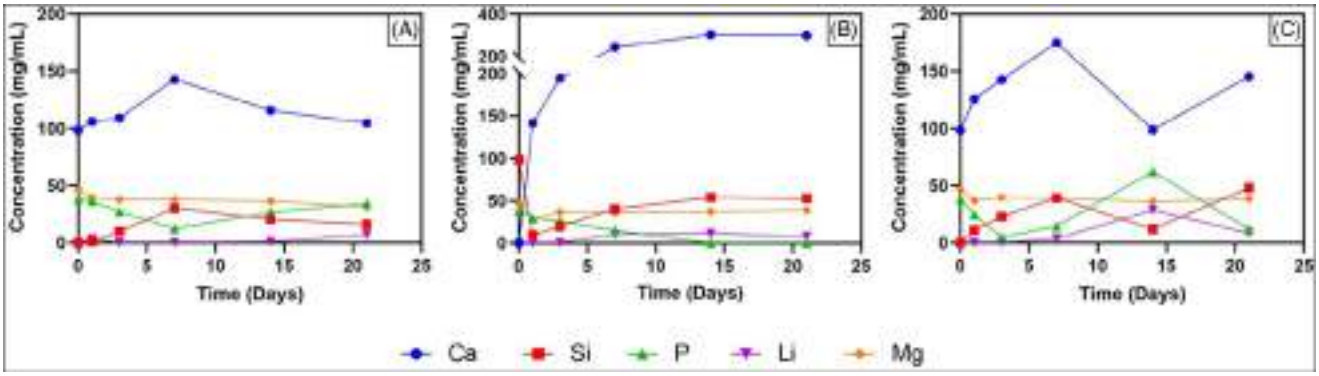

FIGURE 6 Changes in the concentration of Ca, Si, P, Li and Mg in simulated body fluid (SBF) as the immersion time of scaffolds W-0 (A), W-05 (B), and W-075 (C) in SBF increases.

and W-05-21D, although it was also observed in W-05-0D and W-05-7D. After 48 h, the differences were no longer statistically significant for the W-05-7D scaffold, while they persisted for W-05-0D, W-05-3D, and W-05-21D. Furthermore, W-05-7D exhibited increased cell proliferation compared to W-05-0D and W-05-21D. After 72 h of incubation, W-05-7D showed an increase in cell viability compared to W-05-21D. It is important to note that both control and scaffold-exposed wells showed a general growth trend over time.

Figure 7B,C shows the viability of cells incubated with the different DPs. The MTT assay results for the 15 mg/mL concentration (Figure 1B) showed a significant increase in cell proliferation in cells incubated with conditioned medium compared to the control, particularly for DP-3D and DP-7D, although to a lesser extent also for DP-1D. These differences persisted throughout the study. Similarly, DP at 30 mg/mL (Figure 7C) induced higher cell viability compared to cells incubated in plastic, again particularly for DP-3D and DP-7D.

4 | DISCUSSION

In this study, three types of multilayer 3D porous ceramic scaffolds with different surface morphologies were fabricated using the sol–gel method. It is challenging to find a single material that can mimic all the characteristics of the bone extracellular matrix.[38] Recognizing the versatility of the sol–gel method, which offers the possibility of depositing coatings on other materials,[39] multilayer scaffolds have been developed in this research. This has enabled the creation of novel and more biomimetic structures for potential clinical applications.

Four different coatings, each with a specific function, were applied to a polyurethane sponge template using the polymer sponge replication technique. The first step was to synthesize the ceramic–glass core W-P6-Li, followed by chemical etching with TRIS solution, to remove the excess glassy phase.

On the basis of XRD results, it was found that the W-P6-Li core is primarily composed of silicon dioxide and calcium pyrophosphate crystalline phases, with a residual amount of β-TCP (Figure 1A). These phases were likely formed through ionic migration during the sintering treatment from the innermost layer of wollastonite to the following layer, P6-Li.

This migration is attributed to $Ca_2P_6O_{17}$, a calcium ultraphosphate comprising layers of rings of six phosphorus atoms bonded through oxygen atoms. The negative charge from the phosphorus atoms is balanced by two calcium atoms.[40] The structure is characterized by high energy, which it is able to reduce by capturing calcium and breaking the rings. The phase obtained by this process is $Ca_2P_2O_7$. In the presence of an adequate calcium concentration, calcium pyrophosphate can be formed. In this instance, the 1-W wollastonite serves as a source of calcium, facilitating the transformation of ultraphosphate to pyrophosphate. Consequently, the wollastonite undergoes a transformation, adopting the form of SiO_2 (Figure 1A,B), a calcium-free phase. FESEM–EDX analysis of the core (Table S1) corroborated these data. Crystals found in the core, had a Ca/P ratio of about 1.5 within the central region, consistent with β-TCP. Additionally, the Ca/P ratio decreased to approximately 1 at the edge, which coincides with the Ca/P of calcium pyrophosphate. Upon closer inspection of the crystals, a small central grain (▲) that is rich in Si and poor in Ca is visible, indicating the presence of SiO_2. Based on these data, it can be inferred that the SiO_2 grain was most likely wollastonite. However, after releasing Ca^{2+} ions to the surrounding glassy phase, it remains as SiO_2. Consequently, the nearby zones will receive a greater calcium contribution, promoting the formation of β-TCP. Meanwhile, the distant regions, such as grain boundaries, will be forced to form another stable phase with a lower calcium content, namely calcium pyrophosphate.

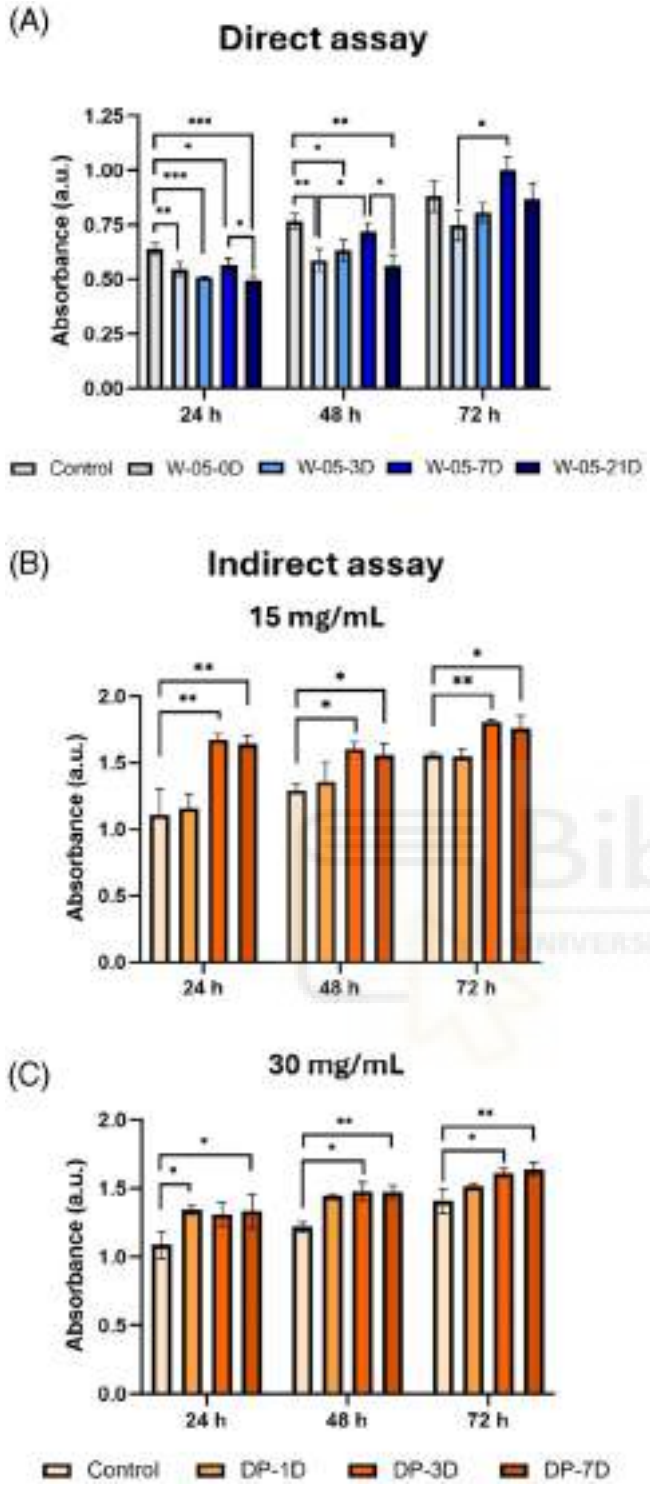

FIGURE 7 Cell viability study of 3T3 cells directly exposed to the different surface morphologies displayed by the W-05 scaffold (A) or to its dissolution products, at a concentration of 15 mg/mL (B) or 30 mg/mL (C). Data were shown as means ± SD. N = 3, * $p < 0.05$, ** $p < 0.01$, *** = $p < 0.001$.

All these crystals are surrounded by a glassy phase which, in addition to matching the elemental composition of 2-P6-Li, was rich in Si. This is probably a consequence of the wollastonite transformation in which some of the Si migrates into the glassy phase and changes its composition. Although the glassy phases do not produce characteristic peaks to identify them, the low 2θ region in the XRD pattern is sensitive to amorphous phases and can manifest itself as increased background, as observed in Figure 1A.

The core was then subjected to a chemical attack with TRIS to remove the excess vitreous phase. The attack was characterized by ICP-OES (Figure 1D), which indicated the liberation of P, Li, and Si. This suggests the hydrolysis of P6-Li. XRD validated this elimination by showing a reduction in background in the amorphous region (Figure 1A). This was also visually verified by FESEM–EDX (Figure 1C). Although there is evidence of calcium migration into the sample, the amount is negligible and does not affect the mineralogical composition.

W-0, W-05 and W-075 scaffolds shared most of the phases (Figure 2). Among them, SiO_2 and $Ca_2P_2O_7$ were formed through ion migration, while the $Ca_5(PO_4)_3Cl$ crystals likely originated from the HCl catalyst used during synthesis. Furthermore, the phases $Ca_3(PO_4)_2$ and $CaSiO_3$ were also detected. The W-05 and W-075 samples contained two extra phases: akermanite ($Ca_2MgSi_2O_7$), a bioceramic with excellent bioactivity and degradation rates that is known for its osteoinductive properties,[41,42] and whitlockite, a non-stoichiometric phase derived from β-TCP that is rich in magnesium ($Ca_{10.115}Mg_{0.385}(PO_4)_6$). This is an interesting finding considering that whitlockite consolidates as the second most abundant inorganic phase in bone, after HA.[43,44] It stands out for its biocompatibility and superior osteogenic properties compared to β-TCP and HA.[44,45] For this reason, it has been the subject of much research in recent years.[44–46]

FESEM–EDX scanning of the scaffolds revealed that even small variations in the amount of dopant Mg in the wollastonite coating produced significant microstructural changes (Figure 3). The presence of surface calcium phosphates was found to be directly correlated with the amount of Mg used as a dopant, showing a proportional relationship. A plausible explanation is that Mg serves to compensate for the calcium deficit resulting from ionic interlayer migration. This phenomenon could also explain the presence of whitlockite, in the XRD spectra of samples W-05 and W-075 (Figure 2). β-TCP could compensate for its loss of Ca^{2+} by sequestering Ca^{2+} or Mg^{2+} from the surface wollastonite, resulting in the formation of whitlockite.

Mechanical compatibility between implants and bone is an important consideration. Trabecular bone strength varies with age and anatomical region, with compressive

strength previously measured between 1.5 and 9.3 MPa.[47] The compressive strength of the scaffolds was approximately 1.79–1.93 MPa, as shown in Table 2.

Although these scaffolds demonstrate mechanical properties similar to those of trabecular bone, their clinical application only becomes meaningful when combined with sufficient porosity to allow cellular infiltration, product exchange, and vascular growth.[48] The results (Figure 4B,C) reveal pore diameters ranging from approximately 150 to 0.06 μm, this range of pore diameters is divided into inter- and intraporosity (Table 2). The porosity for W-P6-li is 20.8%, for W-0 it is 25.6%, and for W-05 it is 30.4%. The evolution of the porosity can be justified on the basis that W-P6-Li is a ceramic structure (W), characterized by being coated with a glassy phase (P6-Li). Consequently, the interparticle porosity is the lowest at 9.38%. This is because of the fact that the glass provides cohesion between the grains, thereby reducing the interparticle porosity. Subsequently, the aforementioned structure was coated with an undoped wollastonite ceramic (W-0), resulting in the generation of a granular structure and an increase in interparticle porosity (18.11%). When the coating was doped with Mg, a slight increase in the size of the porosity (27.13%) was observed. However, both scaffolds remained within the same range of interparticle porosity.

With regard to the intraparticle porosity, the application of successive coatings involving thermal treatments has been observed to result in a notable densification of the structure. This is evidenced by a reduction in the intraparticle porosity, obtaining values of 11.38% for W-P6-Li and in the range of 7.47–3.24% for W-0 and W-05, respectively.

One of the objectives of this research was to modulate the morphology of the precipitated HA-like in the in vitro tests by doping the outer coating with Na^+, K^+, and Mg^{2+} ions. Upon exposure to SBF, these ions are released into the solution and can be incorporated into the precipitated HA-like. The integration of ions into the crystal lattice of apatites is extensively documented in scientific literature.[49–52] This mineral group has a loose structure that allows the inclusion of non-lattice atoms or particles substituting for Ca^{2+} and PO_4^{3-}.[49,50,53] The accumulation of these ion substitutions induces lattice distortions, which explains why the crystallinity of ion-doped HA is usually, but not always, lower than that of its pure counterpart.[49,52]

The presence of ions such as Mg, which have a higher volumetric charge density than Ca^{2+}, can result in the phenomenon known as Ostwald ripening.[54–56] This process, which involves dissolution and recrystallisation, ultimately leads to the formation of hollow sphere. In the initial stages of the HA-like precipitation process, the HA-like contains a higher amount of Mg^{2+}, being in a less crystalline form. As the precipitate develops, the concentration of Mg^{2+} in the solution will decrease, thereby increasing the crystallinity of the HA-like. The initial HA-like structure, with a high Mg^{2+} content, is stressed. The dissolution of this structure results in the formation of an HA-like hollow sphere, which is characterized by a reduction in stress. The evolution of this process is accelerated in confined areas such as crevices, due to the smaller volume of the dissolution that occurs in these spaces. An example of this can be seen in sample W-05-7D (Figure 5), where the needles are thinner and more crystalline as compared to the rest of the micrographs.

As mentioned earlier, these modifications in the unit cell are expected to induce morphological changes in the precipitated HA-like. Following this objective, the samples W-0, W-05 and W-075 were scanned for apatite-like precipitates by FESEM-EDX as the SBF soaking time increased (Figure 5).

Sample W-0 showed a trend of losing Si and gaining P over time, until reaching an almost stoichiometric HA-like on day 7. The high Si content detected at 14 days resulted in a Ca/P ratio of approximately 2.35. Since high ratios promote HA dissolution,[49] it is not unexpected that the precipitate began to dissolve and eventually disappeared at 21 days, giving way to CaP crystals. This theory was confirmed by ICP-OES (Figure 6A). The increasing P content of the precipitate until day 7 led to a decrease in the P concentration in the SBF. However, from day 14 onward, the dissolution of the precipitate resulted in an increase in the P concentration, which was observable until day 21.

As for scaffold W-05, it showed a very interesting surface morphology. This composition was not only bioactive on all days of the study, but also showed great morphological changes. The initial precipitate has a crystalline structure in the form of needles forming spheres, which could be considered typical. However, after 3 days, it adopts a square shape, which, contrary to the above, indicates a lower crystallinity. A plausible explanation for the decrease in crystallinity is ionic substitutions. Among the possible replacements that can occur in HA-like is the substitution of PO_4^{3-} tetrahedra by SiO_4^{4-} tetrahedra.[49,52,57] When this occurs, the crystal size is reduced and the grain structure of the material changes,[21,52,57] assuming a square shape as shown in Figure 5 (W-05-3D) and consistent with the results of the EDX analysis, which shows significant amounts of Si (Table S3). This is very interesting from a therapeutic point of view, since silicate groups in the calcium-phosphate system are associated with a significant increase in the rate of osteogenesis in vivo after implantation. Furthermore, it is known that bone tissue remodeling is approximately twice as fast in silica-rich HA as in silica-deficient HA.[52,57]

After 1 week in SBF, spheres of approximately 2–3 μm appear, which are hollow. It is hypothesized that this phenomenon is the result of the dissolution process occurring at a faster rate in confined areas. As previously stated, these spheres were located in a crevice where the concentration of ions of high volumetric charge density, such as Mg^{2+}, is lower. As internal atomic mobility and reorganization reduce crystalline defects over time, the higher crystallinity of HA-like on day 7 compared to day 14 demonstrates the significant effect of ionic exposure on HA-like.

The ICP-OES results demonstrate a constant decrease of the P concentration in the SBF (Figure 6B), associated with apatite precipitation. This precipitate is shown in Figure 5 sample W-05, where a continue bioactivity over times is noticed.

With regards to scaffold W-075, CaP precipitates were observed after 1 and 3 days of immersion in SBF, but disappeared on days 7, 14 and 21. Similar to W-05-3D, a high Si content was detected on the precipitate on day 1, which modified the HA-like morphology by thickening it and reducing the size of the crystals.[57] Although the morphology of the precipitate is similar to that of W-05-7D, the spheres in this case are compact and lack the capacity for drug loading. On the third day, the Si content decreased, resulting in thinner and more crystalline HA needles. There was a decrease in P concentration in SBF on Days 1 and 3 (Figure 6C), which corresponds mainly to the deposition of HA-like. Conversely, on Days 7, 14 and 21, the precipitate dissolves and the phosphorus concentration increases. These results suggest the progressive dissolution of the scaffold. Initially, the sample is bioactive, followed by the detection of β-TCP (Figure 5-7D), the third layer of the scaffold. After 14 days (Figure 5-14D), pyrophosphate, the main component of the W-P6-Li core along with cristobalite, is observed on the surface. Between Day 7 and 14, there is a significant increase in lithium concentration (only present in P6) in the SBF, indicating core dissolution.

Although all scaffolds showed interesting behavior, scaffold W-05 stands out for its consistent bioactivity throughout the 21-day study period. Additionally, on the seventh day following immersion in SBF, the formation of hollow HA-like spheres is observed. The three-dimensional porous structure and biodegradability of HA-like hollow spheres make them an optimal vehicle for controlled drug release.[58,59] This discovery represents a remarkable therapeutic advantage, allowing the combination of tissue engineering with sustained drug release.

This involves the integration of a scaffold into the damaged area to facilitate the restoration of the structure and function of the damaged tissue, together with the action of bioactive molecules, such as drugs or growth factors, which are released directly at the target site. This in turn avoids side effects due to systemic distribution or first-pass hepatic metabolism, allowing the dose administered to be reduced.[58] Given all these advantages, the combination of scaffolds for tissue engineering and drug delivery has been the subject of intense research in recent years.[60–62]

In this sense, the MTT cell viability assay was performed on 3T3 fibroblasts exposed to the W-05 scaffold (direct assay) and its DP (indirect assay). This was done not only to assess the potential cytotoxicity of the samples, but also to determine whether variations in the surface morphology of the W-05 scaffold exhibited biologically enhanced properties.

In the direct assay (Figure 7A), lower cell proliferation was observed in fibroblasts seeded on the scaffolds compared to the control group cultured on plastic during the first 48 h. However, these differences disappeared by 72 h, indicating that the scaffolds are biocompatible. Furthermore, when comparing the different scaffolds, higher cell growth was observed on scaffold W-05-7D, which even exceeded that of the control group after 72 hours. These results suggest that surface morphology, based on hollow HA spheres, induces greater cell proliferation. This behavior has already been described by other authors. Jun Ji et al. fabricated nano-HA/chitosan/gelatin (nHA/CG) scaffolds with rod-nHA and sphere-nHA particles and found that sphere-nHA/CG significantly enhanced the proliferation and osteogenic differentiation of hiPSCs from hGF in vitro.[63] In particular, the cell number in sphere-nHA/CG was almost twice as high as in rod-nHA/CG after 12 weeks.

The results of the indirect assay showed higher cell viability in the wells containing DP-3D and DP-7D. While this difference was more pronounced for the 15 mg/mL concentration (Figure 7B), a very similar trend is observed for the 30 mg/mL concentration (Figure 7C). These results are very encouraging as they indicate that the degradation products are not only nontoxic but also cell division inducing.

5 | CONCLUSIONS

In this research work, innovative multilayer glass–ceramic scaffolds, with surface morphology modulation, have been developed for BTE through the application of the sol–gel method. The scaffolds' core, composed mainly of silicon dioxide, calcium pyrophosphate, and the vitreous phase P6-Li, provides mechanical strength comparable to that of cancellous bone. This characteristic, combined with a total porosity of the complete scaffolds over 87%, provides an environment conducive to cell infiltration and other physiological processes, making them suitable for load bearing applications.

Concerning the bioactive coatings, the outer layer modulates the morphological and bioactive behavior of the scaffolds through ion doping. Scaffold W-05, in particular, presented a surface covered by hollow HA spheres after 1 week of immersion in SBF, demonstrating its potential as an agent for controlled drug release. Additionally, this scaffold proved to be biocompatible, showing no evidence of toxicity on cells, either through direct contact or mediated by its dissolution products. Notably, the hollow spheres of W-05-7D were found to stimulate cell proliferation compared to the other scaffolds and the control. Additionally, the dissolution products of W-05 were found to increase cell viability compared to the control. These results suggest the potential for combining tissue engineering and drug delivery to provide significant therapeutic benefits while promoting bone regeneration.

ACKNOWLEDGMENTS

This work is part of the project PID2020-116693RB-C21, funded by MCIN/AEI/10.13039/501100011033 Spain. In addition, P. M. Riosalido has received a grant PID2020-116693RB-C21 funded by the Generalitat Valenciana Spain. We are sincerely grateful for the valuable technical support provided by M. Desiree González Gras during the conduct of cellular studies.

ORCID

Pablo Velásquez https://orcid.org/0000-0002-5142-4992
Piedad N. De Aza https://orcid.org/0000-0001-9316-4407

REFERENCES

1. Malliappan SP, Yetisgin AA, Sahin SB, Demir E, Cetinel S. Bone tissue engineering: anionic polysaccharides as promising scaffolds. Carbohydr Polym. 2022;283. https://doi.org/10.1016/j.carbpol.2022.119142
2. Tsiklin IL, Shabunin Av, Kolsanov Av, Volova LT. In vivo bone tissue engineering strategies: advances and prospects. Polymers. 2022;14(15). https://doi.org/10.3390/polym14153222
3. Fu R, Liu C, Yan Y, Li Q, Huang RL. Bone defect reconstruction via endochondral ossification: a developmental engineering strategy. J Tissue Engg. 2021;12. https://doi.org/10.1177/20417314211004211
4. Zhang Y, Wu D, Zhao X, Pakvasa M, Tucker AB, Luo H, et al. Stem cell-friendly scaffold biomaterials: applications for bone tissue engineering and regenerative medicine. Front Bioeng Biotechnol. 2020;8. https://doi.org/10.3389/fbioe.2020.598607
5. Perić Kačarević Ž, Rider P, Alkildani S, Retnasingh S, Pejakić M, Schnettler R, et al. An introduction to bone tissue engineering. Int J Artif Organs. 2020;43(2). https://doi.org/10.1177/0391398819876286
6. Kim HD, Amirthalingam S, Kim SL, Lee SS, Rangasamy J, Hwang NS. Biomimetic materials and fabrication approaches for bone tissue engineering. Adv Healthc Mater. 2017;6(23). https://doi.org/10.1002/adhm.201700612
7. Turnbull G, Clarke J, Picard F, Riches P, Jia L, Han F, et al. 3D bioactive composite scaffolds for bone tissue engineering. Bioact Mater. 2018;3(3). https://doi.org/10.1016/j.bioactmat.2017.10.001
8. Wubneh A, Tsekoura EK, Ayranci C, Uludağ H. Current state of fabrication technologies and materials for bone tissue engineering. Acta Biomater. 2018;80. https://doi.org/10.1016/j.actbio.2018.09.031
9. Ribas RG, Schatkoski VM, Montanheiro TL, do A, de Menezes BRC, Stegemann C, et al. Current advances in bone tissue engineering concerning ceramic and bioglass scaffolds: a review. Ceram Int. 2019;45(17). https://doi.org/10.1016/j.ceramint.2019.07.096
10. Pina S, Rebelo R, Correlo VM, Oliveira JM, Reis RL. Bioceramics for osteochondral tissue engineering and regeneration. Adv Exp Med Biol. 2018;1058. https://doi.org/10.1007/978-3-319-76711-6_3
11. Baino F, Novajra G, Vitale-Brovarone C. Bioceramics and scaffolds: a winning combination for tissue engineering. Front Bioeng Biotechnol. 2015;3. https://doi.org/10.3389/fbioe.2015.00202
12. Stastny P, Sedlacek R, Suchy T, Lukasova V, Rampichova M, Trunec M. Structure degradation and strength changes of sintered calcium phosphate bone scaffolds with different phase structures during simulated biodegradation in vitro. Mater Sci Eng, C. 2019;100. https://doi.org/10.1016/j.msec.2019.03.027
13. Xiao D, Zhang J, Zhang C, Barbieri D, Yuan H, Moroni L, et al. The role of calcium phosphate surface structure in osteogenesis and the mechanisms involved. Acta Biomater. 2020;106. https://doi.org/10.1016/j.actbio.2019.12.034
14. Denry I, Kuhn LT. Design and characterization of calcium phosphate ceramic scaffolds for bone tissue engineering. Dent Mater. 2016;32(1). https://doi.org/10.1016/j.dental.2015.09.008
15. Kang HJ, Makkar P, Padalhin AR, Lee GH, Im S-B, Lee BT. Comparative study on biodegradation and biocompatibility of multichannel calcium phosphate based bone substitutes. Mater Sci Eng, C. 2020;110. https://doi.org/10.1016/j.msec.2020.110694
16. Liao F, Peng XY, Yang F, Ke QF, Zhu ZH, Guo YP. Gadolinium-doped mesoporous calcium silicate/chitosan scaffolds enhanced bone regeneration ability. Mater Sci Eng, C. 2019;104:109999. https://doi.org/10.1016/j.msec.2019.109999
17. Xin X, Wu J, Zheng A, Jiao D, Liu Y, Cao L, et al. Delivery vehicle of muscle-derived irisin based on silk/calcium silicate/sodium alginate composite scaffold for bone regeneration. Int J Nanomedicine. 2019;14:1451-67. https://doi.org/10.2147/IJN.S193544
18. Ros-Tárraga P, Murciano Á, Mazón P, Gehrke SA, de Aza PN. In vitro behaviour of sol-gel interconnected porous scaffolds of doped wollastonite. Ceram Int. 2017;43(14):11034-38. https://doi.org/10.1016/j.ceramint.2017.05.146
19. Ghamor-Amegavi EP, Yang X, Qiu J, Xie L, Pan Z, Wang J, et al. Composition control in biphasic silicate microspheres on stimulating new bone regeneration and repair of osteoporotic femoral bone defect.J Biomed Mater Res B Appl Biomater. 2020;108(2):377-90. https://doi.org/10.1002/jbm.b.34396
20. Zenebe CG. A review on the role of wollastonite biomaterial in bone tissue engineering. Biomed Res Int. 2022;2022. https://doi.org/10.1155/2022/4996530
21. Zhou X, Zhang N, Mankoci S, Sahai N. Silicates in orthopedics and bone tissue engineering materials. J Biomed Mater Res—Part A. 2017;105(7). https://doi.org/10.1002/jbm.a.36061

22. Truong LB, Medina Cruz D, Mostafavi E, O'connell CP, Webster TJ. Advances in 3d-printed surface-modified ca-si bioceramic structures and their potential for bone tumor therapy. Materials. 2021;14(14). https://doi.org/10.3390/ma14143844
23. Jafari N, Habashi MS, Hashemi A, Shirazi R, Tanideh N, Tamadon A. Application of bioactive glasses in various dental fields. Biomater Res. 2022;26(1). https://doi.org/10.1186/s40824-022-00274-6
24. Kaou MH, Furkó M, Balázsi K, Balázsi C. Advanced bioactive glasses: the newest achievements and breakthroughs in the area. Nanomaterials. 2023;13(16):2287. https://doi.org/10.3390/nano13162287
25. Montazeri M, Karbasi S, Foroughi MR, Monshi A, Ebrahimi-Kahrizsangi R. Evaluation of mechanical property and bioactivity of nano-bioglass 45S5 scaffold coated with poly-3-hydroxybutyrate. J Mater Sci: Mater Med. 2015;26(2):62. https://doi.org/10.1007/s10856-014-5369-z
26. Pantulap U, Arango-Ospina M, Boccaccini AR. Bioactive glasses incorporating less-common ions to improve biological and physical properties. J Mater Sci: Mater Med. 2022;33(1). https://doi.org/10.1007/s10856-021-06626-3
27. Parvizifard M, Karbasi S. Physical, mechanical and biological performance of PHB-Chitosan/MWCNTs nanocomposite coating deposited on bioglass based scaffold: potential application in bone tissue engineering. Int J Biol Macromol. 2020;152. https://doi.org/10.1016/j.ijbiomac.2020.02.266
28. Mata NA, Ros-Tárraga P, Velasquez P, Murciano A, de Aza PN. 3D multiphasic porous scaffolds of calcium phosphates doping with silicon and magnesium. Bol Soc Esp Ceram Vidrio. 2022;61(5). https://doi.org/10.1016/j.bsecv.2021.03.004
29. Ding S, Li L, Liu X, Yang G, Zhou G, Zhou S. A nano-micro alternating multilayer scaffold loading with rBMSCs and BMP-2 for bone tissue engineering. Colloids Surf B. 2015;133. https://doi.org/10.1016/j.colsurfb.2015.06.015
30. Sebastián E, Murciano A, Madrigal R, de Aza PN, Velasquez P. 3D CaP porous scaffolds with grooved surface topography obtained by the sol-gel method. Ceram Int. 2021;47(15). https://doi.org/10.1016/j.ceramint.2021.04.158
31. Miri Z, Haugen HJ, Loca D, Rossi F, Perale G, Moghanian A, et al. Review on the strategies to improve the mechanical strength of highly porous bone bioceramic scaffolds. J Eur Ceram Soc. 2024;44(1). https://doi.org/10.1016/j.jeurceramsoc.2023.09.003
32. Vahabzadeh S, Hack VK, Bose S. Lithium-doped β-tricalcium phosphate: effects on physical, mechanical and in vitro osteoblast cell–material interactions. Biomed Mater Res B Appl Biomater. 2017;105(2):391-9. https://doi.org/10.1002/jbm.b.33485
33. Hannon MJ, Verbalis JG. Sodium homeostasis and bone. Curr Opin Nephrol Hypertens. 2014;23(4). https://doi.org/10.1097/01.mnh.0000447022.51722.f4
34. Ha J, Kim SA, Lim K, Shin S. The association of potassium intake with bone mineral density and the prevalence of osteoporosis among older Korean adults. Nut Res Practi. 2020;14(1). https://doi.org/10.4162/nrp.2020.14.1.55
35. Rondanelli M, Faliva MA, Tartara A, Gasparri C, Perna S, Infantino V, et al. An update on magnesium and bone health. Biometals. 2021;34(4). https://doi.org/10.1007/s10534-021-00305-0
36. ISO/FDIS 23317 standard Implants for surgery- in vitro evaluation for apatite-forming ability of implant. https://www.iso.org/standard/36406.html
37. ISO 10993–5 Biological evaluation of medical devices Part 5: Tests for in vitro cytotoxicity. https://www.iso.org/standard/36406.html
38. Pasteris JD, Wopenka B, Valsami-Jones E. Bone and tooth mineralization: why apatite? Elements. 2008;4(2). https://doi.org/10.2113/GSELEMENTS.4.2.97
39. Fernández-Hernán JP, Torres B, López AJ, Rams J. The role of the sol-gel synthesis process in the biomedical field and its use to enhance the performance of bioabsorbable magnesium implants. Gels. 2022;8(7). https://doi.org/10.3390/gels8070426
40. Stachel D, Paulus H, Svoboda I, Fuess H. Crystal structure of calcium ultraphosphate, $Ca_2P_6O_{17}$. Zeits chrift für Kristallographie. 1992;202(1-2) 117–8. https://doi.org/10.1524/zkri.1992.202.1-2.117
41. Putra NE, Borg KGN, Diaz-Payno PJ, Leeflang MA, Klimopoulou M, Taheri P, et al. Additive manufacturing of bioactive and biodegradable porous iron-akermanite composites for bone regeneration. Acta Biomater. 2022;148. https://doi.org/10.1016/j.actbio.2022.06.009
42. Dong X, Li H, Lingling E, Cao J, Guo B. Bioceramic akermanite enhanced vascularization and osteogenic differentiation of human induced pluripotent stem cells in 3D scaffolds: in vitro and vivo. RSC Adv. 2019;9(44). https://doi.org/10.1039/c9ra02026h
43. Lee WB, Wang C, Lee JH, Jeong KJ, Jang YS, Park JY, et al. Whitlockite granules on bone regeneration in defect of rat calvaria. ACS Applied Bio Materials. 2020;3(11). https://doi.org/10.1021/acsabm.0c00960
44. Kazakova G, Safronova T, Golubchikov D, Shevtsova O, Rau Jv. Resorbable Mg^{2+}-containing phosphates for bone tissue repair. Materials. 2021;14(17). https://doi.org/10.3390/ma14174857
45. Kim HD, Jang HL, Ahn HY, Lee HK, Park J, Lee E-s, et al. Biomimetic whitlockite inorganic nanoparticles-mediated in situ remodeling and rapid bone regeneration. Biomaterials. 2017;112. https://doi.org/10.1016/j.biomaterials.2016.10.009
46. Zhou D, Qi C, Chen YX, Zhu YJ, Sun TW, Chen F, et al. Comparative study of porous hydroxyapatite/chitosan and whitlockite/chitosan scaffolds for bone regeneration in calvarial defects. Int J Nanomed. 2017;12:2673–87. https://doi.org/10.2147/IJN.S131251
47. Caeiro JR, González P, Guede D. Biomechanics and bone (& II): trials in different hierarchical levels of bone and alternative tools for the determination of bone strength. Revista de Osteoporosis y Metabolismo Mineral. 2013;5(2).
48. Codrea CI, Croitoru AM, Baciu CC, Melinescu A, Ficai D, Fruth V, et al. Advances in osteoporotic bone tissue engineering. J Clin Med. 2021;10(2). https://doi.org/10.3390/jcm10020253
49. Pupilli F, Ruffini A, Dapporto M, Tavoni M, Tampieri A, Sprio S. Design strategies and biomimetic approaches for calcium phosphate scaffolds in bone tissue regeneration. Biomimetics. 2022;7(3). https://doi.org/10.3390/biomimetics7030112
50. Ratnayake JTB, Mucalo M, Dias GJ. Substituted hydroxyapatites for bone regeneration: a review of current trends.J Biomed Mater Res B Appl Biomater. 2017;105(5):1285-99. https://doi.org/10.1002/jbm.b.33651

51. Radulescu DE, Vasile OR, Andronescu E, Ficai A. Latest research of doped hydroxyapatite for bone tissue engineering. Int J Mol Sci. 2023;24(17). https://doi.org/10.3390/ijms241713157
52. Szurkowska K, Kolmas J. Hydroxyapatites enriched in silicon—bioceramic materials for biomedical and pharmaceutical applications. Progress Nat Sci Mater Int. 2017;27(4). https://doi.org/10.1016/j.pnsc.2017.08.009
53. Vranceanu DM, Ionescu IC, Ungureanu E, Cojocaru MO, Vladescu A, Cotrut CM. Magnesium doped hydroxyapatite-based coatings obtained by pulsed galvanostatic electrochemical deposition with adjustable electrochemical behavior. Coatings. 2020;10(8). https://doi.org/10.3390/COATINGS10080727
54. Wen-shou W, Cheng-Yan X., Li Y, Wen-Zhu S. Controlled synthesis of calcium tungstate hollow microspheres via ostwald ripening and their photoluminescence property. J Phys Chem C. 2008;112:19390–18. https://doi.org/10.1021/jp8074783
55. Jiang SD, Yao QZ, Zhou GT, Fu SQ. Fabrication of hydroxyapatite hierarchical hollow microspheres and potential application in water treatment. J Phys Chem C. 2012;116:4484–92, https://doi.org/10.1021/jp211648x
56. Sebastian E, Murciano A, De Aza PN, Velasquez P. Synthesis of 3D porous ceramic scaffolds obtained by the sol-gel method with surface morphology modified by hollow spheres for bone tissue engineering applications, Ceram Inter. 2023;49:4393–402. https://doi.org/10.1016/j.ceramint.2022.09.326
57. Lyutova E, Borilo L, Izosimova E. The effect of sodium and magnesium ions on the properties of calcium–phosphate biomaterials. Progress Biomater. 2019;8(2). https://doi.org/10.1007/s40204-019-0117-6
58. Halim NAA, Hussein MZ, Kandar MK. Nanomaterials-upconverted hydroxyapatite for bone tissue engineering and a platform for drug delivery. Int J Nanomed. 2021;16. https://doi.org/10.2147/IJN.S298936
59. Lara-Ochoa S, Ortega-Lara W, Guerrero-Beltrán CE. Hydroxyapatite nanoparticles in drug delivery: physicochemistry and applications. Pharmaceutics. 2021;13(10). https://doi.org/10.3390/pharmaceutics13101642
60. Mahanta AK, Senapati S, Paliwal P, Krishnamurthy S, Hemalatha S, Maiti P. Nanoparticle-induced controlled drug delivery using chitosan-based hydrogel and scaffold: application to bone regeneration. Mol Pharmaceutics. 2019;16(1). https://doi.org/10.1021/acs.molpharmaceut.8b00995
61. Chen C, Huang K, Zhu J, Bi Y, Wang L, Jiang J, et al. A novel elastic and controlled-release poly(ether-ester-urethane)urea scaffold for cartilage regeneration. J Mater Chem B. 2020;8(18). https://doi.org/10.1039/c9tb02754h
62. Ji J, Tong X, Huang X, Wang T, Lin Z, Cao Y, et al. Sphere-shaped nano-hydroxyapatite/chitosan/gelatin 3D porous scaffolds increase proliferation and osteogenic differentiation of human induced pluripotent stem cells from gingival fibroblasts. Biomed Mater (Bristol). 2015;10(4). https://doi.org/10.1088/1748-6041/10/4/045005
63. Qin X, Wu Y, Liu S, Yang L, Yuan H, Cai S, et al. Surface modification of polycaprolactone scaffold with improved biocompatibility and controlled growth factor release for enhanced stem cell differentiation. Front Bioeng Biotechnol. 2022;9. https://doi.org/10.3389/fbioe.2021.802311

SUPPORTING INFORMATION

Additional supporting information can be found online in the Supporting Information section at the end of this article.

How to cite this article: Riosalido PM, Velásquez P, Murciano Á, De Aza PN. Surface morphology modulation in multilayer scaffolds via ion doping for bone tissue engineering. J Am Ceram Soc. 2025;108:e20269. https://doi.org/10.1111/jace.20269

Artículo 2

Ceramics International 51 (2025) 13363–13373

Contents lists available at ScienceDirect

Ceramics International

journal homepage: www.elsevier.com/locate/ceramint

Multilayer scaffolds designed with bioinspired topography for bone regeneration

Paula M. Riosalido [a,**], Pablo Velásquez [a], Ángel Murciano [b], Piedad N. De Aza [a,*]

[a] Institute of Bioengineering, Miguel Hernandez University, Avda. Universidad, s/n, 03202, Elche, Spain
[b] Department of Materials, Optical and Electronic Technology, Miguel Hernandez University, Avda. Universidad, s/n, 03202, Elche, Spain

ARTICLE INFO

Handling Editor: Dr P. Vincenzini

Keywords:
A, Sol-gel processes
B, Porosity
D, Glass ceramics
E, Biomedical applications

ABSTRACT

In this investigation, three distinct multiphasic scaffolds, comprising primary crystalline phases of SiO_2, $Ca_2P_2O_7$, and $Ca_3(PO_4)_2$, were developed. These scaffolds feature surface coatings that have been functionalised with Na, K, and varying molar proportions of Mg (0–1%). The samples were extensively characterised to evaluate a number of key properties including microstructure, porosity, mechanical properties, biodegradation profile, biocompatibility and *in vitro* bioactivity. The scaffolds demonstrated a mechanical strength of 1.8 MPa, accompanied by a high macroporosity of over 85 % and micropores ranging from 200 to 6 μm. All scaffolds showed bioactivity. Notably, CS0.7 Mg exhibited a distinctive topography characterised by non-periodic, irregular lamellae at both the micro- and nanoscale. During the bioactivity assays, the lamellae were progressively covered by HA until they were completely obscured after 14 days in SBF. This bioactive behaviour was accompanied by gradual degradation in PBS, with a 15 % weight loss over 21 days, indicating suitability for bone regeneration. In addition, ICP-OES analysis demonstrated ionic exchange from the scaffolds into the culture medium at both concentrations of 15 mg/mL and 30 mg/mL, which promoted the proliferation of 3T3 fibroblasts. Cells seeded on the CS0.7 Mg scaffold also showed sustained cell proliferation over time. This proliferation was found to be influenced by the topography of the scaffold, with the greatest enhancement observed in the CS0.7 Mg-7D samples, which had HA-covered lamellae.

1. Introduction

The regeneration of critical-sized bone defects remains a significant clinical challenge and a substantial burden on the global healthcare system [1–3]. These defects, which exceed the body's natural healing capacity, account for approximately 0.4 % of all bone fractures and 11.4 % of all open fractures, according to a 10-year fracture register [4]. They often require complex surgical interventions, with an associated cost estimated at billions of dollars annually worldwide [5]. Conventional therapeutic approaches, including autografts, allografts, and xenografts, present several disadvantages. These include limitations in the availability of donor and implantation sites, the necessity for additional surgical procedures, the potential for disease transmission, and the occurrence of immune responses following implantation [1,6]. These shortcomings have prompted the search for novel strategies. Among these, biomaterials offer significant advantages, including high availability and the absence of disease risk, which are likely to shift the future trend towards their use.

In this sense, a number of inorganic materials have been demonstrated to be beneficial for bone tissue regeneration. Among these, $CaSiO_3$ (calcium silicate, CS) is recognized for its excellent bioactivity, promoting the formation of hydroxyapatite in body fluids more rapidly than other bioactive glass ceramics, while supporting bone bonding and ultimately osteointegration [7,8]. Another one is tricalcium phosphate ($Ca_3(PO_4)_2$, TCP), a well-known biodegradable material, often used in bone regeneration due to its osteoconductivity, allowing bone cells to grow along its surface, and its controlled degradation rate, which matches the rate of new bone formation [9,10].

Nevertheless, in order to guarantee the full integration of these medical devices and the long-term functionality of the regenerated tissue, it is important to consider not only their bulk properties but also the properties of their surfaces, which interact dynamically with human body tissues [11,12].

In this sense, structural features play a crucial role in resembling the

* Corresponding author. Instituto de Bioingeniería Universidad Miguel Hernández, 03202, Elche, Alicante, Spain.
** Corresponding author.
E-mail addresses: priosalido@umh.es (P.M. Riosalido), pavelasquez@umh.es (P. Velásquez), amurciano@umh.es (Á. Murciano), piedad@umh.es (P.N. De Aza).

https://doi.org/10.1016/j.ceramint.2025.01.180
Received 17 October 2024; Received in revised form 9 January 2025; Accepted 10 January 2025
Available online 11 January 2025

cellular environment at a macroscopic, microscopic and nanoscopic levels [11,12]. A variety of techniques can be employed to design biomimetic scaffolds at the nano- and micrometric scale, with the objective of enhancing the biofunctions of implants. One way of achieving structural modifications along with enhanced biomimicry is ion doping [13–15]. In comparison to other strategies, ion doping is presented as a cost-effective and simple approach, with remarkable stability and high efficacy at low concentrations.

A variety of ions have traditionally been employed for hard tissue regeneration. Among these are alkaline earth metal ions, such as magnesium (Mg) and calcium (Ca). Magnesium plays a pivotal role in bone metabolism, constituting approximately half of the mineral content in bone tissue and directly influencing osteogenesis [13,16]. Previous studies have demonstrated the ability of Mg^{2+} to enhance the expression of vascular endothelial growth factor (VEGF), which is crucial for ensuring adequate blood perfusion to the interior of implants [16,17]. Additionally, calcium, the most abundant mineral in the body and primarily stored in the skeleton, is essential for the deposition of new bone mineral phases [18,19]. The challenge of calcium deficiency in bone regeneration suggests that the ionic dissolution products of these implants may benefit cellular activities and promote osseous regeneration [20–22].

Alkali metal ions like lithium (Li), sodium (Na), and potassium (K), considered labile elements, have been employed to improve the bioactivity of materials used in bone regeneration by generating distortions in the crystal lattice that enhance bioreactivity [14,23–25]. Particularly, lithium has been recognized for its positive effects on bone health, especially in promoting osteogenesis [13,22,25]. It stimulates the differentiation of osteoblasts, enhances mineralization processes, and activates the Wnt/β-catenin signaling pathway, which is crucial for bone development and maintenance [13,17,22,25].

Additionally, non-metallic ions such as silicon (Si) have been utilized [25–27]. Silicon is considered an essential element at sites of active calcification within human bones, participating directly in the mineralization process during bone growth [28–31]. It is particularly noted for its ability to accelerate bone mineralization and stimulate collagen synthesis [29–31].

Despite the advantages of bone regeneration biomaterials over traditional methods, significant challenges remain. These include ineffective vascularisation, poor integration with host tissue and difficulties in balancing mechanical strength with bioactivity [32,33]. Stronger materials often lack the bioactivity needed to promote bone formation and angiogenesis, while more bioactive materials tend to be mechanically weaker [33].

In order to overcome these limitations, this research has developed three distinct types of multilayer scaffolds based on the SiO_2-CaO-P_2O_5 system. These combine the chemical resemblance to the bone mineral phase of ceramic calcium phosphates [34,35], the bioactivity and angiogenic properties of calcium silicates [36,37], mechanical properties of glassy calcium phosphate phases [38], within a single structure. Furthermore, the strategy of ion doping has been employed to modify the surface topography and enhance by optimising material-host integration. The objective of this approach is to provide a viable solution that promotes bone regeneration, vascularisation and the required mechanical strength for effective bone healing.

2. Materials and methods

2.1. Multilayer scaffolds assembly

The multilayer scaffolds were fabricated through the synergistic utilisation of the Sol-Gel methodology and the polymeric sponge replication technique. The polyurethane foams, with a porosity of 20 ppi (Eurofoam-Germany-PU), measuring 1 cm × 1 cm, underwent a coating process using different solutions comprising the distinct layers of the scaffold. The pH of all the solutions was adjusted between 2 and 3. The reagents used to formulate each layer are summarised in Table 1.

● Glass-Ceramic Core

The innermost layer, designated as CS ($CaSiO_3$), was generated by combining 19.28 mL of TEOS, 8.62 g of $CaCO_3$, 5 mL of ethanol (97°), 20 mL of distilled water, and 1 mL of HCl 37 %.

The polyurethane foams were immersed in the aforementioned solution until complete coverage was achieved. Subsequently, the coated foams were subjected to the sintering process. The treatment involved a prolonged ramp over 55 h, reaching a temperature of 1050 °C, which was then held for 8 h to achieve a balance between densification and porosity, thereby improving the mechanical and structural properties of the materials [39–42]. Subsequently, it was permitted to cool to room temperature over a period of approximately 12 h.

Subsequently, the CS scaffold was coated with the glassy phase, designated as P6 ($Ca_2P_6O_{17}$), doped with Li. The composition was achieved by mixing 18.46 mL of TEP, 3.72 g of $CaCO_3$, 1 g of Li_2CO_3, 5 mL of ethanol (97 %), 20 mL of distilled water, and 1 mL of HCl 37 %. Following the coating process, a faster temperature ramp was employed, reaching 1050 °C in 9 h. The temperature was then maintained for 8 h and subsequently allowed to cool to room temperature over a period of approximately 12 h. This procedure was conducted twice.

The excess of P6 was removed by chemical etching using a solution designated as TRIS. The solution was prepared by dissolving 1.17 g of $CaCl_2$ and 7.61 g of tris(hydroxymethyl)aminomethane in water, adjusting the pH to a range of 7.35–7.4 with 1M HCl, and gauging to a final volume of 1L. The scaffolds were immersed in 50 mL of the TRIS solution for a period of 24 h at a temperature of 50 °C, resulting in the formation of the glass-ceramic core (GCC).

● Dual Bioactive Shell

The subsequent step involved the application of a first coating to the GCC, comprising TCP, a well-known bioactive material. This layer was formulated through the chemical reaction of 10.96 mL of TEP, 9.68 g of $CaCO_3$, 5 mL of ethanol (97°), 20 mL of distilled water, and 10 mL of HCl 37 %. Following the application of the coating, the scaffolds were subjected to a sintering process analogous to that employed for the P6 coating. This entailed 9 h of incremental heating to 1050 °C, 8 h of holding, and a final cooling period of approximately 12 h to room temperature.

Finally, the GCC-TCP scaffold was coated with the second coating comprising one of the CS ion-functionalised compositions summarised in Table 2. The name of each coating is derived from the molar percentage of $MgCO_3$ used to dope the CS. In this sense, CS0Mg contains 0 % molar MgO, whereas CS0.7 comprises 0.7 % molar MgO, and CS1Mg contains 1 % molar MgO. The formulation of this layer was achieved as

Table 1
List of chemical reagents with chemical formula and suppliers, used as precursor materials.

Reagents	Chemical Formula	Purity (%)	Supplier
Calcium carbonate	$CaCO_3$	≥99	Sigma-Aldrich
Calcium chloride	$CaCl_2$	97	Riedel-de Haën
Hydrochloric acid	HCl	37	Carlo Erba
Lithium carbonate	Li_2CO_3	≥99	Sigma Aldrich
Magnesium carbonate	$MgCO_3$	≥99	Sigma Aldrich
Potassium carbonate	K_2CO_3	≥99	Sigma-Aldrich
Sodium carbonate	Na_2CO_3	≥99	Riedel-de Haën
Tetraethyl Orthosilicate (TEOS)	$Si(OC_2H_5)_4$	≥99	VWR Chemicals BDH
Triethyl Phosphate (TEP)	$(C_2H_5)_3PO_4$	≥99.8	Sigma-Aldrich
Tris(hydroxymethyl) aminomethane	$C_4H_{11}NO_3$	≥99.8	Sigma-Aldrich
Ethanol	C_2H_5OH	≥96	Carlo Erba

Table 2
Molar distribution of the compositions under study.

Oxide	Composition (mol %)			
	CS-P6	CS0Mg	CS0.7 Mg	CS1Mg
SiO_2	22.4	24.82	24.66	24.75
CaO	41.67	49.35	49.12	48.53
P_2O_5	28.91	20.63	20.36	20.6
Li_2O	7.03	3.8	3.87	3.85
Na_2O	0	0.7	0.72	0.71
K_2O	0	0.58	0.57	0.57
MgO	0	0	0.7	1

previously described, with the addition of 0.5 g of Na_2CO_3, 0.5 g of K_2CO_3 and a varying quantity of $MgCO_3$ (0–0.6 g), resulting in the molar ratios described in Table 2.

Once more, the scaffolds were subjected to a thermal treatment comprising a heating ramp to 1050 °C, which took approximately 9 h, followed by 8 h of holding, and a final cooling period of approximately 12 h to room temperature.

2.2. Physico-chemical characterisation

X-ray diffraction (XRD) patterns for each layer were obtained using an automated Bruker-AXS D8 Advance diffractometer, which was equipped with CuKα radiation (λ = 1.54056 Å). The data were collected in accordance with the vertical geometrical Bragg-Brentano configuration in plane reflection mode. The measurements were taken in increments of 0.05° with a 5-s duration per step. Subsequently, the experimental diffractograms were compared to those stored in the Crystallography Open Database (COD) using Power Diffraction Match! Version 3.16 Build software.

In addition, the microstructure of the different scaffolds, was evaluated using a field emission scanning electron microscope (FESEM, ZEISS SIGMA 300 VP) coupled with energy dispersive X-ray spectroscopy (EDX, ZEISS SmartEDX).

To assess the compressive strength of the scaffold as layers were added, a simple manual testing apparatus (SVL-1000 N, IMADA) was employed. This apparatus enabled the application of pressure manually and in stages until structural failure occurred.

Furthermore, to examine the microporosity (<300 μm), a Poromaster 60 GT device manufactured by Quantachrome Instruments was utilized, operating within a pressure range of 6.393 KPa to 242,995.531 KPa. Finally, to address the macroporosity (>300 μm), a water-filled pycnometer was used.

2.3. In vitro bioactivity test

In accordance with the procedures outlined in ISO 23317 [43], the multilayer scaffolds were placed in falcon tubes containing 50 mL of simulated body fluid (SBF) and incubated for varying periods of time (1–21 days) in a shaking bath at 37 °C, simulating physiological conditions. Subsequently, samples were analysed by FESEM-EDX. This was done both before (control) and after SBF treatment. Prior to analysis, all samples were subjected to palladium sputtering.

Concurrently, the residual SBF was subjected to analysis by inductively coupled plasma optical emission spectrometry (ICP-OES, PerkinElmer Optima 2000™) to ascertain whether any ionic alterations had occurred.

2.4. Biodegradation

2.4.1. Weight loss

Given the significance of biodegradation, a comprehensive investigation was conducted to elucidate the underlying mechanisms. Weight loss was monitored over a 21-day period. Multilayer scaffolds were placed in Falcon tubes containing 50 mL of phosphate-buffered saline (PBS) (pH 7.4) and maintained in a shaking bath at 37 °C to simulate physiological conditions. Subsequently, the samples were dried and weighed in order to calculate the percentage of scaffold degradation. This was achieved by applying the following formula, where W_0 is the initial weight prior to PBS exposure and W_t is the weight at each time point:

$$Degradation\ \% = \frac{(W_0 - W_t)}{Wo}\ x\ 100$$

2.4.2. Ionic characterisation of CCM

In this instance, the scaffold exhibiting the most biologically relevant topography was selected for further *in vitro* biological characterisation, based on the bioactivity results. The scaffolds were subjected to a 4-h ultraviolet (UV) light sterilisation process on each side. Subsequently, the samples were immersed in Dulbecco's modified Eagle medium (DMEM, Gibco) culture medium, which was supplemented with 10 % fetal bovine serum (FBS, Corning) and 1 % penicillin/streptomycin (PS, Gibco). The procedure was conducted at two different concentrations: 15 mg/mL and 30 mg/mL. Following this, the samples were incubated for 24, 48 and 72 h. Finally, the culture medium containing the dissolution products released by the scaffolds was collected. This medium is referred to as the conditioned culture medium (CCM). The CCM was stored at 4 °C for further ICP-OES analysis and cell culture.

2.4.3. Indirect cell viability evaluation

Finally, the effect of the CCM on the viability of 3T3 mouse embryonic fibroblasts was evaluated through the alamarBlue assay (Invitrogen, Thermo Fisher Scientific) following ISO 10993-5 standards [44], after 1–3 days. The cells were cultured in Petri dishes with supplemented DMEM and incubated at 37 °C in a humidified atmosphere with 5 % CO_2. Subculturing was initiated when the cells reached 80 % confluence. Twenty-four hours prior to commencing the assay, 24-well culture plates were seeded at a density of 5000 cells per cm^2, allowing the cells to attach to the plate. Subsequently, the culture medium was carefully replaced with CCM, with the exception of the control wells, where it was renewed with fresh unconditioned culture media. All studies were conducted in triplicate. Subsequently, the alamarBlue assay was conducted in accordance with the instructions provided by the supplier. The absorbance at 570 nm was quantified using the Microplate Reader RT-2100C (Neuvar Inc.).

2.5. 3D direct cell culture

Three-dimensional direct cultures were performed in triplicate to assess the cytotoxicity of the CS0.7 Mg scaffold and to examine the cellular response to its varying surface morphologies, CS0.7 Mg-XD (X = 0–14 days following immersion in SBF).

Following sterilisation, a wetting pre-treatment was performed in order to facilitate cell attachment. This entailed the complete coverage of the scaffolds with culture medium. The plates were then placed in an incubator at 37 °C under a 5 % CO_2 atmosphere for 30 min. Subsequently, the culture medium was aspirated, and a 25-μL drop containing 20,000 cells was carefully deposited onto each scaffold. Once more, the plate was incubated for 30 min to permit the cells to adhere to the scaffold. Lastly, a fresh culture medium was added. Following each study interval (1–10 days), the culture medium was removed, and the scaffolds were transferred to a new 24-well plate. This approach allows for the avoidance of cells adhered to the bottom of the plate instead of the scaffold. Finally, the alamarBlue assay was conducted, and the resulting absorbance was read.

2.6. Statistical analysis

For each specific time point, a one-way ANOVA was employed to

perform between-group comparisons. Subsequently, post-hoc analyses were conducted using Tukey's test to identify specific differences among the groups. The statistical significance was determined using an alpha level of 0.05 and a 95 % confidence interval. The results are presented as mean ± standard deviation (SD). All statistical analyses were conducted using GraphPad version 10.0.

3. Results

3.1. Physico-chemical characterisation

The mineralogical analysis of the ground scaffold, conducted via XRD, revealed the presence of various crystalline structures as new coatings of material were incorporated to the scaffold (Fig. 1).

Fig. 1A illustrates the crystalline phases of the Glass-Ceramic Core. It is evident that the CS layer consists of pseudowollastonite-$CaSiO_3$ (PW) (COD 96-900-2251). However, in the CS-P6 layer, $CaSiO_3$ was absent, and instead, the presence of new crystalline phases was detected. It was found to consist of cristobalite-SiO_2 (CB) (COD 96-900-8225), calcium pyrophosphate-$Ca_2P_2O_7$ (CP) (COD 96-100-1557), and a minor proportion of tricalcium phosphate-$Ca_3(PO_4)_2$ (β-TCP) (COD 96-151-7239). Following chemical etching with TRIS, the GCC scaffold showed no significant variations in the crystalline composition.

Fig. 1B shows the crystalline phases upon the addition of the dual bioactive shell. GCC-TCP scaffold showed the same phase composition as GCC, albeit with a notable increase in the proportion of β-TCP. For the CS0Mg, CS0.7 Mg and CS1Mg scaffolds, SiO_2, $Ca_2P_2O_7$ and β-TCP were identified as the predominant components in addition to wollastonite-$CaSiO_3$ (CS) (COD 96-900-5779) in a smaller proportion. Additionally, in the CS0.7 Mg and CS1Mg samples, Mg-rich phases were identified: akermantite-$Ca_2MgSi_2O_7$ (AK) (COD 96-900-6942) and whitlockite-$Ca_{10.115}Mg_{3.85}(PO_4)_6$ (WH) (COD 96-901-2137), a non-stoichiometric Mg variant of β-TCP. The intensity of the peaks corresponding to these phases was directly proportional to the amount of Mg contained in the structure.

The microstructure of each layer of the scaffold was examined using FESEM-EDX, as illustrated in Fig. 2. The EDX data are presented in Supplementary Table 1. The CS scaffold scan revealed a globular morphology with a Ca/Si ratio of 0.9 ± 0.1, which is very close to that of stoichiometric $CaSiO_3$. In contrast, CS-P6 exhibited large polygonal crystals with a Ca/P ratio of 1.4 ± 0.2 in the centre, which closely approximates the TCP ratio. The Ca/P ratio at the periphery was 1.1 ± 0.1, similar to that of calcium pyrophosphate. The crystals were wrapped and completely covered by an amorphous matrix (▲) comprising primarily P and Si, with a minor contribution from Ca. The Ca/P + Si ratio was maintained within the range 0.017 ± 0.005. Following treatment with TRIS, a more exposed surface is visible as a result of the removal of the excess glassy phase. This has resulted in the exposure of the calcium phosphate crystals, which have become more prominent and angular.

Finally, sample GCC-TCP displayed a laminated surface. The elemental analysis revealed that the samples were primarily composed of calcium and phosphorus, with a Ca/P ratio of 1.5 ± 0.1.

The scaffold CS0Mg, exhibited the presence of small spherical structures that were uniformly dispersed over the surface, with a Ca/Si ratio of 0.5 ± 0.3 (Fig. 5). Furthermore, larger and angular crystalline formations with a Ca/P ratio of 1.4 ± 0.2 were observed.

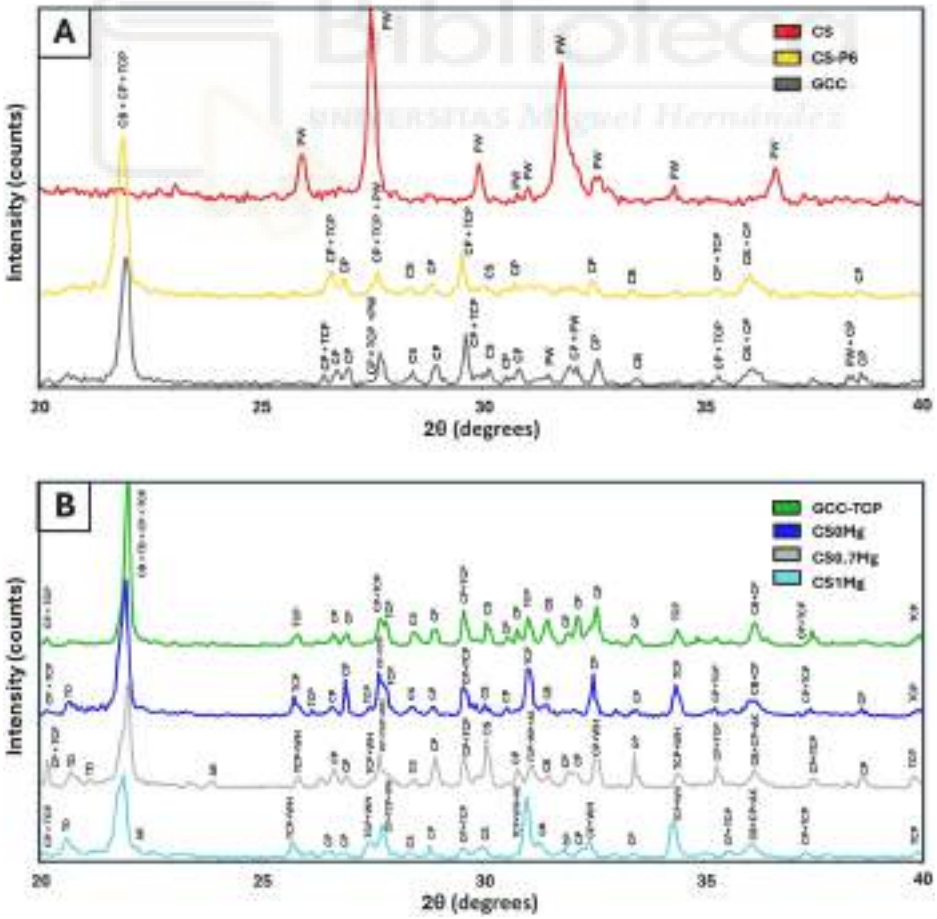

Fig. 1. XRD spectra of the scaffold as successive coatings were applied to form the GCC (A) and the Dual Bioactive Shell (B). Identified phases include PW - Pseudowollastonite ($CaSiO_3$), CB - Cristobalite (SiO_2), TD - Tridymite (SiO_2), CP - Calcium Pyrophosphate ($Ca_2P_2O_7$), β-TCP - Tricalcium Phosphate ($Ca_3(PO_4)_2$), CS - Wollastonite ($CaSiO_3$), WH - Whitlockite ($Ca_{10.115}Mg_{3.85}(PO_4)_6$), AK - Akermanite ($Ca_2MgSi_2O_7$).

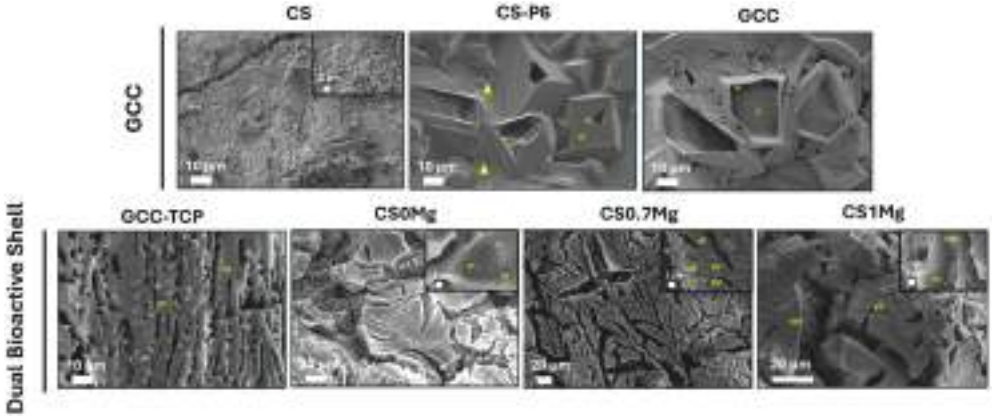

Fig. 2. FESEM-EDX micrographs of the microstructure of each **layer** of the scaffolds. The locations of elemental analysis are indicated by the numbers I-XII.

In contrast, the CS0.7 Mg sample, exhibited a ribbed surface (Fig. 5). The lamellas were identified within the microscale with a thickness of 4.1 ± 0.1 μm and an average lamellar spacing of 7.0 ± 0.1 μm. These features were composed of small calcium silico-phosphates crystals with a minor magnesium contribution. The lamellae body is composed primarily of small, rounded grains with a Ca + Mg/P + Si ratio of 0.8 ± 0.2, interspersed with slightly larger, angular grains with a Ca + Mg/P + Si ratio of 1.0 ± 0.1. While both have silicon and phosphorus as their main components, the rounded crystals have a greater silicon contribution than the polygonal ones, which have a larger phosphorus contribution.

With regard to CS1Mg, it exhibited similar characteristics to those observed in CS0Mg (Fig. 5), namely spherical structures with a Ca/Si ratio of 0.5 ± 0.2. However, in this case, the quantity of accompanying Ca-P grains, with a Ca/P ratio of 1.5 ± 0.2, was considerably higher.

Fig. 3 and Table 3 provide a detailed analysis of the microporosity (<300 μm) of the scaffold layers, obtained through Hg porosimetry. The CS scaffold exhibits a predominant interparticle porosity (>1 μm), representing a 27 %. This porosity is characterised by a pore size distribution comprising three distinct ranges of gas incorporation. The first range encompasses pores between 200 μm and 61 μm, while the second ranges from 25 μm to 4 μm. Lastly, pores within the intraparticle region (0.1–0.01 μm), account for 18.4 %, resulting in a total microporosity value of 45 %.

Table 3
Microporosity study of scaffolds with successive material layer additions.

Sample	Interparticle Porosity (%)	Intraparticle Porosity (%)	Total Microporosity (%)
CS	27	18	45
CS-P6	16	17	33
GCC-TCP	25	11	35
CS0Mg	23	13	36
CS0.7 Mg	22	12	34
CS1Mg	26	11	37

Following the addition of the glassy P6 phase, a shift in the pore size distribution to the left was observed in the CS-P6 scaffold, which is likely attributed to the viscous nature of the material. This results in a reduction in the volume of intruded mercury and an increase in the proportion of intraparticle porosity, which represents 17 % of the total porosity, with pore sizes ranging from 4.6 μm to 0.05 μm. This was accompanied by a notable reduction in interparticle porosity, which decreased to 16 % with pores between 200 and 4 μm, and in total microporosity, which decreased to 33 %.

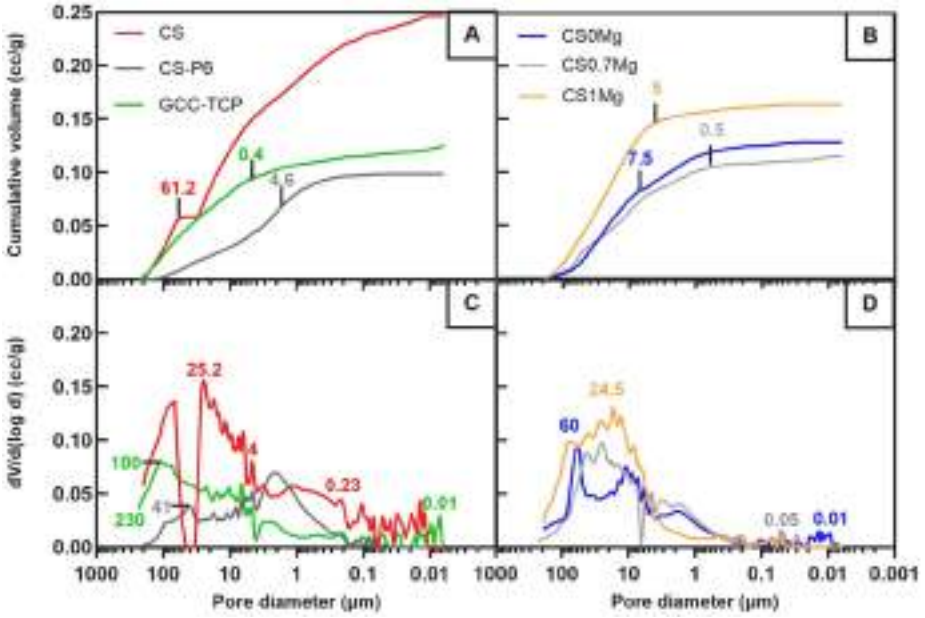

Fig. 3. Mercury porosimetry curves: cumulative porosity (A, B) and differential porosity (C, D).

The TCP coating resulted in a partial compensation of the total microporosity, which increased to 35 % of which 11 % was intraparticle and 25 % intraparticulate. This was reflected by an increase in the volume of intruded mercury. Two distinct pore size regions were identified, spanning from 230 μm to 0.4 μm and a second region corresponding to pores between 0.2 μm and 0.01 μm.

The CS0Mg, CS0.7 Mg, and CS1Mg scaffolds exhibit two distinct regions in their pore size distribution. The first region exhibited an increased intruded volume, corresponding to pores of larger diameter (200 μm–5 μm), indicative of a predominant interparticle porosity (11 %–13 %). The second region encompasses smaller pore sizes, ranging from 0.2 to 0.01 μm, indicative of an intra-particle porosity between 22 % and 26 %. The total porosity of the scaffolds is observed to range between 34 % and 37 %.

Fig. 4 provides a comprehensive analysis of the physical characterisation as new coatings are applied to the CS core. The CS Core scaffold obtained through the indicated methodology and with a porosity of 95 % presents a mechanical resistance that hardly allowed its manipulation, preventing its mechanical characterization. For this reason, no value is shown in Fig. 4 A. The addition of 0.3 g of P6, representing 80 % of the total weight of the sample (Fig. 4B), resulted in a notable enhancement in compressive strength, reaching approximately 2.4 MPa (Fig. 4A). This incorporation also led to a reduction in macroporosity from 93 % to 89 %, which exemplifies the inverse correlation between mechanical strength and porosity. However, after TRIS etching, approximately 0.06 g (20 % of the total P6) is hydrolysed, resulting in a reduction in compressive strength to 1.9 MPa and a slight increase in porosity to 90 %. In particular, the application of the dual bioactive shell, TCP and ion-functionalised CS, contribute 0.08 g and 0.07 g respectively, without significantly altering the mechanical properties or the overall macroporosity, which remains above 85 % of the total volume.

The CS1Mg scaffold displayed comparable physical properties to the CS0.7 Mg scaffold, suggesting that the additional 0.3 % molar MgO did not exert a significant influence.

3.2. *In vitro bioactivity assay*

The microstructure of the samples CS0Mg, CS0.7 Mg, and CS1Mg was examined using FESEM-EDX, both before SBF exposure (control, 0D) and after 1, 7, 14, and 21 days of treatment, as depicted in Fig. 5 and in Supplementary Table 2.

The control scaffold CS0Mg (0D), exhibited the calcium-silicate small spherical structures with a Ca/Si ratio of 0.5 ± 0.1 with large polygonal calcium phosphate grains with a Ca/P of 1.5 ± 0.1 (Fig. 5). After one day of immersion in SBF, entangled filamentary structures with a Ca/Si ratio of 0.6 ± 0.1 and a lower P content (1.5 ± 0.2 at. %) were identified. However, on the seventh day, apatite-type precipitates forming spheres were detected, with a Ca/P ratio of 1.6 ± 0.1, which is very close to the stoichiometric value of 1.67 for HA. Upon closer examination, the typical HA needle-like structures were observed, which, according to EDX analysis, had a low content of Na (1.2 ± 0.1 at. %), Mg (0.7 ± 0.1 at. %), and Si (0.6 ± 0.1 at. %). This precipitate persisted until day 14, exhibiting greater uniformity and compactness. Moreover, the HA-needles displayed a Ca/P ratio of 1.7 ± 0.1, accompanied by an almost unchanged Na and Mg content and an increased Si content (2.6 ± 0.1 at. %). Finally, after 21 days of immersion, the surface exhibited no needle-like precipitates, but a microstructure that was strikingly similar to that of the CS0Mg-0D scaffold, consisting of spherical structures with a Ca/Si ratio of 0.5 ± 0.01.

In contrast, the CS0.7 Mg sample at 0 days, exhibited a ribbed surface (Fig. 5). The lamellas were identified within the microscale with a thickness of 4.1 ± 0.2 μm and an average lamellar spacing of 7.0 ± 0.1 μm. These features were composed of the small calcium silicophosphates rounded (▲) and angular grains (●) with a Ca + Mg/P + Si ratio of 0.8 ± 0.1, interspersed with slightly larger, angular grains (●) with a Ca + Mg/P + Si ratio of 1.0 ± 0.1. Upon immersion in SBF for one day, the lamellae experienced a notable reduction in thickness, resulting in more defined structures. Both the nanolamellae (700 ± 100 nm) and the microlamellae (1.5 ± 0.9 μm) can be distinguished with an average spacing of 2.8 ± 0.4 μm and 9.4 ± 2.2 μm length. In addition, an apatite-like precipitate was observed after seven days of immersion, with a Ca/P ratio of 1.7 ± 0.1. Furthermore, it was rich in Si (2.2 ± 0.1 at. %), Mg (0.7 ± 0.1 at. %), and Na (0.9 ± 0.1 at. %). While the precipitate maintained the original lamellar structure, it had widened the thickness to approximately 3.2 μm ± 0.8 μm and narrowed interlamellar gap to 1.0 μm ± 0.2 μm. However, after two weeks, the lamellar structure was no longer visible, giving way to a dense HA mantle with a Ca/P ratio of 1.6 ± 0.1, which is closer to the stoichiometric HA ratio. This was accompanied by a diminished Si content (0.2 ± 0.1 at. %). Furthermore, the emergence of channels with a diameter of 263 ± 65.7 nm can be observed. Finally, after 21 days, the density of the channels was reduced, while the HA precipitate remained with a practically unchanged elemental composition.

The CS1Mg-0D sample exhibited a microstructure that was very similar to that of the CS0Mg-0D sample, characterised by the presence of Ca-Si rounded structures (Ca/Si = 0.5 ± 0.1) and large polygonal Ca-P crystals (Ca/P = 1.5 ± 0.1). This microstructure is similarly maintained after one day of treatment with SBF. After one week of immersion, an apatite-like precipitate with a Ca/P ratio of 1.6 ± 0.1 appeared in the form of isolated tangled spheres on top of Ca-P crystals with a Ca/P of 1.4 ± 0.1. Furthermore, the previously detected ions Si (3.0 ± 0.1 at. %), Mg (1.2 ± 0.1 at. %) and Na (1.6 ± 0.1 at. %) were identified in the HA precipitate. Although the quantity of precipitate increased after 14 days, it exhibited a lower Ca/P ratio of 1.4 ± 0.1, with a less defined and flattened shape, accompanied by a decline in Si content (0.2 ± 0.1 at. %) and an increase in Mg content (2.1 ± 0.1 at. %) while Na remained unchanged. The HA precipitate finally disappeared on day 21,

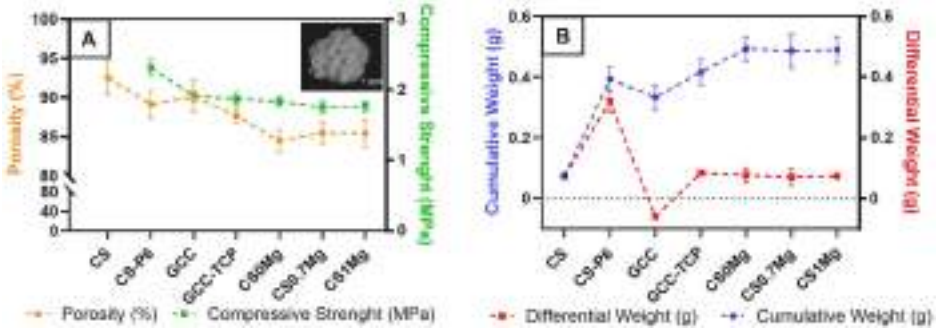

Fig. 4. Evolution of physical properties with deposition of new coatings. Representative optical image of scaffolds (window). Evolution of porosity and compressive strength of the scaffolds (A). Evolution of the total weight of the sample (cumulative weight) and weight contribution at each stage of scaffold formation (differential weight) (B).

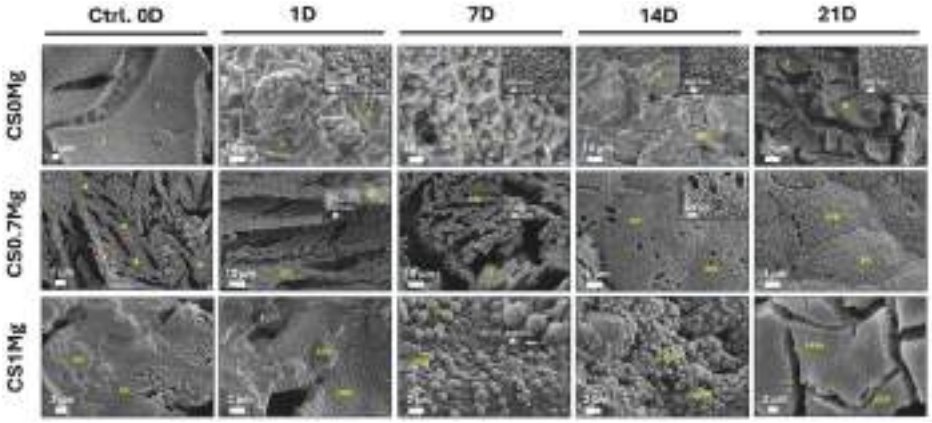

Fig. 5. *In vitro* bioactivity micrographs of the samples CS0Mg, CS0.7 Mg, CS1Mg, prior to SBF exposure (control, 0D), and following 1, 7, 14 and 21 days of treatment. The EDX analysis points are indicated by Roman numerals (I-XXIX). In the microstructure of sample CS0.7 Mg-0D, ▲ symbols indicate rounded grains, while ● symbols denote angular grains.

revealing the sphered structures of the control.

The concentration of specific ions was monitored as the immersion time elapsed during the *in vitro* bioactivity assay (Fig. 6). The ICP-OES results demonstrate the ionic interaction between the samples and the SBF. It can be observed that when the scaffolds presents an apatite-like precipitate and is therefore bioactive, there is a reduction in the concentration of P, which is used to deposit HA. Conversely, when HA is dissolved and bioactivity is lost, the concentration of P increases. Additionally, a contrary trend is evident in the behaviour of Si and P: an increase in the concentration of one is accompanied by a decrease in the concentration of the other.

3.3. Biodegradation

Fig. 7A depicts the biodegradation of the scaffolds in PBS (pH 7.4; 37 °C) over a period of 21 days. During the first week, the CS0Mg sample exhibited slightly lower degradation compared to CS0.7 Mg and CS1Mg. However, after 14 days of immersion, the degradation levels were found to be nearly identical. Ultimately, after 21 days, the total degradation of all the samples under study was approximately 15 %.

The CS0.7 Mg scaffold was identified as a promising candidate for further biological characterisation, based on its demonstrated capacity for sustained bioactivity *in vitro* and its topographical resemblance to native bone tissue.

The ICP-OES technique was employed to detect ionic variations in CCM and to relate them to cellular behaviour (Fig. 7B–E). At a concentration of 15 mg/mL, the CS0.7 Mg scaffold was observed to release quantifiable amounts of P and Si base ions, in addition to K and Li dopant ions. However, the variations in Mg and Na were found to be negligible. Conversely, the concentration of calcium in the CCM was observed to decrease. Similarly, for the 30 mg/mL concentration, P and Si were released into the solution along with K and Li in slightly higher concentrations than for the 15 mg/mL concentration. Once more, there was no significant alteration in the concentrations of Mg and Na, while a decrease was observed in the concentration of Ca.

Cell viability of cells exposed to the CCM are depicted in Fig. 7F–G. The results reveled that at a concentration of 15 mg/mL, CCM-48 was capable of inducing a statistically significant increase in cell proliferation compared to the control on Day 3 (***$p < 0.001$), and a moderate but significant increase on Day 2 (*$p < 0.05$) when compared to the control. Also, CCM-72 was found to enhance cellular viability (**$p < 0.05$) on Day 3. For the 30 mg/mL concentration, a significant increase in cellular population was observed on fibroblast exposed to CCM-48 on Days 1 and 3 (**$p < 0.01$), and a highly significant increase on Day 2 (***$p < 0.001$).

3.4. 3D cell culture

In light of the *in vitro* bioactivity test results for the CS0.7 Mg sample, which reveal interesting modifications in surface topography along with bioactivity, an alamarBlue assay was conducted to assess the impact of microstructure on cellular behaviour. This test was performed on CS0.7 Mg samples both prior to SBF immersion and after up to 14 days of immersion, given that the lamellar morphology is lost due to the formation of a dense HA precipitate.

The 3D direct assay revealed variations in cell viability based on CS0.7 Mg surface topography (Fig. 8). Initially, higher cell proliferation was observed in CS0.7 Mg-7D scaffolds, whose surface morphology consists of HA-coated lamellae (see Fig. 5), as well as in CS0.7 Mg-14D scaffolds, which present ion leakage channels on their surface, compared to CS0.7 Mg-0D scaffolds not exposed to SBF. After three days, the differences between the CS0.7 Mg-0D and CS0.7 Mg-1D groups disappear, but the difference between the CS0.7 Mg-1D and CS0.7 Mg-7D groups becomes statistically significant. After five days of culture, these differences are maintained, and statistically significant differences between the CS0.7 Mg-0D and CS0.7 Mg-7D groups reappear. Although no

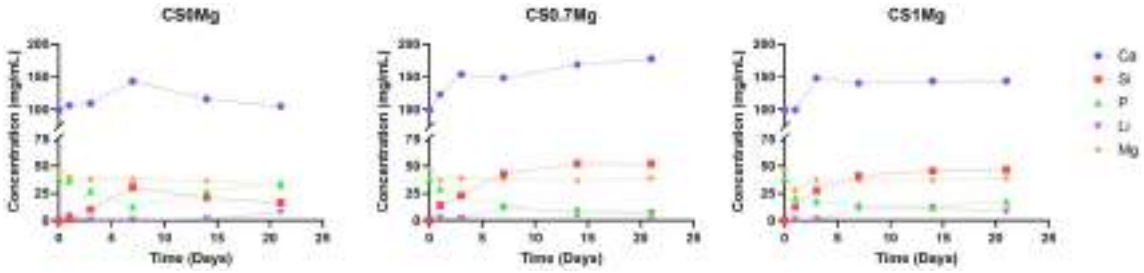

Fig. 6. SBF Ionic release during *in vitro* bioactivity assessment.

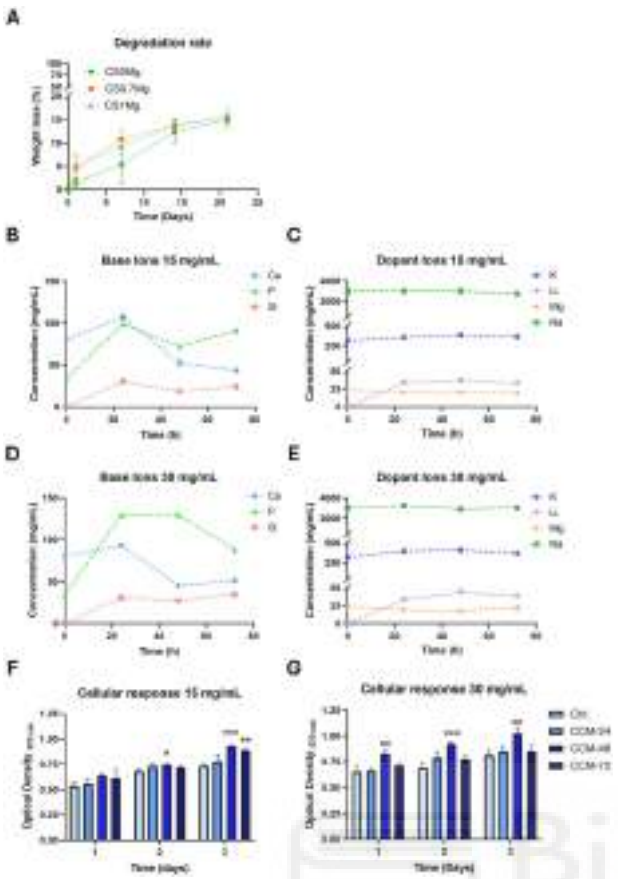

Fig. 7. Biodegradation study: (A) weight loss in PBS of the overall scaffolds; (B–E) ionic characterization of the dissolution products from the CS0.7 Mg scaffold; and (G–H) cellular response to the degradation products of CS0.7 Mg *p < 0.05, **p < 0.01, ***p < 0.001.

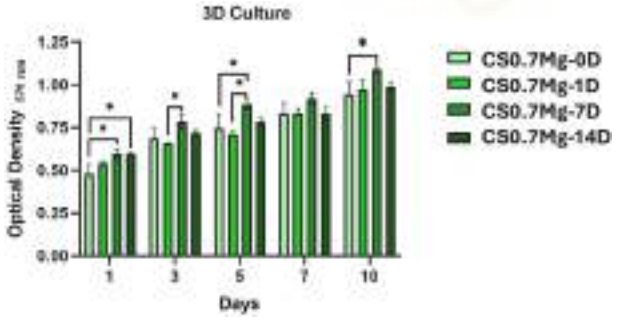

Fig. 8. Cellular proliferation based on CS0.7 Mg scaffold topography. Data are shown as means ± SD. N = 3, *p < 0.05.

differences between the groups are apparent at 7 days, a significant difference between CS0.7 Mg-0D and CS0.7 Mg-7D is observed at 10 days. As illustrated in Fig. 8, over time, there is constant cell growth, indicating desirable cytocompatibility *in vitro*.

4. Discussion

The design of bone scaffolds that support tissue regeneration in a safe and efficient manner presents a multifaceted challenge. In this study, multilayer scaffolds, based on the SiO_2-CaO-P_2O_5 system, were developed, which enables a strategic material integration to achieve more biomimetic scaffolds. Additionally, ion doping was employed to modify the surface topography and enhance bioactivity. The objective of these scaffolds is to closely mimic the natural bone environment, thereby enhancing their integration and performance in clinical settings.

Although the material composition consists of a Glass-Ceramic Core with a Dual Bioactive Shell functionalised with Na, K, and Mg (0–1% molar), the high temperatures employed during multiple sintering processes facilitated ionic migration between layers and phase transformation. Consequently, while the XRD analysis (Fig. 1A) indicated the presence of CS in the innermost layer, new crystalline phases, namely SiO_2 and $Ca_2P_2O_7$, along with minor amounts of $Ca_3(PO_4)_2$, appeared following coating with P6. This is likely due to the sequestration of calcium ions from CS ($CaSiO_3$) layer into the P6 ($Ca_2P_6O_{17}$), forming SiO_2 and $Ca_2P_2O_7$, and to a lesser extent $Ca_3(PO_4)_2$, due to its higher Ca/P ratio. This is clearly observed in the FESEM-EDX micrographs of the CS-P6 and GCC microstructure (Fig. 2). Polygonal crystals are observed with a decreasing Ca/P ratio from the centre towards the periphery. The regions with a higher calcium supply, are able to form β-TCP, while the more distal regions form calcium pyrophosphate. Regarding the glassy phase binding the crystals, it also underwent ionic exchange reactions, transitioning from an amorphous calcium phosphate ($Ca_2P_6O_{17}$) to a silicon-phosphate with reduced calcium content (Ca/P + Si ≈ 0.017). Furthermore, following TRIS-etching, although no appreciable variations were detected on XRD analysis (Fig. 1A), FESEM-EDX demonstrated that the presence of the glassy phase was significantly reduced (Fig. 2). This phase, due to its high reactivity, could cause local pH disruptions that not only impede the bioactivity of the system but also adversely affect cell metabolism and survival [45]. For this reason, various methods of preconditioning glass-based materials have been described in the scientific literature, including TRIS buffer solutions [45,46].

These phases detected in the GCC contribute to the synergistic functionality of the scaffolds. This is corroborated by the findings of Pattanashetti et al., who demonstrated that the incorporation of silica into polycaprolactone scaffolds led to a notable enhancement in cell proliferation in pre-osteoblast cells (MC3T3-E1), particularly at higher silica percentages [47]. Furthermore, this modification resulted in an improvement in the mechanical properties of the scaffold, which renders it a promising option for use in bone tissue engineering applications [47]. $Ca_2P_2O_7$ is traditionally viewed as an inhibitor of bone mineralization [48], but its role becomes more complex in the presence of alkaline phosphatase (ALP), a key enzyme involved in bone formation and mineralization. Normally inhibitory, calcium phosphate undergoes enzymatic hydrolysis by ALP, resulting in the release of phosphate ions that serve as essential precursors for HA formation [49,50].

In the GCC-TCP scaffold, an increase in the intensity of the β-TCP peaks was observed (Fig. 1B), which was confirmed by FESEM-EDX as a β-TCP layer covering the entire surface (Fig. 2). Upon the application of the dual bioactive shell, the presence of CS was again detected, along with other phases derived from ion doping. These included whitlockite, a non-stoichiometric phase of β-TCP with Mg, and akermanite, a calcium magnesium silicate (Fig. 1B).

Porosity represents a pivotal factor that exerts a profound impact on cellular processes. In addition to providing a structural framework, it facilitates cell infiltration and differentiation, affects extracellular matrix deposition, waste removal and vascularisation [51]. In this sense, the overall multilayer scaffolds (GCC + Dual Bioactive Shell) demonstrated comparable microporosity (<300 μm) (Fig. 3) and microporosity (>300 μm) (Fig. 4B) values regardless of the proportion of doping ions. The microporosity constituted 35 % of the total volume, with pore sizes ranging from 200 to 5 μm. These findings are encouraging, as pore diameters of 50–150 μm have been demonstrated to create an optimal environment for bone cell infiltration, while smaller pores facilitate nutrient and waste exchange throughout the scaffold and enhance pore interconnectivity [52,53]. In contrast, the macroporosity constituted 85 % of the total volume, which is notably high in comparison to other ceramic-glass scaffolds. Li et al. reported a similar total porosity of 75 %, which was demonstrated during *in vivo* studies to promote angiogenesis,

thereby supporting osteogenesis [54].

These porosity values become particularly significant when combined with a mechanical strength of approximately 2 MPa, which, according to G. Kaur et al., falls within the range of trabecular bone strength (1.7–7.5 MPa) [55].

However, to achieve optimal osteointegration, it is essential for the scaffolds to form a layer of HA on their surface upon exposure to SBF. *In vitro* bioactivity tests (Fig. 5) revealed that the three samples, CS0Mg, CS0.7 Mg, and CS1Mg, exhibited distinct behaviours over the 21-day study period. Initially, the control samples CS0Mg and CS1Mg, exhibited similar microstructures. These were characterised by the presence of plates covered with spherical calcium silicates (Ca/Si ≈ 0.5) and larger polygonal grains of β-TCP (Ca/P ≈ 1.5). In contrast, the surface of CS0.7 Mg exhibited striations, with grains of calcium silicophosphates containing a small amount of magnesium. This resulted in a Ca + Mg/P + Si ratio of approximately 0.8 (▲) or 1 (●), which suggests a wollastonite structure substituted with PO_4^{3-} tetrahedra and Mg^{2+}.

Upon early exposure to SBF (1 day), none of the samples exhibited the presence of HA. The surface of CS0Mg evolved into a filamentous structure, while CS1Mg remained practically unchanged. However, the striated structure of CS0.7 Mg became more defined, with thinner micro- and nanolamellae distributed arbitrarily. Given that bone microstructure is also irregular and lamellar, CS0.7 Mg-1D exhibited a high degree of trabecular bone mimicry, which is beneficial from both cellular and biomechanical perspectives, enabling proper load distribution.

Following seven days of SBF exposure, all three samples demonstrated bioactivity, as indicated by HA nucleation on their surfaces. Notably, clear differences were observed among the samples. CS0Mg displayed extensive HA deposits covering the entire surface, whereas CS1Mg showed small HA spheres on a still visible β-TCP background. CS0.7 Mg, on the other hand, retained its previously detected lamellar structure, now covered with HA doped with Si, Na and Mg. This further enhances bone mimicry by combining structural lamellar similarity with the presence of HA, the primary mineral phase in bone. Additionally, biological apatites are typically Ca-deficient and doped with other ions such as Si, Mg, and Na, which enhance their reactivity and bioactivity [56,57]. This finding positions CS0.7 Mg as a promising candidate for bone tissue regeneration.

After 14 days, all scaffolds maintained their HA deposits. In the case of CS0.7 Mg, the HA deposits significantly increased, obscuring the lamellae. In contrast, the HA deposits in CS1Mg increased to a lesser extent, allowing the underlying β-TCP crystals to be seen. After 21 days, CS0Mg and CS1Mg lost their HA deposits, which dissolved, exposing surfaces that were very similar to their controls. In contrast, the HA deposit on CS0.7 Mg remained.

This behaviour has been previously described by N. Mata et al., who report an intermittent bioactive behaviour [58]. The general behaviour is based on the inverse correlation between the concentrations of silicon and phosphorus in the SBF. An increase in the concentration of silicon and a decrease in that of phosphorus result in the precipitation of HA. Conversely, an increase in phosphorus concentration and a decrease in silicon indicates that previously precipitated HA is dissolved. This occurs because the previous elevation of silicate concentration reaches a saturation point, resulting in the precipitation of silicon- and calcium-rich phases that extract calcium from the previously precipitated HA. The dissolution of HA will result in an increase in the concentration of phosphate groups, which will eventually cause HA reprecipitation and thus generate a cyclic behaviour.

In consideration of the variations in bone remodelling throughout the lifespan, which are most pronounced during childhood and less active in adulthood, this approach allows for the potential customisation of the Mg content of implants to exhibit continuous or discontinuous bioactivity, according to the age and needs of the patient [58,59].

Biodegradation represents a fundamental aspect of third-generation ceramics, which are intended to regenerate rather than replace bone. The process allows for the progressive replacement of an implant with regenerated tissue, while also conferring therapeutic benefits derived from the dissolution products [60]. In this context, the biodegradation profiles of overall multilayer scaffolds as potential therapeutic candidate for bone injuries, were studied.

Firstly, the weight loss of the samples was monitored over a period of 21 days in PBS (Fig. 7A). Initially, CS0Mg exhibited a less pronounced biodegradation profile; however, over time, its degradation rate became similar to that of CS0.7 Mg and CS1Mg, reaching approximately 15 % by the 21st day. Ding et al. reported comparable *in vitro* biodegradability in SBF in GSG-1 hydrogels, which, in subsequent *in vivo* studies, correlated well with new bone deposition in rat models [61].

To gain further insight into the impact of biodegradation products on cells, fibroblasts were incubated with CCM at concentrations of 15 and 30 mg/mL (Fig. 7F–G). This indirect approach simulates the *in vivo* environment, providing valuable information about the impact on surrounding cells that are not in direct contact with the implant but contribute to extracellular matrix formation [62].

The results demonstrated that cell viability was enhanced in CCM-treated cultures, with the most pronounced improvement observed in those treated with CCM-3D and, to a lesser extent, in those treated with CCM-7D. The ionic composition of CCM, as determined by ICP-OES (Fig. 7B–E), indicated an increase in the ionic concentration of Si, P, K, and Li at both concentrations. This suggests that the observed improvement in cell proliferation is due to the synergistic effect of these ions. It is noteworthy that Na and Mg were not significantly released. While the simultaneous doping of scaffolds with Li, P and Si ions has not been documented in the literature, previous studies have highlighted the individual contributions of these ions to cell proliferation. Alali et al. demonstrated that lithium-doped titanium surfaces significantly enhanced the proliferation of human gingival fibroblasts [63]. Similarly, Pattanashetti et al. reported that silicon positively affects cell proliferation [47]. Furthermore, Shirali-Pour et al. found a positive correlation between the amount of β-TCP in poly(ε-caprolactone)/TCP composites and the proliferation of mesenchymal stem cells, highlighting the role of P in this process [64]. Furthermore, potassium is intimately linked with bone metabolism [65], and may facilitate cell viability by sustaining homeostasis and regulating membrane potential [66].

However, it is also essential to study the effect of the scaffold on the cells with which it is in direct contact. This direct approach, which involved three-dimensional cultures, revealed different proliferation rates depending on the topographies of CS0.7 Mg scaffold. While all topographies demonstrated an increase in cell population over time (Fig. 8), indicating good cytocompatibility, CS0.7 Mg-7D, which has the highest bone mimicry based on HA-coated lamellas, exhibited the highest proliferation among all time points studied. This effect can be attributed to the higher surface area, which provides more anchorage points for cells, thus enhancing cell adhesion and ultimately proliferation [67].

In addition, lamellar microstructures are well suited for drug loading and controlled release applications. Their layered nature provides multiple interlamellar pockets, which can serve as reservoirs for bioactive molecules such as drugs or growth factors. Lamellae also provide directional guidance for cells [67]. In this regard, osteoblasts may align with the lamellae, promoting the formation of organized bone tissue.

5. Conclusions

It is of great importance to optimise the structural properties of the bone scaffold in order to enhance its performance. By employing a combination of strategic material integration and ion doping, multilayer scaffolds were engineered to optimise their biological behaviour and osteointegration.

The designed scaffolds comprise a core primarily composed of SiO_2, $Ca_2P_2O_7$, and a Ca-deficient Si-P glass phase. Together, these phases provide a structural support with mechanical properties comparable to those of trabecular bone. Furthermore, the dual bioactive shell, confers

bioactive properties, thereby facilitating osseointegration and osteoconduction.

The differences in molar percentage of MgO led to the formation of distinct microstructures, while no significant variations were evident in the physical properties. Among the scaffolds studied, CS0.7 Mg exhibited an interesting lamellar topography, which was maintained during *in vitro* bioactivity tests (0–21 days), covered by a HA deposit until obscured. This microstructure has a high biomimicry with native bone and is suitable as a drug carrier due to its multiple interlamellar pockets. Biodegradation of this scaffold resulted in the release of Li, P, Si and K, which in indirect cell studies were found to increase cell viability of 3T3 fibroblasts compared to the control. In direct cell studies involving the different CS0.7 Mg scaffold topographies, the CS0.7 Mg-7D HA lamellar scaffold showed the highest cell proliferation, demonstrating its biocompatibility.

CRediT authorship contribution statement

Paula M. Riosalido: Writing – original draft, Investigation, Formal analysis. **Pablo Velásquez:** Methodology, Formal analysis. **Ángel Murciano:** Methodology, Formal analysis. **Piedad N. De Aza:** Validation, Supervision, Funding acquisition, Formal analysis.

Funding

This work is part of the project PID2020-116693RB-C21, funded by MCIN/AEI/10.13039/501100011033 Spain.

Declaration of competing interest

The authors declare that they have no known competing financial interests or personal relationships that could have appeared to influence the work reported in this paper.

Acknowledgements

P. M. Riosalido has received a grant CIAICO/2021/157 funded by the Generalitat Valenciana Spain.

Appendix A. Supplementary data

Supplementary data to this article can be found online at https://doi.org/10.1016/j.ceramint.2025.01.180.

References

[1] I.L. Tsiklin, A.v. Shabunin, A.v. Kolsanov, L.T. Volova, In vivo bone tissue engineering strategies: advances and prospects, Polymers 14 (15) (2022), https://doi.org/10.3390/polym14153222.
[2] P. Toogood, T. Miclau, Critical-sized bone defects: sequence and planning, J. Orthop. Trauma 31 (2017), https://doi.org/10.1097/BOT.0000000000000980.
[3] E. Roddy, M.R. DeBaun, A. Daoud-Gray, Y.P. Yang, M.J. Gardner, Treatment of critical-sized bone defects: clinical and tissue engineering perspectives, Eur. J. Orthop. Surg. Traumatol. 28 (Issue 3) (2018), https://doi.org/10.1007/s00590-017-2063-0.
[4] J.F. Keating, A.H.R.W. Simpson, C.M. Robinson, The management of fractures with bone loss, J. Bone Joint Surg. - Series B 87 (Issue 2) (2005), https://doi.org/10.1302/0301-620X.87B2.15874.
[5] R.J. O'Keefe, J. Mao, Bone tissue engineering and regeneration: from discovery to the clinic-an overview, Tissue Eng. B Rev. 17 (Issue 6) (2011), https://doi.org/10.1089/ten.teb.2011.0475.
[6] J.R. Perez, D. Kouroupis, D.J. Li, T.M. Best, L. Kaplan, D. Correa, Tissue engineering and cell-based therapies for fractures and bone defects, Front. Bioeng. Biotechnol. 6 (2018), https://doi.org/10.3389/fbioe.2018.00105.
[7] R.A. Youness, D.M. Tag El-deen, M.A. Taha, A review on calcium silicate ceramics: properties, limitations, and solutions for their use in biomedical applications, Silicon 15 (Issue 6) (2023), https://doi.org/10.1007/s12633-022-02207-3.
[8] P.N. de Aza, Z.B. Luklinska, A. Martinez, M.R. Anseau, F. Guitian, S. de Aza, S. de Aza, Morphological and structural study of pseudowollastonite implants in bone, J. Microsc. 197 (1) (2000), https://doi.org/10.1046/j.1365-2818.2000.00647.x.
[9] R.G. Carrodeguas, S. de Aza, α-Tricalcium phosphate: synthesis, properties and biomedical applications, Acta Biomater. 7 (10) (2011), https://doi.org/10.1016/j.actbio.2011.06.019.
[10] J. Jeong, J.H. Kim, J.H. Shim, N.S. Hwang, C.Y. Heo, Bioactive calcium phosphate materials and applications in bone regeneration, Biomater. Res. 23 (Issue 1) (2019), https://doi.org/10.1186/s40824-018-0149-3.
[11] S. Bauer, P. Schmuki, K. von der Mark, J. Park, Engineering biocompatible implant surfaces: Part I: materials and surfaces, Prog. Mater. Sci. 58 (3) (2013), https://doi.org/10.1016/j.pmatsci.2012.09.001.
[12] E. Martínez, E. Engel, J.A. Planell, J. Samitier, Effects of artificial micro- and nano-structured surfaces on cell behaviour, Ann. Anat. 191 (1) (2009), https://doi.org/10.1016/j.aanat.2008.05.006.
[13] V.M. Schatkoski, T. Larissa do Amaral Montanheiro, B.R. Canuto de Menezes, R. M. Pereira, K.F. Rodrigues, R.G. Ribas, D. Morais da Silva, G.P. Thim, Current advances concerning the most cited metal ions doped bioceramics and silicate-based bioactive glasses for bone tissue engineering, Ceram. Int. 47 (3) (2021), https://doi.org/10.1016/j.ceramint.2020.09.213.
[14] B. Yilmaz, A.Z. Alshemary, Z. Evis, Co-doped hydroxyapatites as potential materials for biomedical applications, Microchem. J. 144 (2019), https://doi.org/10.1016/j.microc.2018.10.007.
[15] D.E. Radulescu, O.R. Vasile, E. Andronescu, A. Ficai, Latest research of doped hydroxyapatite for bone tissue engineering, Int. J. Mol. Sci. 24 (Issue 17) (2023), https://doi.org/10.3390/ijms241713157.
[16] P. Gao, B. Fan, X. Yu, W. Liu, J. Wu, L. Shi, D. Yang, L. Tan, P. Wan, Y. Hao, S. Li, W. Hou, K. Yang, X. Li, Z. Guo, Biofunctional magnesium coated Ti6Al4V scaffold enhances osteogenesis and angiogenesis in vitro and in vivo for orthopedic application, Bioact. Mater. 5 (3) (2020), https://doi.org/10.1016/j.bioactmat.2020.04.019.
[17] L. Cao, W. Weng, X. Chen, J. Zhang, Q. Zhou, J. Cui, Y. Zhao, J.W. Shin, J. Su, Promotion of in vivo degradability, vascularization and osteogenesis of calcium sulfate-based bone cements containing nanoporous lithium doping magnesium silicate, Int. J. Nanomed. 12 (2017), https://doi.org/10.2147/IJN.S124965.
[18] L. Vannucci, C. Fossi, S. Quattrini, L. Guasti, B. Pampaloni, G. Gronchi, F. Giusti, C. Romagnoli, L. Cianferotti, G. Marcucci, M.L. Brandi, Calcium Intake in bone health: a focus on calcium-rich mineral waters, Nutrients 10 (Issue 12) (2018), https://doi.org/10.3390/nu10121930.
[19] K.H. Min, D.H. Kim, K.H. Kim, J.-H. Seo, S.P. Pack, Biomimetic scaffolds of calcium-based materials for bone regeneration, Biomimetics 9 (2024) 511, https://doi.org/10.3390/biomimetics9090511.
[20] S. Ma, Y. Yang, D.L. Carnes, K. Kim, S. Park, S.H. Oh, J.L. Ong, Effects of dissolved calcium and phosphorous on osteoblast responses, J. Oral Implantol. 31 (2) (2005), https://doi.org/10.1563/0-742.1.
[21] I.A. Fernández, H.J. Haugen, L.P. Nogueira, M.L. Álvarez, P. González, M.L. Peña, A.G. Cantalapiedra, F.M. Guzón, Bone regeneration in rabbit cranial defects: 3D printed polylactic acid scaffolds gradually enriched with marine bioderived calcium phosphate, Materialia 38 (2024) 102240, https://doi.org/10.1016/j.mtla.2024.102240.
[22] E. O'Neill, G. Awale, L. Daneshmandi, O. Umerah, K.W.H. Lo, The roles of ions on bone regeneration, Drug Discov. Today 23 (Issue 4) (2018), https://doi.org/10.1016/j.drudis.2018.01.049.
[23] M. Šupová, Substituted hydroxyapatites for biomedical applications: a review, Ceram. Int. 41 (8) (2015), https://doi.org/10.1016/j.ceramint.2015.03.316.
[24] T. Liu, M. Jin, Y. Zhang, W. Weng, T. Wang, H. Yang, L. Zhou, K+/Sr2+/Na+ triple-doped hydroxyapatites/GelMA composite hydrogel scaffold for the repair of bone defects, Ceram. Int. 47 (21) (2021), https://doi.org/10.1016/j.ceramint.2021.07.277.
[25] P. Keikhosravani, H. Maleki-Ghaleh, A.K. Khosrowshahi, M. Bodaghi, Z. Dargahi, M. Kavanlouei, P. Khademi-Azandehi, A. Fallah, Y. Beygi-Khosrowshahi, M. H. Siadati, Bioactivity and antibacterial behaviors of nanostructured lithium-doped hydroxyapatite for bone scaffold application, Int. J. Mol. Sci. 22 (17) (2021), https://doi.org/10.3390/ijms22179214.
[26] A.M. Pietak, J.W. Reid, M.J. Stott, M. Sayer, Silicon substitution in the calcium phosphate bioceramics, Biomaterials 28 (Issue 28) (2007), https://doi.org/10.1016/j.biomaterials.2007.05.003.
[27] C.L. Camiré, S.J. Saint-Jean, C. Mochales, P. Nevsten, J.S. Wang, L. Lidgren, I. McCarthy, M.P. Ginebra, Material characterization and in vivo behavior of silicon substituted α-tricalcium phosphate cement, J. Biomed. Mater. Res. B Appl. Biomater. 76 (2) (2006), https://doi.org/10.1002/jbm.b.30385.
[28] X.W. Li, H.Y. Yasuda, Y. Umakoshi, Bioactive ceramic composites sintered from hydroxyapatite and silica at 1200°C: preparation, microstructures and in vitro bone-like layer growth, J. Mater. Sci. Mater. Med. 17 (6) (2006), https://doi.org/10.1007/s10856-006-8942-2.
[29] C.T. Price, K.J. Koval, J.R. Langford, Silicon: a review of its potential role in the prevention and treatment of postmenopausal osteoporosis, Int. J. Endocrinol. 2013 (2013), https://doi.org/10.1155/2013/316783.
[30] W. Wang, K.W.K. Yeung, Bone grafts and biomaterials substitutes for bone defect repair: a review, Bioact. Mater. 2 (Issue 4) (2017), https://doi.org/10.1016/j.bioactmat.2017.05.007.
[31] M. Arora, E. Arora, The Promise of Silicon: bone regeneration and increased bone density, J. Arthrosc. Joint Surg. 4 (Issue 3) (2017), https://doi.org/10.1016/j.jajs.2017.10.003.
[32] A.R. Amini, C.T. Laurencin, S.P. Nukavarapu, Bone tissue engineering: recent advances and challenges, Crit. Rev. Biomed. Eng. 40 (5) (2012).
[33] G.L. Koons, M. Diba, A.G. Mikos, Materials design for bone-tissue engineering, Nat. Rev. Mater. 5 (Issue 8) (2020), https://doi.org/10.1038/s41578-020-0204-2.

[34] F. Barrère, C.A. van Blitterswijk, K. de Groot, Bone regeneration: molecular and cellular interactions with calcium phosphate ceramics, Int. J. Nanomed. 1 (Issue 3) (2006).
[35] Y.C. Chai, A. Carlier, J. Bolander, S.J. Roberts, L. Geris, J. Schrooten, H. van Oosterwyck, F.P. Luyten, Current views on calcium phosphate osteogenicity and the translation into effective bone regeneration strategies, Acta Biomater. 8 (11) (2012), https://doi.org/10.1016/j.actbio.2012.07.002.
[36] S.K. Venkatraman, S. Swamiappan, Review on calcium- and magnesium-based silicates for bone tissue engineering applications, J. Biomed. Mater. Res., Part A 108 (Issue 7) (2020), https://doi.org/10.1002/jbm.a.36925.
[37] X. Liu, M. Morra, A. Carpi, B. Li, Bioactive calcium silicate ceramics and coatings, Biomed. Pharmacother. 62 (8) (2008), https://doi.org/10.1016/j.biopha.2008.07.051.
[38] L. Jeevithan, P.M. Riosalido, Á. Murciano, P. Velásquez, P.N. De Aza, J. Elango, W. Wu, J.E. Mate Sanchez de Val, In vitro biocompatibility and stem cell regenerative assessment of hollow hydroxyapatite spheres deposited wollastonite/Ca2P6O17/TCP/doped-wollastonite scaffolds, Ceram. Int. 50 (20) (2024) 37779–37789, https://doi.org/10.1016/j.ceramint.2024.07.141.
[39] H. Ismail, M.N.Z. Zakri, A. Ahmad, H. Mohamad, Effect of sintering temperature on the phase, microstructural, physical, mechanical, and in vitro biomineralisation properties of porous wollastonite ceramics fabricated using the gel casting method, Ceram. Int. 49 (9) (2023), https://doi.org/10.1016/j.ceramint.2023.01.003.
[40] K. Yoshida, M. Kobayashi, H. Hyuga, N. Kondo, H. Kita, K. Hashimoto, Y. Toda, Reaction sintering of β-tricalcium phosphates and their mechanical properties, J. Eur. Ceram. Soc. 27 (10) (2007), https://doi.org/10.1016/j.jeurceramsoc.2006.12.004.
[41] P.M. Riosalido, P. Velásquez, Á. Murciano, P.N. De Aza, Surface morphology modulation in multilayer scaffolds via ion doping for bone tissue engineering, J. Am. Ceram. Soc. (2024), https://doi.org/10.1111/jace.20269. American Ceramic Society.
[42] L. Jeevithan, P.M. Riosalido, Á. Murciano, P. Velásquez, P.N. De Aza, J. Elango, W. Wu, J.E. Mate Sanchez de Val, In vitro biocompatibility and stem cell regenerative assessment of hollow hydroxyapatite spheres deposited wollastonite/Ca2P6O17/TCP/doped-wollastonite scaffolds, Ceram. Int. 50 (20) (2024) 37779–37789, https://doi.org/10.1016/j.ceramint.2024.07.141.
[43] International Organisation for Standardisation, Implants for Surgery — in Vitro Evaluation for Apatite-Forming Ability of Implant Materials (ISO Standard No. 23317:2014), 2014.
[44] International Organisation for Standardisation, Biological Evaluation of Medical Devices. Part 5: Tests for in Vitro Cytotoxicity (ISO Standard No. 10993-5:2009), 2009.
[45] F.E. Ciraldo, E. Boccardi, V. Melli, F. Westhauser, A.R. Boccaccini, Tackling bioactive glass excessive in vitro bioreactivity: preconditioning approaches for cell culture tests, Acta Biomater. 75 (2018), https://doi.org/10.1016/j.actbio.2018.05.019.
[46] M. Cerruti, D. Greenspan, K. Powers, Effect of pH and ionic strength on the reactivity of Bioglass® 45S5, Biomaterials 26 (14) (2005), https://doi.org/10.1016/j.biomaterials.2004.07.00941.
[47] N.A. Pattanashetti, S. Biscaia, C. Moura, G.R. Mitchell, M.Y. Kariduraganavar, Development of novel 3D scaffolds using BioExtruder by the incorporation of silica into polycaprolactone matrix for bone tissue engineering, Mater. Today Commun. 21 (2019), https://doi.org/10.1016/j.mtcomm.2019.100651.
[48] H. Fleisch, S. Bisaz, Mechanism of calcification: inhibitory role of pyrophosphate, Nature 195 (4844) (1962), https://doi.org/10.1038/195911a0.
[49] W.C. O'Neill, Pyrophosphate, alkaline phosphatase, and vascular calcification, Circ. Res. 99 (Issue 2) (2006), https://doi.org/10.1161/01.RES.0000234909.24367.a9.
[50] H. Fleisch, R.G.G. Russell, F. Straumann, Effect of pyrophosphate on hydroxyapatite and its implications in calcium homeostasis, Nature 212 (5065) (1966), https://doi.org/10.1038/212901a0.
[51] B. Bisht, A. Hope, A. Mukherjee, M.K. Paul, Advances in the fabrication of scaffold and 3D printing of biomimetic bone graft, Ann. Biomed. Eng. 49 (Issue 4) (2021), https://doi.org/10.1007/s10439-021-02752-9.
[52] C.I. Codrea, A.M. Croitoru, C.C. Baciu, A. Melinescu, D. Ficai, V. Fruth, A. Ficai, Advances in osteoporotic bone tissue engineering, J. Clin. Med. 10 (2) (2021), https://doi.org/10.3390/jcm10020253.
[53] M. Rasoulianboroujeni, N. Kiaie, F.S. Tabatabaei, A. Yadegari, F. Fahimipour, K. Khoshroo, L. Tayebi, Dual porosity protein-based scaffolds with enhanced cell infiltration and proliferation, Sci. Rep. 8 (1) (2018), https://doi.org/10.1038/s41598-018-33245-w.
[54] S. Li, Y. Cui, H. Liu, Y. Tian, Y. Fan, G. Wang, J. Wang, D. Wu, Y. Wang, Dual-functional 3D-printed porous bioactive scaffold enhanced bone repair by promoting osteogenesis and angiogenesis, Materials Today Bio 24 (2024), https://doi.org/10.1016/j.mtbio.2024.100943.
[55] G. Kaur, V. Kumar, F. Baino, J.C. Mauro, G. Pickrell, I. Evans, O. Bretcanu, Mechanical properties of bioactive glasses, ceramics, glass-ceramics and composites: state-of-the-art review and future challenges, Mater. Sci. Eng. C 104 (2019), https://doi.org/10.1016/j.msec.2019.109895.
[56] C. Combes, S. Cazalbou, C. Rey, Apatite biominerals, Minerals 6 (Issue 2) (2016), https://doi.org/10.3390/min6020034.
[57] Q. Liu, S. Huang, J.P. Matinlinna, Z. Chen, H. Pan, Insight into biological apatite: physiochemical properties and preparation approaches, BioMed Res. Int. 2013 (2013), https://doi.org/10.1155/2013/929748.
[58] N.A. Mata, P. Velasquez, A. Murciano, P.N. de Aza, Multilayer Mg-pyrophosphate glass ceramic with discontinuous bioactivity. Physicochemical characterization, Ceram. Int. 47 (10) (2021), https://doi.org/10.1016/j.ceramint.2021.02.044.
[59] L. del Rio, A. Carrascosa, F. Pons, M. Gusinyé, D. Yeste, F.M. Domenech, Bone mineral density of the lumbar spine in white mediterranean Spanish children and adolescents: changes related to age, sex, and puberty, Pediatr. Res. 35 (3) (1994), https://doi.org/10.1203/00006450-199403000-00018.
[60] A. Hoppe, N.S. Güldal, A.R. Boccaccini, A review of the biological response to ionic dissolution products from bioactive glasses and glass-ceramics, Biomaterials 32 (Issue 11) (2011), https://doi.org/10.1016/j.biomaterials.2011.01.004.
[61] P. Ding, O.V. Okoro, Y. Sun, L. Wang, X. Wei, S. Liu, Y. Deng, L. Fan, G. Jiang, L. Wang, A. Shavandi, L. Nie, Graphene oxide-reinforced alginate/gelatin hydrogel via Schiff-base bond and thiol-Michael addition for bone regeneration, Mater. Today Commun. 33 (2022), https://doi.org/10.1016/j.mtcomm.2022.104904.
[62] F. Westhauser, S. Decker, Q. Nawaz, F. Rehder, S. Wilkesmann, A. Moghaddam, E. Kunisch, A.R. Boccaccini, Impact of zinc-or copper-doped mesoporous bioactive glass nanoparticles on the osteogenic differentiation and matrix formation of mesenchymal stromal cells, Materials 14 (8) (2021), https://doi.org/10.3390/ma14081864.
[63] A.Q. Alali, A. Abdal-Hay, K. Gulati, S. Ivanovski, B.P.J. Fournier, R.S.B. Lee, Influence of bioinspired lithium-doped titanium implants on gingival fibroblast bioactivity and biofilm adhesion, Nanomaterials 11 (11) (2021), https://doi.org/10.3390/nano11112799.
[64] F. ShiraliPour, S.S. Shafiei, Y. Nikakhtar, Three-dimensional porous poly (ε-caprolactone)/beta-tricalcium phosphate microsphere-aggregated scaffold for bone tissue engineering, Int. J. Appl. Ceram. Technol. 18 (5) (2021), https://doi.org/10.1111/ijac.13770.
[65] F.A. Tylavsky, L.A. Spence, L. Harkness, The importance of calcium, potassium, and acid-base homeostasis in bone health and osteoporosis prevention, J. Nutr. 138 (1) (2008), https://doi.org/10.1093/jn/138.1.164s.
[66] R. Kettritz, J. Loffing, Potassium homeostasis – physiology and pharmacology in a clinical context, Pharmacol. Therapeut. 249 (2023), https://doi.org/10.1016/j.pharmthera.2023.108489.
[67] R.B. Vernon, M.D. Gooden, S.L. Lara, T.N. Wight, Microgrooved fibrillar collagen membranes as scaffolds for cell support and alignment, Biomaterials 26 (16) (2005), https://doi.org/10.1016/j.biomaterials.2004.08.011.

Artículo 3

Ceramics International 50 (2024) 37779–37789

Contents lists available at ScienceDirect

Ceramics International

journal homepage: www.elsevier.com/locate/ceramint

In vitro biocompatibility and stem cell regenerative assessment of hollow hydroxyapatite spheres deposited wollastonite/$Ca_2P_6O_{17}$/TCP/doped-wollastonite scaffolds

Lakshmi Jeevithan [a,1], Paula M. Riosalido [b,1], Ángel Murciano [c], Pablo Velásquez [b], Piedad N. De Aza [b], Jeevithan Elango [a,d,e], Wenhui Wu [a,**], Jose Eduardo Mate Sanchez de Val [d,*]

[a] Department of Marine Biopharmacology, College of Food Science and Technology, Shanghai Ocean University, Shanghai, 201306, China
[b] Instituto de Bioingeniería, Universidad Miguel Hernández, Avda. Ferrocarril s/n, Elche, Alicante, 03202, Spain
[c] Departamento de Materiales, Óptica y Tecnología Electrónica, Universidad Miguel Hernández, Avda. Universidad s/n, Elche, Alicante, 03202, Spain
[d] Department of Biomaterials Engineering, Faculty of Health Sciences, UCAM Universidad Católica San Antonio de Murcia, Guadalupe, 30107, Murcia, Spain
[e] Center of Molecular Medicine and Diagnostics (COMManD), Department of Biochemistry, Saveetha Dental College and Hospitals, Saveetha Institute of Medical and Technical Sciences (SIMATS), Saveetha University, Chennai, 600 077, India

ARTICLE INFO

Handling Editor: Dr P. Vincenzini

Keywords:
Multilayer scaffolds
Hydroxyapatite hollow spheres
Biocompatibility
Fibroblasts
Mesenchymal stem cells

ABSTRACT

This research examines the biological behavior of multilayer ceramic-glass scaffolds for bone tissue engineering. The scaffolds consist of a high-strength core of wollastonite and P6 ($Ca_2P_6O_{17}$), with a sequential coating of TCP and wollastonite doped with Na^+, K^+ and Mg^{2+} ions to confer bioactivity to the system. Two formulations were investigated: a magnesium-deficient one, which served as a microstructure control, and a magnesium-rich one in which hollow hydroxyapatite (HA) spheres precipitated after one week of immersion in simulated body fluid (SBF). These formulations are denoted as C-Scaffold and HA-Scaffold, respectively. Further exploration and comparison of the physiological effects of both scaffolds is necessary to fully understand their potential as drug release agents and associated therapeutic advantages. The study considered aspects such as protein adhesion, cell morphology, and the inflammatory response. The results showed that the HA-Scaffold had over 34 % more plasma protein adhesion compared to the C-Scaffold. Similarly, cell proliferation assays showed increased cell growth in both HFF-1 fibroblasts and mesenchymal stem cells (MSCs) treated with HA-Scaffold compared to C-Scaffold. This may be attributed to the higher protein adsorption, which acts as a facilitator for cell adhesion. Three-dimensional photography from computerized microtomography confirmed that the scaffolds have a similar morphology and porosity to the intricate structure of trabecular bone in the humeral head. The study shows that the scaffolds made of Wollastonite/$Ca_2P_6O_{17}$/TCP/Doped-Wollastonite with HA hollow spheres are highly suitable for use in this bone segment due to their overall porosity of over 86 % and approximate mechanical strength of 1.6 MPa. These findings demonstrate the biocompatibility and enhanced biological properties of the scaffolds, making them an excellent material for bone tissue engineering.

1. Introduction

The world population, characterized by constant aging, is facing a significant increase in the frequency of bone defects [1–3]. This phenomenon is reflected in concerning statistics, highlighting the urgent need to address these conditions effectively. While bone transplantation remains the gold standard for treating skeletal defects, it is burdened by substantial drawbacks, encompassing high costs and associated risks such as inflammation, neurovascular damage, immune rejection, or inadequate osseointegration [4–7].

The limitations of current therapeutic options drive research efforts toward more effective and innovative solutions. In this context, bone

* Corresponding author.
** Corresponding author.
E-mail addresses: lakshmijeevithan@gmail.com (L. Jeevithan), priosalido@umh.es (P.M. Riosalido), amurciano@umh.es (Á. Murciano), pavelasquez@umh.es (P. Velásquez), piedad@umh.es (P.N. De Aza), jelango@ucam.edu (J. Elango), whwu@shou.edu.cn (W. Wu), jemate@ucam.edu (J.E. Mate Sanchez de Val).
[1] These authors contributed equally.

https://doi.org/10.1016/j.ceramint.2024.07.141
Received 26 March 2024; Received in revised form 25 June 2024; Accepted 11 July 2024
Available online 14 July 2024

tissue engineering arises to overcome the inherent challenges in osseous regeneration by formulating artificial, functional structures that exhibit properties and an architecture resembling those of native bone [3,7,8]. In this regard, the careful choice of both the material and the fabrication method is critical [7,8]. Among the various methodologies available, the Sol-Gel approach stands out as an essential tool, distinguished by its versatility and ability to generate scaffolds with specific properties [9–11]. This method offers the possibility of integrating different materials into a single structure through the deposition of various coatings, resulting in the formation of multilayer scaffolds.

The strategic choice of these materials seeks to provide beneficial and essential functions to stimulate and direct bone regeneration, highlighting properties such as mechanical strength, crucial in osseous defects affecting bone under load, as well as biocompatibility, bioactivity and osteoinduction.

The multilayer scaffolds under study are comprised, progressively from the core outwards, of wollastonite, the glassy phase known as P6 ($Ca_2P_6O_{17}$), tricalcium phosphate (TCP) and, as the surface phase, wollastonite doped with Na^+, K^+ and Mg^{2+} ions. The combination of the properties of P6 as a cohesive agent, TCP as a source of Ca and P, and the bioactivity of wollastonite, together with the ion doping strategy, makes these scaffolds a promising clinical alternative to current treatments. Our recent study reported the fabrication of alumina based-wollastonite multilayer porous scaffolds for bone tissue engineering [12]. Earlier studies also attempted to investigate the bone regenerative ability of multilayer wollastonite scaffolds combined with TCP [13,14], fibrin [15], poly(lactic acid) [16], Zn and Mg doping [17], poly(L-lactide)/apatite [18], and chitosan/apatite [19]. Furthermore, previous studies have outlined that, upon immersing these scaffolds in simulated body fluid (SBF), hollow spheres of hydroxyapatite (HA) precipitate, revealing their potential as agents for controlled drug release [20–22]. Given the associated advantageous prospects, this study investigated the interaction of these scaffolds with biological systems, aiming to predict their *in vivo* response.

2. Materials and methods

2.1. Fabrication of multilayer scaffolds

The multilayer scaffolds were fabricated using the Sol-Gel method along with the polymer sponge replication technique. A 20 ppi polyurethane sponge served as a template for depositing the different materials that comprise the scaffolds, selecting the indicated porosity of the polyurethane sponge in order to obtain a final open porosity within the range 50–300 μm. The wollastonite internal layer was formed by combining 19.28 mL of Tetraethyl Orthosilicate (TEOS, Aldrich 98 %), 8.62 g of calcium carbonate ($CaCO_3$, Sigma ≥99 %), 5 mL of ethanol, 20 mL of distilled water, and 1 mL of hydrochloric acid (HCl 37 %, Ensure). After sintering, the polymer sponge was replaced by wollastonite, which served as the new ceramic template for the following layers.

Next, a layer containing the vitreous phase P6 was added to the scaffold in order to enhance the mechanical strength and tackle the brittleness of the wollastonite core. The composition was created by mixing 18.46 mL of Triethyl Phosphate (TEP, Aldrich ≥99.8 %), 3.72 g of $CaCO_3$, 1 g of lithium carbonate (Li_2CO_3, Sigma-Aldrich ≥99 %), 5 mL of ethanol, 20 mL of distilled water, and 2 mL of HCl 37 %. The excess glassy phase was removed from the core through a chemical attack process using an etching solution called TRIS. To create this solution, 7.6 g of tris(hydroxymethyl)aminomethane ($NH_2C(CH_2OH)_3$, Sigma Aldrich ≥99.8 %); and 1.168 g of calcium chloride ($CaCl_2$, Riedel-de Haën ≥97 %) were diluted in distilled water and HCl to a final volume of 1 L. The pH was finally adjusted to a value ranging from 7.3 to 7.4. The cores were then immersed in 50 mL of the solution and maintained at 50 °C for 24 h. The subsequent step involved the application of a third layer, comprising TCP, which served as a source of calcium and phosphate ions to facilitate HA deposition. The layer was formed through a chemical reaction involving 10.965 mL of TEP, 9.68 g of $CaCO_3$, 5 mL of ethanol, 20 mL of distilled water, and 2 mL of 37 % HCl.

Finally, wollastonite was once again chosen as the surface layer. The layer was formulated as described above, with the addition of 0.5 g sodium carbonate (Na_2CO_3, Sigma ≥99 %), 0.5 g of potassium carbonate (K_2CO_3, Sigma ≥99 %) (C-Scaffold), and an additional 0.5 g of magnesium carbonate ($MgCO_3$, Sigma Aldrich ≥99 %) (HA-Scaffold). It is worth noting that the pH of all syntheses was adjusted to a value of 2–3. After applying sufficient layers of each material, the sample underwent a sintering process. The temperature was gradually increased from room temperature to 1050 °C, with a holding time of 8 h, and finally cooled to room temperature. The heating rate for the initial layer was approximately 0.32 °C/min, while it was significantly accelerated up to 2 °C/min for the subsequent layers.

To enhance the bio-functional properties, the hollow HA spheres were precipitated on the HA-Scaffold after 7 days of immersion in simulated body fluid (SBF) and were sustained for an additional 7 days during *in vitro* bioactivity tests (ISO 23317). Subsequently, HA-Scaffold samples were immersed in Falcon tubes containing 50 mL of SBF and incubated for 7 days in a shaking water bath set to physiological temperature (37 ± 0.5 °C). Therefore, the C-Scaffold, which lacks Mg^{2+} and HA, was used as the control scaffold. Table 1 shows the molar percentages of both specimens.

Table 1
The molar fraction of the studied scaffolds.

Component	Molar fraction	
	C-Scaffold	HA-Scaffold
SiO_2	0.248	0.244
CaO	0.494	0.494
P_2O_5	0.207	0.204
Li_2O	0.039	0.038
Na_2O	0.007	0.007
K_2O	0.005	0.005
MgO	–	0.008

2.2. Characterization

2.2.1. Mineralogical characterization

Once the two types of scaffolds were obtained, the mineralogical characterization was carried out by X-ray diffraction (XRD). A Bruker-AXR D8 Advance automated diffractometer using Cu-Kα radiation (1.54056 Å) was used. The Bragg-Brentano theta-2thetha (θ/2θ) geometry was employed to collect the experimental data between 15° and 40° (2θ) at 0.05 steps, and a scanning speed of 5 s. The experimental data was analyzed with the Power Diffraction Match! version 3.16 Build 288 software. The thermal degradation profile of the fabricated scaffold was done by thermogravimetric analysis (TG, Japan Hitachi STA200) in a nitrogen atmosphere with a temperature ranging from 35 to 1100 °C.

2.2.2. Macro and microstructure characterization

The macrostructure of the scaffolds was analyzed using a Nikon SMZ1500 stereomicroscope equipped with a Nikon DXM1200F digital camera. Additionally, the microstructure of the scaffolds was investigated through Field Emission Scanning Electron Microscopy (FESEM) using a ZEISS Sigma 300 VP instrument, coupled with Energy-dispersive X-ray spectroscopy (EDX) from ZEISS SmartEDX. The scanning resolution was set to 5 kV. To improve electrical conductivity and acquire more precise images and spectral data, the samples were metalized with palladium before electron microscopy.

2.2.3. Physical characterization

Given the importance of scaffold porosity, a study of this feature was carried out using the mercury porosimetry technique. A Poromaster 60 GT (Quantachrome Instruments) was used, which worked with a

pressure between 6.393 KPa and 242,995.531 KPa. Pycnometric analysis was also used to determine the macroporosity of the sample. These data were supplemented with the mechanical strength of samples. A compression test was conducted using a Simple Manual Test Stand (SVL-1000 N, IMADA) where samples were subjected to increasing values of manually applied pressure until the sample breakage occurred.

2.3. Effect of scaffolds in plasma protein adhesion

In order to determine the plasma protein adhesion, both the C-Scaffold and HA-scaffolds were incubated in Fetal Bovine Serum (FBS) at 37 °C for 4 h. Then, the FBS was removed, and the scaffolds were washed with Phosphate Buffer Saline (PBS) gently twice, followed by staining with Coomassie Brilliant blue (CBB) G-250 for 2 h at 37 °C. The excess stain was washed out with a destaining solution containing a methanol-water-acetic acid mixture overnight. The FBS untreated scaffolds (Blank) were also stained with CBB G-250. The amount of protein absorbed on the scaffold was determined by measuring the optical density of the supernatant at 590 nm as per our previous method [23].

2.4. Cell culture

The Mesenchymal Stem Cells (MSC) from human bone marrow (CTCC-113-HUM) and Human Foreskin Fibroblasts (HFF-1) (CTCC-001-0346) were purchased from Zhejiang Matson Cell Technology Co., Ltd. (MeisenCTCC), Shanghai, China). The cells were cultured as per the seller's recommendations. Briefly, the MSC cells were cultured in mesenchymal stem cell growth medium (Cat No: CTCC-S019-HUM-M, Lot No: M23SF2204) without FBS and HFF-1 cells were cultured in Dulbecco's Modified Eagle Medium (DMEM) medium containing 15 % FBS with 1 % antibiotics (Penicillin and Streptomycin). The cells were cultured in a standard way until 80 % confluence and then sub-cultured. The cells from passages 3–8 were used for the following experiments. Samples (C-Scaffold and HA-Scaffold) were UV-sterilized for 30 min before cell culture use. The sterilized samples were briefly washed with PBS and equilibrated with respective culture mediums for cell culture.

2.5. Effect of the scaffold on MSC proliferation

The effect of both the C-Scaffold and HA-Scaffold on the proliferation of MSCs was determined as per the previous method [24]. Briefly, the MSCs with a cell density of 5×10^5 seeded on scaffolds in 48 well plates were cultured with a mesenchymal stem cell growth medium.

In parallel, the cells were cultured with Scaffold Conditioned Medium (SCM). The SCM was prepared by incubating scaffolds in mesenchymal stem cell growth medium for 24 h and collected by centrifuge at 2000 g for 5 min. The cells without scaffold or SCM were considered as controls. Both scaffold-seeded and SCM-treated cells were cultured for 3 days and 7 days. After the treatment, the cells were briefly washed with PBS prior to the cck-8 experiment. The proliferation rate of cells was determined by culturing the cells with basal culture medium containing cck-8 reagent for 2 h and measured at 450 nm.

2.6. Biocompatibility

The biocompatibility of both the C-Scaffold and HA-Scaffold was investigated by using HFF-1 cells. Briefly, the HFF-1 cells with a cell density of 1×10^6 per well in 48 well plates, were seeded on both the C-Scaffold and HA-Scaffold and were cultured with DMEM medium containing 15 % FBS for 3 days and 7 days. The compatibility of scaffolds on HFF-1 cells was investigated by the cck-8 method following the previous method. The cells cultured without scaffolds were considered as control.

2.7. Effect of the scaffolds in inflammatory response

To further confirm the biocompatibility, the cellular inflammatory response was measured after treating cells with scaffolds. The MSCs and HFF-1 cells with a cell density of 5×10^5 per well in 98 well plates were seeded on scaffolds and cultured with mesenchymal stem cell growth medium and DMEM medium, respectively, for 3 days and 7 days. After treatment, the cell supernatant was collected after centrifuge at 2000 g for 5 min, and stored at −20 °C until use. The level of cellular cytokines was determined by using IL-2 and IL-6 ELISA kits. The quantitative measurement of IL-2 and IL-6 was determined by following the manufacturer's instructions. The reference standard curves for IL-2 with gradient concentrations (0, 20 pg, 40 pg, 80 pg, 160 pg and 320 pg) and for IL-6 with gradient concentrations (0, 10 pg, 20 pg, 40 pg, 80 pg and160 pg) were plotted (Supplementary Fig. S1 and Fig. S2) for measuring the test sample concentrations.

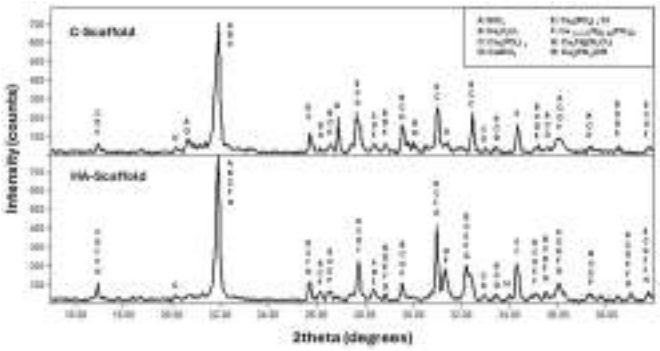

Fig. 1. XRD diffraction patterns of the C-Scaffold (A) and HA-Scaffold (B).

2.8. Effect of the scaffolds on cell morphology

Changes in the morphological features of MSC and HFF-1 after being cultured on scaffolds were determined by SEM [Oxford Xplore, ZEISS GeminiSEM 300]. For this purpose, the MSCs and HFF-1 cells with a cell density of 1×10^6 per well in 24 well plates were cultured on both the C-Scaffold and HA-Scaffold with respective culture media for 3 days and 7 days. After cell culture, the cells on scaffolds were washed with PBS and fixed with 2.5 % glutaraldehyde for 30 min and 4 % formaldehyde for 30 min. After fixation, the scaffold samples with cells were dehydrated with gradient alcohol concentrations (0, 25 %, 50 %, 75 % and 100 % ethanol in PBS) for 10 min each. The dehydrated scaffold cells were air-dried overnight in a sterile biosafety cabinet. Then, scaffold cells were sputter-coated with gold and images were captured by SEM at different magnifications with 15 kV resolution.

2.9. Osteogenic differentiation

The ability of scaffolds in stem cell regeneration was further confirmed by osteogenic differentiation of MSCs culturing with scaffold condition medium. In brief, the MSCs (1×10^6/well) were seeded in 24 well plates and cultured for 21 days with osteogenic medium containing supplements (Shanghai QiDa Biotechnology Co., Ltd, Lot No: P1301) along with scaffold conditioned medium. Osteogenic differentiation was confirmed by standard osteogenic staining methods using alizarin red and von Kossa stains for calcium deposition, and alkaline phosphatase stain.

2.10. Statistical analysis

All the experiments were conducted with triplicate samples, and a concordant value was obtained from these experiments. The values were expressed as means ± SD unless otherwise indicated. The statistical difference and comparisons were made using one-way ANOVA analysis and a p-value less than 0.05 was noted as statistical significance after treating the data in GraphPad Prism 9.4.0 software.

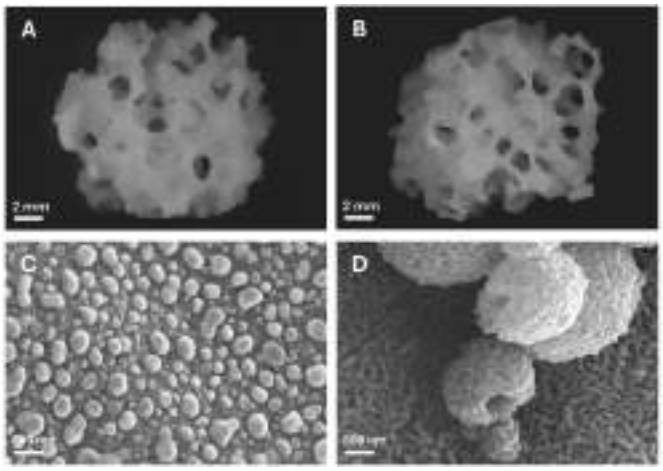

Fig. 2. Structural study of multilayer scaffolds. Optical images of the macrostructure in the top (A) and front view (B), together with FESEM-EDX images of the microstructure of the C-Scaffold (C) and HA-Scaffold (D).

3. Results and discussion

3.1. Mineralogical characterization

As for the mineralogical examination, Fig. 1 shows the XRD spectra of C-Scaffold (Fig. 1A) and HA-Scaffold (Fig. 1B). The XRD spectra confirmed the presence of three layers in both C-Scaffold and HA-Scaffold, and several phases were identified in both scaffolds. These phases were cristobalite (A) (COD 96-900-8225), calcium diphosphate (B) (COD 96-100-1557), TCP (C) (COD 96-151-7239), wollastonite (D) (COD 96-900-5779), and chlorapatite (E) (COD 96-210-5266). In addition, the HA-Scaffold also exhibited magnesium-rich compounds, namely whitlockite, with $Ca_{10.115}\,Mg_{3.85}PO_4$ formula, (F) (COD 96-901-2137) and akermanite, $Ca_2MgSi_2O_7$, (G) (COD 96-900-6942), as well as HA (H) (COD 96-901-4314).

Considering that ionic conductivity is directly proportional to temperature, ionic migration is expected to increase during sintering [25]. This would explain the formation of cristobalite and calcium pyrophosphate (from $CaSiO_3$ and $Ca_2P_6O_{17}$) and whitlockite (from $CaSiO_3$–Na^+, K^+, Mg^{2+} and TCP). However, the chlorapatites was likely formed due to the HCl used in the synthesis process.

The presence of HA peak in the HA-Scaffold confirmed the successful deposition of HA during SBF incubation and the bioactivity of the sample. HA ($Ca_{10}(PO_4)_6(OH)_2$) is the primary inorganic component of human bone [3,7] and is commercially used in bone implants due to its good biocompatibility and ability to integrate seamlessly with natural bone tissue [3,26–28].

3.2. Microstructure

The scaffolds exhibited a macrostructure with open porosity and interconnected porosity, as shown in Fig. 2A and B. As for the microstructure, the surface of the C-Scaffold (Fig. 2C) showed a regular pattern consisting of circular structures mainly composed of calcium and silicon, with a Ca/Si ratio of 0.5 ± 0.07, suggesting the presence of calcium disilicide ($CaSi_2$). Silicates are thought to play an important role in promoting bone matrix formation, given their ability to form a surface HA layer, activated by the dissolution of calcium and silicate ions [29,30].

Upon scanning the HA-Scaffold, their surface was completely covered by a dense, and elongated precipitate (Fig. 2D). This precipitate was rich in calcium and phosphorus at a ratio of 1.62 ± 0.07, which is very similar to the stoichiometric HA Ca/P ratio of 1.67. Additionally, hollow spheres formed by the same elongated structures with a Ca/P ratio of 1.69 ± 0.11 were observed on this deposit. The precipitation of HA can be attributed to the silicate outer layer of the scaffold. This layer promotes the formation of a HA layer through ionic exchange reactions, as described by Hench [31]. Also, this HA layer is capable of binding to bone and a potentially a pro-osteoinductive factor [29]. The morphology of the hollow HA spheres is controlled by the magnesium concentration, while the amount of HA spheres precipitated is controlled by the days of immersion in SBF. Only with seven days of soaking in SBF hollow HA spheres are deposited.

3.3. Physical characterization

As for the physical characterization, the Hg porosimetry technique was used to evaluate the microporosity (<300 μm) of both the C-Scaffold and the HA-Scaffold. The C-Scaffold presented a total porosity of 26.61 %, of which 19.22 % was attributed to interparticle porosity, with a diameter range of 121 - 5.21 μm. The remaining 7.39 % corresponded to intraparticle porosity, characterized by smaller pores with diameters ranging from 0.342 to 0.018 μm. In comparison, the HA-Scaffold

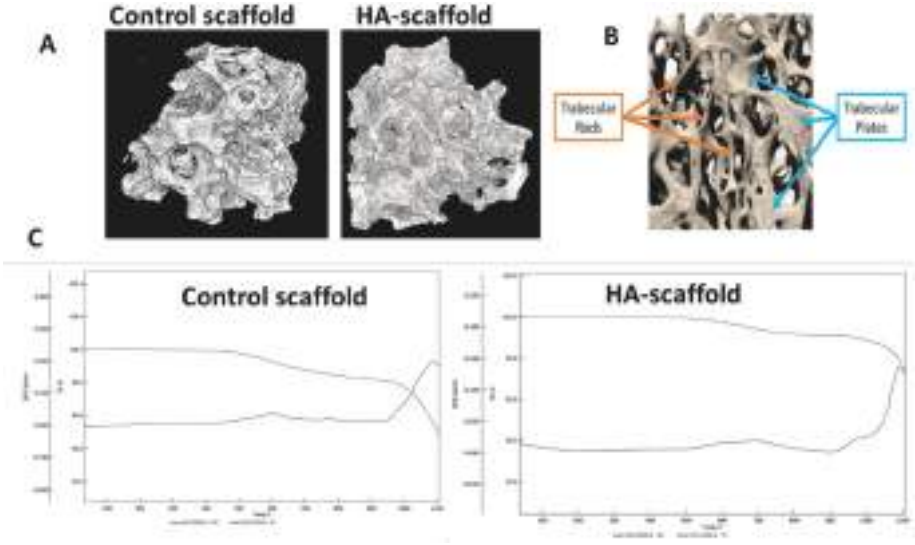

Fig. 3. Micro-CT images (A), Reference image (B) showing Rod and plate distribution in a human humeral head [41] and Thermogravimetry analysis (C) of C-Scaffold and HA-scaffold.

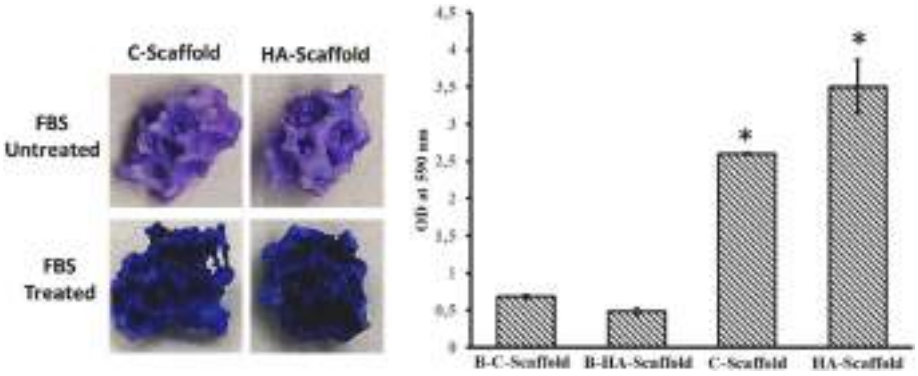

Fig. 4. The efficiency of Protein adsorption of C-Scaffold and HA-Scaffold treated with fetal bovine serum (FBS). B–C-Scaffold: Blank control scaffold (FBS untreated), B-HA-Scaffold: Blank HA-scaffold (FBS untreated), C-scaffold: control scaffold after FBS treatment, HA-scaffold: HA-scaffolds after FBS treatment. * denotes statistical significance with respective blank, $p < 0.05$.

showed, on average, total values, and a larger pore size. Total porosity was 32.4 %, distributed as 28.06 % interparticle porosity and 4.34 % intraparticle porosity. Interpore diameters varied from 172 to 6.16 μm, while intrapore diameters ranged from 0.82 to 0.034 μm. These findings are of biological significance since previous research has shown that pore sizes between 50 and 150 μm promote the exchange of nutrients and waste products through the scaffold, as well as facilitating cell colonization [32].

Furthermore, pycnometry results showed a total macroporosity, corresponding to pores >300 μM, of 86.1 ± 0.4 % in the C-Scaffold and 87.3 ± 0.6 % in the HA scaffold, relative to the total volume of the samples. These values are quite high compared to other ceramic scaffolds [33–35]. In addition, a higher rate of angiogenesis has been demonstrated to be directly related to the high scaffold macroporosity [36]. These data were complemented by the results of the compression test. The mechanical behavior of both samples was very similar, showing an approximate strength of 1.57 ± 0.2 MPa for the C-Scaffold and 1.68 ± 0.17 MPa for the HA-Scaffold. The reported strength is within the range of trabecular bone as reported by Caeiro et al. [37].

3.4. Micro-CT

Micro-CT images of both the C-Scaffold and HA-Scaffold are presented in Fig. 3A. The 3D images of micro-CT results showed that both scaffolds possessed more interconnected micro- and macro-porous structures. Interestingly, in the present study, the porous structures of scaffolds exactly mimic the trabecular spacing, trabecular rods and trabecular plates of the human humeral head (Fig. 3B).

The TGA analysis investigated the thermal denaturation profile of both the C-Scaffold and HA-scaffolds (Fig. 3C). The results showed that the first derivative of the TGA curve i.e. DTG curve, which measures the rate of sample decomposition with regards to time and temperature, was decreased slowly with respect to temperature in both the C-Scaffold and HA-scaffold. The maximum percentage of DTG was obtained at 1086.56 °C for the C-Scaffold and 1092.21 °C for HA-Scaffold, respectively. Previously, the decomposition of wollastonite hydrogel composed of silicon, Sr/Se/Zn/Mg-substituted hydroxyapatite/chitosan had a maximum TGA curve at ~850 °C [38]. In another study, the degradation behavior of β-wollastonite derived from natural waste showed that the exothermic peak observed at 778 °C indicated the starting temperature for crystallization of β-wollastonite [39]. These authors further concluded that the thermal decomposition of β-wollastonite takes place in different steps, i.e. 8.4 % weight loss from room temperature to 220 °C, 5.18 % weight loss from 220 to 600 °C and 2.5 % weight loss from 600 to 750 °C were occurred due to removal of residual water, low-temperature, and high-temperature decarbonisation, respectively [39,40].

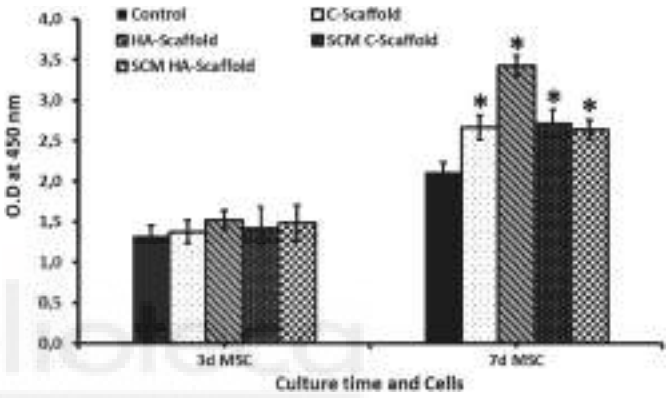

Fig. 5. The MSCs proliferative effect of C-Scaffold, HA-Scaffold and their conditioned medium (SCM). Control: cells cultured without scaffolds, C-Scaffold: cells cultured on control scaffold, HA-scaffold: cells cultured on HA-scaffold, SCM C-Scaffold: cells cultured on SCM of control scaffolds, SCM HA scaffold: cells cultured on scaffold conditioned medium of HA scaffolds. * denotes statistical significance compared to the control group (without scaffold), $P < 0.05$.

3.5. Protein adsorption

To evaluate the interaction ability of scaffolds with plasma protein receptors, scaffolds were treated with FBS and stained with CBB G-250. The protein adsorption of the C-Scaffold was about 2.6 ± 0.26 (61.2 %), which was lower than the HA-Scaffold (3.5 ± 0.11, 82.4 %), proving that the HA precipitate on the scaffold stimulated the interaction between matrix and plasma protein (Fig. 4). In addition, the blank C-Scaffold (15.9 %) and blank HA-Scaffold (11.3 %) were also partially stained with CBB G-250, even without FBS incubation, which might be due to the possible interaction of CBB G-250 dye with the active functional groups present in wollastonite and HA, respectively. Interestingly, the protein adsorption highly occurred in the interior component (inside the porous structure) of both the C-Scaffold and HA-Scaffold as evidenced by the high staining intensity of CBB G-250 observed in those regions. Our previous studies also claimed the same effect of protein adsorption in germanium-coated hydroxyapatite biomaterials and the surface coating of these materials with ethanol did not contribute to protein adsorption [23]. In the present study, the adsorption of plasma protein by scaffold was increased by HA precipitation, which was supported by earlier reports [42,43].

3.6. Effect of the scaffold on MSC proliferation

In order to investigate the cell proliferative effect of C-Scaffold and

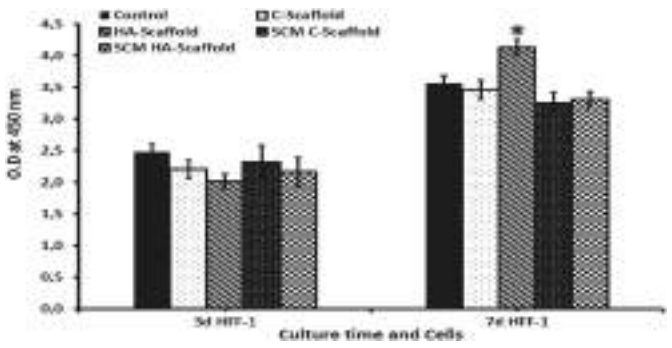

Fig. 6. The HFF-1 proliferative effect of C-Scaffold, HA-Scaffold and their conditioned medium (SCM). Control: cells cultured without scaffolds, C-Scaffold: cells cultured on control scaffold, HA-scaffold: cells cultured on HA-scaffold, SCM C-Scaffold: cells cultured on SCM of control scaffolds, SCM HA scaffold: cells cultured on scaffold conditioned medium of HA scaffolds. * denotes statistical significance compared to the control group (without scaffold), $P < 0.05$.

HA-Scaffold, the MSCs were cultured on scaffolds for 3 days and 7 days followed by the cck-8 experiment. As expected, the number of cells was higher in the 7-day culture compared to the 3-day culture in all the groups (Fig. 5). On day 3, the cell number was not altered between control cells and scaffold cultured cells, except for cells cultured on HA-Scaffold. There was not much difference between scaffold cultured cells and SCM cultured cells on 3 days of culture. On day 7, the proliferation rate of MSCs was much higher in cells cultured on HA-Scaffolds compared to control cells ($P < 0.05$) and other scaffold-cultured cells. At the same time, the cells cultured on C-Scaffold and SCM also had a higher proliferative rate than control cells ($P < 0.05$). In contrast, the cells cultured in HA-SCM did not accelerate the proliferation of MSCs compared to cells cultured on HA-scaffold and there was no significant difference in the proliferative rate of cells cultured on C-Scaffold and C-SCM on day 7.

To support the present results, many studies substantially proved the MSCs proliferative effect of wollastonite [44], wollastonite scaffold containing chitosan/carboxymethyl cellulose [45], apatite-wollastonite [46,47], apatite/wollastonite-derived porous bioactive glass-ceramic scaffolds [48], and collagen/wollastonite nanowire hybrid scaffolds [49]. Our recent data concluded that the C2S(2P6)C2S) 3D-porous scaffold coated with strontium accelerated the proliferation of mesenchymal stem cells (MSCs) [50].

3.7. Biocompatibility

The *in vitro* biocompatibility of both the C-scaffold and HA-Scaffold was investigated by culturing HFF-1 cells on both scaffolds for different periods, followed by cck-8 experiments. As shown in Fig. 6, cells cultured on day 7 had higher proliferation in C-Scaffold and scaffold-cultured cells compared to cells cultured on day 3. The cell proliferation rate of control was higher than C-Scaffold and their respective conditioned medium on day 3, however, they were not statistically significant. Interestingly, the cells cultured on HA-Scaffold had significantly higher proliferation than control and C-Scaffold or SCM cultured cells ($P < 0.05$), however, this effect was not observed in HA-SCM cultured cells.

To support the present findings, several authors investigated the biocompatibility of silk fibroin/wollastonite composite scaffolds in L929 mouse fibroblasts [51], chitosan/carboxymethyl cellulose/mesoporous wollastonite in MG-63 cells [45], wollastonite–gelatin scaffold in human mesenchymal amniotic fluid stem cells [52] and wollastonite/β-TCP in fibroblasts [53].

3.8. Effect of the scaffolds in inflammatory response

The *in vitro* biocompatibility and proliferative effect of C-Scaffold and HA-Scaffold was further confirmed by measuring cellular cytokines (IL-2 and IL-6) levels in MSCs and HFF-1 cells using ELISA experiments. On day 3, the level of IL-2 was decreased in C-Scaffold treated HFF-1 cells compared to control, however, it was not observed in HA-Scaffold treated cells. In contrast, the HA-Scaffold decreased the IL-2 level of HFF-1 cells than control and C-Scaffold cells on day 7. There were no significant changes observed in IL-2 level of MSCs between control and Scaffold cultured cells on day 3 and day 7 (Fig. 7). On the other hand, the level of IL-6 in MSCs and HFF-1 cells was not altered by either scaffold compared to their respective controls on day 3 and day 7. Recently, Kamboj et al. investigated the cytokines and anti-inflammatory factors

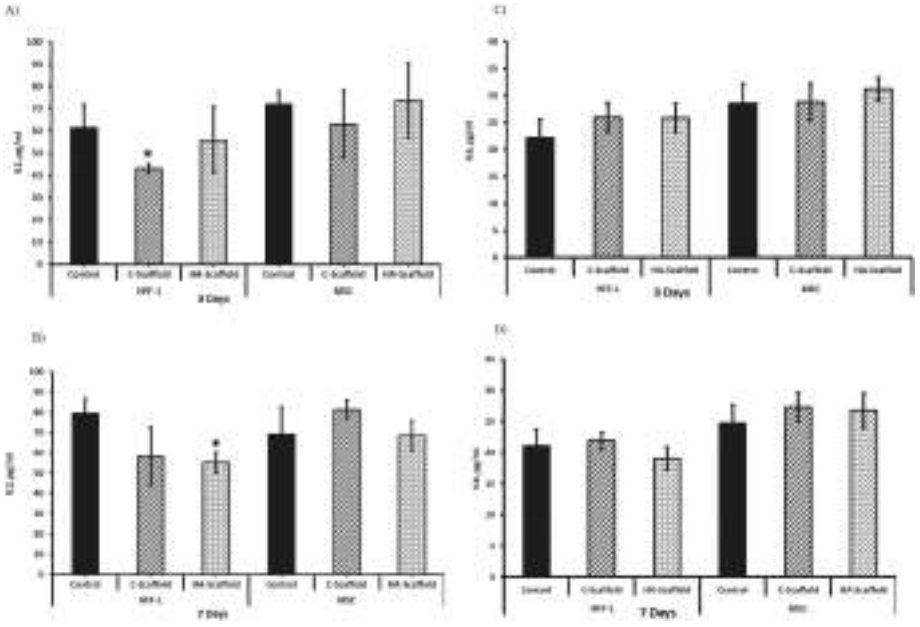

Fig. 7. The level of inflammatory cytokines (IL-2. and IL-6) in MSCs and HFF-1 cultured on C-scaffold and HA-scaffold. A-Level of IL-2 on day 3, B-Level of IL-2 on day 7, C-Level of IL-6 on day 3 and D-Level of IL-6 on day 7. Control-cells cultured without scaffolds. * denotes statistical significance compared to control, $P < 0.05$.

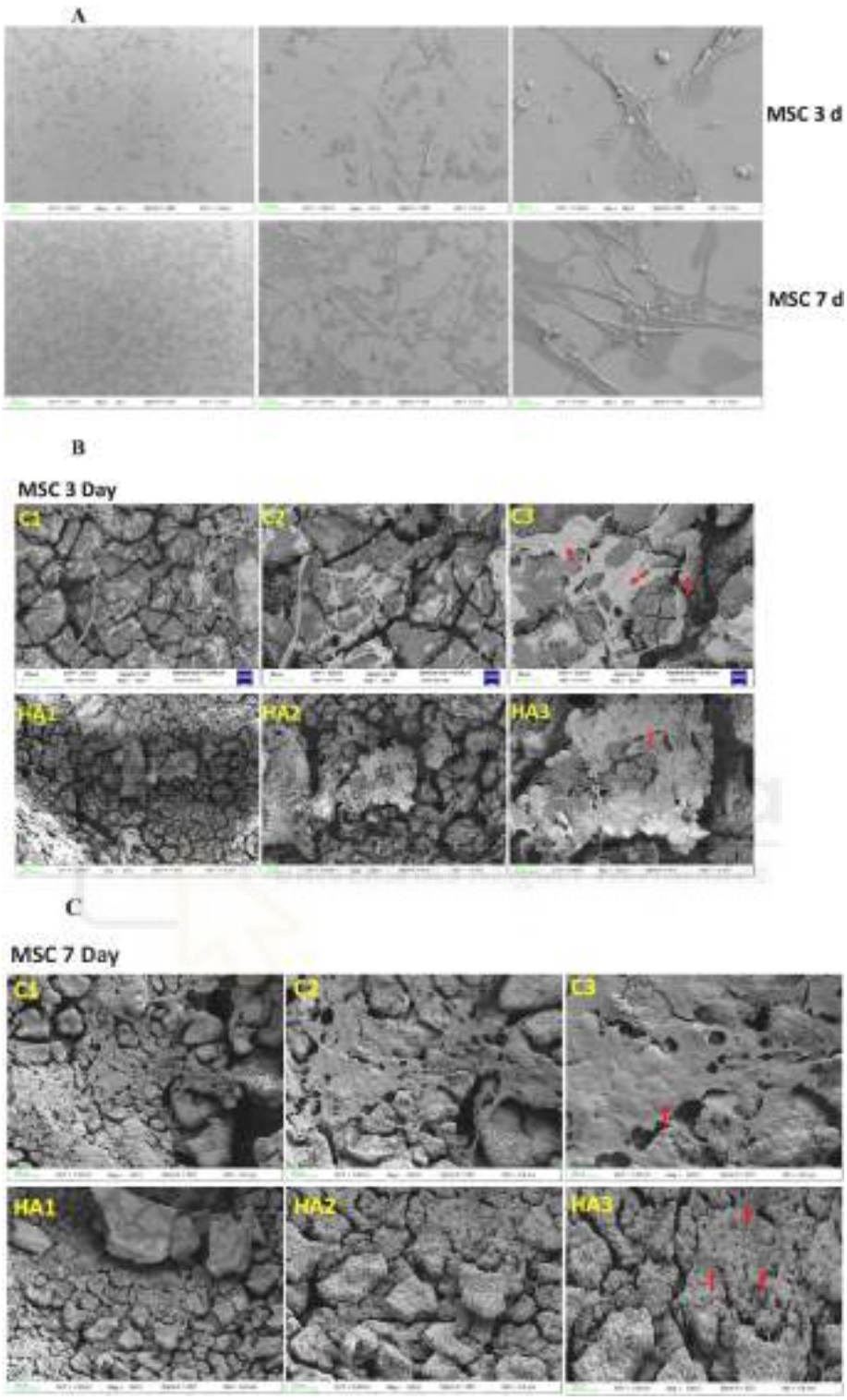

Fig. 8. Morphological structure of MSCs cultured on both C-Scaffold (C) and HA-Scaffold (HA). A- Cells without scaffolds on day 3 and day 7, B and C -Scaffolds with cells on day 3 and 7, respectively, 1, 2 and 3: images with 100, 50 and 20 μM scale bars, respectively.

of MSCs cultured on laser-sintered bio-inspired silicon-wollastonite scaffolds and concluded that the level of certain cytokines such as TGFβ, IL8, TSG6 and TGFβ was affected by the scaffolds, demonstrating possible immunomodulation effect and bone remodeling [54].

3.9. *Effect of the scaffolds on cell morphology*

The surface morphology of MSCs cultured on both C-Scaffold and HA-Scaffold is shown in Fig. 8. MSCs cultured on glass slides showed spindle and flattened shapes in both 3-day and 7-day cultures, however, the distribution of cells was increased on day 7 than on day 3 (Fig. 8A). On day 3, MSCs cultured on the C-Scaffold had a more flattened structure, whereas fibrillar cell clumps with nodules were observed in HA-Scaffold cultured cells (Fig. 8B). Fig. 8C clearly shows that on day 7 there were more cells than on day 3 and that they firmly adhered to both the control scaffold and the HA scaffolds. In the C-scaffold, the cells had

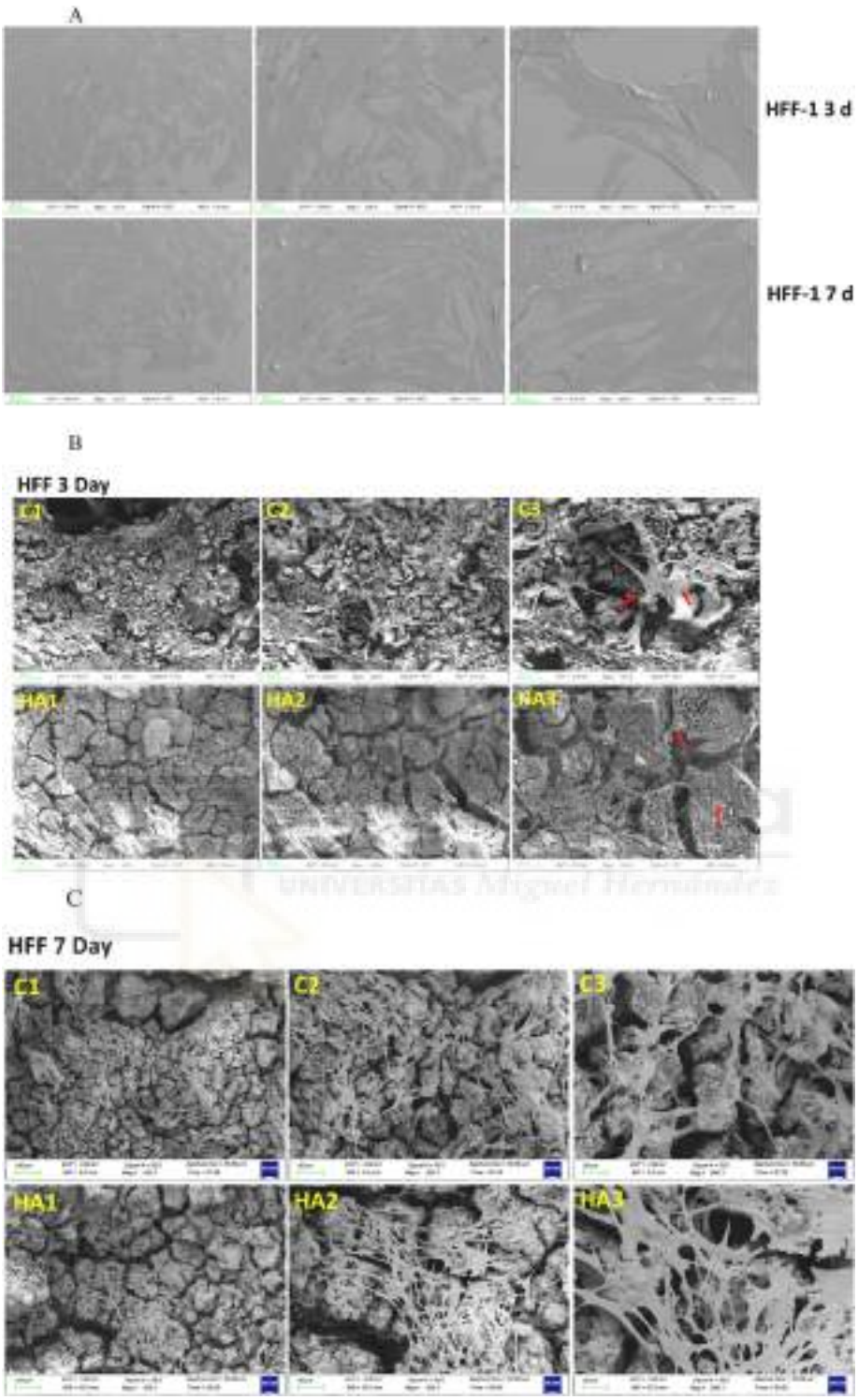

Fig. 9. Morphological structure of HFF-1 cultured on C-Scaffold (C) and HA-scaffold (HA). A- Cells without scaffolds on day 3 and day 7, B and C -Scaffolds with cells on day 3 and 7, respectively, 1, 2 and 3: images with 100, 50 and 20 μM scale bars, respectively.

a more flattened dense fibrous structure, while in the HA-scaffold cultured cells grew more in the hydroxyapatite crystal deposited region. Earlier studies reported an elongated spindle shape of MSCs cultured on apatite-wollastonite-glass ceramics for 7, 14 and 21 days [55] and long filopodia or lamellipodia shapes of Human bone marrow-derived stromal cells cultured on poly-hydroxybutyrate-*co*-hydroxyvalerate/wollastonite composite scaffolds for 7 days and 14 days [56].

Fig. 9 shows the microstructural images of HFF-1 cells cultured on scaffolds. Similar to MSCs, the HFF-1 cells were firmly grown on both the C-Scaffold and the HA-Scaffold. As observed earlier, the cell numbers were higher in 7 days culture compared to 3 days culture and more fibrillar cell structures were observed in cells cultured on C-Scaffold for 3 days than HA-Scaffold cultured cells. Compared to MSCs, the HFF-1 cells grew faster and covered all the scaffold surfaces on day 7. For instance, the surfaces of the C-Scaffold and HA-Scaffold were closely

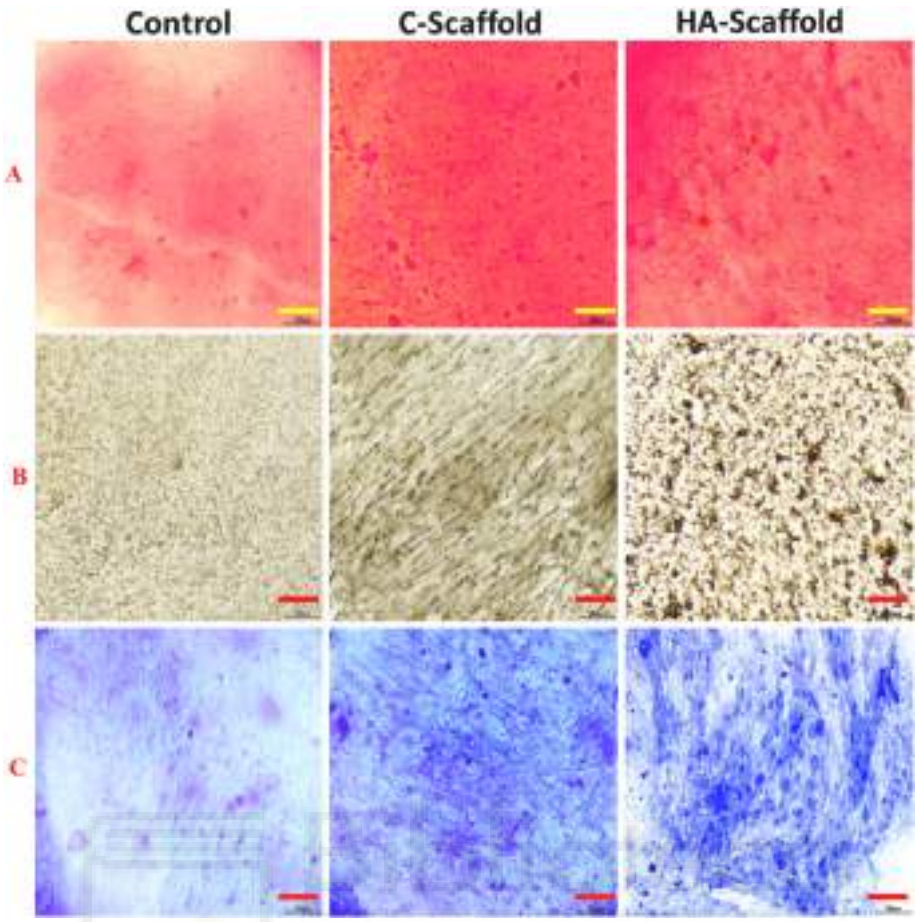

Fig. 10. Osteogenic stimulatory effect of C-Scaffold and HA-scaffold. Control-cells cultured without scaffolds, C-scaffold- cells cultured with control scaffold conditioned medium, and HA-scaffold- cells cultured with HA-scaffold condition medium. Images A- Alizarin red stain, images B- von Kossa stain and images C- Alkaline phosphatase stain. Scale bar- 100 μM.

covered by HFF-1 cells, which directly confirmed the compatibility of both scaffolds in fibroblast cell culture.

3.10. Effect of the scaffolds on cell differentiation

To test the cell regenerative ability of scaffolds, MSCs were differentiated into osteogenic cells in presence of scaffold conditioned medium. The differentiation of osteogenic cells from MSCs was confirmed by three major staining methods such as alizarin-red, von Kossa and alkaline phosphatase staining (Fig. 10). The results revealed that the control cells cultured without scaffold conditioned medium showed less staining intensity compared to those cells cultured with scaffold conditioned medium. Among the scaffold's groups, HA-scaffold conditioned medium significantly accelerated the staining intensity especially in von Kossa and alkaline phosphatase stains. Previously, Chen et al. reported that heparinised gelatine-hydroxyapatite-tricalcium phosphate scaffold enhanced the new bone regeneration and bone mineral density [57]. Similarly, Fu et al. observed the osteogenic stimulatory effect of Nano−/micro-scaled hydroxyapatite bioceramics [58]. The bone regeneration mechanism of Wollastonite and tricalcium phosphate was extensively reviewed by dos Santos et al. and concluded that the regenerative ability of these bioceramics depends on their physical-chemical, structural, functional (osteoinductivity and osteoconductivity) and biomimetic properties [59]. The present study results revealed that the osteogenic stimulatory effect of MSCs was accelerated by scaffolds, especially HA-scaffold, which directly proved the regenerative ability of this scaffolds.

4. Conclusion

The present investigation explores a novel multilayer scaffold composed of Wollastonite/$Ca_2P_6O_{17}$/TCP/Doped-Wollastonite, in which hollow hydroxyapatite spheres precipitate upon immersion in SBF. The scaffold design adheres to a structural configuration comprising a core consisting of the two innermost layers and a dual bioactive coating. Mineralogical analysis revealed that the core was predominantly composed of SiO_2 and $Ca_2P_2O_7$, possibly attributed to interlayer ionic migration. In addition, TCP and wollastonite, representing the outer bioactive layers, were also identified as predominant phases. Physical characterization of the scaffolds revealed an average overall macroporosity exceeding 85 % of their volume, along with a mechanical strength of approximately 1.6 MPa. The fabricated scaffolds resemble the trabecular spacing, trabecular rods and trabecular plates of the human humeral head. The MSCs proliferation rate was 61 % increased by HA-Scaffold compared to control cells, whereas it was 16 % in HFF cells. Interestingly, the scaffolds did not accelerate IL-2 and IL-6 cytokine levels in both MSCs and HFF cells, which further evidence the biocompatibility of these samples in tissue engineering applications. The osteogenic ability of MSCs was accelerated by HA-Scaffolds, proving their regenerative ability in stem cells. Overall, the fabricated multilayer Wollastonite/$Ca_2P_6O_{17}$/TCP/Doped-Wollastonite scaffold could be a suitable biomaterial for tissue engineering applications. However, the abilities of these materials in bone and dental cell differentiation using stem cells need to be addressed with extensive molecular signaling studies.

CRediT authorship contribution statement

Lakshmi Jeevithan: Writing – original draft, Methodology, Investigation. **Paula M. Riosalido:** Writing – original draft, Investigation. **Ángel Murciano:** Validation, Formal analysis. **Pablo Velásquez:** Visualization, Methodology. **Piedad N. De Aza:** Writing – original draft, Project administration. **Jeevithan Elango:** Writing – review & editing, Project administration. **Wenhui Wu:** Writing – review & editing, Supervision, Project administration. **Jose Eduardo Mate Sanchez de Val:** Supervision, Project administration, Funding acquisition.

Declaration of competing interest

The authors declare no conflicts of interest.

Acknowledgment

This work is part of the project PID2020-116693RB-C21 and PID2020-116693RB-C22 funded by MCIN/AEI/10.13039/501100011033 Spain. Also CIAICO/2021/157 grant funded by Generalitat Valenciana Generalitat Valenciana Spain.

Appendix A. Supplementary data

Supplementary data to this article can be found online at https://doi.org/10.1016/j.ceramint.2024.07.141.

References

[1] A. Nauth, E. Schemitsch, B. Norris, Z. Nollin, J.T. Watson, Critical-Size bone defects: is there a consensus for diagnosis and treatment? J. Orthop. Trauma 32 (2018) S7–S11, https://doi.org/10.1097/BOT.0000000000001115.
[2] J.A. Sterling, S.A. Guelcher, Biomaterial scaffolds for treating osteoporotic bone, Curr. Osteoporos. Rep. 12 (2014) 48–54, https://doi.org/10.1007/s11914-014-0187-2.
[3] H.D. Kim, S. Amirthalingam, S.L. Kim, S.S. Lee, J. Rangasamy, N.S. Hwang, Biomimetic materials and fabrication approaches for bone tissue engineering, Adv. Healthcare Mater. 6 (2017) 1700612, https://doi.org/10.1002/adhm.201700612.
[4] G. Zhu, T. Zhang, M. Chen, K. Yao, X. Huang, B. Zhang, Y. Li, J. Liu, Y. Wang, Z. Zhao, Bone physiological microenvironment and healing mechanism: basis for future bone-tissue engineering scaffolds, Bioact. Mater. 6 (2021) 4110–4140, https://doi.org/10.1016/j.bioactmat.2021.03.043.
[5] S. Bandopadhyay, N. Bandyopadhyay, S. Ahmed, V. Yadav, R.K. Tekade, Current research perspectives of orthopedic implant materials, in: Biomater. Bionanotechnol., Elsevier, 2019, pp. 337–374, https://doi.org/10.1016/B978-0-12-814427-5.00010-X.
[6] M.M. Stevens, Biomaterials for bone tissue engineering, Mater. Today 11 (2008) 18–25, https://doi.org/10.1016/S1369-7021(08)70086-5.
[7] Ž. Perić Kačarević, P. Rider, S. Alkildani, S. Retnasingh, M. Pejakić, R. Schnettler, M. Gosau, R. Smeets, O. Jung, M. Barbeck, An introduction to bone tissue engineering, Int. J. Artif. Organs 43 (2020) 69–86, https://doi.org/10.1177/0391398819876286.
[8] T.M. Koushik, C.M. Miller, E. Antunes, Bone tissue engineering scaffolds: function of multi-material hierarchically structured scaffolds, Adv. Healthcare Mater. 12 (2023) 2202766, https://doi.org/10.1002/adhm.202202766.
[9] G.J. Owens, R.K. Singh, F. Foroutan, M. Alqaysi, C.-M. Han, C. Mahapatra, H.-W. Kim, J.C. Knowles, Sol–gel based materials for biomedical applications, Prog. Mater. Sci. 77 (2016) 1–79, https://doi.org/10.1016/j.pmatsci.2015.12.001.
[10] K. Deshmukh, T. Kovářík, T. Křenek, D. Docheva, T. Stich, J. Pola, Recent advances and future perspectives of sol–gel derived porous bioactive glasses: a review, RSC Adv 10 (2020) 33782–33835, https://doi.org/10.1039/D0RA04287K.
[11] S.N.L. Ramlee, N.S.A.N. Sharifulden, H. Mohamad, S.N.F.M. Noor, Sol-gel derived bioactive glass scaffolds incorporated with polyvinyl-alcohol and pluronic P123 polymers using sponge replication technique, Mater. Today Proc. 17 (2019) 966–975, https://doi.org/10.1016/j.matpr.2019.06.463.
[12] M. González-Sánchez, C. Zamora-Ledezma, J. Elango, V. Morales-Flórez, Novel bioactive and biocompatible alumina-wollastonite porous constructs mimicking physical properties of human cortical bone, J. Eur. Ceram. Soc. 44 (2024) 4699–4708, https://doi.org/10.1016/j.jeurceramsoc.2024.02.001.
[13] C. Baudín, P. Pena, Review: tailored microstructures in the system tricalcium phosphate-wollastonite-diopside for bone regeneration scaffolds, Open Ceram 16 (2023) 100483, https://doi.org/10.1016/j.oceram.2023.100483.
[14] X. Yu, T. Zhao, Y. Qi, J. Luo, J. Fang, X. Yang, X. Liu, T. Xu, Q. Yang, Z. Gou, X. Dai, In vitro chondrocyte responses in Mg-doped wollastonite/hydrogel composite scaffolds for osteochondral interface regeneration, Sci. Rep. 8 (2018) 17911, https://doi.org/10.1038/s41598-018-36200-x.
[15] T. Shen, Y. Dai, X. Li, S. Xu, Z. Gou, C. Gao, Regeneration of the osteochondral defect by a wollastonite and macroporous fibrin biphasic scaffold, ACS Biomater. Sci. Eng. 4 (2018) 1942–1953, https://doi.org/10.1021/acsbiomaterials.7b00333.
[16] I. Tcacencu, N. Rodrigues, N. Alharbi, M. Benning, S. Toumpaniari, E. Mancuso, M. Marshall, O. Bretcanu, M. Birch, A. McCaskie, K. Dalgarno, Osseointegration of porous apatite-wollastonite and poly(lactic acid) composite structures created using 3D printing techniques, Mater. Sci. Eng. C 90 (2018) 1–7, https://doi.org/10.1016/j.msec.2018.04.022.
[17] X. Wang, M. Ye, J. Shen, J. Li, Y. Li, Z. Bao, H. Chen, T. Wu, M. Shen, C. Zhong, X. Yang, Z. Gou, S. Zhao, S. Xu, Core-shell-typed selective-area ion doping wollastonite bioceramic fibers enhancing bone regeneration and repair in situ, Appl. Mater. Today 32 (2023) 101849, https://doi.org/10.1016/j.apmt.2023.101849.
[18] P. Melo, A.-M. Ferreira, K. Waldron, T. Swift, P. Gentile, M. Magallanes, M. Marshall, K. Dalgarno, Osteoinduction of 3D printed particulate and short-fibre reinforced composites produced using PLLA and apatite-wollastonite, Compos. Sci. Technol. 184 (2019) 107834, https://doi.org/10.1016/j.compscitech.2019.107834.
[19] S. Sharma, D.J. Patil, V.P. Soni, L.B. Sarkate, G.S. Khandekar, J.R. Bellare, Bone healing performance of electrophoretically deposited apatite–wollastonite/chitosan coating on titanium implants in rabbit tibiae, J. Tissue Eng. Regen. Med. 3 (2009) 501–511, https://doi.org/10.1002/term.186.
[20] R. Sun, K. Chen, Y. Lu, Fabrication and dissolution behavior of hollow hydroxyapatite microspheres intended for controlled drug release, Mater. Res. Bull. 44 (2009) 1939–1942, https://doi.org/10.1016/j.materresbull.2009.06.015.
[21] X. Zhang, W. Zhang, Z. Yang, Z. Zhang, Nanostructured hollow spheres of hydroxyapatite: preparation and potential application in drug delivery, Front. Chem. Sci. Eng. 6 (2012) 246–252, https://doi.org/10.1007/s11705-012-1299-9.
[22] E. Sebastián, A. Murciano, P.N. De Aza, P. Velasquez, Synthesis of 3D porous ceramic scaffolds obtained by the sol-gel method with surface morphology modified by hollow spheres for bone tissue engineering applications, Ceram. Int. 49 (2023) 4393–4402, https://doi.org/10.1016/j.ceramint.2022.09.326.
[23] J. Elango, R. Bushin, A. Lijnev, P.N. De Aza, C.P.-A. Martínez, J.M.G. Marín, A. B. Hernandez, L.R.M. Olmo, J.E.M.S.D. Val, The effect of germanium-loaded hydroxyapatite biomaterials on bone marrow mesenchymal stem cells growth, Cells 11 (2022) 2993, https://doi.org/10.3390/cells11192993.
[24] J. Elango, K. Saravanakumar, S.U. Rahman, Y. Henrotin, J.M. Regenstein, W. Wu, B. Bao, Chitosan-collagen 3D matrix mimics trabecular bone and regulates RANKL-mediated paracrine cues of differentiated osteoblast and mesenchymal stem cells for bone marrow macrophage-derived osteoclastogenesis, Biomolecules 9 (2019) 173, https://doi.org/10.3390/biom9050173.
[25] N. Luo, Y. Lin, J. Guo, E. Quattrocchi, H. Deng, J. Dong, F. Ciucci, F. Boi, C. Hu, S. Grasso, Spark plasma sintering of LiFePO4: AC Field suppressing lithium migration, Materials 14 (2021) 2826, https://doi.org/10.3390/ma14112826.
[26] Y. Zhao, H. Chen, K. Ran, Y. Zhang, H. Pan, J. Shangguan, M. Tong, J. Yang, Q. Yao, H. Xu, Porous hydroxyapatite scaffold orchestrated with bioactive coatings for rapid bone repair, Biomater. Adv. 144 (2023) 213202, https://doi.org/10.1016/j.bioadv.2022.213202.
[27] M.Y. Bajuri, N. Selvanathan, F.N. Dzeidee Schaff, M.H. Abdul Suki, A.M.H. Ng, Tissue-Engineered hydroxyapatite bone scaffold impregnated with osteoprogenitor cells promotes bone regeneration in sheep model, Tissue Eng. Regen. Med. 18 (2021) 377–385, https://doi.org/10.1007/s13770-021-00343-2.
[28] X. Niu, M. Qin, M. Xu, L. Zhao, Y. Wei, Y. Hu, X. Lian, S. Chen, W. Chen, D. Huang, Coated electrospun polyamide-6/chitosan scaffold with hydroxyapatite for bone tissue engineering, Biomed. Mater. 16 (2021) 025014, https://doi.org/10.1088/1748-605X/abd68a.
[29] X. Zhou, N. Zhang, S. Mankoci, N. Sahai, Silicates in orthopedics and bone tissue engineering materials, J. Biomed. Mater. Res. 105 (2017) 2090–2102, https://doi.org/10.1002/jbm.a.36061.
[30] M. Sanmartin De Almeida, G.V.D.O. Fernandes, A.M. De Oliveira, J.M. Granjeiro, Calcium silicate as a graft material for bone fractures: a systematic review, J. Int. Med. Res. 46 (2018) 2537–2548, https://doi.org/10.1177/0300060518770940.
[31] H.R. Fernandes, A. Gaddam, A. Rebelo, D. Brazete, G.E. Stan, J.M.F. Ferreira, Bioactive glasses and glass-ceramics for healthcare applications in bone regeneration and tissue engineering, Materials 11 (2018) 2530, https://doi.org/10.3390/ma11122530.
[32] L. Zhu, D. Luo, Y. Liu, Effect of the nano/microscale structure of biomaterial scaffolds on bone regeneration, Int. J. Oral Sci. 12 (2020) 6, https://doi.org/10.1038/s41368-020-0073-y.
[33] M. Hamvar, H.R. Bakhsheshi-Rad, M. Omidi, A.F. Ismail, M. Aziz, F. Berto, X. Chen, Biocompatibility and bioactivity of hardystonite-based nanocomposite scaffold for tissue engineering applications, Biomed, Phys. Eng. Express 6 (2020) 035011, https://doi.org/10.1088/2057-1976/ab7284.
[34] J.A. Najafinezhad, M. Abdellahi, S. Nasiri-Harchegani, A. Soheily, M. Khezri, H. Ghayour, On the synthesis of nanostructured akermanite scaffolds via space holder method: the effect of the spacer size on the porosity and mechanical properties, J. Mech. Behav. Biomed. 69 (2017) 242–248, https://doi.org/10.1016/j.jmbbm.2017.01.002.
[35] A. Najafinezhad, M. Abdellahi, H. Ghayour, A. Soheily, A. Chami, A. Khandan, A comparative study on the synthesis mechanism, bioactivity and mechanical properties of three silicate bioceramics, Mater. Sci. Eng. C 72 (2017) 259–267, https://doi.org/10.1016/j.msec.2016.11.084.
[36] C.M. Walthers, A.K. Nazemi, S.L. Patel, B.M. Wu, J.C.Y. Dunn, The effect of scaffold macroporosity on angiogenesis and cell survival in tissue-engineered smooth muscle, Biomaterials 35 (2014) 5129–5137, https://doi.org/10.1016/j.biomaterials.2014.03.025.

[37] J.R. Caeiro, P. González, D. Guede, Biomecánica y hueso (y II): ensayos en los distintos niveles jerárquicos del hueso y técnicas alternativas para la determinación de la resistencia ósea, Rev. Osteoporos. Metab. Miner. 5 (2013) 99–108, https://doi.org/10.4321/S1889-836X2013000200007.
[38] A. Ressler, N. Kamboj, M. Ledinski, A. Rogina, I. Urlić, I. Hussainova, H. Ivanković, M. Ivanković, Macroporous silicon-wollastonite scaffold with Sr/Se/Zn/Mg-substituted hydroxyapatite/chitosan hydrogel, Open Ceram 12 (2022) 100306, https://doi.org/10.1016/j.oceram.2022.100306.
[39] S. Palakurthy, G.R.K. V, R.K. Samudrala, A.A. P, In vitro bioactivity and degradation behaviour of β-wollastonite derived from natural waste, Mater. Sci. Eng. C 98 (2019) 109–117, https://doi.org/10.1016/j.msec.2018.12.101.
[40] D.S. Klimesch, A. Ray, The use of DTA/TGA to study the effects of ground quartz with different surface areas in autoclaved cement: quartz pastes. Part 1: a method for evaluating DTA/TGA results, Thermochim. Acta 289 (1996) 41–54, https://doi.org/10.1016/S0040-6031(96)03033-X.
[41] G. Molino, G. Montalbano, C. Pontremoli, S. Fiorilli, C. Vitale-Brovarone, Imaging techniques for the assessment of the bone osteoporosis-induced variations with particular focus on micro-CT potential, Appl. Sci. 10 (2020) 8939, https://doi.org/10.3390/app10248939.
[42] B. Fernández-Montes Moraleda, J.S. Román, L.M. Rodríguez-Lorenzo, Influence of surface features of hydroxyapatite on the adsorption of proteins relevant to bone regeneration, J. Biomed. Mater. Res. 101A (2013) 2332–2339, https://doi.org/10.1002/jbm.a.34528.
[43] K. Chen, P. Ustriyana, F. Moore, N. Sahai, Biological response of and blood plasma protein adsorption on silver-doped hydroxyapatite, ACS Biomater. Sci. Eng. 5 (2019) 561–571, https://doi.org/10.1021/acsbiomaterials.8b00996.
[44] S. Saravanan, S. Vimalraj, M. Vairamani, N. Selvamurugan, Role of mesoporous wollastonite (calcium silicate) in mesenchymal stem cell proliferation and osteoblast differentiation: a cellular and molecular study, J. Biomed. Nanotechnol. 11 (2015) 1124–1138, https://doi.org/10.1166/jbn.2015.2057.
[45] R. Sainitya, M. Sriram, V. Kalyanaraman, S. Dhivya, S. Saravanan, M. Vairamani, T. P. Sastry, N. Selvamurugan, Scaffolds containing chitosan/carboxymethyl cellulose/mesoporous wollastonite for bone tissue engineering, Int. J. Biol. Macromol. 80 (2015) 481–488, https://doi.org/10.1016/j.ijbiomac.2015.07.016.
[46] J.A. Lee, C.A. Knight, X. Kun, X.B. Yang, D.J. Wood, K.W. Dalgarno, P.G. Genever, *In vivo* biocompatibility of custom-fabricated apatite-wollastonite-mesenchymal stromal cell constructs: custom aw-cell constructs *IN VIVO*, J. Biomed. Mater. Res. 103 (2015) 3188–3200, https://doi.org/10.1002/jbm.a.35448.
[47] S. Müller, L. Nicholson, N. Al Harbi, E. Mancuso, E. Jones, A. Dickinson, X. N. Wang, K. Dalgarno, Osteogenic potential of heterogeneous and CD271-enriched mesenchymal stromal cells cultured on apatite-wollastonite 3D scaffolds, BMC Biomed. Eng. 1 (2019) 16, https://doi.org/10.1186/s42490-019-0015-y.
[48] H. Zhang, X.-J. Ye, J.-S. Li, Preparation and biocompatibility evaluation of apatite/wollastonite-derived porous bioactive glass ceramic scaffolds, Biomed. Mater. 4 (2009) 045007, https://doi.org/10.1088/1748-6041/4/4/045007.
[49] Q. Zhang, T. Nakamoto, S. Chen, N. Kawazoe, K. Lin, J. Chang, G. Chen, Collagen/wollastonite nanowire hybrid scaffolds promoting osteogenic differentiation and angiogenic factor expression of mesenchymal stem cells, J. Nanosci. Nanotechnol. 14 (2014) 3221–3227, https://doi.org/10.1166/jnn.2014.8607.
[50] J. Elango, K. Salazar, P. Velasquez, A. Murciano, P.N. De Aza, W. Wu, J.M. Granero Marín, J.E. Mate Sanchez De Val, Fabrication of novel strontium-coated bioactive ceramic-glass (C2S(2P6)C2S) 3D-porous scaffold for the proliferation and osteogenic differentiation of bone marrow-derived mesenchymal stem cells, Ceram. Int. (2024), https://doi.org/10.1016/j.ceramint.2024.02.175. S0272884224006734.
[51] H. Zhu, J. Shen, X. Feng, H. Zhang, Y. Guo, J. Chen, Fabrication and characterization of bioactive silk fibroin/wollastonite composite scaffolds, Mater. Sci. Eng. C 30 (2010) 132–140, https://doi.org/10.1016/j.msec.2009.09.009.
[52] F. Curti, I.-C. Stancu, G. Voicu, H. Iovu, C.-I. Dobrita, L.T. Ciocan, R. Marinescu, F. Iordache, Development of 3D bioactive scaffolds through 3D printing using wollastonite–gelatin inks, Polymers 12 (2020) 2420, https://doi.org/10.3390/polym12102420.
[53] W.T. Barbosa, K.V. De Almeida, G.G. De Lima, M.A. Rodriguez, M.V. Lia Fook, R. García-Carrodeguas, V. Amaro Da Silva Junior, F.A. De Sousa Segundo, M.J. C. De Sá, Synthesis and in vivo evaluation of a scaffold containing wollastonite/β-TCP for bone repair in a rabbit tibial defect model, J. Biomed. Mater. Res. B Appl. Biomater. 108 (2020) 1107–1116, https://doi.org/10.1002/jbm.b.34462.
[54] N. Kamboj, J. Kazantseva, R. Rahmani, M.A. Rodríguez, I. Hussainova, Selective laser sintered bio-inspired silicon-wollastonite scaffolds for bone tissue engineering, Mater. Sci. Eng. C 116 (2020) 111223, https://doi.org/10.1016/j.msec.2020.111223.
[55] J.A. Dyson, P.G. Genever, K.W. Dalgarno, D.J. Wood, Development of custom-built bone scaffolds using mesenchymal stem cells and apatite-wollastonite glass-ceramics, Tissue Eng 13 (2007) 2891–2901, https://doi.org/10.1089/ten.2007.0124.
[56] H. Li, W. Zhai, J. Chang, Effects of wollastonite on proliferation and differentiation of human bone marrow-derived stromal cells in PHBV/wollastonite composite scaffolds, J. Biomater. Appl. 24 (2009) 231–246, https://doi.org/10.1177/0885328208096043.
[57] X. Chen, C.Y. Gao, X.Y. Chu, C.Y. Zheng, Y.Y. Luan, X. He, K. Yang, D.L. Zhang, VEGF-loaded heparinised gelatine-hydroxyapatite-tricalcium phosphate scaffold accelerates bone regeneration via enhancing osteogenesis-angiogenesis coupling, Front. Bioeng. Biotechnol. 10 (2022) 915181, https://doi.org/10.3389/fbioe.2022.915181.
[58] S. Fu, H. Li, Y. Wu, J. Wang, Nano−/micro-scaled hydroxyapatite ceramic construction and the regulation of immune-associated osteogenic differentiation, J. Biomed. Mater. Res. 112 (2024) 193–209, https://doi.org/10.1002/jbm.a.37606.
[59] G.G. dos Santos, L.Q. Vasconcelos, I.C. Barreto, F.B. Miguel, R.P.C. de Araújo, Wollastonite and tricalcium phosphate composites for bone regeneration, Res. Society Develop 11 (2022) e12011931662, https://doi.org/10.33448/rsd-v11i9.31662.

Artículo 4

BOLETIN DE LA SOCIEDAD ESPAÑOLA DE
Cerámica y Vidrio
www.elsevier.es/bsecv

Original

Bioactive scaffolds harnessing ionic modifications to promote osteogenesis and angiogenesis in bone regeneration

Paula M. Riosalido[a], *Marcela Arango-Ospina*[b], *Pablo Velasquez*[a], *Angel Murciano*[c,*], *Aldo R. Boccaccini*[b], *Piedad N. De Aza*[a]

[a] *Institute of Bioengineering, Miguel Hernandez University, Avda. Universidad s/n, 03202 Elche, Spain*
[b] *Institute of Biomaterials, University of Erlangen-Nuremberg, Cauerstr. 6, 91058 Erlangen, Germany*
[c] *Department of Materials, Optical and Electronic Technology, Miguel Hernandez University, Avda. Universidad s/n, 03202 Elche, Spain*

ARTICLE INFO

Article history:
Received 24 March 2025
Accepted 19 May 2025

Keywords:
Multilayer scaffolds
Sol–gel
Bone regeneration
Biocompatible

ABSTRACT

This study proposes the modification of multilayer scaffolds based on the SiO_2–CaO–P_2O_5 system by incorporating bioactive ions, such as magnesium or lithium, with the aim of enhancing the cellular processes involved in bone regeneration. Two types of scaffolds, CS04 and CS05, were prepared, varying the amount of MgO (0.38; 0.49% w/w). The prepared scaffolds exhibited an interconnected porous structure, with SiO_2, $Ca_2P_2O_7$ and β-$Ca_3(PO_4)_2$ as predominant crystalline phases, a compressive strength of 1.8 MPa and a porosity above 75%. Bioactivity tests demonstrated that minor variations in the amount of MgO altered the surface topography and bioactive behaviour, resulting in a lamellar microstructure (CS04) and precipitation of hollow HA spheres (CS05). From a biological point of view, the scaffolds proved to be biocompatible, as were their dissolution products at 10 and 100 mg/mL. Both promoted MC3T3-E1 cell proliferation, calcium deposition and osteoblastic differentiation, as reflected by increased ALP activity. In addition, they induced VEGF release in MC3T3-E1, thereby demonstrating their angiogenic potential. Taken together, these results suggest that the scaffolds possess optimal properties for bone regeneration applications.

* *Corresponding author.*
E-mail address: amurciano@umh.es (A. Murciano).
https://doi.org/10.1016/j.bsecv.2025.100447

Andamios bioactivos con modificaciones iónicas para promover la osteogénesis y la angiogénesis en la regeneración ósea

Palabras clave:
Andamios multicapa
Sol-gel
Regeneración ósea
Biocompatible

RESUMEN

Este estudio propone la modificación de andamios multicapa basados en el sistema SiO_2-CaO-P_2O_5 mediante la incorporación de iones bioactivos, como el magnesio o el litio, con e objetivo de potenciar los procesos celulares implicados en la regeneración ósea. Se prepararon dos tipos de andamios, CS04 y CS05, con diferentes concentraciones de MgO (0,38%; 0,49% p/p). Los andamios obtenidos presentaron una estructura porosa interconectada, con fases cristalinas predominantes de SiO_2, $Ca_2P_2O_7$ y β-$Ca_3(PO_4)_2$, una resistencia a la compresión de 1,8 MPa y una porosidad superior al 75%. Los ensayos de bioactividad mostraron que pequeñas variaciones en la cantidad de MgO modificaron la topografía superficial y el comportamiento bioactivo, generando una microestructura laminar (CS04) y a la precipitación de esferas huecas de HA (CS05). Desde una perspectiva biológica, los andamios demostraron ser biocompatibles, al igual que sus productos de disolución a 10 y 100 mg/mL. Ambos andamios estimularon la proliferación celular en MC3T3-E1, la deposición de calcio y la diferenciación osteoblástica, reflejado en un incremento de la actividad de la ALP. Además, se observó liberación de VEGF en MC3T3-E1, sugiriendo su potencial angiogénico. Estos resultados indican que los andamios presentan propiedades óptimas para su aplicación en regeneración ósea.

Introduction

Advancements in medicine and healthcare have significantly increased human life expectancy, leading to a shift in the global demographic profile [1,2]. Consequently, there has been an escalating prevalence of various age-related conditions, including bone fractures, which are frequently attributed to bone fragility and bone loss [2–5]. While individuals with healthy bones generally experience natural healing and regeneration of fractures [6], especially smaller ones, more severe fractures or those complicated by comorbidities such as osteoporosis, diabetes or other chronic inflammatory conditions can overwhelm the bone's ability to regenerate [7,8]. In such cases, external intervention becomes necessary to promote effective healing. This is where the field of biomaterials has made significant advancements, offering promising solutions to enhance bone regeneration [9–11].

The first generation of biomaterials employed for osseous regeneration focused primarily on bioinert materials intended to simply replace lost bone mass [12,13]. Such materials included metallic implants (*e.g.* titanium and stainless steel), synthetic polymers (*e.g.* polymethyl methacrylate and Teflon), and ceramics (*e.g.* alumina and zirconia) [9,12,14]. However, these materials are inert and do not integrate with surrounding tissues, failing to support biological regeneration despite minimising immune responses and foreign body reactions [12,13].

Consequently, the field advanced to second-generation biomaterials, which function not only as structural replacements but are also engineered to elicit controlled responses in the physiological environment, thereby facilitating integration with host bone tissue [12,13]. These materials include synthetic and natural biodegradable polymers, including collagen and polyesters, bioactive bioceramics such as calcium silicate (CS) or bioactive glasses (both silica and non-silica based), as well as bioresorbable bioceramics like tricalcium phosphate (TCP) and hydroxyapatite (HA) [9,12,14,15].

The advent of third-generation biomaterials has led to the development of scaffolds that support bone regeneration while guiding self-healing processes through the induction of favourable cellular responses [9,12,13]. This can be achieved through various strategies, including surface modifications, the use of external stimuli, or the sustained release of soluble factors, such as growth factors, cytokines, or other chemical substances, such us biologically active ions, to enhance tissue repair and regeneration [9].

Despite these advances, there remain significant clinical challenges, particularly in achieving full biological integration and vascularisation of bone grafts, which is imperative for their long-term functionality and success [16,17]. The present study proposes a cost-effective approach to address these issues by means of ionic modification, with the aim of achieving improved biological performance. Through ionic substitutions, it is possible to alter the surface structure, electric charge and reactivity of materials, which may influence its behaviour in physiological environments [18,19]. The bioengineered third-generation scaffolds combine bioactive CS ($CaSiO_3$), resorbable β-TCP ($Ca_3(PO_4)_2$) and the lesser-known vitreous phase P6 ($Ca_2P_6O_{17}$) into a single structure, seeking to create a scaffold that mimics the natural bone structure. Along with the ion-doping strategy, this combination is intended to enhance regeneration related processes of bone tissue and enable implant long-term functionality.

Materials and methods

Materials preparation

The preparation of the multilayer scaffolds was achieved through the implementation of the sol–gel process and the foam replica method, following the methodology illustrated in Fig. 1.

The various stages of this process have been described in detail in previous publications [20,21]. In summary, for the CS core, as well as the CS04 and CS05 outer layers, the raw materials were simply mixed and stirred to facilitate the hydrolysis of the precursors (Fig. 1A). For the P6 and TCP coatings, the mixture was subjected to agitation and heating to facilitate the complete evaporation of the water. Prior to the application of the TCP coating and after the P6 layer, a preconditioning chemical treatment with TRIS (pH 7.35–7.4) was conducted. The TRIS solution was prepared by dissolving 1.17 g of $CaCl_2$ and 7.61 g of tris(hydroxymethyl)aminomethane (tris) in 1 L of distilled water. This step was essential to prevent the excessive reactivity of the glassy phase, which could alter the pH of the solutions during *in vitro* bioactivity and cellular assays [19]. Following the application of each layer, a sintering process was carried out (Fig. 1B). The resulting multilayer scaffolds consisted of four layers: an internal CS ($CaSiO_3$) core, followed by a P6 ($Ca_2P_6O_{17}$) glassy phase coating doped with Li to improve the mechanical strength and tackle the brittleness of the CS core. A third layer of β-TCP ($Ca_3(PO_4)_2$) was then added, followed by an outer CS layer doped with Na, K, and varying amounts of Mg, which defined the nomenclature of the resulting scaffolds. Thus, CS04 contains 0.4 g of $MgCO_3$, while CS05 contains 0.5 g.

Materials characterisation

The X-ray diffraction (XRD) technique was employed for the mineralogical characterisation of the multilayer scaffolds. An automated Bruker-AXR D8 Advance diffractometer, equipped with a secondary graphite monochromator and Cu Kα radiation (1.5418740 Å), was utilised in accordance with the Bragg–Brentano geometry in θ–2θ configuration. The X-ray tube operating conditions were set to 40 kV and 30 mA, and the angle range was set from 15° to 40° with 0.05° increments, with 5 s assigned for each step. Subsequently, the resulting diffractograms were analysed using the Match! software, version 4.1. Peak analysis was conducted using the database provided by the Crystallography Open Database (COD).

The chemical composition was analysed by Fourier Transform Infrared Spectroscopy (FTIR) using a IRAffinity-1S Shimadzu spectrometer. Spectra were scanned in transmittance mode over a wavenumber range of 1400 to 400 cm^{-1} with 40 scans at a resolution of 4 cm^{-1}.

Given the critical role of mechanical resistance and porosity in scaffolds performance, macroporosity was assessed using a water-filled pycnometer. Additionally, a manual compression test was conducted using an SVL-1000N device (IMADA) to evaluate the compressive strength of the scaffolds ($n = 5$).

Additionally, the microstructure of the multilayer scaffolds was examined using a field emission scanning electron microscope (FESEM, ZEISS SIGMA 300 VP) coupled with energy dispersive X-ray spectroscopy (EDS, ZEISS SmartEDX). This was conducted both before and after one week of Simulated Body Fluid (SBF) treatment in accordance with ISO 23317 [22], and based on our previous investigations showing that the resulting bioactive topography promotes cellular proliferation [20,21].

In vitro biocompatibility assessment

Cell culture

Cell assays were conducted on the murine preosteoblast cell line MC3T3-E1. The cells were cultured in 75 cm^2 culture flasks with α-MEM culture medium (Gibco), supplemented with 10% Foetal Bovine Serum (FBS, Corning), 1% penicillin–streptomycin (PS, Gibco) and 1% L-glutamine (L-Glu, Gibco). The flasks were incubated at 37 °C in a humidified atmosphere with 5% CO_2. Once the cells had reached 80% confluence, they were passaged in accordance with standard laboratory practice.

Prior to initiating the cytotoxicity assays, the scaffolds CS04 and CS05 were dry-sterilised in a furnace at 160 °C for a period of two hours. The cytotoxicity was evaluated through two distinct approaches: an indirect approach, in which preosteoblasts were incubated as Culture Medium containing Ionic Dissolution Products (CM-IDP) and a direct approach, whereby cells were seeded on the scaffolds.

Indirect approach

For this purpose, solutions containing powders from powdered scaffolds at a concentration of 10 mg/mL and 100 mg/mL were prepared in supplemented α-MEM, designated as CM-IDP, which was renewed every two days. Following each study interval (1, 3, 7, 14 and 21 days) CM-IDP aliquots were collected and stored at 4 °C for subsequent analysis of the ionic composition by inductively coupled plasma optical emission spectrometry (ICP-OES, Perkin-Elmer Optima 2000™) and for monitoring of any pH alterations. The remaining medium was entirely removed and replenished with fresh supplemented α-MEM, simulating the clearance processes observed *in vivo*. This approach enabled the extraction of the dissolution products after each interval, preventing its accumulation and facilitating an understanding of its potential *in vivo* effects.

In parallel and 24 h prior to assay commencing, preosteoblasts were seeded at a density of 5000 cells/cm^2 to allow cell attachment with supplemented α-MEM. Subsequently, the supplemented α-MEM was removed from the wells and replaced with the CM-IDP, except for the control wells, where it was renewed. The aliquots for ICP-OES and pH measurement were also collected. After 24 h of exposure (day 1), the viability assay WST-8 (CCK-8, Sigma–Aldrich) was performed and absorbance was read (FLUOstar Omega, BMG LabTech).

Afterwards wells were rinsed with Dulbecco's Phosphate Buffered Saline (DPBS, Gibco) and incubated with CM-IDP except from control wells. This procedure was repeated on days 3, 7, 14 and 21 of the study.

To complement WST-8 assay, cells were live stained with calcein acetoxymethyl-ester (Calcein AM, Invitrogen), fixed

A

MATERIALS	CS Core	P6	TCP	CS04	CS05
PRECURSORS					
• TEOS (mL)	19.28	-	-	19.28	19.28
• TEP (mL)	-	18.46	10.96	-	-
• $CaCO_3$ (g)	8.62	3.72	8.64	8.62	8.62
SOLVENTS (mL)					
• Ethanol	5	5	5	5	5
• H_2O	20	20	20	20	20
CATALYZER (mL)					
• HCl 37%	1	2	2	1	1
DOPANTS (g)					
• Li_2CO_3	-	1	-	-	-
• $MgCO_3$	-	-	-	0.4	0.5
• Na_2CO_3	-	-	-	0.5	0.5
• K_2CO_3	-	-	-	0.5	0.5

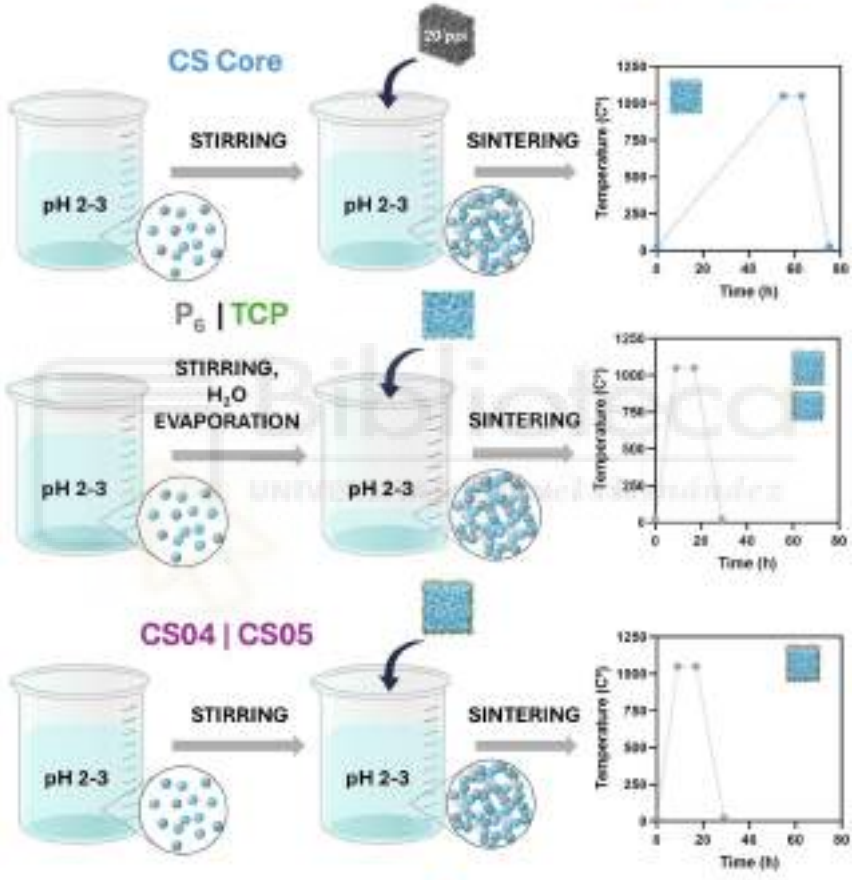

B

Fig. 1 – Diagram of the multilayer scaffold preparation process: sol–gel method and sintering (A); assembly of layers and scaffold preconditioning (B).

with 3.7% formaldehyde for and finally stained with DAPI (Sigma Aldrich) to evaluate their morphology after DP-CM exposure. Images were adquired through a Axio Scope A.1, Carl Zeiss Fluorescence Microscope.

Direct approach

MC3T3-E1 cells were plated at a density of 5000 cells/cm^2 onto the scaffolds CS04 and CS05. WST-8 assays were conducted at 1, 3, 7, 14, and 21 days, as previously described.

After the various study periods, the cells were subjected to a process of fixation and subsequent examination using SEM, with the objective of assessing the morphology of the cells. Two distinct fixation solutions were utilised for 1 h each: the initial solution consisted of 0.1% glutaraldehyde, 2% formaldehyde and 5% sucrose, while the second solution included 0.3% glutaraldehyde, 3% formaldehyde. Subsequently, a dehydration process was conducted utilising a series of ethanol solutions, ranging from 30% to 99.9%, with each concentration applied for a period of 30 min. Subsequently, the samples were subjected to critical point drying (Leica EM CPD300) and analysed using SEM (Auriga CrossBeam, Carl Zeiss).

Osteogenic assessment

For osteogenic assays, 50 μg/mL L-ascorbic acid (Sigma Aldrich), 10 mM β-glycerophosphate (Sigma), and 10 nM dexamethasone (Sigma Aldrich) were added to the supplemented α-MEM to create an osteogenic differentiation medium for culturing MC3T3-E1.

Alizarin red staining (ARS) was employed to assess the deposition of calcium on CS04 and CS05 scaffolds. In brief, cells were seeded on scaffolds for 7, 14, and 21 days, after which they were fixed with 3.7% formaldehyde for 1 h, stained for 10 min with ARS (2%; pH 4.3) in darkness, and rinsed with DPBS and dH$_2$O as many times as necessary until the washing solution was transparent. A qualitative analysis was conducted using images of the scaffolds obtained through an optical microscope (Primo vert, Carl Zeiss). For the quantitative analysis, a 10% acetic acid solution was employed for 30 min with gently shaking to remove the stain, and the absorbance was subsequently quantified at 405 nm. In consideration of the elevated calcium content of the scaffolds, the baseline staining of the scaffolds was assessed and employed for the standardisation of the values.

To assess the impact of multilayer scaffolds on osteoblast differentiation, the specific alkaline phosphatase (ALP) activity was quantified at 3, 7, 14 and 21 days. The activity of ALP was evaluated through an enzymatic and colorimetric assay, whereby the formation of yellow p-nitrophenol (pNP) resulting from the hydrolysis of nitrophenylphosphate (p-NPP) by ALP was quantified. In this regard, the cells were lysed and subjected to centrifugation to obtain the proteins present in the supernatant. Subsequently, 150 μL of the supernatant were combined with 50 μL of the ALP mixture (1 M Tris, 2 mM $MgCl_2$, 9 mM p-NPP), which provides the requisite conditions and substrate for ALP. The mixture was incubated at 37 °C until a colour change was observed, after which 1 M NaOH was added to terminate the reaction. The absorbance was determined at a wavelength of 405 nm. Concurrently, the total protein content of the supernatants was determined through the Bradford assay. For this purpose, 25 μL of cell lysates supernatants were mixed with 975 μL of the Bradford reagent, which were incubated for 10 min in the dark. The absorbance was measured at 595 nm. The specific ALP activity was calculated based on the ALP measurement and the Bradford assay and is presented as the activity of hydrolysing a certain amount of nanomolar pNPP per minute and milligramme of total protein.

Angiogenic assessment

In order to investigate the potential angiogenic impact of multilayer scaffolds on the MC3T3-E1 cell line, the RayBio® Mouse VEGF-A ELISA Kit was utilised to quantify the liberation of VEGF in cell supernatants, in accordance with the instructions provided by the suppliers [23]. The data are presented as the percentage of VEGF secretion relative to the control mean (considered as 100%) for each time point of the study.

Statistical analysis

One-way ANOVA was utilised to compare groups at each time point. Following this, *post hoc* analyses were carried out using Tukey's test to determine specific differences between the groups. Statistical significance was established with an alpha level of 0.05 and a 95% confidence interval. Results are expressed as mean ± standard deviation (SD). All statistical analyses were performed using GraphPad version 10.3.1.

Results

The resulting scaffolds exhibited an interconnected porous structure with final dimensions of 0.9 ± 0.1 cm in diameter and 0.8 ± 0.1 cm in height (inset Fig. 2A).

Materials characterisation

The XRD patterns (Fig. 2) revealed the crystalline composition of the multiphasic scaffolds which included calcium phosphates, silicates, and magnesium-rich phases. Among the calcium phosphates, characteristic peaks of calcium pyrophosphate ($Ca_2P_2O_7$) (COD 96-100-1557) were observed at $2\theta = 29.6°$, 33.5°, while those of β-tricalcium phosphate (β-TCP, $Ca_3(PO_4)_2$) (COD 96-151-7239) appeared at $2\theta = 31.01°$ and 34.3°. For the silicates, wollastonite ($CaSiO_3$) (COD 96-900-5779) was identified with peaks at $2\theta = 29.9°$, while cristobalite (SiO_2) (COD 96-900-8225) was detected at $2\theta = 21.9°$.

The magnesium-rich phases included akermanite (AK, $Ca_2MgSi_2O_7$) (COD 96-900-6942), with peaks at $2\theta = 31.1°$ and whitlockite (WH, $Ca10.115Mg0.385(PO_4)_7$) (COD 96-901-2137) displays characteristic diffraction signals that are slightly shifted to the right with respect to those of β-TCP, at $2\theta = 31.1°$ and 27.8°. The magnesium substitution within whitlockite results in lattice parameter distortion, leading to slight shifts in its diffraction peaks in comparison to the stoichiometric β-TCP. The superposition of the peaks from whitlockite and β-TCP results in a broadening effect in the XRD patterns, as observed at $2\theta = 31°$ and 27.8° (*e.g.*).

Fig. 2B depicts the FTIR spectra of scaffolds CS04 and CS05. The presence of Si—O—Si and PO_4^{3-} groups was confirmed,

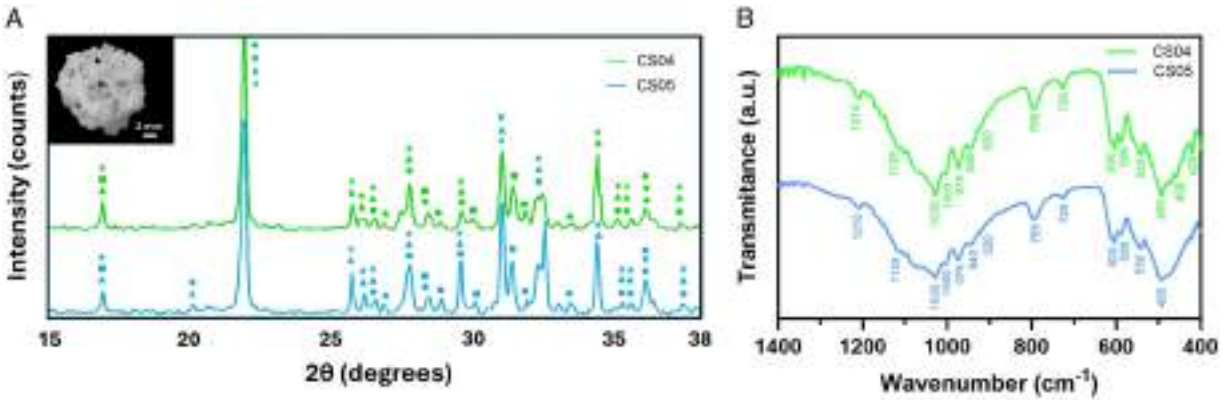

Fig. 2 – Materials characterisation. Chemical composition assessed using XRD (a) and FTIR (b). A small inset showing an optical image of the scaffold (top view) is included in (a). XRD legend: ♦ SiO_2; ● $Ca_2P_2O_7$; ▲ $Ca_3(PO_4)_2$; ■ $CaSiO_3$; ★ $Ca_{10.115}Mg_{3.85}(PO_4)_7$; ▼ $Ca_2MgSi_2O_7$.

with some overlapping bands. Furthermore, the presence of $P_2O_7^{2-}$ and HPO_4^{2-} groups was identified.

The PO_4^{3-} groups gave rise to the appearance of several bands, which were associated with various vibrational modes: (i) asymmetric stretching peaks at 1000 and 1030 cm^{-1}; (ii) symmetric stretching at 940 and 975 cm^{-1}; and (iii) bending modes at 600, 588 and 550 cm^{-1}. Furthermore, the HPO_4^{2-} group was identified at 920 cm^{-1}.

With regard to the Si—O—Si group, bands were observed in two principal regions. (i) asymmetric stretching or bending in the range 1216–1000 cm^{-1}, and (ii) symmetric stretching, with bands at 975 and 795 cm^{-1}. In addition to these regions, a Si—O—Si rocking band was also observed at 458 cm^{-1}, as well as a new band corresponding to Si—O—NBO at 920 cm^{-1}.

Finally, the pyrophosphate group ($P_2O_7^{2-}$) was present, with signals at 725, 920 and 1216 cm^{-1} detected in both scaffolds.

A comparison of the two spectra reveals that, despite the similarity in background and the majority of peaks, the bands corresponding to the phosphates in CS05 are markedly broader than those observed in CS04.

With regard to their physical properties, CS04 and CS05 exhibited comparable characteristics. Both exhibited a compressive strength of 1.8 ± 0.1 MPa and a porosity greater than 75%. CS04 demonstrated a macroporosity of 76 ± 2%, while CS05 revealed a slightly higher macroporosity of 77 ± 1%.

The SEM characterisation of the microstructure of the scaffolds prior and after SBF exposure is shown in Fig. 3. The surface of CS04 exhibits elongated and interconnected channels, which manifest a lamellar appearance. The lamellae were composed of Ca–P–Si grains, with a similar contribution of P and Si resulting in a Ca/P+Si of 0.7 ± 0.1. In terms of dimensions, the lamellas range from 5 to 10 μm in length and 1 to 3 μm in thickness, exhibiting an overall rough texture and irregular edges.

In contrast, CS05 displayed a surface characterised by a granular texture and elongated grains, with a rod shape morphology (▲), rich in calcium and silicon (Ca/Si ratio of 2 ± 0.1) (Fig. 3). These rod-shaped Ca–Si structures were observed to have a length of between 5 and 15 μm and a width of between

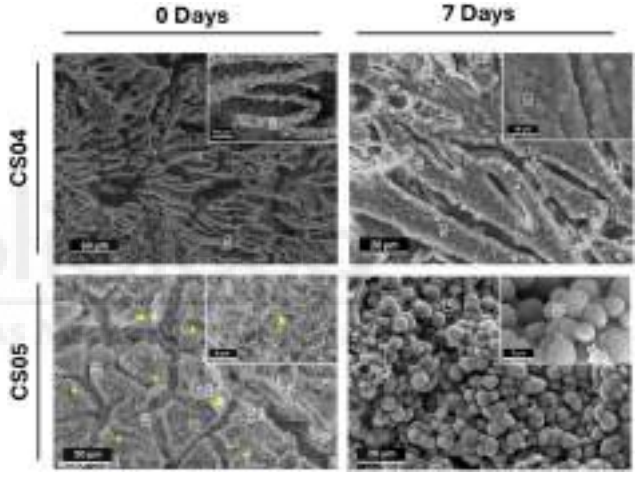

Fig. 3 – Surface analysis. FESEM-EDS micrographs depicting the microstructure of the scaffolds prior to (0D) and following 7 days of SBF exposure.

1 and 2 μm. Big angular Ca–P–Si grains (●) were also detected with a Ca/P+Si ratio of 0.6 ± 0.1.

Following a seven-day immersion period in SBF, both scaffolds exhibited evidence of mineral deposition on their surfaces. In the case of CS04, the original lamellar structure is still discernible, but it is now covered by a precipitate. The elemental composition of the mineral layer, as determined by EDS, indicates a composition based on Ca and P (Ca/P of 1.6 ± 0.1), with variable amounts of substituent ions such as Mg^{2+} (0.8 ± 0.1 at%), SiO_4^{4-} (2.6 ± 0.2 at%) or Na^+ (1.2 ± 0.1 at%) which are typically found in biological apatites [24,25]. However, CS05 displays a distinctive bioactive behaviour. The surface is observed to be densely covered with spherical Ca–P particles (Ca/P ratio of 1.7 ± 0.1), with a diameter of approximately 1–3 μm. A close-up view of the precipitated particles reveals the presence of a central cavity, suggesting the presence of a hollow structure. Furthermore, the precipitates were found to contain Mg^{2+} (0.9 ± 0.1 at%), SiO_4^{4-} (2.7 ± 0.1 at%) and Na^+ (1.2 ± 0.1 at%) dopants upon elemental examination

Table 1 – EDS analysis of the scaffold surface before and after 7 days of immersion in SBF.

EDS spot	Atomic %				
	Ca	P	Si	Mg	Na
1	38.6	34.3	27.1	–	–
2	43.6	30.4	26	–	–
3	41.3	25.2	33.5	–	–
4	60.2	35.1	2.8	0.7	1.2
5	57.3	38.2	2.5	0.9	1.1
6	58.1	36.9	2.7	0.9	1.4
7	67.7	–	32.3	–	–
8	65.5	–	34.5	–	–
9	66.2	–	33.8	–	–
10	37.5	20.8	41.7	–	–
11	40.7	21.2	38.1	–	–
12	39.3	21.5	39.2	–	–
13	61	34.2	2.6	0.9	1.3
14	58.2	37.2	2.8	0.8	1
15	59.3	36	2.6	1	1.2

(Fig. 3B). Lithium and potassium were found to be below the equipment's detection limit. For further details regarding the EDS analysis, see Table 1.

In vitro biocompatibility assessment

Following the physicochemical characterisation of the scaffolds, cell viability and cell morphology was evaluated to assess scaffolds biocompatibility.

Firstly, an indirect method was employed to evaluate the cytocompatibility of CM-IDPs *in vitro* and their effect on cell behaviour. This approach was used to assess the effect of the scaffolds on neighbouring cells, which also contribute to the deposition of new ECM. In order to achieve this, the solutions described in Section "Indirect approach" were prepared and the ionic variations of the CM-IDPs were monitored over 21 days (Fig. 4).

The ion release patterns observed in the scaffolds can be categorised into three distinct behaviours: release, absorption, and stability. For releasing ions, calcium was leaked in greater amounts at higher concentrations (100 mg/mL) compared to lower concentrations (10 mg/mL), with CS04 showing a higher release at the same concentration. A comparable trend was observed for silicon, which was released to a greater extent at higher concentrations, with CS04 exhibiting a higher release than CS05. A direct relationship between lithium liberation and concentration was also observed, albeit with CS05 releasing more lithium. It was observed that the released ions remained within a range of 30 mg/mL above the basal level.

With regard to the absorbed ions, magnesium demonstrated enhanced incorporation into the sample at elevated concentrations, with a slight increase in uptake observed for CS05. Conversely, phosphorus exhibited higher levels of precipitation or uptake at higher concentrations, particularly for CS04. It is noteworthy that phosphorus and silicon demonstrated an inverse relationship; as one increased, the other decreased.

Finally, sodium and potassium concentrations fluctuated but remained close to baseline levels throughout the study. As anticipated, the ionic variations resulted in alterations in the mean pH. With regard to CS0X at 100 mg/mL, there is a tendency towards alkalinisation in comparison to the control (pH 8.3). However, for CS0X at 10 mg/mL, the pH variations are not particularly marked and remain closer to the baseline. While CS04 initially basifies the pH of the medium, CS05 acidifies it. At day 21, both pH values are almost equal, indicating a slight acidification.

The results of the WST-8 assay show that CS04 and CS05 scaffolds, through an indirect approach and direct approach, are biocompatible and favour cell viability of murine MC3T3-E1 preosteoblasts (Fig. 5).

Fig. 5A illustrates a gradual increase in cell population over time in each treatment group, indicating that the scaffold dissolution products are cytocompatible. A more detailed analysis reveals that, during the initial three-day period, cell viability is slightly lower in the treatment groups relative to the control, particularly for CS04 at 100 mg/mL. However, these differences are not statistically significant. By day 7, cell viability is notably higher in all treated groups, with CS05 at both concentrations demonstrating statistically higher and significant values in comparison to the control and CS04 at the same concentration. From day 14 onwards, cell proliferation appears to reach a saturation state, given that the 2D culture has occupied the available surface area, thereby limiting further growth. However, in the case of CS04 100 mg/mL, due to the smaller initial cell population, a slight increase in viability was still observed, likely because there was still some surface area available for proliferation.

In the direct approach (Fig. 5B), increasing cell viability is observed over time for all scaffolds tested, confirming their cytocompatibility. Although no statistically significant differences were found between CS04 and CS05, a slightly higher cell viability was generally observed for CS05.

Fig. 6A depicts the behaviour of MC3T3-E1 preosteoblasts treated with the different CM-IDP preparations over a seven-day period. The assay was limited to day 7 because, as indicated in Fig. 5A, a saturation point was reached due to complete colonisation of the culture plate, which prevented the visualisation of individual cell morphology and provided no additional information. At the 24-h mark, cell adhesion is evident across all treatment groups. The cells exhibit their characteristic spindle-like morphology, indicating good

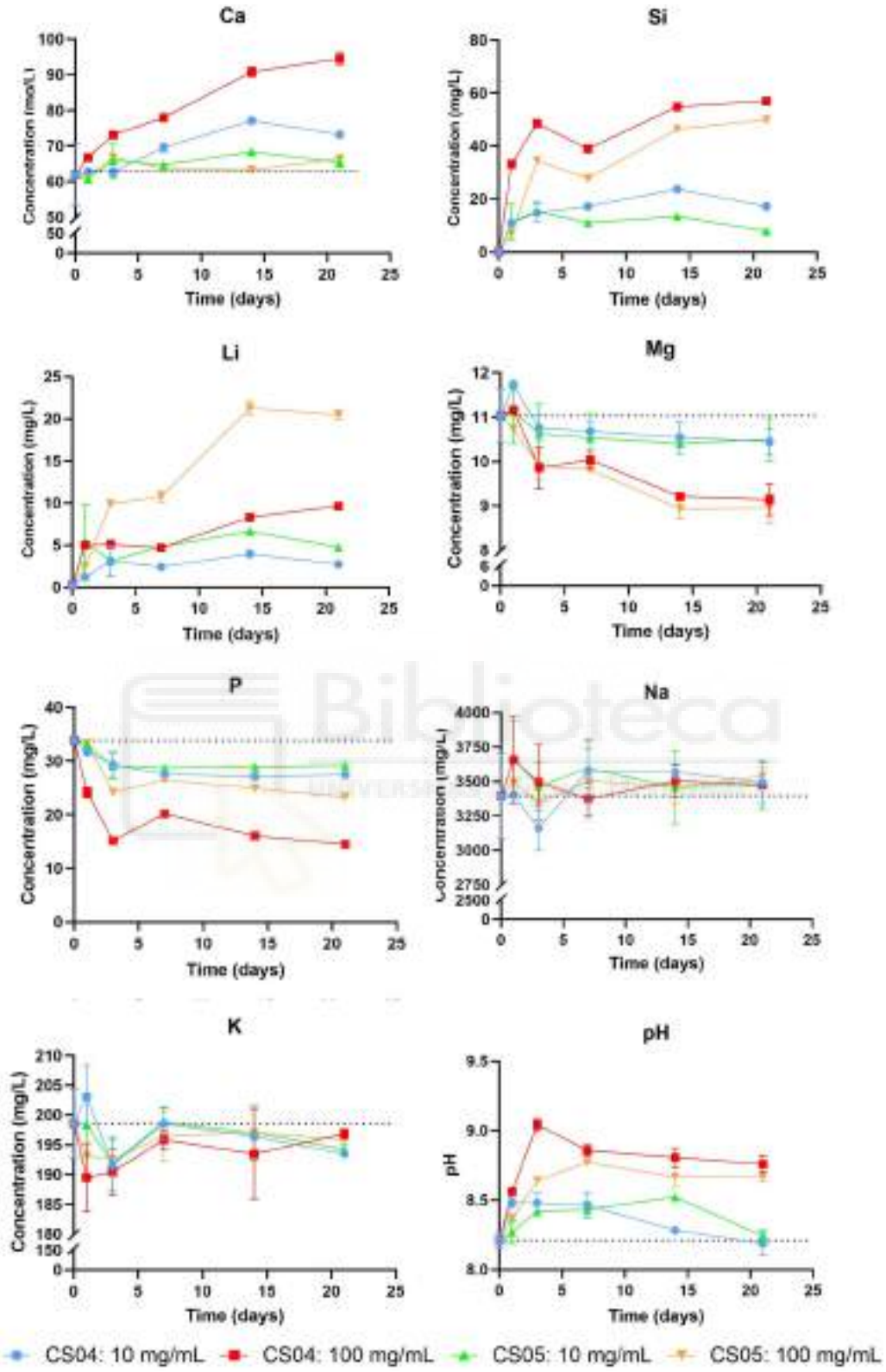

Fig. 4 – Monitoring of ionic concentration and pH variations of CM-IDP over 21 days.

cellular health. However, a lower cell density is observed for CS04-100 mg/mL compared to the control and other treatments, a trend that persists throughout the seven-day study period. Additionally, a consistent increase in cell population is noted over time, with the cells progressively spreading and nearly reaching confluence by day seven.

As shown in Figure 6B, the SEM micrographs demonstrate evidence of cell adhesion within 24 hours. While the

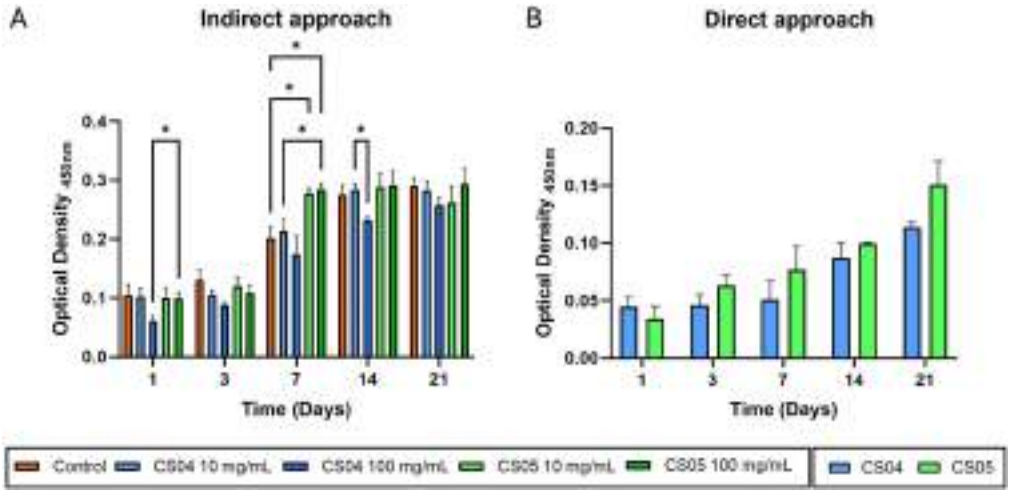

Fig. 5 – Results of the cell viability assay WST-8 from an indirect (A) and direct approach (B).

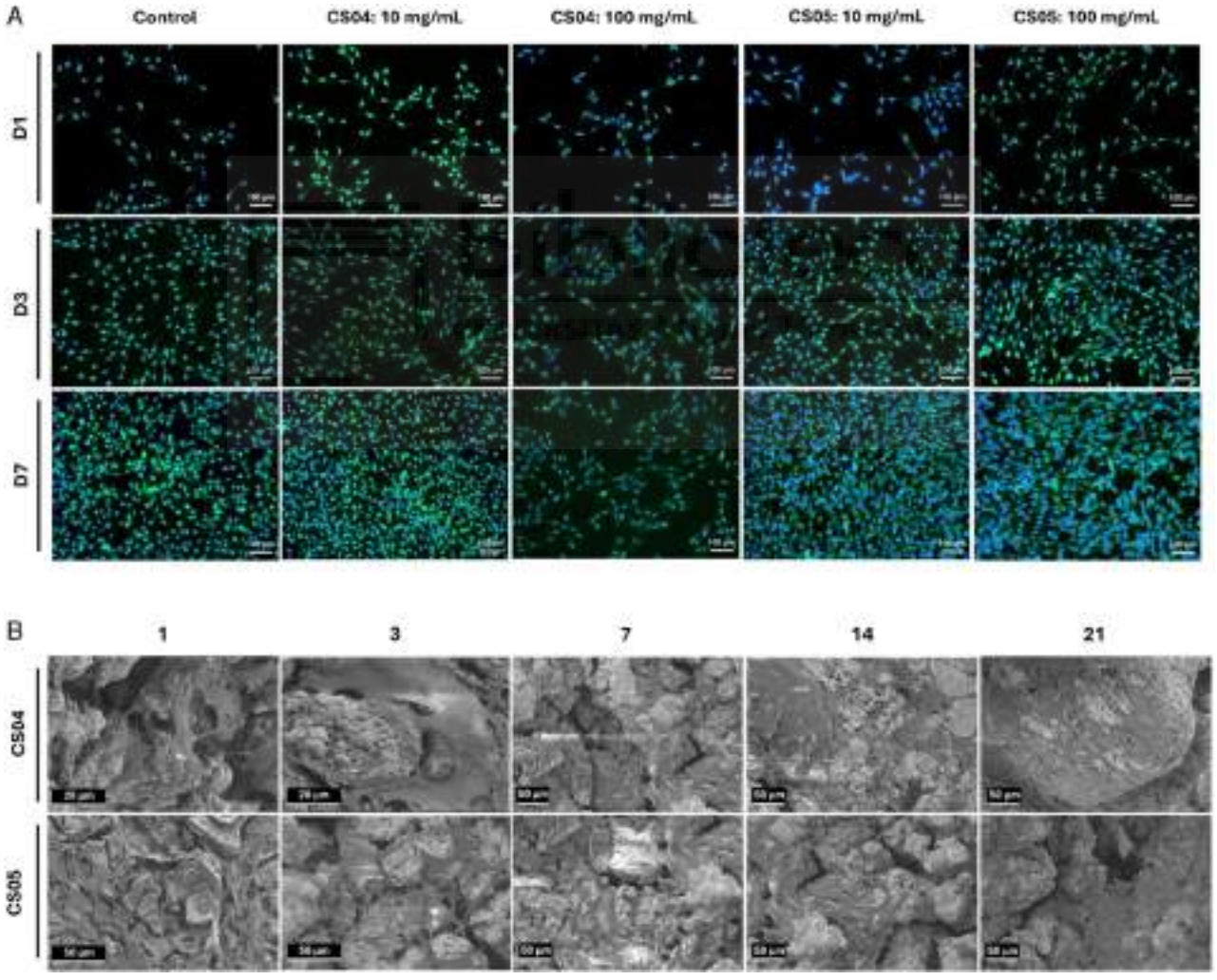

Fig. 6 – Evaluation of MC3T3-E1 morphology upon exposure to CM-IDP (A) and plated on scaffolds CS04 and CS05 (B).

morphology varies, displaying both star-shaped cells and spindle-like cells (e.g., CS0X, 1D), which are particularly evident in CS05 at 21 days, the cells in all cases appear flattened and well-spread on the scaffold surface. Furthermore, well-defined filopodia are evident, indicating a robust interaction with the material. With time, the cells are seen to disperse throughout the surface of the scaffold, although they do not achieve complete confluence.

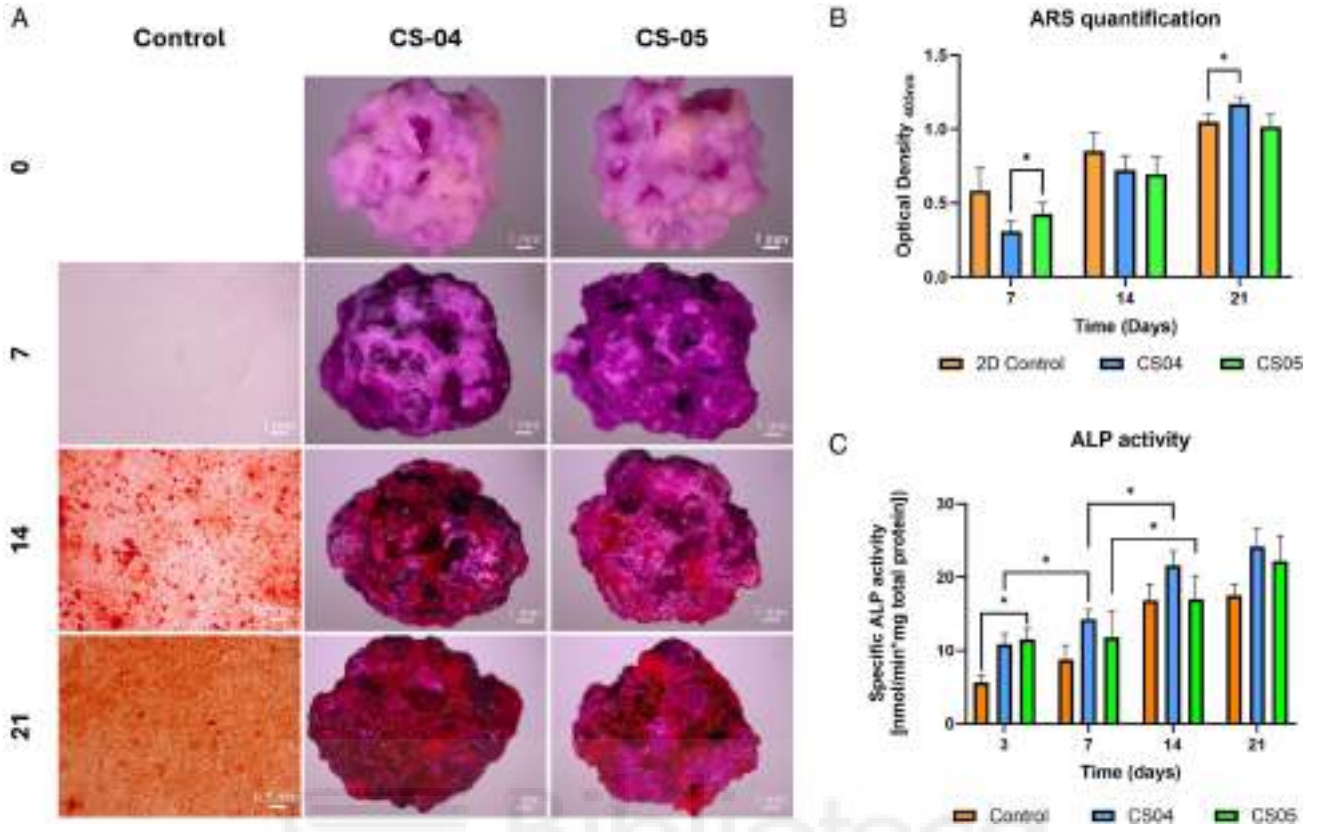

Fig. 7 – Osteogenic assessment. Qualitative (A) and quantitative (B) ARS staining results, along with the quantification of ALP specific activity (C).

Osteogenic assessment

To assess the osteogenic potential of the scaffolds, ARS and specific quantification of ALP activity were performed (Fig. 7). To initiate the study, ARS staining was performed on the cell-free scaffolds to avoid background interference during the mineralisation assessment. The staining at day 0 generated a basal pinkish hue which subsequently evolved into a more intense purple on day 7. Finally, the scaffolds exhibited a reddish hue by day 14, with an intensification observed after 21 days, particularly at CS04. Fig. 7B quantifies the ARS staining, demonstrating a notable elevation in optical density (OD_{405}) for the scaffolds on day 14.

With regard to ALP activity, an overall enhancement in specific activity was observed in cells seeded on the scaffolds in comparison to the 2D control, indicating an augmented osteoblastic activity in cells exposed to the scaffold.

Angiogenic assessment

The angiogenic potential of the CS04 and CS05 scaffolds was evaluated by quantifying the release of VEGF in cell supernatants, with the release observed in the control group considered as the 100% reference (Fig. 8). It was observed that, while no statistically significant differences were found between the control cells and those seeded on the scaffolds during the first week of the study, after 14 days, these differences became pronounced, with VEGF release levels of 160% for CS05 and 170% for CS04. These differences remained significant at 21 days, with an increase in the level of significance.

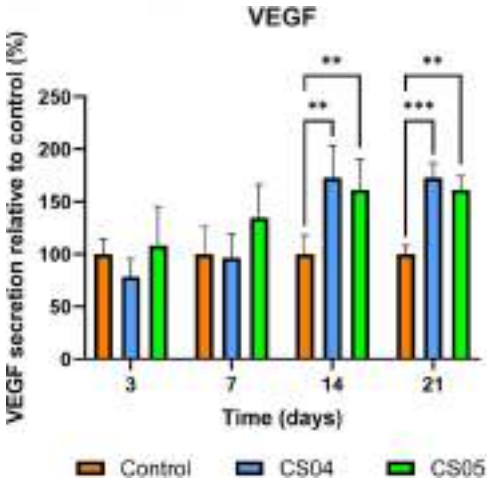

Fig. 8 – Assessment of angiogenic potential. VEGF secretion in the supernatants of cells cultured on 2D control or scaffolds CS04 and CS05.

Discussion

In this study, the design of third-generation multilayer porous scaffolds aims to optimise scaffold performance by combining

phases that closely mimic the mineral composition and physiological properties of bone tissue. The strategic incorporation of inorganic elements such as magnesium, lithium and other bioactive ions into the scaffold matrix has the potential to significantly enhance the bioactivity of the materials, the biochemical cell-material interactions, as well as the mechanical strength and biological performance of the materials.

The resulting scaffolds with a final diameter of 0.9 ± 0.1 cm and a height of 0.8 ± 0.1 cm displayed an interconnected porous structure. According to the experimental XRD spectra, the predominant phases identified in the scaffolds were $Ca_2P_2O_7$, β-$Ca_3(PO_4)_2$, SiO_2, together with $CaSiO_3$, $Ca_{10.115}Mg_{0.385}(PO_4)_6$, and $Ca_2MgSi_2O_7$ to a lesser extent (Fig. 2A). While CS and β-TCP were initially formulated, the additional phases were formed as a result of ionic doping with magnesium (*e.g.*, $Ca_{10.115}Mg_{0.385}(PO_4)_6$ and $Ca_2MgSi_2O_7$) or due to ionic migration between layers during the sintering process (*e.g.*, $Ca_2P_2O_7$ and SiO_2). The latter process can be described as a calcium migration phenomenon induced by the interaction between CS and the amorphous phosphate coating P6. At 1050 °C, calcium migration from $CaSiO_3$ to $Ca_2P_6O_{17}$ destabilises CS, resulting in its transformation to SiO_2. At the same time, the ultraphosphate phase $Ca_2P_6O_{17}$, which exhibits structural disorder, is transformed into a more stable crystalline phase, calcium pyrophosphate ($Ca_2P_2O_7$), by incorporating calcium from the CS [26].

In consideration of the *in vivo* behaviour of each material, the scaffolds incorporate rapidly resorbable phases, including β-TCP and WH [12,14]. These phases facilitate the release of essential ions that promote matrix mineralisation and other osseous-related processes [13,27,28]. They also contain bioactive materials, such us CS and AK, which enhance the scaffold's capacity to bond with hard tissue [28,29]. Additionally, the incorporation of calcium pyrophosphate and silica plays a pivotal role in improving the mechanical properties and modulating the degradation rates of the scaffold, respectively, thus ensuring compatibility with physiological processes [27,29,30].

The presence of these phases was additionally corroborated by FTIR (Fig. 2B). The signals at 724 cm^{-1}, 919 cm^{-1} and 1208 cm^{-1} indicate the presence of the pyrophosphate group, which is characteristic of $Ca_2P_2O_7$. Additionally, another phosphate vibrational mode, PO_4^{3-}, was identified, which is associated with the β-TCP and WH phases. The Si—O—Si group was also detected, which is indicative of the cristobalite, calcium silicate and akermanite phases.

As mentioned above, the crystal structures of β-TCP and WH are closely related, resulting in almost identical XRD patterns. Therefore, reliable identification of WH is not possible without the use of vibrational spectroscopy, which allows the observation of signals from the $HPO4^{2-}$ group at 920 cm^{-1} (Fig. 2B). This structural unit can be used as a reliable spectral marker as it is only present in the crystal structure of WH [31].

FTIR spectra also revealed that increasing the magnesium content broadened the phosphate bands and reduced their intensities, reflecting reduced crystallinity due to competition between Mg^{2+} and Ca^{2+} for binding with pyrophosphate ($P_2O_7^{2-}$) and phosphate (PO_4^{3-}) [32]. The ionic radius mismatch between Mg^{2+} and Ca^{2+} caused lattice distortions leading to a disruption of crystallinity.

With regard to the physical characterisation of the scaffolds, a compressive strength of 1.8 ± 0.1 was observed, along with a porosity over 75%, which is in accordance with the requirements for bone tissue regeneration applications [16,33]. While the compressive strength is lower than that of cortical bone, it is comparable to that of trabecular bone (1.7–7.5 MPa) [34]. In particular, the mechanical strength is expected to increase as new mineral phase is deposited, compensating for scaffold degradation, as reported in previous studies of ceramic scaffolds *in vivo* [35].

The porosity of the scaffolds is beneficial for facilitating angiogenesis and vascular infiltration, which are essential for the transportation of nutrients, oxygen and growth factors [10,16,33]. In addition, increased porosity increases the surface area of the scaffold, promoting enhanced cell infiltration, adhesion and migration – key processes for effective bone regeneration [17,36].

However, porosity should be coupled with an appropriate microstructure that facilitates optimal cell-material adhesion while promoting the deposition of bone-like minerals. Both scaffolds, CS04 and CS05, exhibited surface characteristics consistent with materials tailored for bone regeneration (Fig. 3) [9,13,16,17]. The lamellar structure of CS04, composed of calcium silico-phosphate crystals, provides nucleation sites for HA formation due to its silicon content. Although these lamellae are not strictly classified as "pores", they create voids that significantly increase the surface area of the scaffold. Similarly, CS05 had a Ca–Si based surface which also provided nucleation sites for mineral deposition.

Subtle variations in Mg content were found to influence both the scaffold topography and the bioactive behaviour. After one week in SBF, both scaffolds showed deposition of apatite-like precipitates enriched in Mg^{2+}, SiO_4^{4-} or Na^+ as substitutes for Ca^{2+}, PO_4^{3-} and OH^- ions and deviating from the stoichiometric formula of hydroxyapatite, $Ca_{10}(PO_4)_6(OH)_2$. For CS04, the lamellar structure was maintained under these precipitates, whereas CS05 developed hollow microspheres (1–3 μm) on its surface. Similarly, Bauer et al. reported that the incorporation of Mg^{2+} ions into calcium phosphate scaffolds resulted in surface morphology modifications and precipitation of microspheres during SBF tests, with sizes tunable as a function of Mg content [32].

The chemical composition of these apatite-like precipitates underlines the ability of the scaffold to mimic physiological bone mineralisation, considering that biological apatites are deficient in calcium [24,25]. This ability is essential to allow the scaffold to integrate with the surrounding bone. In addition, these biomimetic, non-stoichiometric apatites offer distinct advantages over stoichiometric synthetic HA. While synthetic HA is widely used for implants due to its high stability, its low solubility results in slower resorption rates compared to physiological tissue regeneration [37]. In contrast, biomimetic substituted HA ensures higher biodegradability and bioactivity, as well as sustained release of biologically active ions [38].

The field of ion-releasing scaffolds for biomedical applications has experienced significant growth over the past two

decades, driven by the recognition of the potential benefits of ion release for tissue repair therapies [28].

In this regard, the concentration of constituting ions (P, Si and Ca^{2+}) as well as doping ions (Li^{+}, Mg^{2+}, Na^{+} and K^{+}) were monitored over a 21-day period in a non-cumulative degradation study (Section "Indirect approach"). The ions that were predominantly released were calcium, silicon and lithium (Fig. 4).

Calcium plays an essential role in bone and its metabolism, as a key component of the mineral phase in the form of HA [33]. Previous research has shown that the release of calcium *in vitro* is associated with enhanced osteogenic differentiation [39,40], proliferation of bone marrow stem cells [40], and increased ALP activity [28,41], among other beneficial effects.

Silicon has been extensively documented to play a pivotal role in a number of biological processes, including bone mineralisation, collagen synthesis and osteogenesis [12,29,42,43]. These processes include ALP expression and the early differentiation of osteoblasts, as previously reported by Sun et al. [44]. Additionally, Si ions have been demonstrated to facilitate the formation of apatite layers, thereby enhancing bioactivity [12,29].

Although lithium is a toxic alkaline metal, it has been demonstrated to exhibit angiogenic and osteogenic properties when incorporated into bioactive glasses in both *in vitro* and *in vivo* conditions [45–47]. Tal et al. demonstrated that lithium concentrations of 125 μm to 1 mM had a pro-proliferative effect on bone mesenchymal stem cells, being 500 μm the optimal concentration [46]. This concentration, which equals to approximately 3.5 mg/L, was found, additionally, to activate Wnt signalling, needed for VEGF expression and bone regeneration, even in the presence of XAV-939 inhibitor [46]. In Fig. 4 it can be appreciated that for both scaffold and concentrations, lithium liberation remained above this value, being closer to 3.5 mg/L at 10 mg/L concentration. In addition, Clément-Lacroix et al. reported an increase in both bone mass and bone formation in mice treated with lithium chloride, a result of the activation of the Wnt canonical signalling [47]. Consequently, the liberation of lithium may contribute to the osteogenic and angiogenic potential of these scaffolds.

Regarding the constituting ions P and Si, an inverse relationship is evident between their respective concentrations: a reduction in phosphorus concentration is accompanied by an increase in silicon concentration, and *vice versa*. Given that the scaffolds are bioactive in SBF, and alpha-MEM is supersaturated with respect to HA, this could suggest the dissolution of a silicon-rich surface phase, followed by the precipitation of HA in a cyclic manner. This behaviour has already been described by Mata et al. [30]. Furthermore, this process is accompanied by a decline in magnesium levels, which may indicate the precipitation of Mg-enriched HA, as observed in bioactivity assays. While this would typically be expected to coincide with a decrease in calcium concentration, similar behaviour has been previously observed in our studies conducted in SBF [20,21]. This phenomenon may be attributed to a higher release of calcium from the scaffold, due to its high CaO content (37 wt%), which outpaces the rate of HA precipitation.

Lastly, the fluctuating behaviour of the doping ions sodium and potassium, which are consistently near baseline levels, may suggest that they could be incorporated as substituents in the precipitating and dissolving HA phases. This substitution is aligned with the dynamic ion exchange processes inherent to bioactive materials. The results suggest that, although there is no release of Mg^{2+}, Na^{+}, or K^{+}, in a context involving osteoclasts where the mineral phase is resorbed, these ions could still have a beneficial effect on osteogenic processes, particularly considering the crucial role of magnesium in osteogenic processes [28,48].

These mechanisms were accompanied by a change in pH. A general trend of alkalinisation was observed at concentrations of 100 mg/mL for both scaffolds. In contrast, at 10 mg/mL, the pH remained closer to control values, demonstrating a decrease by the end of the study. It has been previously demonstrated that an alkaline pH exerts beneficial effects on MC3T3-E1 preosteoblasts [49,50]. Gallow et al. reported that this alkalinisation not only enhanced the expression of genes typically activated at pH 7.4 but also induced the expression of additional genes related to osteogenesis [49]. Moreover, Gallow et al. observed enhanced MC3T3-E1 proliferation at pH levels between 8.2 and 8.8 [50].

In vitro biological characterisation of the scaffolds demonstrated their overall robust performance. WST-8 assays were conducted to evaluate the biocompatibility of the CM-IDP of the scaffolds and the material itself. The results demonstrated consistent cell population growth, confirming the biocompatibility of both the scaffold in solution and in solid form (Fig. 5). In the indirect approach, a lower cell viability was observed for CS04-100 mg/mL, particularly during the initial seven days of the study (Fig. 5A). From the ICP-OES results it can be concluded that this decrease is due to the increased release of silicon and combined with a pH of 9, which is above the level recommended by Gallow et al. [50]. Conversely, the findings from the direct approach (Fig. 5B) corroborate the biocompatibility of the scaffolds, as evidenced by the sustained proliferation of cells over time.

The biocompatibility of the material was further confirmed through fluorescence microscopy and SEM (Fig. 6). The cellular morphology observed during the indirect study revealed no differences between the treatment groups and the control, indicating that the IDP are cytocompatible (Fig. 6A). Additionally, in the direct approach, cells plated on the scaffolds displayed an extended morphology throughout the study, indicating a good cell-material interaction (Fig. 6B). If this were not the case, contracted cells minimising contact with the interface would have been observed.

Given the previous *in vitro* bioactivity (Fig. 3, Table 1) and ICP-OES results (Fig. 4) suggesting good osteogenic properties, the specific activity of alkaline phosphatase in cell lysates, a recognised marker of osteoblast differentiation, was quantified. The results showed a higher specific ALP activity compared to the control group. The high content of calcium phosphates in the scaffolds, mainly calcium pyrophosphate and β-TCP, together with its partially Mg-substituted phase, whitlockite, provides a substrate for the enzyme. This, together with the alkalinisation of the medium induced by SiO_4^{-4}, creates an optimal biochemical environment for ALP activity, as the enzyme functions more efficiently under alkaline conditions, which would explain its increased activity.

Calcium deposition was also evaluated using the ARS assay. The results showed the formation of mineralised nodules in the 2D control group after 14 days (Fig. 7A). Similarly, an increase in red staining was observed in both CS04 and CS05 scaffolds on day 14, with the effect becoming more pronounced after 21 days. These results are consistent with previous studies showing that the MC3T3-E1 subclone begins to deposit a well mineralised extracellular matrix (ECM) as early as 10 days [51]. In addition, Deliormanlı et al. reported comparable behaviour in MC3T3-E1 cells cultured on graphene-containing PCL/bioactive glass scaffolds, with a significant increase in mineralisation after 21 days [52].

These scaffolds also demonstrated their angiogenic potential, as evidenced by the stimulation of VEGF release compared to the control, which was detected from day 14 onwards. This, combined with their appropriate porosity could support the formation of a vascular network that infiltrates the scaffold, in turn facilitating tissue regeneration.

Conclusion

Third generation porous multilayer scaffolds were designed based on the SiO_2–CaO–P_2O_5 system, incorporating Li_2O, Na_2O, K_2O, and MgO (0.38; 0.49 wt%) as network modifiers. The MgO content was varied to optimise the physical, topographical, and biological properties of the scaffolds. While the physical characteristics remained unchanged, the MgO content influenced the scaffold's topography and bioactive behaviour, leading to the formation of either a lamellar structure (CS04) or the precipitation of HA hollow microspheres (CS05) upon 7-day SBF exposure.

In vitro biological characterisation yielded promising results in three key areas: (i) the scaffolds and their degradation products were biocompatible, promoting cellular proliferation and osteogenic processes, (ii) the scaffolds induced osteogenic differentiation, as evidenced by calcium deposit formation and increased ALP specific activity, and (iii) the scaffolds stimulated VEGF release by up to 170% compared to the control. The structural and functional optimisation potential of these scaffolds highlights their promise in addressing critical challenges in bone tissue engineering.

Future investigations will focus on studying the capacity for loading therapeutic agents, utilising the interlamellar spaces and hollow microspheres of the scaffolds. These structures offer significant potential for the localised delivery of bioactive molecules tailored to specific clinical needs. Moreover, preclinical studies in animal models will assess the osteoinductive and osteoconductive properties of the scaffolds, in addition to their effects on the quality of bone tissue, vascularisation, integration with the host bone, and immune response.

Acknowledgements

This work is part of the project PID2020-116693RB-C21, funded by MCIN/AEI/10.13039/501100011033 Spain.

REFERENCES

[1] B. Lunenfeld, P. Stratton, The clinical consequences of an ageing world and preventive strategies, Best Pract. Res. Clin. Obst. Gynaecol. 27 (5) (2013), http://dx.doi.org/10.1016/j.bpobgyn.2013.02.005.
[2] T. Mastnak, U. Maver, M. Finšgar, Addressing the needs of the rapidly aging society through the development of multifunctional bioactive coatings for orthopedic applications, Int. J. Mol. Sci. 23 (5) (2022), http://dx.doi.org/10.3390/ijms23052786.
[3] A.M. Wu, C. Bisignano, S.L. James, G.G. Abady, A. Abedi, E. Abu-Gharbieh, R.K. Alhassan, V. Alipour, J. Arabloo, M. Asaad, W.N. Asmare, A.F. Awedew, M. Banach, S.K. Banerjee, A. Bijani, T.T.M. Birhanu, S.R. Bolla, L.A. Cámera, J.C. Chang, T. Vos, Global, regional, and national burden of bone fractures in 204 countries and territories, 1990–2019: a systematic analysis from the Global Burden of Disease Study 2019, Lancet Healthy Longev. 2 (9) (2021), http://dx.doi.org/10.1016/S2666-7568(21)00172-0.
[4] E. Seeman, Pathogenesis of bone fragility in women and men, Lancet 359 (9320) (2002), http://dx.doi.org/10.1016/S0140-6736(02)08706-8.
[5] M.A. Clynes, N.C. Harvey, E.M. Curtis, N.R. Fuggle, E.M. Dennison, C. Cooper, The epidemiology of osteoporosis, Br. Med. Bull. 133 (1) (2020), http://dx.doi.org/10.1093/bmb/ldaa005.
[6] H. Newman, Y.V. Shih, S. Varghese, Resolution of inflammation in bone regeneration: from understandings to therapeutic applications, Biomaterials 277 (2021), http://dx.doi.org/10.1016/j.biomaterials.2021.121114.
[7] C.S. Bahney, R.L. Zondervan, P. Allison, A. Theologis, J.W. Ashley, J. Ahn, T. Miclau, R.S. Marcucio, K.D. Hankenson, Cellular biology of fracture healing, J. Orthop. Res. 37 (1) (2019), http://dx.doi.org/10.1002/jor.24170.
[8] L. Steppe, M. Megafu, M.E.A. Tschaffon-Müller, A. Ignatius, M. Haffner-Luntzer, Fracture healing research: recent insights, Bone Rep. 19 (2023), http://dx.doi.org/10.1016/j.bonr.2023.101686.
[9] X. Yu, X. Tang, S.V. Gohil, C.T. Laurencin, Biomaterials for bone regenerative engineering, Adv. Healthc. Mater. 4 (9) (2015) 1268–1285, http://dx.doi.org/10.1002/adhm.201400760.
[10] Ž. Perić Kačarević, P. Rider, S. Alkildani, S. Retnasingh, M. Pejakić, R. Schnettler, M. Gosau, R. Smeets, O. Jung, M. Barbeck, An introduction to bone tissue engineering, Int. J. Artif. Organs 43 (2) (2020), http://dx.doi.org/10.1177/0391398819876286.
[11] J. Henkel, M.A. Woodruff, D.R. Epari, R. Steck, V. Glatt, I.C. DIckinson, P.F.M. Choong, M.A. Schuetz, W. Di Hutmacher, Bone regeneration based on tissue engineering conceptions – a 21st century perspective, Bone Res. 1 (2013), http://dx.doi.org/10.4248/BR201303002.
[12] M. Navarro, A. Michiardi, O. Castaño, J.A. Planell, Biomaterials in orthopaedics, J. R. Soc. Interface 5 (27) (2008), http://dx.doi.org/10.1098/rsif.2008.0151.
[13] L.L. Hench, I. Thompson, Twenty-first century challenges for biomaterials, J. R. Soc. Interface 7 (SUPPL. 4) (2010), http://dx.doi.org/10.1098/rsif.2010.0151.focus.
[14] M. Vallet-Regí, A.J. Salinas, Ceramics as bone repair materials, in: bone repair biomaterials: regeneration and clinical applications, second edition, 2018, http://dx.doi.org/10.1016/B978-0-08-102451-5.00006-8.
[15] H. Ismail, H. Mohamad, Bioactivity and biocompatibility properties of sustainable wollastonite bioceramics from rice husk ash/rice straw ash: a review, Materials 14 (18) (2021), http://dx.doi.org/10.3390/ma14185193.

[16] A.R. Amini, C.T. Laurencin, S.P. Nukavarapu, Bone tissue engineering: recent advances and challenges, Crit. Rev. Biomed. Eng. 40 (5) (2012), http://dx.doi.org/10.1615/CritRevBiomedEng.v40.i5.10.
[17] Á.E. Mercado-Pagán, A.M. Stahl, Y. Shanjani, Y. Yang, Vascularization in bone tissue engineering constructs, Ann. Biomed. Eng. 43 (3) (2015), http://dx.doi.org/10.1007/s10439-015-1253-3.
[18] H.-H. Lu, D. Ege, S. Salehi, A.R. Boccaccini, Ionic medicine: exploiting metallic ions to stimulate skeletal muscle tissue regeneration, Acta Biomater. 190 (2024) 1–23, http://dx.doi.org/10.1016/j.actbio.2024.10.033.
[19] F.E. Ciraldo, E. Boccardi, V. Melli, F. Westhauser, A.R. Boccaccini, Tackling bioactive glass excessive in vitro bioreactivity: preconditioning approaches for cell culture tests, Acta Biomater. 75 (2018), http://dx.doi.org/10.1016/j.actbio.2018.05.019.
[20] P.M. Riosalido, P. Velásquez, Á. Murciano, P.N. De Aza, Surface morphology modulation in multilayer scaffolds via ion doping for bone tissue engineering, J. Am. Ceram. Soc. Am. Ceram. Soc. 108 (3) (2025), http://dx.doi.org/10.1111/jace.20269.
[21] P.M. Riosalido, P. Velásquez, Á. Murciano, P.N. De Aza, Multilayer scaffolds designed with bioinspired topography for bone regeneration, Ceram. Int. (2025), http://dx.doi.org/10.1016/j.ceramint.2025.01.180.
[22] International Organisation for Standardisation. Implants for surgery—*in vitro* evaluation for apatite-forming ability of implant materials (ISO Standard No. 23317:2014) (2014).
[23] Mouse VEGF ELISA Kit. (2024). RayBiotech. https://doc.raybiotech.com/pdf/Manual/ELM-VEGF.pdf.
[24] Q. Liu, S. Huang, J.P. Matinlinna, Z. Chen, H. Pan, Insight into biological apatite: physiochemical properties and preparation approaches, BioMed Res. Int. 2013 (2013), http://dx.doi.org/10.1155/2013/929748.
[25] C. Combes, S. Cazalbou, C. Rey, Apatite biominerals, Minerals 6 (2) (2016), http://dx.doi.org/10.3390/min6020034.
[26] D. Stachel, H. Paulus, I. Svoboda, H. Fuess, Crystal structure of calcium ultraphosphate, $Ca_2P_6O_{17}$, Zeitschrift Fur Kristallographie – New Cryst. Struct. 202 (1–2) (1992), http://dx.doi.org/10.1524/zkri.1992.202.1-2.117.
[27] K.H. Min, D.H. Kim, K.H. Kim, J.-H. Seo, S.P. Pack, Biomimetic scaffolds of calcium-based materials for bone regeneration, Biomimetics 9 (9) (2024) 511, http://dx.doi.org/10.3390/biomimetics9090511.
[28] A. Hoppe, N.S. Güldal, A.R. Boccaccini, A review of the biological response to ionic dissolution products from bioactive glasses and glass-ceramics, Biomaterials 32 (11) (2011), http://dx.doi.org/10.1016/j.biomaterials.2011.01.004.
[29] M. Sanmartin de Almeida, G.V. de O. Fernandes, A.M. de Oliveira, J.M. Granjeiro, Calcium silicate as a graft material for bone fractures: a systematic review, J. Int. Med. Res. 46 (7) (2018), http://dx.doi.org/10.1177/0300060518770940.
[30] N.A. Mata, P. Velasquez, A. Murciano, P.N. de Aza, Multilayer Mg-pyrophosphate glass ceramic with discontinuous bioactivity. Physicochemical characterization, Ceram. Int. 47 (10) (2021), http://dx.doi.org/10.1016/j.ceramint.2021.02.044.
[31] D. Griesiute, A. Kizalaite, A. Dubnika, V. Klimavicius, V. Kalendra, V. Tyrpekl, S.H. Cho, T. Goto, T. Sekino, A. Zarkov, A copper-containing analog of the biomineral whitlockite: dissolution–precipitation synthesis, structural and biological properties, Dalton Trans. 53 (4) (2023), http://dx.doi.org/10.1039/d3dt03756h.
[32] L. Bauer, M. Antunović, A. Rogina, M. Ivanković, H. Ivanković, Bone-mimetic porous hydroxyapatite/whitlockite scaffolds: preparation, characterization and interactions with human mesenchymal stem cells, J. Mater. Sci. 56 (5) (2021), http://dx.doi.org/10.1007/s10853-020-05489-3.
[33] A.M. Weatherholt, R.K. Fuchs, S.J. Warden, Specialized connective tissue: bone, the structural framework of the upper extremity, J. Hand Therapy 25 (2) (2012), http://dx.doi.org/10.1016/j.jht.2011.08.003.
[34] G. Kaur, V. Kumar, F. Baino, J.C. Mauro, G. Pickrell, I. Evans, O. Bretcanu, Mechanical properties of bioactive glasses, ceramics, glass-ceramics and composites: state-of-the-art review and future challenges, Mater. Sci. Eng. C 104 (2019), http://dx.doi.org/10.1016/j.msec.2019.109895.
[35] N. Tamai, A. Myoui, T. Tomita, T. Nakase, J. Tanaka, T. Ochi, H. Yoshikawa, Novel hydroxyapatite ceramics with an interconnective porous structure exhibit superior osteoconduction in vivo, J. Biomed. Mater. Res. 59 (1) (2002), http://dx.doi.org/10.1002/jbm.1222.
[36] N. Abbasi, A. Abdal-Hay, S. Hamlet, E. Graham, S. Ivanovski, Effects of gradient and offset architectures on the mechanical and biological properties of 3-D Melt Electrowritten (MEW) scaffolds, ACS Biomater. Sci. Eng. 5 (7) (2019), http://dx.doi.org/10.1021/acsbiomaterials.8b01456.
[37] H.L. Jang, G. bin Zheng, J. Park, H.D. Kim, H.R. Baek, H.K. Lee, K. Lee, H.N. Han, C.K. Lee, N.S. Hwang, J.H. Lee, K.T. Nam, In vitro and in vivo evaluation of whitlockite biocompatibility: comparative study with hydroxyapatite and β-tricalcium phosphate, Adv. Healthc. Mater. 5 (1) (2016), http://dx.doi.org/10.1002/adhm.201400824.
[38] F. Ren, Y. Leng, R. Xin, X. Ge, Synthesis, characterization and ab initio simulation of magnesium-substituted hydroxyapatite, Acta Biomater. 6 (7) (2010), http://dx.doi.org/10.1016/j.actbio.2009.12.044.
[39] T. Sugimoto, M. Kanatani, J. Kano, H. Kaji, T. Tsukamoto, T. Yamaguchi, M. Fukase, K. Chihara, Effects of high calcium concentration on the functions and interactions of osteoblastic cells and monocytes and on the formation of osteoclast-like cells, J. Bone Miner. Res. 8 (12) (1993), http://dx.doi.org/10.1002/jbmr.5650081206.
[40] S. Jiang, M. Wang, J. He, A review of biomimetic scaffolds for bone regeneration: toward a cell-free strategy, Bioeng. Transl. Med. 6 (2) (2021), http://dx.doi.org/10.1002/btm2.10206.
[41] K.M. Son, H.C. Park, N.R. Kim, I.S. Lee, H.C. Yang, Enhancement of the ALP activity of C3H10T1/2 cells by the combination of an oxysterol and apatite, Biomed. Mater. 5 (4) (2010), http://dx.doi.org/10.1088/1748-6041/5/4/044107.
[42] W. Götz, E. Tobiasch, S. Witzleben, M. Schulze, Effects of silicon compounds on biomineralization, osteogenesis, and hard tissue formation, Pharmaceutics 11 (3) (2019), http://dx.doi.org/10.3390/pharmaceutics11030117.
[43] K. Jiao, L.N. Niu, Q.H. Li, F.M. Chen, W. Zhao, J.J. Li, J.H. Chen, C.W. Cutler, D.H. Pashley, F.R. Tay, Biphasic silica/apatite co-mineralized collagen scaffolds stimulate osteogenesis and inhibit RANKL-mediated osteoclastogenesis, Acta Biomater. 19 (2015), http://dx.doi.org/10.1016/j.actbio.2015.03.012.
[44] J. Sun, J. Li, X. Liu, L. Wei, G. Wang, F. Meng, Proliferation and gene expression of osteoblasts cultured in DMEM containing the ionic products of dicalcium silicate coating, Biomed. Pharmacother. 63 (9) (2009), http://dx.doi.org/10.1016/j.biopha.2009.01.007.
[45] L. Liu, Y. Liu, C. Feng, J. Chang, R. Fu, T. Wu, F. Yu, X. Wang, L. Xia, C. Wu, B. Fang, Lithium-containing biomaterials stimulate bone marrow stromal cell-derived exosomal miR-130a secretion to promote angiogenesis, Biomaterials 192 (2019), http://dx.doi.org/10.1016/j.biomaterials.2018.11.007.
[46] Z. Tan, B. Zhou, J. Zheng, Y. Huang, H. Zeng, L. Xue, D. Wang, Lithium and copper induce the osteogenesis-angiogenesis coupling of bone marrow mesenchymal stem cells via crosstalk between canonical Wnt and HIF-1 α signaling

pathways, Stem Cells Int. 2021 (2021), http://dx.doi.org/10.1155/2021/6662164.
[47] P. Clément-Lacroix, M. Ai, F. Morvan, S. Roman-Roman, B. Vayssière, C. Belleville, K. Estrera, M.L. Warman, R. Baron, G. Rawadi, Lrp5-independent activation of Wnt signaling by lithium chloride increases bone formation and bone mass in mice, Proc. Natl. Acad. Sci. U.S.A. 102 (48) (2005), http://dx.doi.org/10.1073/pnas.0505259102.
[48] E. O'Neill, G. Awale, L. Daneshmandi, O. Umerah, K.W.H. Lo, The roles of ions on bone regeneration, Drug Discov. Today 23 (4) (2018), http://dx.doi.org/10.1016/j.drudis.2018.01.049.
[49] A.M. Galow, A. Rebl, D. Koczan, J. Gimsa, MC3T3 osteoblast-like cells cultured at alkaline pH: microarray data (Affymetrix GeneChip Mouse 2.0 ST), Data Brief 13 (2017), http://dx.doi.org/10.1016/j.dib.2017.05.013.
[50] A.M. Galow, A. Rebl, D. Koczan, S.M. Bonk, W. Baumann, J. Gimsa, Increased osteoblast viability at alkaline pH in vitro provides a new perspective on bone regeneration, Biochem. Biophys. Rep. 10 (2017), http://dx.doi.org/10.1016/j.bbrep.2017.02.001.
[51] D. Wang, K. Christensen, K. Chawla, G. Xiao, P.H. Krebsbach, R.T. Franceschi, Isolation and characterization of MC3T3-E1 preosteoblast subclones with distinct in vitro and in vivo differentiation/mineralization potential, J. Bone Miner. Res. 14 (6) (1999), http://dx.doi.org/10.1359/jbmr.1999.14.6.893.
[52] A.M. Deliormanlı, H. Atmaca, Biological response of osteoblastic and chondrogenic cells to graphene-containing PCL/bioactive glass bilayered scaffolds for osteochondral tissue engineering applications, Appl. Biochem. Biotechnol. 186 (4) (2018), http://dx.doi.org/10.1007/s12010-018-2758-7.

AGRADECIMIENTOS

En primer lugar, me gustaría expresar mi agradecimiento a la Conselleria de Innovación, Universidades y Sociedad Digital de la Generalitat Valenciana por la concesión del proyecto del programa para grupos de investigación consolidados (CIACO/2021/157), así como a la Agencia Estatal de Investigación y al Ministerio de Ciencia e Innovación (MCIN/AEI/10.13039/501100011033) por la concesión del proyecto PID2020-116693RB-C21, que ha hecho posible la realización de esta Tesis Doctoral.

En segundo lugar, quiero agradecer a mis profesores y mentores, cuya dedicación y orientación han sido fundamentales en mi formación. A mi director de tesis, el Dr. Ángel Murciano, gracias por contagiarnos tu pasión por la investigación, por tu rigurosidad académica y por tu accesibilidad. Tu paciencia y amabilidad han ayudado a que esta etapa, aunque exigente, resultara mucho más llevadera. También me gustaría agradecer a mi co-directora, la Dra. Piedad N. De Aza. Gracias por tu compromiso constante, por guiarme a lo largo de este proceso y por motivarme siempre a mejorar.

Al Dr. Pablo Velásquez, gracias por tu cercanía y por todo el cariño con el que me has acompañado durante esta etapa. Gracias por enseñarme tanto y por hacer que incluso las largas horas frente al microscopio se convirtieran en momentos agradables. Tu apoyo, tus consejos y tu forma de estar presente han sido muy importantes.

También me gustaría expresar mi agradecimiento al Dr. Aldo R. Boccaccini por brindarme la oportunidad de realizar una estancia en el Instituto de Biomateriales de la Universidad de Erlangen-Núremberg. Esta experiencia me permitió adquirir nuevas competencias experimentales y vivir un valioso intercambio cultural. Asimismo, me gustaría agradecer a Marcela Arango Ospina por guiarme durante la estancia y por compartir sus conocimientos.

Quiero extender mi gratitud a todos mis compañeros de laboratorio por haber formado parte de esta etapa y por todas las experiencias vividas. En especial quiero agradecer a Lara Zapardiel: gracias por tu compañía, por tu apoyo incondicional y por tantos buenos momentos que siempre recordaré con cariño. Me siento afortunada de poder llamarte amiga.

Por último, quiero agradecer profundamente a mi familia. A mis padres, a mi hermano, a mi madrina y a mis abuelas: gracias por estar siempre, por escucharme, por animarme y por acompañarme, incluso en la distancia.

A Pablo, gracias por ocupar un lugar tan especial en todo este proceso, por estar siempre en mi equipo, por celebrar conmigo mis logros y sostenerme en los días más difíciles.

Gracias por cuidarme como lo has hecho y, simplemente, por ser tú. Y gracias también a tu familia por su calidez y apoyo, que han significado mucho en esta etapa.

Cada uno, a su manera, me ha dado fuerza y confianza en los momentos clave. Vuestro cariño ha sido esencial para llegar hasta aquí.